

Figure 3. Percentage of the liquid uptake by hydroxypropyl methylcellulose at various time after contact with aqueous medium

Figure 3 shows the percentage of liquid uptake by HPMC at various time intervals after contact with aqueous medium. The results showed that during swelling of the HPMC tablets, an anisotropic swelling phenomena (i.e., more swelling in the axial direction than in the radial direction on exposure to water) was seen. Similar phenomena were observed by Lopes et al. [8] and Van Veen et al. [11] who related the predominantly axial relaxation of the HPMC compacts to the relief of stress induced during compaction and the unidirectional swelling to the orientation of the molecules during compression. So the percentage of HPMC release from difference thickness larger of coating was shown in Figure 4.

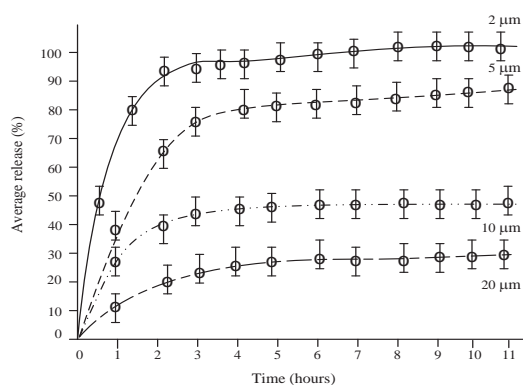


Figure 4. Percentage of HPMC release from difference thickness layer of coating at 1000 particles size

The results in Figure 4 show that the average of release will be low percentage when the thickness layer of film was more than 20 μm . In contrast, the percentage of release will be increased rapidly if the film layer was less than 2 μm . At the same time, the comparative in vitro HPMC particle size and the thickness layer of coating between experiment test and

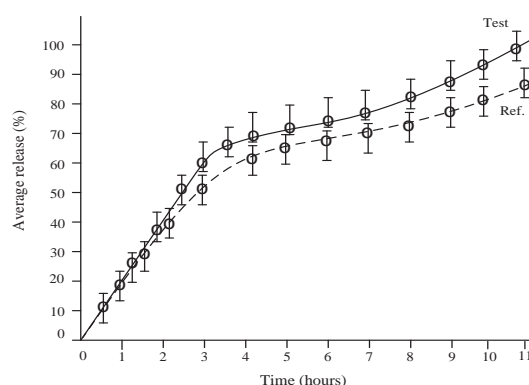


Figure 5. Comparative in vitro HPMC K100 release profile for 800 μm particle size and 10 μm thickness layer of coating and reference is Voveran S.R. tablet [10]

the reference as shown in Figure 5.

4. Conclusions

Cellulose is the most abundant naturally occurring biopolymer. Various natural fibers such as cotton and higher plants have cellulose as their main constituent. It consists of long chains of anhydro-D-glucopyranose units (AGU) with each cellulose molecule having three hydroxyl groups per AGU. Cellulose is insoluble in water and most common solvents; the poor solubility is attributed primarily to the strong intramolecular and intermolecular hydrogen bonding between the individual chains.

However, chemical modification of cellulose is performed to produce cellulose derivatives (cellulosics) which are in general strong, low cost, reproducible, recyclable and biocompatible. So they can be tailored for pharmaceutical applications. Thus cellulose derivatives are often used to modify the release of drugs in tablet and capsule formulations and also as tablet binding, thickening and rheology control agents, for film formulation, water retention, improving adhesive strength for suspending and emulsifying.

Furthermore, the decrease of apparent permeability versus coating level was related to the reduction of the total hole area of porous film. The apparent permeability was found to increase with the HPMC concentration. After a critical concentration was reached, the further addition of HPMC into the film caused a rapid increase in apparent permeability. Therefore, a rapid increase of the drug release was observed when the dissolution profile of a sample made from a regular sugar nonpareil core (soluble) was compared with the sample made from a precoated nonpareil core (insoluble). Thus it suggests that the drug release can be enhanced by the dissolution of the core.

A minimum concentration of the HPMC was required to effectively modify permeability of the film.

Acknowledgements

The author was various supported by Department of Industrial Physics and Medical Instrumentation, Faculty of Applied Science, King Mongkut's University of Technology North Bangkok.

References

- [1] A.M. El-Helw, and M.A. Bayomi, *Saudi Pharma. J.* **8** (2000) 31-38.
- [2] F.N. Kaputskii, E.V. Gert, V.I. Torgashov, and O.V. Zubets, *Fiber Chem.* **37** (2005) 485-489.
- [3] M. Rahmouni, V. Lenaerts, D. M. Johnson, and J.C. Leroux, *Pharma. Dev. and Tech.* **8** (2003) 335-348.
- [4] Y. Miyazaki, S. Yakou, T. Nagai, and K. Takayama, *Drug Dev. Ind. Pharma.* **29** (2003) 795-804.
- [5] P. Kunal, A.K. Banthia, and D.K. Majumdar, *Biomed. Mate.* **1** (2006) 85-91.
- [6] J. Liu, S. Lin, L. Li, and E. Liu, *Inter. J. Pharma.* **298** (2005) 117-125.
- [7] J.R. Nixon, and G.A. Agyilirah, *J. Pharma. Sci.* **73** (1984) 52-54.
- [8] C.M. Lopes, J.M.S. Lobo, P. Costa, and J.F. Pinto, *Drug Dev. Ind. Pharma.* **32** (2006) 95-106.
- [9] R.V. Kulkarni, S. Mutalik, and D. Hirmath, *Indian J. Pharma. Sci.* **64** (2002) 28-31.
- [10] R.C. Rowe, R.J. Sheskey, and P.J. Weller, *Handbook of Pharmaceutical Excipients*. London, UK: Pharmaceutical Press (2003).
- [11] B. Van Veen, G.K. Bolhuis, Y.S. Wu, K. Zuurman, and H.W. Frijlink, *Euro. J. Pharma. and Biopharma.* **59** (2005) 133-138.
- [12] S. Kiil, and J.K. Dam, *J. Control Release* **90** (2003) 1-21.
- [13] S. George, and S. Thomas, *Progress in Polymer Sci.* **26** (2001) 985-1017.
- [14] M. Donbrow, and Y. Samuelov, *J. Pharm. Pharma.* **32** (1980) 463-470.
- [15] T. Higuchi, *J. Pharma. Sci.* **52** (1963) 1145-1149.
- [16] R.W. Korsmeyer, R. Gurny, E.M. Doelker, P. Buri, and N.A. Peppas, *Inter. Pharma.* **15** (1983) 25-35.

FILLER MODIFICATION FOR IMPROVEMENT OF PAPER STRENGTH IN PAPERMAKING

Patcharin Ponklaew¹, Panitnad Chandranupap^{1*}, and Pravitra Chandranupap²

¹ Department of Chemical Engineering, Faculty of Engineering,
King Mongkut's University of Technology North Bangkok, Bangkok 10800, Thailand

² Department of Industrial Chemistry, Faculty of Applied Science,
King Mongkut's University of Technology North Bangkok, Bangkok 10800, Thailand

*E-mail: pnn@kmutnb.ac.th

Abstract: Fillers in papermaking process play an important role in various papers' physical properties. One of the most common fillers is precipitated calcium carbonate (PCC). Modification of PCC with modified starch was investigated in order to improve filler's properties. Effects of poly-aluminum chloride (PAC) coagulant were also investigated. The experimental results showed that starch-coated PCC yielded higher tensile and tear strengths than unmodified PCC. PAC dosages tended to affect coating of starch gel onto PCC particles. Paper brightness, opacity and freeness also increased as the PAC content increased. However, the experimental results also showed that physical and optical properties of the paper depend on PCC content more than PAC in papermaking process.

1. Introduction

Papermaking process in industry utilizes fillers in order to reduce uses of virgin fiber in paper stock. The increase filler content in paper can reduced raw material cost and energy consumption. Because of the water removal rate during papermaking, it can drain and dry more easily on the paper machine [1]. However the level of filler in paper is increased, paper strengths are usually decreased. This is due to the decrease in amount of fibers in the sheet which reduces the amount of fiber-fiber bonding and reduced area of contact between the fibers [2].

Fiber modification can be done in various ways. One interesting method is starch-coated filler. This ability in improving paper strength [1-4]. The typical fillers used in papermaking are kaolin, titanium dioxide, hydrated aluminum, calcium carbonate, silica, talc, etc.[5]. These fillers provide difference properties. Among various fillers, calcium carbonate is the most common. Calcium carbonate filler shows ability to provide fine quality paper and coated paper with firm body and excellent optical, smoothness, writing suitability, tactile sensation, printability, and other properties [3, 4].

Starch has been used as dry strength agent in paper because of its low cost, high performance, easy availability and environmental friendliness of the modifiers [4, 6]. Starch is a glucose polymer which anhydroglucose units are joined to each other by a 1,4-

α -D-glucosidic bond. Glucose chains are either branched chains (amylopectin) or straight chains (amylose) in the starch molecule. In a normal case, in starch have 20-25% amylose. Starch has hydroxyl group [4]. Its ability absorb to wood fiber during wet-end processing, which enhances bonding due to the formation of hydrogen bonds. Although starch can improve the strength of paper [1-4], the starch currently used in the paper industry are modified starch. The modified starch are more expensive than the raw starch because they undergo chemical modification, with either anionic chemical groups or cationic chemical groups being grafted onto the starch molecules [3]. Therefore, handsheets made with the modified PCC with coated starch, starch gel layer on the aggregate surface improve bonding capacity of the aggregate to fiber. Starch has cationic groups, which are capable of forming hydrogen bonds with anionic charges onto wood fiber surfaces to improve paper strength [3, 4].

Previous studies showed that poly-aluminum chlorides (PAC) is the most widely used wet-end additive for the development of dry strength of papermaking. PAC is inorganic coagulant used for enhancing the dry strength of paper and to promote dewatering during the forming process [7, 8]. The cationic species of PAC adsorbed on the fiber surfaces. The anionic carboxylic groups on the fiber surface can react with aluminum ions (Al^{3+} as well as aluminum polymers) to form cationic sites that form ionic or coordination complexes. Therefore, effect of PAC on strength development because of cross-linking improve the strength of paper [9].

This work investigated the paper properties before and after using modified starch and studied the result of PAC when filling PAC in the slurry in order to figure out the suitable condition for papermaking process.

2. Experimental

2.1 Materials

Unbleached Kraft eucalyptus pulp (Kappa number ca. 24, Advance Agro Co.) was used for making paper handsheet. Precipitated calcium carbonate was supplied by Brightchem Sdn. Bhd. Co., Ltd. Modified tapioca

starch was supplied by Big Tree Intertrade Co., Ltd. Poly aluminum chloride (conc. 10-11 %w/w) was supplied by Thai Pac Industry Co., Ltd.

2.2 Filler modification

The PCC suspension was mixed with modified starch powder, the amount of modified starch was 12% based on the dry weight of PCC filler. Suspension of PCC and starch were filtered to remove water. The obtained solid was smashed, then cooked in a water bath at 90°C for 3 hours. The cooked mixture was ground in a mortar for 30 min or until it was powdered.

2.3 Handsheets preparation and determination of paper properties

Modification of PCC filler with starch and PAC were added into pulp slurry. PAC dosages were 4%, 8% and 12% based on the dry weight of modified PCC filler. Handsheets with a target basis weight of 60 g/m² were produced according to standard TAPPI method T 205.

The physical properties of tensile strength, tearing strength, brightness and opacity of the paper were measured according to standard TAPPI method T 494, T 414, T 452 and T 425, respectively. Also the freeness properties were measured according to standard TAPPI method T227.

3. Results and Discussion

3.1 Effect of modified filler on paper strength

The effect of starch-coated PCC modified method on physical paper properties depend on PCC and PAC content as shown in Figure 1 and 2.

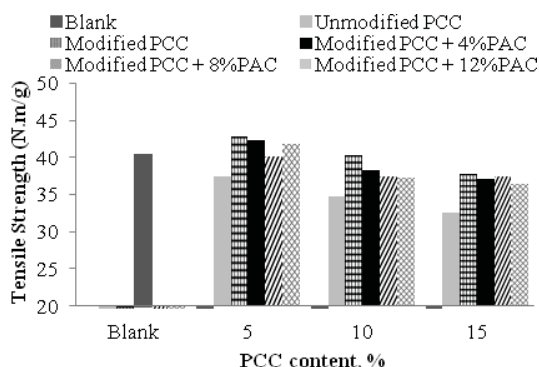


Figure 1. Tensile strength as a function of content for blank, PCC only, starch-coated PCC and starch-coated PCC with PAC-added handsheet.

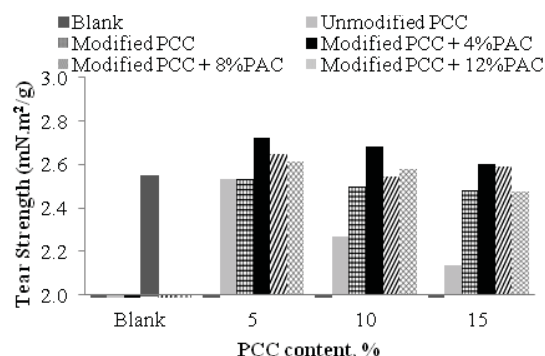


Figure2. Tear strength as a function of content for blank, PCC only, starch-coated PCC and starch-coated PCC with PAC-added handsheet.

Figures 1 and 2 showed that tensile and tear strength of handsheets prepared from modified PCC with starch are higher than that of the handsheet prepared from unmodified PCC. Increase of filler content in handsheet decreased strength properties because fillers can interfere with fiber-fiber bonding. As a result, amount of fiber-fiber bonding and fiber-filler bonding decreased when PAC dosages were 4%, 8%, and 12%. Tensile strength of the filled handsheet was all lower than that of the unfilled handsheet due to the incorporation of fillers in the fiber matrices. On the other hand, tear strength did not show negative influence. At PAC dosage of 4%, the results showed better strength properties. These results showed the improvement of strength paper properties with modified filler, it can be used to achieve high filler content paper while maintaining the paper strength, when compared with blank.

3.2 Effect of modified filler on optical properties

Considering for development of filler is the most important which optical properties of filler-added paper depend on chemical composition of filler, particle morphology, particle size, and filler content [5].

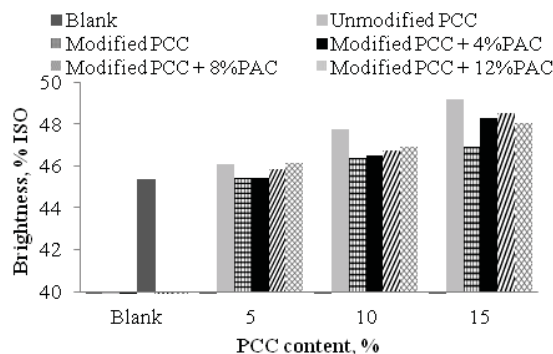


Figure 3. Brightness as a function of content for blank, PCC only, starch-coated PCC and starch-coated PCC with PAC-added handsheet.

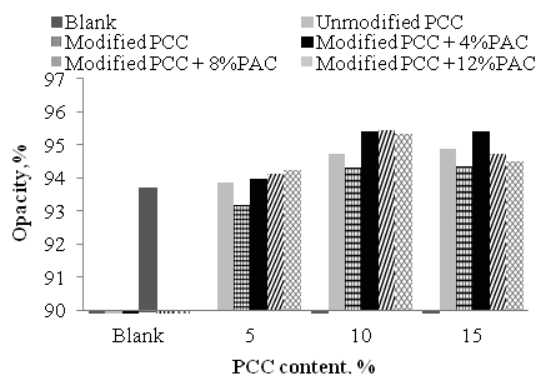


Figure 4. Opacity as a function of content for blank, PCC only, starch-coated PCC and starch-coated PCC with PAC-added handsheet.

Figures 3 and 4 illustrated that the increase of PCC content in handsheet increased brightness and opacity. The handsheet added with PCC filler and PAC tend to improve brightness and opacity properties. Usage of starch-coated PCC with PAC dosage of 12% gave the high optical properties. Brightness was high due to the incorporation of high brightness filler in sheets. However, the PAC dosages of 4%, 8%, and 12% gave similar optical properties.

3.3 Effect of modified filler on drainage properties

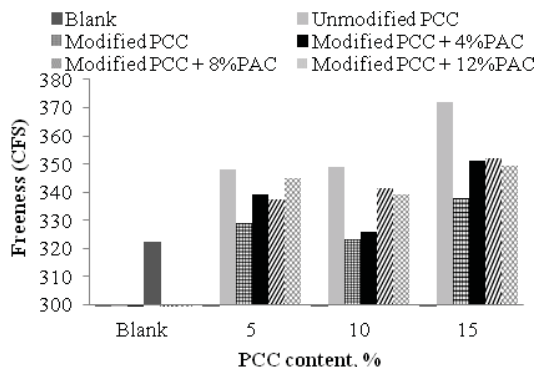


Figure 5. Freeness as a function of filler content for blank, PCC only, starch-coated PCC and starch-coated PCC with PAC-added handsheet.

Figure 5 showed that filler addition to the handsheet increased the freeness. This is due to these fillers inhibited water absorption of fiber. As a result, PCC modified with starch decreased the freeness when compared with unmodified PCC. This is may be due to starch swelling on PCC surface by water. Nevertheless, increase of PAC content had a trend to increase

freeness. This is may be due to penetration of PAC between fibers that made loose fiber.

4. Conclusions

Paper handsheets made with the starch-coated PCC could be used at high filler content while maintaining the paper strength. Increased filler content in the handsheet enhance brightness, opacity, and drainage properties. Improvement of handsheet with PAC gave the high physical and optical properties. However these fillers could reduce pulp fiber in the paper from papermaking process, conserving the environment.

References

- [1] S.Y. Young and Y. Deng, *TAPPI Journal*, Vol. 5, No. 9, September (2006) 3-9.
- [2] S. Chauhan Vipul, K. Bhardwaj Nishi and K. Chakrabarti Swapan, *IPPTA J.*, Vol. 23, No. 2, April-June, (2011) 93-100.
- [3] Y. Zhao, Z. Hu, A. Ragauskas and Y. Deng, *TAPPI Journal*, Vol. 4, No. 2, February (2005) 3-7.
- [4] Z. Yan, Q. Liu, Y. Deng and A. Ragauskas, *Journal of Applied Polymer Science*, Vol. 97, (2005) 44-50.
- [5] J.C. Roberts, *Paper Chemistry*, Vol. 2, (1996) 194-230.
- [6] J. Shen, Z. Song, X. Qian and F. Yang, *Carbohydrate Polymer* **81** (2010) 545-553.
- [7] M.H. Ekhtera, P.R. Charani, O. Ramezani and M. Azadfallah, *Bioresources*, Vol. 3, No.2, (2008) 383-402.
- [8] R.M. Trksak, *Papermakers Conference*, (1990) 229-237.
- [9] Y.Hamzeh, M.H. Ekhtera, M.A. Hubbe, S. Izadyar and K. Pourtahmasi, *Ind. Eng. Chem. Res.*, Vol. 47, (2008) 4302-4307.

INFLUENCE OF USING DIFFERENT GEL RETARDING AGENTS ON THE PROPERTIES OF SOL-GEL DERIVED HYDROXYAPATITE BIOACTIVE COATING

Waraporn Suvannapruk, Faungchat Thammarakcharoen, Jintamai Suwanprateeb*

National Metal and Materials Technology Center, National Science and Technology Development Agency,
114 Paholyothin Road, Klong 1, Klongluang, Pathumthani, 12120 Thailand

* Author for correspondence; E-Mail: jintamai@mtc.or.th, Tel. +66 2 5646500, Fax. +66 2 5646446

Abstract: Recently, the sol-gel technique has been studied as an alternative mean for coating of hydroxyapatite on the metallic implant since it offers several advantages for example better control of the chemical composition of the coating, the homogeneity of films, control of the film microstructure and low processing temperature. In addition, the processing cost is comparatively low since no costly or complicated equipments are needed. It requires only simple laboratory equipments for wet chemistry. This technique is also capable to coat substrates over a wide range and complication of shape and size. The sol-gel system of using calcium nitrate tetrahydrate as calcium source and phosphorus pentoxide as phosphorus source has proved to be simple and did not require stringent controlled atmosphere. This type of mixture has shown to produce monophasic hydroxyapatite powders successfully at low sintering temperature of several hundred degree celcius. This system was applied to produce a thin film coating as well, but the sol tended to gel relatively fast so affecting the coating ability and the shelf-life of the sol. In this study, three gel retarding agents including nitric acid, ammonium hydroxide and ammonium hydrogen carbonate were employed in the system aiming to delay the gelling time of the sol and improve the coating performance. Properties in terms of sol gelling time, pH of the sol, coating uniformity and phase composition of the sintered coating were investigated. It was found that all three gel retarding agents could increase the gelling time from 24 hours to more than 1 week. The nitric acid mixed sol produced a non-uniform and highly shrinkage coating similar to the non-mixed sol whereas both ammonium hydroxide and ammonium hydrogen carbonate mixed sols could produce uniform and non-shrank coatings. pH of the sol decreased from 2 to 1 after mixing nitric acid, but increased to 7 and 11 when adding ammonium hydrogen carbonate and ammonium hydroxide respectively. All the sols were similarly converted to hydroxyapatite after sintering at 550 °C for 1 hour as determined by x-ray diffraction signifying that the use of gel retarding agents in the sol only affected the coating ability, but did not interfere with the formation of hydroxyapatite phase.

1. Introduction

Hydroxyapatite is one of calcium phosphate family that has been widely used as bone analogue implants in dental and orthopaedic applications due to its chemical and crystallographic similarity to natural bone and its ability to bond directly to the bone. Apart from being used as implants, hydroxyapatite is also employed as bioactive coating on the biomedical

metals in order to render the bioactivity to the metallic implants and has become a promising approach to produce bioactive implants for load bearing applications.

Typically, coating of hydroxyapatite on the metallic implant is done by thermal spraying process. However, due to its extremely high temperature technique, phase heterogeneity and coating delamination which could lead to the failure are encountered as a result [1-2]. Recently, the sol-gel technique has been studied as an alternative mean for coating of hydroxyapatite on the metallic implant since it offers several advantages for example better control of the chemical composition of the coating, the homogeneity of films, control of the film microstructure and low processing temperature [3-6]. In addition, the processing cost is comparatively low since no costly or complicated equipments are needed. It requires only simple laboratory equipments for wet chemistry. This technique is also capable to coat substrates over a wide range and complication of shape and size. The sol-gel system of using calcium nitrate tetrahydrate as calcium source and phosphorus pentoxide as phosphorus source has proved to be simple and did not require stringent controlled atmosphere [7-11]. This type of mixture has shown to produce monophasic hydroxyapatite powders successfully at low sintering temperature of several hundred degree celcius. This system was applied to produce a thin film coating as well, but the sol tended to gel relatively fast and affected the coating process. This study was, thus, aimed to modify the sol by using gel retarding agents that could delay the gelling time and compare the properties of the new sol and its coating properties to the non-modified sol.

2. Materials and Methods

2.1 Sol Preparation

Precursors with Ca/P molar ratios of 1.67 were prepared by separately mixing calcium nitrate tetrahydrate (Sigma-Aldrich) and phosphorus pentoxide (BDH) with ethyl alcohol (BDH) at laboratory atmosphere for 30 minutes. The precursors were then mixed together and further stirred for 1 hour to produce a sol, designated Sol A. In addition, either 10 ml of nitric acid (Merck), ammonium hydroxide (Sigma-Aldrich) or ammonium hydrogen carbonate

(Sigma-Aldrich) were also added during precursors mixing to produce sol samples, designated Sol B, C and D respectively. Nitric acid was selected due to the similarity of released acid in the reaction by calcium precursor.

2.2 Coating Preparation

Coating on titanium (cpTi gr2, Pengfa Industry Inc.) was carried out by dip coating technique. This was done by dipping the titanium disc having a diameter of 25 mm and thickness of 0.5 mm into the sol by a dip coater (PTL-200, MTI Corporation) using a dipping and withdrawing rate of 2 mm min⁻¹ and then heated in air at 550 °C for 1 hour before cooling to room temperature.

2.3 Characterization

After mixing, pH of the sols was measured by a pH meter (UB-5, Denver Instrument) at room temperature. Sol gelling time was determined by flipping the glass container up and down and determined the gel characteristic i.e did not flow everyday for up to 30 days. Coating uniformity was carried out by observing the liquid coating on the titanium disc during dipping and withdrawing from the sol solution and the solid coating after sintering. Phase compositions of a coating on Ti were investigated by an X-ray diffractometer (JEOL JDX 3530) using CuK (1.54056 Å) as radiation source in the range of 10-80 ° 2θ. JCPDS files were used to identify the peaks of main components in sample.

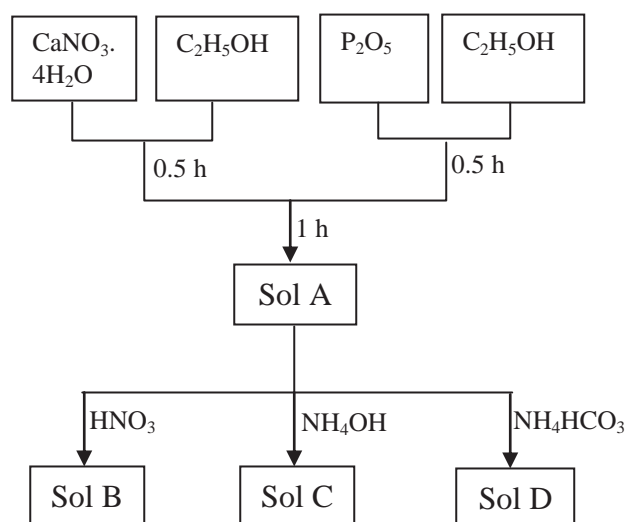


Figure 1. Schematic diagram of sol preparation.

3. Results and Discussion

Figure 2 shows the appearance of the sols at 24 hours after mixing. Sol A readily turned from clear sol to cloudy gel which could not be used for coating while sols B, C and D remained stable liquid sols for up to 30, 7 and 30 days respectively after leaving at the laboratory atmosphere, table 1. Sol B remained

relatively clear throughout the observation period whereas sol C and D became cloudy sols. The pH of the sols changed from 2 in the case of Sol A to 1, 11 and 7 for sol B, C and D sols. These changes in pH were due to the acidic and basic nature of the added gel retarding agents in those sols which were a strong acid, a strong and weak base respectively. Previously, it was noted that the stability of the sols was one of the properties that are needed in coating application. In the case of sol-gel technique, reactants and additives were shown to influence the stability of the sol. Acetic acid was seen to reduce the amount of precipitation of the alkoxide sol-gel and produce a stable sol for coating by depressing the reaction between reactants [12-13] while the use of trifluoroacetic acid and hexafluorophosphoric acid produced more stable sols than using ammoniumhexafluorophosphate for preparation of fluoridated hydroxyapatite film [14]. In the present research, nitric acid, ammonium hydroxide and ammonium hydrogen carbonate were found to be effective in producing stable sols compared to the non-mixed sol.

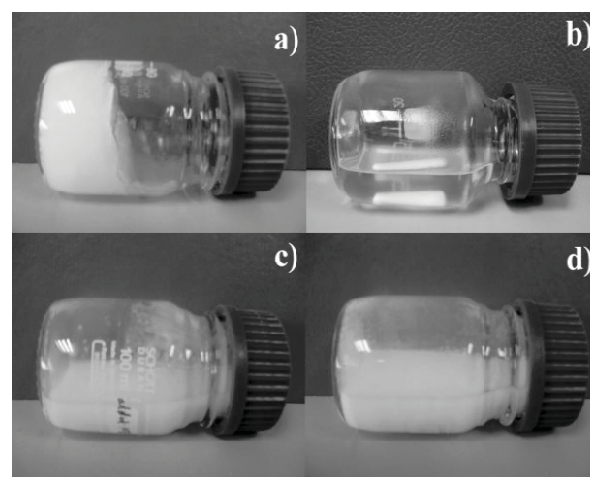


Figure 2. Appearance of the sols after being left at room temperature for 24 hours; a) Sol A; b) Sol B; c) Sol C and d) Sol D.

Table 1: pH and sol gelling time of various sols.

Samples	pH	Sol Gelling Time (days)
Sol A	2	1
Sol B	1	30
Sol C	11	7
Sol D	7	30

In the case of coating uniformity, it was seen that the coating of sol A could be formed on the titanium surface once removing from the sol solution, but gradually shrank toward the center of titanium disc creating a non-uniform coating after leaving on the bench. In contrast, limited coating of sol B was seen on the titanium surface as scattered liquid drops

indicating its poor wetting property. Sols C and D could form uniform and smooth coatings without shrinkage. It was also noted that the coating of Sol A turned to liquid within a few minutes indicating its high hygroscopicity and needed oven drying to maintain its solid state. The coating of sol B did not solidify at all and needed oven drying to produce a dry film. In contrast, the modified sols, either sols C or D, solidified instantly without using high temperature drying and remained solidified coatings for several hours. This may be attributed to the presence of residual water ions and the incomplete reaction between reactants in the case of sols A and B [13]. After sintering at 550 °C, the non-uniformity of the coating produced by sol A converted to a shrunk and irregular thickness coating on the Ti surface, figure 3a. Isolated and limited amount of coating produced by sol B was seen on the titanium surface after sintering, figure 3b. Sols C and D coated sols displayed smooth and uniform thin coating, figures 3c and 3d. These all indicated the superior coating ability and uniformity of sols C and D. After sintering, all the coating remained as solid coating for indefinite storage periods.

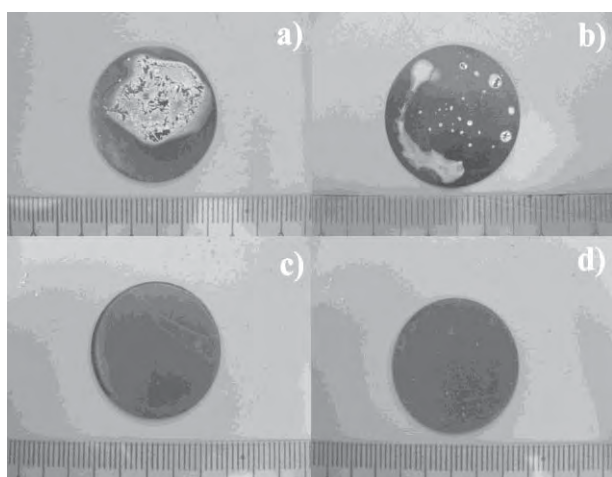


Figure 3. Comparison of coated Ti by using different sols after sintering at 550 °C for 1 hour; a) Sol A; b) Sol B; c) Sol C and d) Sol D.

XRD analysis in figure 4 revealed that the main phase composition of all coatings were hydroxyapatite without other impurity phases. Corresponding to the appearance of the coating on the titanium disc as shown in figure 3, the intensities of the hydroxyapatite characteristic peaks of sols C and D were relatively greater than those of sol A. The peak intensities of hydroxyapatite in sol B were the lowest amongst other sols whereas the peak intensities of titanium were the greatest. This difference was related to the amount of coating coverage on the titanium surface and also the thickness of the coating produced.

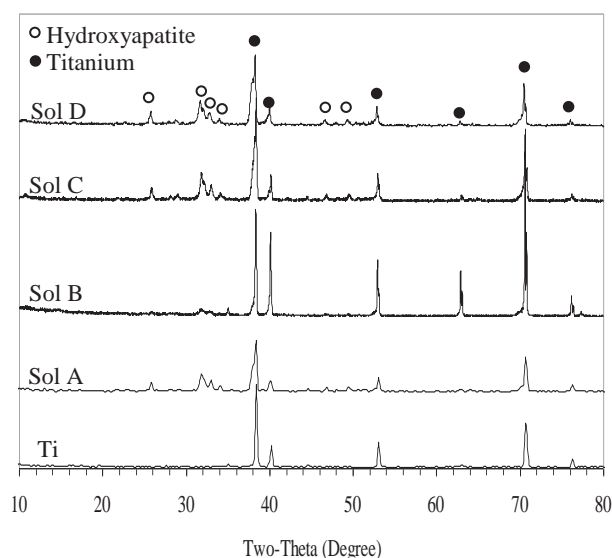


Figure 4. A comparison of phase compositions of sintered coating produced by different sols.

4. Conclusions

It could be concluded that the use of ammonium hydroxide and ammonium hydrogen carbonate as gel retarding agents in the sol mixture based on calcium nitrate tetrahydrate and phosphorus pentoxide could increase the gelling time and improve the coating process without affecting the formation of hydroxyapatite phase in the sintered coating. This could be used to improve the sol-gel coating process.

Acknowledgements

National Metal and Materials Technology Center, National Science and Technology Development Agency is thanked for financial support.

References

- [1] L. Sun, C.C. Berndt, K.A. Gross and A. Kucuk, *J. Biomed. Mater. Res.* **58** (2001) 570-592.
- [2] R. Heimann, N. Schürmann and R. Müller, *J. Mater. Sci.: Mater. in Med.* **15** (2004) 1045-1052.
- [3] K.A. Gross, C.S. Chai, G.S.K. Kannangara, B. Ben-Nissan and L. Hanley, *J. Mater. Sci.: Mater. in Med.* **9** (1998) 839.
- [4] L. Guo and H. Li, *Surf. Coat. Tech.* **185** (2004) 268-274.
- [5] W. Weng, G. Shen and G. Han, *J. Mater. Sci. Lett.* **19** (2000) 2187-2188.
- [6] A. Montener, G. Gnappi, F. Ferrari, M. Cesari and M. Fini, *J. Mater. Sci.* **35** (2000) 2791-2797.
- [7] W. Feng, Li Mu-sen, Lu Yu-peng and Qi Yong-xin, *Mater. Lett.* **59** (2005) 916-919.
- [8] M.H. Fathi and A. Hanifi, *Mater. Lett.* **61** (2007) 3978-3983.
- [9] K. Il-Seok and P. N. Kumta, *Mater. Sci. Eng. B.* **111** (2004) 232-236.
- [10] P. Q. Franco, C. F. C. Joao, J. C. Silva and J. P. Borges., *Mater. Lett.* **67** (2012) 233-236.

- [11] W. Weng and J.L. Baptista, *J. Mater. Sci.: Mater. in Med.* **9** (1998) 159-163.
- [12] W. Weng and J.L. Baptista, *Biomaterials*. **19** (1998) 125-131.
- [13] W. Weng, L. Huang and G. Han, *Appl. Organometal Chem.* **13** (1999) 555-564.
- [14] K. Cheng, G. Han, W. Weng, H Qu, P. Du, G. Shen, Y. Yang and J.M.F. Ferreira, *Mater. Res. Bull.* **38** (2003) 89-97.

TOUGHENING OF POLY(LACTIC ACID) BY REACTIVE BLENDING WITH HYPER-BRANCHED POLY(LACTIC ACID-CO-CAPROLACTONE)

Tippawan Chuenta¹, Atitsa Petchsuk², Pakorn Opaprakasit³, Mantana Opaprakasit^{1*}

¹ Department of Materials Science, Faculty of Science, Chulalongkorn University, Pathumwan, Bangkok, 10330 Thailand

² National Metal and Materials Technology Center (MTEC), Klong Luang, Pathum Thani, 12120 Thailand

³ School of Bio-Chemical Engineering and Technology, Sirindhorn International Institute of Technology (SIIT), Thammasat University, Pathum Thani, 12121 Thailand

* Author for correspondence; E-Mail: mantana.o@chula.ac.th, Tel. +66 2185559, Fax. +66 22185561

Abstract: This research work is aimed to develop toughened poly(lactic acid) (PLA) *via* reactive blending of PLA with hyper-branched PLA copolymers (HBP) and polyanhydride (PA). Effects of HBP's chemical structures and the presence of PA on the blends mechanical and thermal properties are investigated. The hyper-branched copolymers, *i.e.*, LA HBP and LA-co-CL HBP, are synthesized from lactide (LA) and caprolactone (CL) at molar ratios of 1:0 and 1:1, respectively. PLA/HBP blends are prepared by an internal mixer with 20 phr. of HBP. The LA-co-CL HBP blend exhibits higher elongation at break and toughness, compared to that of LA HBP. Although the elongation at break of LA-co-CL HBP blend is higher than neat PLA, its tensile strength, modulus and toughness are lower. Therefore, PLA/HBP/PA blends are further investigated. The presence of PA in the blends leads to a decrease in tensile strength, modulus, elongation at break and toughness. It is revealed from the blend morphology taken from SEM that poor mixing of PA into PLA/ LA-co-CL HBP blend is likely a resulting in a property deterioration of the blend.

1. Introduction

Environmental concerns on the rapidly-increased usage of non-degradable plastics and the sustainability issue associated with commodity plastics derived from petroleum resources have recently brought many research and developments to environmental-friendly and sustainable polymers. Poly(lactic acid) (PLA) is biodegradable and renewable polymer, which is extensively researched. However, its brittleness limits its use in large-scale applications.[1] Many studies have focused on improving of PLA toughness. An addition of plasticizers, *e.g.* citrate esters, low molecular weight polyethylene glycol, and lactide oligomers, effectively enhance % elongation of PLAs, in the cost of lowering their tensile strength and modulus. [2-5] This is because low MW molecules have tendency to immigrate to the specimen's surface after storage.[1,5]

Blending of PLA with other flexible polymers, which have low T_g , or rubbers is another effective approach. The introduction of dispersed phase of filler polymers imposes similar effect on the blend's mechanical properties, compared to the addition of plasticizers. Although improvements in % elongation, toughness and impact strength are achieved, a deterioration in tensile strength and modulus is

observed, and is typically dependent on phase compatibility.[6-9] Therefore, an increase in toughness without affecting the sample's strength and stiffness is challenging. Reactive blending of PLA with hyper-branched polymer (HBP) and polyanhydride (PA) was reported in ref. 10 and 11, where the blended specimen's toughness and elongation at break largely increased, with a slight decrease in tensile strength and modulus, compared to neat PLA. Bhardwaj and Mohanty[10] reported that polyanhydride (PA) acted as a crosslinking agent for commercial HBP with dendritic structure consisting of 6 hydroxyl end groups. The resulting PLA/HBP/PA blend contained crosslinked HBP as a dispersed phase in PLA matrix, leading to an increase in elongation at break and toughness of ~847% and ~570%, respectively.

This research is aimed to develop toughened PLA product *via* a reactive blending method by using HBPs. HBPs with 2 different structures, *i.e.*, LA HBP and LA-co-CL HBP, are synthesized and used as a dispersed phase in PLA. Efficiency of the HBPs component on the improvement of the PLA blend's tensile properties is examined. Effect of adding PA component to PLA/HBP blends on properties of the blends are also investigated.

2. Materials and Methods

2.1 Materials

Poly(lactic acid) (PLA), Ingeo™ Biopolymer 2003D, was supplied by NatureWorks LLC. Hyper-branched PLA (HBP) samples were synthesized in this laboratory. LA HBP is a hyper-branched poly (lactic acid) with $M_n \sim 11,300$ g/mol, PDI ~ 3.3 and a branched number of ~ 34.5 . LA-co-CL HBP is a hyper-branched poly(lactic acid-co-caprolactone) with $M_n \sim 10,600$ g/mol, PDI ~ 3.1 and branched number ~ 26.1 . Polyanhydride (PA) was supplied by Sigma-Aldrich ($M_n = 30,000$ -50,000 g/mol).

2.2 Reactive Blending

PLA, HBP and PA samples were dried at 60°C for 12 hours in a convection oven before blending. The blends were prepared by melt mixing in an internal mixer (MX500-D75L90, Chareon tut, Thailand). The mixing condition was 170°C at 50 rpm for 8 minutes.

2.3 Characterizations

Tensile testing: The tensile properties were measured by Universal Testing Machine (LLOYD LR 100K). The test specimens were prepared by compression moulding in thin sheet and tested following ASTM D882. The crosshead speed was 10 mm/min.

Differential scanning calorimetry (DSC): The glass transition temperature (T_g), melting temperature (T_m), crystallization temperature (T_c), enthalpy of melting (ΔH_m) and enthalpy of crystallization (ΔH_c) of the blends were measured by differential scanning calorimetry (DSC). The heating and cooling rate were a 20°C/min. while the rate of temperature was -60°C to 200°C in heat-cool-heat cycle. Glass transition temperature (T_g) is determined from the 1st heating thermogram. Crystallization temperature (T_c) and enthalpy of crystallization (ΔH_c) are determined from the cooling thermogram. The melting temperature (T_m), enthalpy of melting (ΔH_m), and degree of crystallinity (χ) are examined from the 2nd heating cycle. The degree of crystallinity (χ) was calculated by the equation as below;

$$\chi = \frac{\Delta H_m}{f \cdot \Delta H_m^0} \times 100\%$$

Where f is weight fraction of PLA in the blend and ΔH_m^0 is 93.7 J/g reported in ref. 11 as the enthalpy of melting of 100% fully crystalline PLA.

Scanning Electron Microscopy (SEM): The interphase compatibility and morphology of the blends were characterized by scanning electron microscopy (SEM) (JSM-5410LV, JEOL) at 20kV.

3. Results and Discussion

2.1 Tensile properties

Stress-strain behaviors of neat PLA and its blends are compared in Figure 1, where the tensile properties are summarized in Table 1. All blends show brittle deformation behaviors. Tensile strength and modulus of the PLA/HBP blends are much lower than those of neat PLA. In contrast, adding of 20 phr of HBPs into PLA leads to an increase in the elongation at break of these blends. Table 1 shows that toughness of all blends is comparable to that of neat PLA. This implies that LA-co-CL HBP possesses much better tendency in softening of PLA matrix, compared to LA HBP. This is likely a result from their different T_g , where LA-co-CL HBP has much lower T_g (-32°C) than LA HBP (42°C). Effect of adding 10 phr PA to PLA and PLA/HBP blends on tensile properties is also investigated. Tensile modulus of all blends is slightly affected by the presence of PA. On the other hand, their tensile strength, elongation at break and toughness are depleted dramatically. This is in contrast to the findings of Bhardwaj and Mohanty[10], which were derived from blends of PLA, PA, and commercial HBP consisting of 6 hydroxyl end groups. The authors found that the addition of PA for crosslinking of the HBP dispersed phase, led to an increase in toughness and elongation at break of Table 1: Tensile properties of PLA and its blends.

~570% and ~847%. On the other hand, the tensile strength and modulus of the samples decreased.

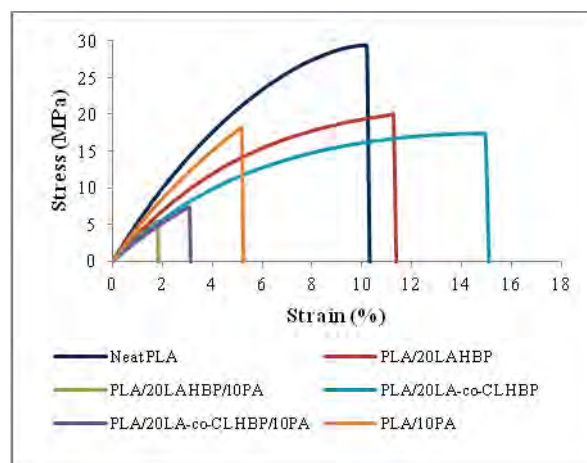


Figure 1. Stress-strain curve of PLA and its blends.

2.2 Thermal properties

Table 2 summarizes thermal properties of the samples, where T_g and T_m of the processed PLA are ~44.9°C and 116°C. PLA/PA, PLA/LA HBP and PLA/LA HBP/PA blends show single T_g at a temperature close to that of PLA. For blends containing LA-co-CL HBP, additional T_g of HBP is observed at -29°C. This reflects that LA-co-CL HBP is phase separated from PLA matrix. However, miscibility of LA HBP blends cannot be examined, as T_g 's of the constituent components are very close. All blends show single T_m at a similar temperature. When normalized % crystallinity (χ) is taken into a consideration, the addition of both PA and HBPs leads to an increase in the blend's crystallinity. Types of HBP have no effect on degree of crystallinity of the blends. The presence of PA does not significantly affect transition temperatures of PLA and its blends.

2.3 Morphology of fracture surfaces

SEM images of fractured surfaces of neat PLA and PLA/PA blend are shown in Figure 2. Features observed from the SEM images of neat PLA (Figure 2A-C) are different from those of PLA/PA blend (Figure 2D-F). The fractured surface of PLA shows smooth and homogenous features. Figure 2E and F, high magnification images of the top - right and bottom - left areas of Figure 2D, reveal rough features and phase separated morphology of PLA/PA blends.

SEM images of PLA/20LA HBP (Figure 3A) and PLA/20LA-co-CL HBP (Figure 3B) show similar surface features, in which dispersed phase with spherical shape is randomly distributed in PLA matrix. The size of dispersed phase in PLA/20LA HBP blend (0.1µm) is smaller than PLA/20LA-co-CL HBP (1µm). This implies that LA HBP is more compatible with PLA than LA-co-CL HBP. Figure 3C-E presents morphology of PLA/LA HBP blends containing PA. Although no different features of PLA/LA HBP/PA

Formulation	Tensile strength (MPa)	Tensile modulus (MPa)	Elongation at break (%)	Toughness (mJ/mm ³)
Neat PLA	28.7 ±1.72	490.3 ±40.16	10.9 ±0.85	2.2 ±0.33
PLA/20LA HBP	20.2 ±0.97	342.3 ±24.18	11.4 ±0.57	1.9 ±0.14
PLA/20LA-co-CL HBP	18.5 ±1.50	316.9 ±14.94	14.6 ±1.80	2.4 ±0.34
PLA/20LA HBP/10PA	6.1 ±1.79	357.9 ±31.03	2.0 ±0.52	0.2 ±0.05
PLA/20LA-co-CL HBP/10PA	7.8 ±0.99	294.0 ±16.18	3.2 ±0.63	0.3 ±0.07
PLA/10PA	18.4 ±1.21	485.3 ±33.94	5.3 ±0.71	0.8 ±0.15

Table 2: Transition temperatures, enthalpy of melting and crystallization (ΔH_m , ΔH_c) and normalized % crystallinity of PLA and its blends.

Formulation	T _g (°C)	T _m (°C)	T _c (°C)	ΔH_m (J/g)	ΔH_c (J/g)	χ (%)
Neat PLA	44.9	116.0	71.0	64.93	64.12	69.3
PLA/20LA HBP	47.5	116.0	68.0	60.16	54.50	77.4
PLA/20LA-co-CL HBP	-28.9, 43.8	115.3	72.0	59.92	56.92	77.0
PLA/20 LA HBP/10PA	46.7	116.7	67.3	56.83	51.13	78.8
PLA/20LA-co-CL HBP/10PA	-29.0, 44.6	116.3	67.0	56.75	51.91	78.7
PLA/10PA	44.0	116.0	67.0	61.31	59.86	71.9

(Figure 3C) and PLA/LA HBP blend (Figure 3A) is observed. Some areas in PLA/20LA-co-CL HBP/PA blend contains features as seen in Figure 3E, which obviously differs from those of PLA/20LA-co-CL HBP/PA (Figure 3D). Moreover, features observed in Figure 3E are merely similar to those of PLA/PA blend (Figure 2F). This indicates that PA is not effectively incorporated into the dispersed of 20LA-co-CL HBP, *i.e.*, crosslinked structures of HBP are not successfully developed. This implies that the poor mixing of PA into PLA/20LA-co-CL HBP is possibly a major cause of the ineffective improvement of tensile properties for PLA/20LA-co-CL HBP/PA.

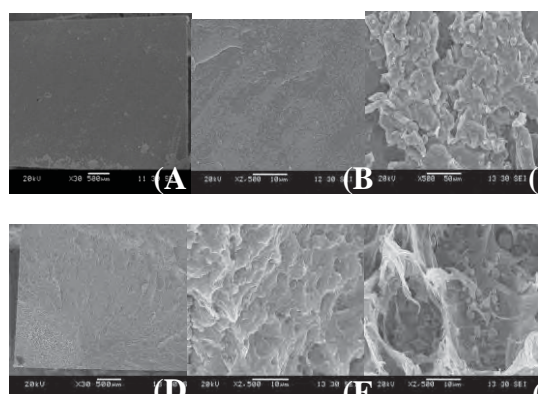


Figure 2. SEM images of fracture surface of neat PLA (A-C) and PLA/10PA blend (D-F)

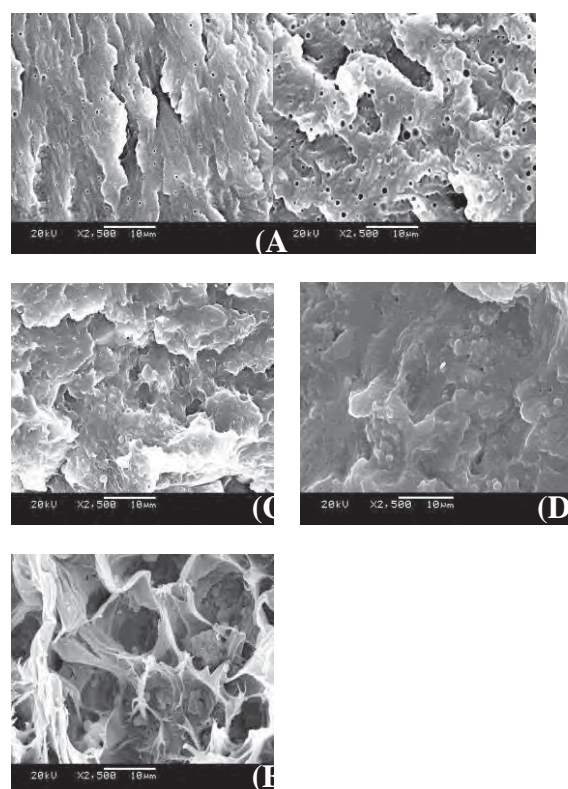


Figure 3. SEM images of fracture surface of PLA/20LA HBP (A), PLA/20LA-co-CL HBP (B), PLA/20LA HBP/10PA (C) and PLA/20LA-co-CL HBP/10PA (D, E)

4. Conclusions

An introduction of LA HBP and LA-co-CL HBP into PLA leads to an increase in their elongation at break. However, other tensile properties are depleted. Toughening of these blends *via* reactive mixing with an incorporation of PA component is not successfully observed in this current study. SEM results reveal

that poor mixing of PA into the disperse phase is likely a major cause.

Acknowledgements

Financial supports of this research are partly provided from MTEC platform grant (P1100047) and Chulalongkorn University. T. C. gratefully thanks the Thailand Graduate Institute of Science and Technology (TGIST) and Faculty of Science, Chulalongkorn for financial supports.

References

- [1] R.M Rasal, A.V Janorkar and D.E Hirt, *Prog. Polym. Sci.* **35** (2010) 338-356.
- [2] K. Baiardo, G. Frisoni, M. Scandola, M. Rimelen, D. Lips, K. Ruffieux and E. Wintermantel, *J. Appl. Sci.* **90** (2003) 1731-1738.
- [3] S. Jacobsen and H.G Fritz, *Polym. Eng. Sci.* **39** (1999) 1303-1310.
- [4] Z. Kulinski, and E. Piorkowska, *Polymer.* **46** (2005) 10290-10300.
- [5] N. Ljungberg, T. Anderson and B. Wesslén, *Appl. Polym. Sci.* **88** (2003) 3239-3247.
- [6] M.E Broz, D.L VanderHart and N.R Washburn, *Biomaterials.* **24** (2003) 4181-4190.
- [7] Y. Li and H. Shimizu, *Eur. Polym. J.*, **45** (2009) 738-746.
- [8] S. Ishida, R. Nagasaki, K. Chino, T. Dong, and Y. Inoue. *Appl. Polym. Sci.*, **113** (2009) 559-566.
- [9] N. Bitinis, R. Verdejo, P. Cassagnau and A.M Lopez-Manchado, *Mater. Chem. Phys.*, **129** (2011) 823-831.
- [10] R. Bhardwaj and A.K Mohanty, *Biomacromolecules*, **8** (2007) 2476-2484.
- [11] C. Nyambo, M. Misra and A.K Mohanty, *J. Mater. Sci.*, **47** (2012) 5158-5168.

SYNTHESIS AND PHOTOCATALYTIC ACTIVITY OF ZnO NANOPARTICLES VIA ARC DISCHARGE IN WATER

Chortip Termpornvithit¹ and Varong Pavarajarn^{1*}

¹Center of Excellence in Particle Technology, Faculty of Engineering, Chulalongkorn University, Phayathai Rd., Patumwan, Bangkok 10330, Thailand

* Author for correspondence; E-Mail: Varong.P@chula.ac.th

Abstract: Zinc oxide (ZnO), which is a semiconductor suitable for various applications, has attracted intensive research effort in the past decades. In this research, nanoparticles of ZnO were synthesized by electrical arc discharge in water. The process is essentially an application of a high direct current (DC) between anode and cathode, both of which are immersed in deionized water. The anode was zinc, while the cathode was graphite rod with holes drilled so that air can be introduced into the system. The arc discharge was initiated by moving the anode toward the cathode, during which, air was continuously supplied through the holes in the cathode. Immense energy generated by the arc vaporizes zinc from the anode. The zinc vapor reacts with the supplied air and quickly removed from the arc zone to the surrounding water. The products were observed at different part of the system, but XRD results indicated that all products were crystalline ZnO in hexagonal lattice structures. SEM image illustrated ZnO nanoparticles in spheroid shape and distributed uniformly. The average particle size observed by TEM was around 20-40 nm. The particle size was found to increase with an increase in the arc current. The photocatalytic activity of the synthesized ZnO was evaluated for methylene blue (MB) degradation.

1. Introduction

Zinc oxide (ZnO), a direct wide band gap (3.37 eV) semiconductor with large exciton binding energy of 60 meV, has received intensive scientific attention because of its unique properties and applications in photocatalysis, electronic nano-devices, ultraviolet (UV) light emitters, piezoelectric nano-generators, chemical sensors and biodevices [1]. Much attention has been drawn toward photocatalytic properties of ZnO. Several researches in recent years have shown that ZnO nanoparticles can be used as a photocatalyst for the degradation of organic pollutants from water and the sterilization of pernicious bacteria and viruses [2-4].

In a photocatalytic system, photo-induced reactions occur at the interface between catalyst surface and organic pollutants. The morphology and crystal size of catalyst, which affect surface atomic arrangements and coordination, play an important role in this system [5, 6]. The requirements to improve the photocatalytic activity include the increase of specific surface area and the crystallinity enhancement of the catalyst. Consequently, large efforts have been focused on the

synthesis of ZnO nanoparticles which are used as catalyst for photodegradation [2-4, 7].

Various methods have been used to prepare ZnO nanoparticles [8-10]. However, most methods require high temperature, complicated procedures, special conditions and high-cost experiment. As a result, electrical arc discharge in liquid is considered in this research because of simplicity in experimental set up, no need for complicated equipments and high yield of nanoparticle products. Effects of synthesis conditions on morphology, size distribution and photocatalytic activity of the nanoparticle products were investigated.

2. Materials and Methods

2.1 Synthesis of ZnO nanoparticles

In this experiment, graphite rod and zinc rod were used as electrodes. The electrodes were submerged vertically in deionized water. The zinc rod, which is 3 mm in diameter, was used as the anode. The 12 mm hollow graphite rod was used as the cathode. The anode was moved into the cavity of the graphite cathode at controlled speed. The current was applied between two electrodes by the direct current (DC) power supply. The schematic diagram of experimental set up is shown in Fig 1. The arc discharge was initiated and the reaction took place when the gap between these two electrodes reached optimum value (about 1-2 mm). At the same time, gas was supplied to the system through the 1-mm holes in the cathode rod to convey zinc oxide from the hot arc spot to the cold surrounding water. After the arc discharge was terminated, fine powders suspending in the water together with the powder deposit in the cathode and that settling down at the bottom of the container were collected and dried in an oven to eliminate moisture before characterizations.

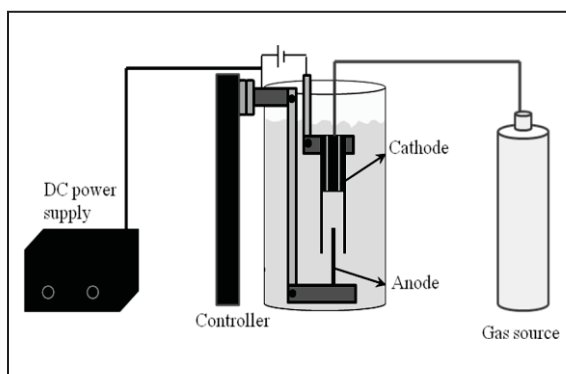


Figure 1. Schematic diagram of experimental set up.

2.2 Characterizations

The crystalline structure of the synthesized product was performed by X-ray diffraction (XRD, Bruker AXS D8 Advance with $\text{CuK}\alpha$ radiation in 2θ range from 20° to 80° by $0.02^\circ \text{ sec}^{-1}$ steps). The crystallite size of the synthesized product was estimated from the full-width at half-maximum of the (101) diffraction peak using the Scherrer equation. The morphology of the product was investigated by scanning electron microscopy (SEM, Jeol JSM-6400) and transmission electron microscopy (TEM, Jeol JEM 2100). For TEM measurement, the sample was prepared by dropping a dispersion of ZnO nanoparticles product in water directly onto copper grid.

2.3 Photocatalytic experiment

The photocatalytic activity of as-prepared ZnO nanostructures was evaluated for methylene blue (MB) degradation under UV irradiation. A mixture of 20 mg ZnO products used as catalyst and 200 ml of 10 ppm MB solution was put in a 100 ml Pyrex beaker. The solution was initially stirred in the dark for 30 min to reach the adsorption equilibrium of MB on the catalyst. Then the solution was irradiated with six UV-A lamps (Phillips TLC 15w/05) while continuously stirred by a magnetic stirrer to keep the catalyst uniformly dispersed within the solution. The solution was periodically sampled to be measured by UV-Vis spectrophotometer (Shimadzu, UV-1700) at the maximum absorption wavelength of MB (664 nm). The photoluminescence (PL) measurement was also made using Xenon lamp as a source with excited wavelength of 325 nm.

3. Results and Discussion

3.1 Particles characterization

Fig. 2 shows the XRD patterns of ZnO nanoparticles, synthesized using 20A arc current with flow rate of O_2 and N_2 at 3.0 l/min. The peaks at 2θ of 31.72° , 34.36° , 36.20° , 47.50° and 56.56° , correspond to the crystal planes of (100), (002), (101), (102), and (110) of ZnO in wurtzite structure, respectively. The diffraction peaks corresponding to zinc were also detected indicating incomplete reaction of the Zn vapor and oxygen supplied to the system. The average

crystallite size calculated by using the Scherrer equation based on (100) peak, was 35.9 nm. It should be noted that XRD patterns for the samples synthesized at arc current of 40 and 60 A were similar to that presented in Fig. 2.

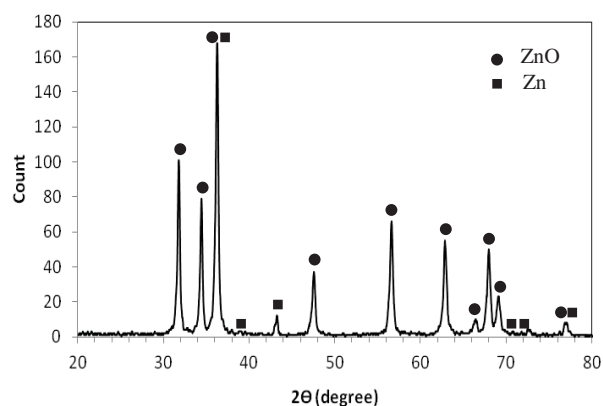


Figure 2. XRD pattern of the products synthesized at 20 A arc current.

Fig. 3 shows SEM images of the ZnO nanoparticles synthesized using different arc current of 20A, 40A and 60A, respectively. It can be seen that, for every synthesizing condition, the size and morphology of the obtained ZnO particles are uniform. However, measurement of the particle size could not be done from the SEM images due to agglomeration of the particles.

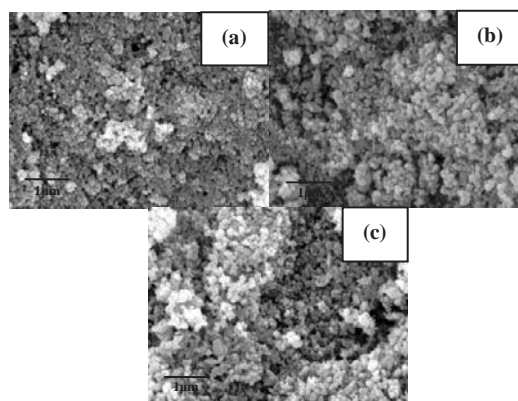


Figure 3. SEM images of the ZnO nanoparticles synthesized by using different arc current: (a) 20A, (b) 40A and (c) 60A. The scale bar is 1 μm .

The morphology and particle size distribution of the ZnO nanoparticles prepared under different arc current were also investigated by TEM analysis. The results are shown in Fig. 4. The morphology of the ZnO particles was found to be rod-like as well as spheroid. According to the particle size distribution, measured from 50 particles in TEM images, the synthesized ZnO particles are about 20-40 nm in size. The average particles size seems to be larger when higher arc current is used since high arc current

releases more energy to evaporate greater amount of zinc vapor. Consequently, highly concentrated zinc vapor reacts with supplied oxygen to form larger ZnO particles.

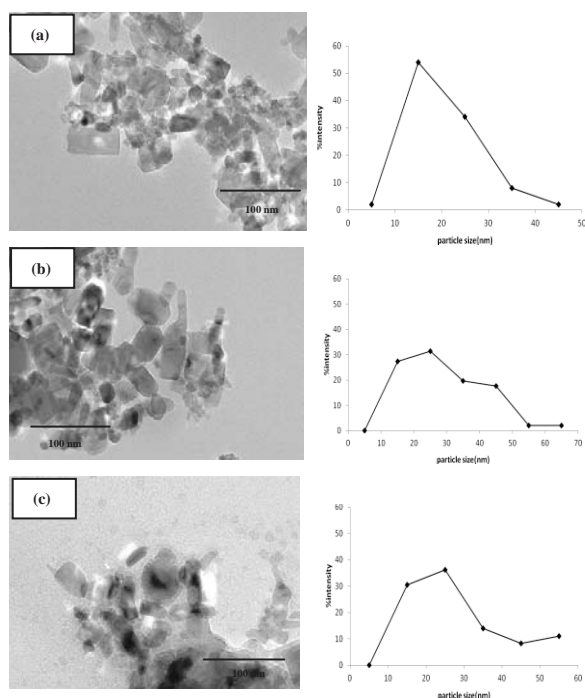


Figure 4. TEM images and particle size distribution of the as-synthesized ZnO particles using different arc current: (a) 20A, (b) 40A and (c) 60A

3.2 Photocatalytic activity

Fig. 5 shows UV-vis absorbance spectra of MB after being exposed with UV illumination in the presence of ZnO nanoparticles. The decrease in the absorbance with respect to the exposure time indicates photocatalytic activity of the synthesized ZnO.

Fig. 6 compares photocatalytic degradation of MB by ZnO synthesized using various values of arc current. It can be seen that ZnO which is synthesized at 40A possessed higher photocatalytic activities than at 20A and 60A. For the case of 60A arc current, the photodegradation rate is decreased because the synthesized particles are larger and therefore have lower surface area. Nevertheless, the fact at the ZnO nanoparticles synthesized using 40A arc current is more active than those synthesized at 20A indicated that surface area is not the main factor affecting the photocatalytic activity of the synthesized ZnO. Instead, it has been proposed that the content of oxygen vacancy on the surface of ZnO nanoparticles, may be responsible for the observed increase of the photocatalytic activity [12].

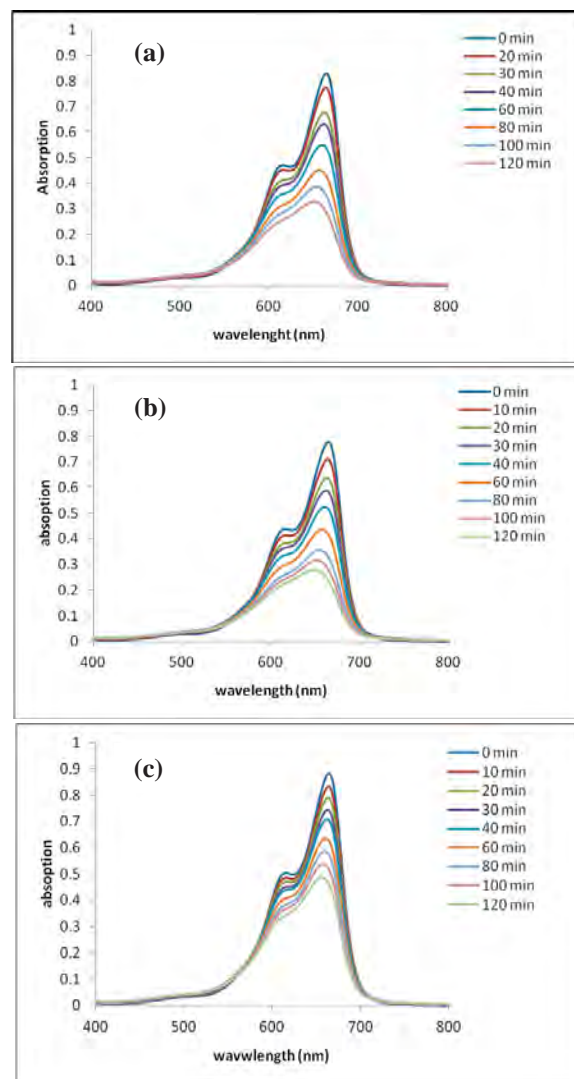


Figure 5. UV-vis spectra of photocatalytic activity of ZnO nanostructures by photodegradation of MB (a) 20A, (b) 40 A and (c) 60 A arc current.

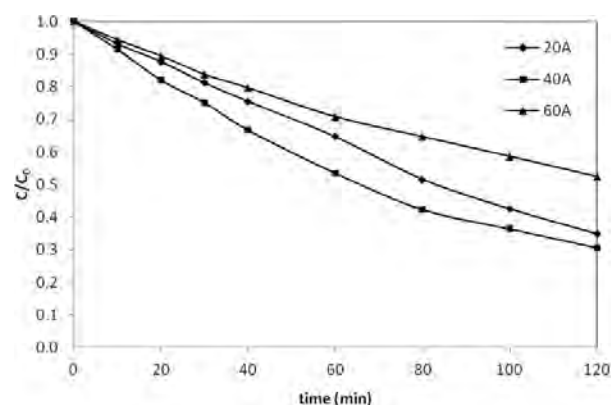


Figure 6. Process of photocatalytic degradation of MB under UV light illumination using ZnO as a photocatalysts: (a) 20A, (b) 40A and (c) 60A.

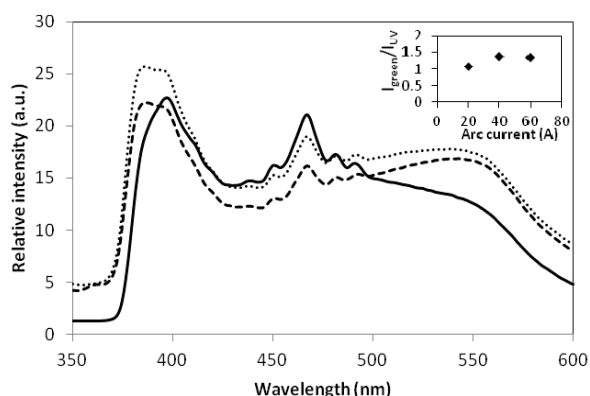


Figure 7. Photoluminescence spectra of ZnO synthesized at: (—) 20A (---) 40A (.....) 60A

Fig.7 shows the PL spectra of the obtained products synthesized using various values of arc current. There were two significant peaks at c.a. 385 nm in UV range and c.a. 490 nm in visible range. It should be noted that the green emission at c.a. 490 nm has been reported as the result from oxygen vacancy in ZnO lattice, which plays an important role in enhancing the photocatalytic activity [12]. In the inset of Fig. 7, the intensity ratio of green-to-UV emission ($I_{\text{green}}/I_{\text{UV}}$) was observed. The product synthesized at 40A arc current showed the highest of $I_{\text{green}}/I_{\text{UV}}$ which verified that oxygen vacancy plays an important role for photocatalytic activity of the synthesized product.

4. Conclusion

ZnO nanostructures can be prepared by an inexpensive and one-step procedure via a high current electrical arc discharge in water. XRD results indicated the formation of ZnO in hexagonal crystalline phase. SEM images illustrated ZnO nanoparticles in semi-spherical shape that were distributed uniformly. TEM

images showed semi-spherical as well as rod-like nanostructures with average particles size of 20-40 nm. The particle size was found to increase with an increase in the arc current. The photocatalytic activity of ZnO nanostructures was investigated. It was found that not only the particle size and surface area affects photocatalytic activity of the synthesized ZnO but also the oxygen vacancy on the surface.

Acknowledgements

This work is supported by the centenary fund of Chulalongkorn University for Center of Excellence in Particle Technology.

References

- [1] Z. Fan and J.G. Lu, *Zinc Oxide Nanostructures Synthesis and Properties*, University of California, (2005).
- [2] H.L. Liu and Thomas C.K.Yang, *Proc. Biochem.* **39**(2003) 475-481.
- [3] C. Hariharan, *Appl. Catal. A: Gen.* **304**(2006) 55-61.
- [4] S.S.Shinde, P.S. Shinde, C.H. Bhosale, K.Y. Rajpure, *Photochem. Photobiol. B: Biol.* **104**(2011) 425-433.
- [5] J.P.Cheng, Z.M. Liao, D. Shi, F. Liu, X.B. Zhang, *J. All. Comps.* **480**(2009) 741-746.
- [6] R.M. Mohamed, M.A. Al-Rayyani, E.S. Baeissa, I.A. Mkhaliid, *J. All. Comps.*, **509**(2011) 6824-6828.
- [7] D. Fu, G. Han, Y. Chang, J. Dong, *Mat. Chem. Phys.* **132**(2012) 673-681.
- [8] F. Liu, P. J. Cao, H. R. Zhang, J. Q. Li and H. J. Gao, *Nanotechnology.* **15**(2004) 949-952.
- [9] Z. Liu, J. Li, J. Ya, Y. Xin, Z. Jin, *Mat. Lett.* **62**(2008) 1190-1193.
- [10] B. Cao, W. Cai, G. Duan, Y. Li, Q.Zhao and D. Yu, *Nanotechnology.* **16**(2005) 2567-2574.
- [11] A. Becheri, M. Durr, P.L. Nostro, P. Baglioni, *J. Nanoparticle Res.***10**(2008) 679-689.
- [12] Y.Wang, X. Li, N. Wang, X. Quan, Y. Chen, *Sep. Purif. Technol.* **62**(2008) 727-732.

EFFECT OF CRYSTALLINITY OF POLY(LACTIC ACID) (PLA) ON MECHANICAL PROPERTIES OF PINEAPPLE LEAF FIBER (PALF) REINFORCED PLA COMPOSITE

Treechada Numpanon^{1,2}, Taweetchai Amornsakchai^{1,2*}, Sombat Thanawan¹

¹ Department of Chemistry, Faculty of Science, Mahidol University, Phuttamonthon 4 Road, Salaya, Nakhon Pathom, 73170 Thailand

² Center of Excellence for Innovation in Chemistry, Faculty of Science, Mahidol University, Phuttamonthon 4 Road, Salaya, Nakhon Pathom 73170 Thailand

*Corresponding Author : taweetchai.amo@mahidol.ac.th

Abstract: Fully bio-based composite was prepared from pineapple leaf fiber (PALF) and poly (lactic acid) (PLA). Effect of fiber orientation and crystallinity of PLA on mechanical properties of PALF/PLA composite were investigated. The composites were prepared by melt processing on a two roll mill with different PALF contents up to 20 wt%. Composites with PLA matrix in two different states, i.e. fully amorphous and crystallized states, were prepared. The crystallinity of PLA was determined with a Differential Scanning Calorimetry (DSC) analysis. The mechanical properties of the composites were determined from flexural and impact testings. It was found that flexural modulus of the composites increased significantly with increasing PALF content. Other properties, however, slightly increased or, at least, maintained. Composites with crystallized state presented better mechanical properties than composites with amorphous state. In addition, composites with uniaxial fiber orientation displayed better properties than random orientation fiber.

1. Introduction

The uses of plastics from petroleum-based have caused serious global environmental problems because they are non-degradable in nature although, some wastes can be recycled or energy be recovered. Amount of plastic waste is ever increasing due to increase in population, developmental activities, changes in life style, and socio-economic conditions. Also, the production method of plastic represents a major source of air and water pollution. Therefore, biodegradable and environmentally acceptable materials have attained increasing interest over the past decades due to environmental pressure derived from the consumption of petroleum-based materials and increased price of crude oil and global warming. The uses of biodegradable polymers made from renewable sources will have a less negative effect on the environment compared to petroleum based materials [1,2]. Among the biodegradable polymers, in particular, poly(lactic acid) (PLA) has received more attention academically and commercially. PLA is a thermoplastic polymer which can either be synthesized by condensation of lactic acid or ring opening polymerization of lactide which is the diester of lactic

acid. Lactic acid is produced by fermentation of dextrose which itself is gained from renewable resources like corn [3].

PLA is becoming increasingly popular as a biodegradable engineering plastic owing to its high mechanical strength and easy processability compared to other biopolymers and it is mainly used in applications as plastic bags for household wastes, barriers for sanitary products and diapers, planting and disposable cups and plates. However, low heat resistant, brittleness and slow crystallization limit the wider applications of PLA. Therefore, bio-fillers derived from renewable resources (e.g., natural fibers, starches, proteins) have attracted a great deal of interest for the reinforcement of PLA due to their sustainable supply and environmentally benign production. Some products of natural fibre-reinforced PLA are already established at the market: Jakob Winter (Satzung, Germany) produces biodegradable urns from flax and PLA by compression moulding [4].

Natural fibers, as actual and potential reinforcement for composites, offer many advantages over traditional reinforcing materials such as glass and carbon fibers: low cost, low density, renewable, high toughness, acceptable specific strength properties, non-abrasive behavior and biodegradability [5-7]. Natural fibers like pineapple fibers (PALF) come as viable and abundant substitutes for the expensive and non-renewable synthetic fibers. PALF is an important natural fiber that exhibits high specific strength and stiffness. The superior mechanical properties of PALF are associated with its high cellulose content and comparatively low microfibrillar angle (14°). Due to the unique properties exhibited by pineapple leaf fiber (PALF) they can be used as excellent potential reinforcement in composite matrices [8]. The aim of this research is to improve mechanical properties of PLA with high modulus and high impact by using PALF with different proportions. Composite materials are prepared by melt blending technique and shaped into samples by shaping technique. The samples are then characterized for mechanical properties .

2. Materials and Methods

2.1 Materials

Poly (lactic acid) (PLA) was used as a main matrix throughout this work. The melt flow index MFI for PLA is 5 g/10 min (at 190°C and 2.16 kg). The molecular weight distribution was determined by a size exclusion chromatography. It was found that $M_n = 85,951$ Da and $M_w = 158,812$ Da. Before processing, the material was dried for 24 h under a temperature of 60°C. Pineapple leaf fiber (PALF) was produced from leaves of pineapple. PALF was used as reinforcing agent.

2.2 Preparation of PLA/PALF composites

The pineapple leaf fibers and PLA were blended using a two-roll mill at 170°C for 45 min and the amount of PALF were 5, 10 and 20 %wt. The composites were hot pressed using upper and lower press temperatures of 165°C and 175°C, respectively. The sample was pre-heated without pressure for 10 min and then a pressure of 500 psi was applied for 5 min. After that the samples were either immediately quenched in cool water to obtain an amorphous state or cool in the cold press at room temperature for 5 min under a pressure of 1000 psi to obtain crystallized samples. The sheet of 1 mm thickness was used for tensile testing whereas the sheet of 3 mm thickness was used for flexural and impact testings.

2.3 Characterization

2.3.1 Flexural testing

Specimens were manufactured and subjected to a three-point bending test using an Instron 5569. Modulus and bending strength were thus determined. The span was set to 30 mm and the crosshead speed was 5 mm/min

2.3.2 Impact properties

To determine the notched Izod impact strength, the flexural coupon far samples were cut. Notched Izod impact testing was performed on a Testing Machines Inc. 43-02-01 Monitor/Impact machine as per the ASTM D256 standard. A 5 ft lb impactor was used to strike the samples. Nine specimens were measured for each sample.

3. Results and Discussion

3.1 Flexural properties of composites

The effect of PALF reinforcement in the PLA matrix, we studied the flexural properties of composite in the amorphous state. Afterward, the composite samples were crystallized, allowing us to effect of crystallization of PLA on the flexural properties of PALF/PLA composite.

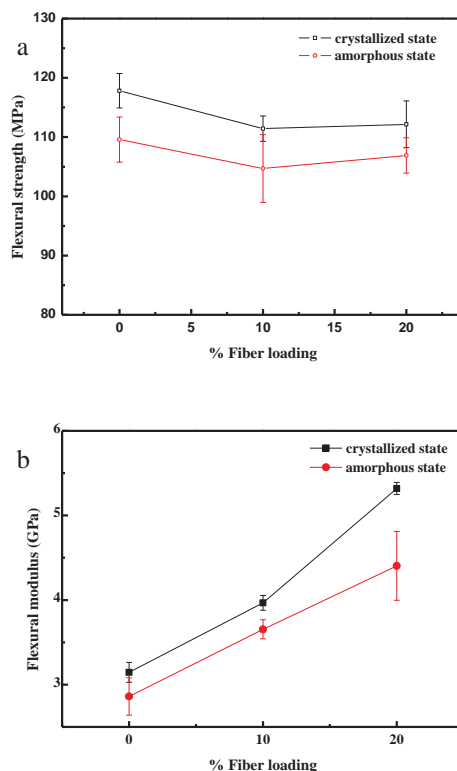


Figure 1. Flexural properties of amorphous and crystallized PLA and PALF/PLA composites : (a) flexural strength and (b) flexural modulus

Fig.1a shows flexural properties of amorphous and crystallized PALF reinforced composites. The flexural strength of the PLA composites slightly decreases with the addition of PALF both amorphous and crystallized composites. However, the flexural modulus of the PLA composites (Fig.1b) increases significantly with the addition of PALF both amorphous and crystallized composites. The addition of PALF will not improve the flexural strength. It is probable that poor adhesion between the PALF and PLA was the cause of reduced flexural strength. The stress is not transferred from the matrix to fibers [9]. The high flexural strength of PLA makes it difficult to improve strength in PLA composites according to Shibata et al. [10]. However, the flexural strength of composite was not reduced but maintained close to that of neat PLA. When the flexural properties of crystallized PLA and composites were compared to amorphous state, it was found that crystallization of PLA increased the flexural strength and flexural modulus. In the case of crystallized state, the flexural modulus of the composite at 20 wt% PALF content was improved from 3.1 GPa to 5.3 GPa. In the case of amorphous state, the flexural modulus of the composite at 20 wt% PALF content was improved from 2.7 GPa to 4.1 GPa. These results indicate clearly that PALF reinforcement and crystallization of PLA improve the composite flexural modulus.

3.2 Impact strength of composites

The notched Izod impact strength of composites is shown in Fig 3. Impact strength is ability of material to absorb energy. Impact strength of composites was higher than that neat PLA both for amorphous and crystallized composites. In the case of crystallized composites, the impact strength of the PLA improved from 3.7 kJ/m² to 5.3 kJ/m² for the presence of 10 wt% PALF content and from 3.5 kJ/m² to 4.5 kJ/m² for amorphous composites. However, the impact strength was slightly decreases (from that of 10 wt%) when PALF was added at 20 wt%. Toughness is the major factor that controls the impact strength. Generally, the toughness of fiber reinforced polymer composites is dependent on the fiber, the polymer matrix and their interfacial bonding strength [11]. It is probable that fibers were not evenly distributed in PLA matrix both for amorphous and crystallized composites. Impact strength increases, indicating that PALF able to improve the properties of PLA.

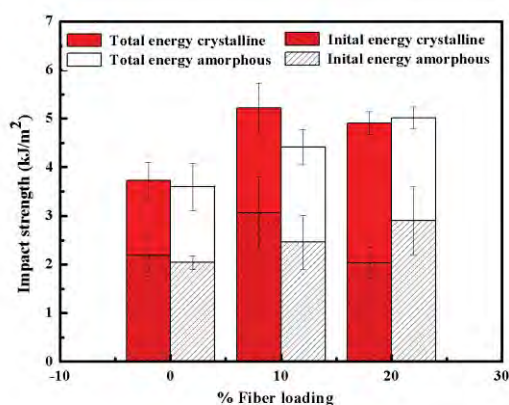


Figure 2. Impact properties of amorphous and crystallized PLA and PALF/PLA composites

4. Conclusions

Fully bio-based composite with improved mechanical properties was successfully prepared from PLA and PALF. The addition of PALF increased the flexural modulus of neat PLA at PALF content 20 wt% both for amorphous and crystallized composites. In the same way, impact strength increased with the addition of PALF. Flexural strength, however, decreased only slightly. These results confirm that the combination of PALF reinforcement and crystallization of PLA can be used to improve both flexural modulus and impact strength of PLA composite.

Acknowledgements

The authors would like to thank Center of Excellence for Innovation in Chemistry (PERCH-CIC) for its support with research grant.

References

- [1] E.T.H. Vink, K. R. Rabago, D.A Glassner and P.R. Gruber, *Polym Degrad Stabil.* **80**(3) (2003) 403-419.
- [2] A. Torres, S.M. Li, S. Roussos and M. Vert, *J Appl Polym Sci.* **62** (1996) 2295-2302.
- [3] D.E. Henton, P. Gruber, J. Randall In: A.K. Mohanty, M. Misra, L.T. Drzal, Editors. *Boca Raton: CRC Press.* (2005), p.p. 527-577.
- [4] C. Grashorn In: Nova Institut, Hürth, Germany. Hürth 21st-22nd Mai. (2007).
- [5] A.K. Mohanty, M. Misra, G. Hinrichsen, *Macromol Mater Eng.* **Vol. 276-277** (2000) 1-24.
- [6] R. Karnani, M. Krishnan, R. Narayan, *Polym Eng Sci.* **37** (1997) 476-283.
- [7] A.L. Martínez-Hernández, C. Velasco-Santos, M. de-Icaza, V.M. Castaño, *Compos Part B: Eng.* **38**(3) (2007) 405-410.
- [8] D.J. Gardner, G.S. Oporto, R. Mills, M.A.S.A. Samir, *J Adhes Sci Technol.* **22.** 545-567.
- [9] K. Oksman, M. Skrifvars, J.F. Selin. *Composites Science and Technology.* **63** (2003) 1317-1324.
- [10] M. Shibata, K. Ozawa, N. Teramoto, R. Yosmiya, H. Takeishi, *Macromol Mater Eng* **288** (2003) 35-43.
- [11] S.H. Masud, T.D. Lawrence, M. Manjusri, *Ind Eng Chem Res.***44** (2005) 5593-601.

MECHANICAL PROPERTIES AND FLAMMABILITY OF SAWDUST/RECYCLED HIGH DENSITY POLYETHYLENE COMPOSITES

Rapisa Jarapanyacheep^{1, 2}, Kasama Jarukumjorn^{1, 2*}

¹School of Polymer Engineering, Institute of Engineering, Suranaree University of Technology, Nakhon Ratchasima 30000, Thailand

²Center of Excellence on Petrochemical and Materials Technology, Bangkok 10330, Thailand

* Author for correspondence; E-mail: kasama@sut.ac.th, Tel. +66 44224437, Fax. +66 44 224605

Abstract: Sawdust/recycled high density polyethylene (rHDPE) composites were prepared at sawdust contents of 30, 40, and 50 wt%. The composites were prepared using a twin screw extrusion and test specimens were molded by a compression molding machine. Mechanical properties, flammability, and morphology of the composites were investigated. With increasing sawdust content, tensile modulus of the composites increased while tensile strength and elongation at break decreased. Burning rate of the composites increased with increasing sawdust content. In order to enhance the flame retardancy of the composites, aluminum trihydrate (ATH) was used at a content of 10 phr. ATH improved the flame retardancy of the composites at all sawdust contents without deterioration of the mechanical properties. Moreover, maleic anhydride grafted polyethylene (MAPE) was added at 5 phr to improve the compatibility of the composites. The mechanical and flame retarding properties of the composites at all sawdust contents were enhanced with incorporating MAPE.

1. Introduction

Lignocellulosic filler/Polymer composites have attracted much attention from a number of researchers and manufactures in recent years. The addition of the lignocellulosic filler in polymer aims to produce unique characteristics of light weight and recyclability. In comparison with other fillers such as traditional glass fibers and inorganic mineral fillers, lignocellulosic fillers have received much attention for being used as reinforcing materials because of their biodegradability and low cost. Sawdust (SWD) is the one of lignocellulosic filler obtaining from wood industry. The most utilization of this material is used as fuel or made the particles board [1]. The use of sawdust in wood polymer composites is an alternative method to add value to sawdust. Basically, sawdust is light, cheap and stiffness, thus it can be added to commodity matrix in certain loading level hence offering the best solutions for the utilization of waste wood with good mechanical properties and low cost [2].

Nowadays, plastics are widely used as packaging, furniture, electronic parts, and housewares. This has caused an increasing concern regarding the environment and problem of plastic waste disposal. Alternative methods for handling plastic waste include burial, incineration, depolymerization and recycling. Plastic recycling is a convenient way to solve the problem of the waste management. High density polyethylene (HDPE) is thermoplastics commonly used

as packaging (bottles, films, etc.). HDPE is chosen to produce the composites since it is a major portion of the post-consumer household wastes. In addition, HDPE possesses outstanding properties such as high toughness, good impact resistance and good chemical resistance.

Wood/thermoplastic composites (WRPCs) have been known for many years. WRPCs containing recycled plastics and wood fibers offer interesting combinations of cost and properties. The utilization of recycled plastic for the manufacture of WRPCs has been studied [3-4]. Najafi [5] found that the wood flour/rHDPE showed similar mechanical properties but were much cheaper when compared to wood flour/virgin HDPE composites.

However, there are two major problems facing the production of SWD/rHDPE composites. The first one is the flammability of the composites rHDPE and SWD are flammable materials. This problem limits the application of the composites in many areas. Therefore, the improvement of flame retardancy of the composite must be considered. Generally, the method to improve fire resistance of flammable materials is directly incorporate flame retardants into the materials. Flame retardants are often preferred to provide low flammability to polymeric materials because the use of flame retardants is an acceptable compromise between cost and properties [6]. Aluminum trihydrate (ATH) is a widely used flame retardant for plastics. The particular benefits of ATH include low health hazard, cost effectiveness and smoke suppressant [7]. ATH decomposes in an environmental friendly mechanism known as dehydration. This reaction results in the formation of aluminum oxide, which forms an inert residue acting as protective layer, and water which dilutes the smoke and combustible gases [8].

Another problem is the poor interfacial adhesion between hydrophobic PE and hydrophilic SWD resulting in the composites with poor mechanical properties [9]. The compatibility of the composites can be improved by various methods such as fiber surface treatment, matrix modification and addition of compatibilizer. Maleic anhydride grafted polyethylene (MAPE) is generally introduced as a compatibilizer to improve the compatibility between SWD and HDPE matrix. The PE segments of MAPE form compatible blends with HDPE. The anhydride groups of MAPE form hydrogen and chemical bonds with the hydroxyl groups of cellulose, which strongly anchored the

reactive groups onto SWD surface [10]. Moreover, the addition of MAPE can also improve the compatibility and dispersion of ATH in HDPE matrix. The polar part of MAPE can interact with hydroxyl groups of ATH and MAPE anchors its nonpolar HDPE part to the HDPE matrix resulting in the better compatibility and the dispersion of ATH and rHDPE matrix [11].

In this study, the effects of SWD content and ATH on mechanical properties and flame retardancy of SWD/rHDPE composites were studied. In addition, the influence of MAPE as a compatibilizer on the properties of the composites was investigated.

2. Materials and Methods

2.1 Materials

Recycled high density polyethylene (rHDPE) was purchased from a local plastic recycling plant. Indian Walnut sawdust (*Albizia lebbbeck Benth*) with particle sizes of 425-600 μm was obtained from Huathalae saw mill, Nakhon Ratchasima. Maleic anhydride grafted polyethylene (MAPE, Fusabond[®] MB100D, DuPont) was used as a compatibilizer. Aluminum trihydrate (ATH, APYRAL[®] 40CD, Nabaltec), was used as a flame retardant.

Table 1: Composition and their designation of rHDPE and rHDPE composites

Name	rHDPE (wt%)	SWD (wt%)	ATH (phr)	MAPE (phr)
rHDPE	100	-	-	-
30SWD	70	30	-	-
40SWD	60	40	-	-
50SWD	50	50	-	-
30SWD/10ATH	70	30	10	-
40SWD/10ATH	60	40	10	-
50SWD/10ATH	50	50	10	-
30SWD/10ATH/5MAPE	70	30	10	5
40SWD/10ATH/5MAPE	60	40	10	5
50SWD/10ATH/5MAPE	50	50	10	5

2.2 Composite preparation

Composition of rHDPE composites and their designation used in this study are shown in Table 1. rHDPE composites were prepared using a twin screw extruder (Brabender, 35/17D). The temperatures of the four processing zones were 175, 180, 185 and 190°C. The screw speed was 20 rpm. The test specimens were processed by a compression molding machine (Labtech, LP20-B) at 190°C.

2.3 Composite characterization

Mechanical properties: Tensile tests were examined according to ASTM D638 using a universal testing machine (Instron, 5565) with a load cell of 5 kN and a crosshead speed of 50 mm/min. Five samples were investigated.

Flammability: Flammability of rHDPE and rHDPE composites was examined by a horizontal burning test according to ASTM D635. The specimen was held horizontally and a flame was applied to one end of the specimen. A burning time from the first reference mark, i.e. 25 mm from the end, to the second reference mark, i.e. 100 mm from the end, was recorded. Three specimens from each composite were tested. Then, burning rates of the composites were calculated.

Morphological properties: Tensile fracture surfaces of rHDPE composites were examined using a scanning electron microscope (SEM, NeoScope JCM-6010). The fracture surface of the specimens was coated with gold before analysis.

Table 2: Tensile strength, tensile modulus and elongation at break of rHDPE and rHDPE composites.

Name	Tensile strength (MPa)	Tensile Modulus (GPa)	Elongation at break (%)
rHDPE	25.81±6.90	0.60±0.02	109.27±3.15
30SWD	20.29±0.23	0.88±0.10	4.48±0.13
40SWD	19.97±0.14	0.96±0.01	4.26±0.50
50SWD	16.05±2.79	1.05±0.03	2.12±0.13
30SWD/10ATH	22.42±0.19	0.93±0.08	4.45±0.21
40SWD/10ATH	21.95±2.25	1.05±0.01	4.25±0.10
50SWD/10ATH	19.39±3.14	1.07±0.04	2.10±0.31
30SWD/10ATH/5MAPE	29.13±0.78	0.94±0.03	6.10±0.33
40SWD/10ATH/5MAPE	27.63±0.43	1.04±0.01	5.40±0.42
50SWD/10ATH/5MAPE	21.58±1.87	1.05±0.01	2.69±0.23

3. Results and Discussions

3.1 Mechanical properties

Tensile properties of rHDPE and rHDPE composites are illustrated in Table 2. Tensile strength of the composites decreased with adding SWD. Moreover, tensile strength of the composites decreased continuously with increasing SWD content. This indicated the poor compatibility between polar filler SWD and nonpolar rHDPE matrix. When ATH was added, tensile strength of rHDPE composites increased. The results suggested that ATH acted as reinforcing filler in this system. Tensile strength of the compatibilized rHDPE composites was higher than the

rHDPE composites. This was probably due to improved interfacial adhesion between SWD and HDPE matrix. The chemical (ester bond) can be formed between hydroxyl groups of SWD and anhydride groups of MAPE. The PE segment of MAPE formed compatible blends with HDPE matrix. Therefore, the surface adhesion between SWD and HDPE matrix enhanced with incorporating MAPE compatibilizer [10]. Moreover, the addition of MAPE also improved the compatibility and dispersion of ATH in rHDPE matrix resulting in better tensile strength [11].

Table 3: Burning rate of rHDPE and rHDPE composites

Name	Burning rate (mm/min)
rHDPE	21.48±0.60
30SWD	30.61±0.35
40SWD	31.51±2.44
50SWD	32.83±2.75
30SWD/10ATH	24.51±2.14
40SWD/10ATH	29.65±0.33
50SWD/10ATH	31.30±1.84
30SWD/10ATH/5MAPE	18.99±1.38
40SWD/10ATH/5MAPE	22.22±0.23
50SWD/10ATH/5MAPE	22.04±1.46

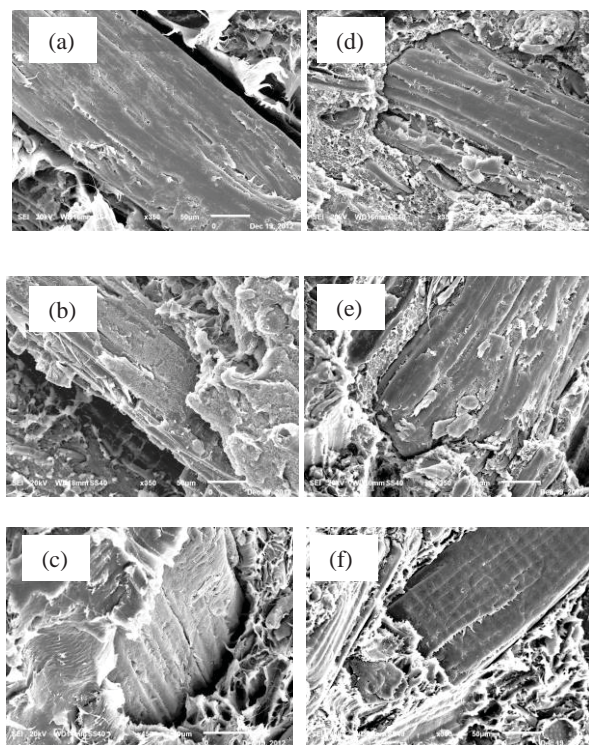


Figure 1. SEM micrographs of fracture surfaces of composites at 350x (a) 30SWD, (b) 40SWD and (c) 50SWD, (d) 30SWD/10ATH/5MAPE, (e) 40SWD/10ATH/5MAPE and (f) 50SWD/10ATH/5MAPE

Tensile modulus of rHDPE composites increased with increasing SWD content. This indicated the ability of SWD to impart greater stiffness to the composites. With the addition of ATH, the tensile modulus of the composites was increased. However, the tensile modulus of the composites was insignificantly changed with the presence of MAPE.

Elongation at break of the composites decreased with increasing SWD content. This was because the presence of SWD caused matrix to lose its ability against elastic deformation. Hence, the composites broke at a lower elastic deformation. When ATH was added, elongation at break of rHDPE composites was slightly decreased. Moreover, MAPE marginally improved the elongation at break of the composites.

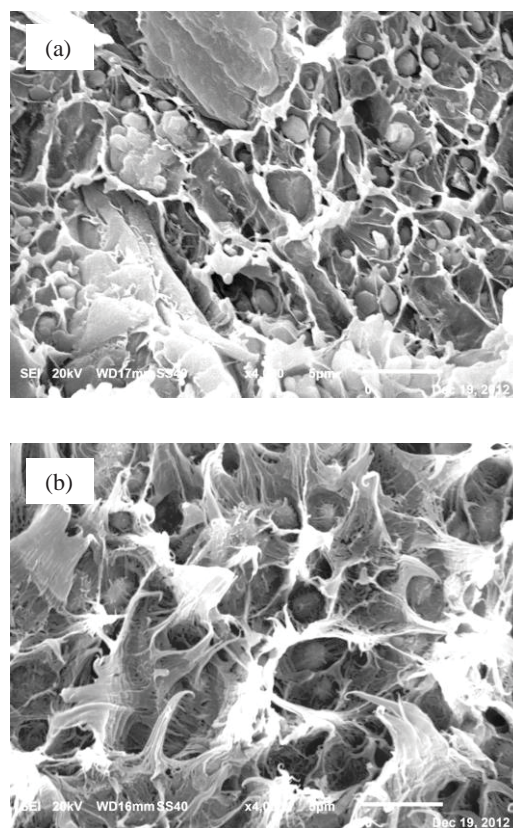


Figure 2. SEM micrographs of fracture surfaces of composites at 4000x (a) 50SWD and (b) 50SWD/ATH/MAPE

3.2 Flammability

Burning rates of rHDPE and rHDPE composites measured by horizontal burning test are shown in Table 3. rHDPE composite showed higher burning rate than rHDPE and the burning rate increased with increasing sawdust content. This indicated that sawdust filled rHDPE composite had high sensitivity to flame. Li and He [12] reported that the thermal degradation temperature of LLDPE in wood fiber/LLDPE composites was lower than neat LLDPE due to the low thermal stability of wood fiber.

On the other hand, the burning rate of the rHDPE composite with 10 phr of ATH was decreased compared with rHDPE composite without ATH. These results indicated that the addition of ATH decreased flammability of the rHDPE composite due to the production of water vapor and char protective layer during the combustion of ATH [13]. The burning rate of the composites reduced with the presence of MAPE. This may be due to a better dispersion of ATH in rHDPE resin. The anhydride group of MAPE can interacted with hydroxyl groups of ATH and PE segment of MAPE anchored to the HDPE matrix. This resulted in the better compatibility and the dispersion of ATH and rHDPE matrix [11].

3.3 Morphological properties

SEM micrographs of tensile fracture surfaces of rHDPE composites are shown in Figure 1. As shown in Figure 1(a-c), gap between rHDPE and SWD was observed indicating the poor compatibility between SWD and rHDPE matrix. This result supported a decrease in the mechanical properties of rHDPE when SWD was added [14].

From Figure 1(d-f), the better adhesion between SWD and rHDPE matrix was observed. Adding MAPE improved the interfacial adhesion between SWD and rHDPE matrix [10]. This resulted in the improvement of the mechanical properties of the composites.

SEM micrographs of the 50SWD and 50SWD/10ATH/5MAPE composites at magnification of 4000x are illustrated in Figure 2. It can be seen that not only agglomeration of ATH was found but also poor compatibility between ATH and rHDPE matrix was observed as shown in Figure 2(a). From Figure 2(b), as MAPE was incorporated into the composites, ATH well dispersed in rHDPE matrix due to improved adhesion between ATH and rHDPE matrix [11].

4. Conclusions

Tensile strength and elongation at break of the rHDPE composites were lower than neat rHDPE whereas tensile modulus was higher. With increasing SWD content, tensile strength and elongation at break decreased but modulus increased. Burning rate of rHDPE composites was higher than rHDPE and further increased with SWD content. With the addition of ATH, the burning rate of the composites was decreased. With the incorporation of ATH, tensile strength and modulus of the composites were increased but elongation at break was slightly decreased at all sawdust content. Moreover, the addition of MAPE enhanced the mechanical and the flame retardancy of the composites.

Acknowledgements

The authors wish to acknowledge Suranaree University of Technology and Center of Excellence on Petrochemical and Materials Technology for the

financial support, Chemical Innovation Co., Ltd. for providing maleic anhydride grafted polyethylene Fusabond® E MB 100D, Behn Meyer Chemical (T) Co., Ltd. for providing aluminum trihydrate APYRAL® 40CD and Huathalae saw mill for providing sawdust.

References

- [1] M. Idrus, S. Hamdan, R. Rahman and S. Islam, *J. Bio. Nano.* **2** (2011) 435-444.
- [2] A. K. Bledzki and J. Gassan, *Progr. Polym. Sci.* **24** (1999) 221-274.
- [3] Y. Cui, S. Lee, B. Noruziaan, M. Cheung and J. Tao, *Compos. Appl. Sci. Manuf.* **39** (2008) 655-661.
- [4] S.E. Selke and I. Wichman, *Compos. Appl. Sci. Manuf.* **35** (2004) 321-326.
- [5] S.K. Najafi, E. Hamidinia and M. Tajvidi, *J. Appl. Polym. Sci.* **100** (2006) 3641-3645.
- [6] S. Bourbigot and G. Fortaine, *Polym. Chem.* **1** (2010) 1413-1422.
- [7] A. A. A. Aziz, S. M. Alauddin, R. M. Salleh, and M. Sabet, *Int. J. Chem. Eng. App.* **3** (2012) 437-440.
- [8] A. B. Morgan and C. A. Wilkie, *Flame retardant polymer nano composites*, John Wiley & Sons, Inc., Hoboken, New Jersey, USA.
- [9] Y. Wang, F. C. Yeh, S. M. Lai, H. C. Chan and H. F. Shen, *Polym. Eng. Sci.* **43** (2003) 933-945.
- [10] S. M. Lai, F. C. Yeh, Y. Wang, H. C. Chan and H. F. Shen, *J. App. Polym. Sci.* **87** (2003) 487-496.
- [11] U. Hippel, J. Mattila, M. Korhonen and J. Seppala, *Polymer* **44** (2003) 1193-1201.
- [12] B. Li and J. He, *Polym. Degrad. Stab.* **83** (2004) 241-246.
- [13] M. B. A. Bakar, Z. A. M. Ishak, R. M. Taib, H. D. Rozman and S.M. Jani, *J. Appl. Polym. Sci.* **116** (2010) 2714-2722.
- [14] K. B. Adhikary, S. Pang and M. P. Staiger, *Compos. Appl. Sci. Manuf.* **39** (2008) 807-815.

MECHANICAL AND MORPHOLOGICAL PROPERTIES OF SAWDUST/POLY(LACTIC ACID) COMPOSITES: EFFECTS OF ALKALI TREATMENT AND SAWDUST CONTENT

Jiraporn Nomai^{1,2} and Kasama Jarukumjorn^{1,2*}

¹ School of Polymer Engineering, Institute of Engineering, Suranaree University of Technology, Nakhon Ratchasima 30000, Thailand

² Center of Excellence on Petrochemical and Materials Technology, Bangkok 10330, Thailand

* Author for correspondence; E-mail: kasama@sut.ac.th, Tel. +66 44224437, Fax. +66 44 224605

Abstract: Sawdust/poly(lactic acid) (PLA) composites were prepared using a twin screw extruder and test specimens were molded using an injection molding machine. Sawdust with particle size between 300 and 425 μm was used at contents of 20, 30, and 40 wt%. Mechanical and morphological properties of the composites were investigated. With increasing sawdust content, tensile modulus and flexural modulus of the PLA composites increased whereas tensile strength, flexural strength, impact strength, and elongation at break decreased. In addition, the effect of alkali treatment on the properties of sawdust/PLA composites was studied. Sawdust was treated with 2% w/v sodium hydroxide (NaOH) for 30 min at room temperature. Tensile, flexural, and impact properties of alkali treated sawdust/PLA composites were higher than those of untreated sawdust/PLA composites at all sawdust contents. The composites prepared from 40 wt% sawdust showed an improvement of tensile strength by 16.64%, tensile modulus by 7.90%, flexural strength by 28.95%, flexural modulus by 16.59%, and impact strength by 24.19% compared to those of untreated sawdust/PLA composites. SEM micrographs revealed that alkali treatment enhanced the interfacial adhesion between sawdust and PLA matrix.

1. Introduction

Increasing concerns about the environmental impact and sustainability of petrochemical polymer materials have motivated industries to develop biodegradable polymers from renewable resources. Among the biodegradable polymers, poly(lactic acid) (PLA) has attracted increasing interest in various industrial applications such as packaging, biomedical, and automotive, etc. PLA has a number of interesting properties including biodegradability, high strength, and high modulus [1]. However, its high brittleness and high cost limit its large scale commercial application [2]. One of the possible methods to minimize effective end product costs is to incorporate filler into biodegradable polymers [3]. Lignocellulosic fillers are widely used as reinforcing fillers in thermoplastic composites to provide positive environmental benefits with respect to ultimate disposability. The major advantages of these composite materials are low cost, light weight, high specific strength, and recyclability. In wood industries, sawdust is wood processing residue from consumer

good manufacture. Basically, sawdust is used as a fuel source or used to make others furniture product such as particle board. However, in many countries, sawdust is often disposed as landfill or incinerated causing environmental problems. Therefore, using sawdust as reinforcing fillers for polymers composites is an alternative way to add value to sawdust and also benefit the environment [4]. However, the main problem of using lignocellulosic filler to reinforce PLA is the incompatibility between lignocellulosic filler and PLA matrix, leading to poor mechanical properties of the composites. The interfacial adhesion between lignocellulosic filler and PLA can be improved by various methods such as matrix modification [5-6], addition of compatibilizer [7-9], and filler surface treatment [10-12]. Alkali treatment is found to be an effective way to improve interfacial adhesion of lignocellulosic filler/PLA composites. Alkali treatment can remove a certain amount of lignin, hemicellulose, and pectin covering the external surface of filler. The removal of surface impurities made the filler cleaner and rougher than untreated filler resulted in better mechanical interlocking with PLA matrix [10,13-14].

In this work, the effects of sawdust content and alkali treatment on mechanical and morphological properties of sawdust/PLA composites were investigated.

2. Materials and Methods

2.1 Materials

A commercial grade of PLA (PLA 3052D) was purchased from Natural Works LLC. Iron wood sawdust (*Hopea odorata* Roxb) with particle size between 300 and 425 μm was supplied by Piyarat sawmill, Nakhon Ratchasima, Thailand. Sodium hydroxide (RPE-ACS, Carlo Erba) was purchased from Italmar (Thailand) Co., Ltd. Tris(2,4-ditert-butylphenyl)phosphite antioxidant (Irgafos 168, Ciba) and pentaerythritol tetrakis(3-(3,5-di-tert-butyl-4-hydroxyphenyl)propionate) antioxidant (Irganox 1010, Ciba) were purchased from Merit Solution Co., Ltd.

2.2 Alkali treatment of sawdust

Sawdust was treated with 2% w/v sodium hydroxide solution (NaOH) with vigorous stirring for

30 min at room temperature. Then, sawdust was washed several times with water until pH7 was attained. Then sawdust was dried at 70 °C for 24 h.

2.3 Composites preparation

Designation and composition of the composites are shown in Table 1. Before mixing, PLA, untreated (UT) or alkali treated (AT) sawdust were dried at 70 °C in oven for 4 h. The compounds were mixed using a co-rotating intermeshing twin screw extruder (Brabender, DSE 35/17D) at the barrel temperature of 175/170/165/160/155 °C. The screw speed was 15 rpm. Then, test specimens were molded using an injection molding machine (Chuan Lih Fa model CLF 80P).

2.4 Composites characterization

Mechanical properties: Tensile properties were obtained according to ASTM D638 using an Universal testing machine (Instron, 5565) with a load cell of 5 kN and crosshead speed of 5 mm/min. Five samples were tested for each composition.

Flexural properties were obtained according to ASTM D790 using an Universal testing machine (Instron, 5565) with a load cell of 5 kN, span length of 53 mm, and crosshead speed of 1.4 mm/min. Five samples were evaluated for each composition.

Izod impact test was performed according to ASTM D256 using an Atlas testing machine (model BPI). Unnotched impact strength was tested at room temperature using the impact pendulum with impact energy of 2.7 J. Five samples were investigated for each composition.

Morphological properties: Morphology of the tensile fractured surface of sawdust/PLA composites was performed by a scanning electron microscope (JEOL, JSM5000). Acceleration voltage of 10 kV was used to collect SEM images of the samples. The fractured surface of specimens was coated with gold before analysis.

Table 1: Designation and composition of the composites

Designation	PLA wt%	Sawdust wt%		Irgafos 168 phr	Irganox 1010 phr
		UT	AT		
PLA	100	-	-	0.5	0.5
PLA/UT20	80	20	-	0.5	0.5
PLA/UT30	70	30	-	0.5	0.5
PLA/UT40	60	40	-	0.5	0.5
PLA/AT20	80	-	20	0.5	0.5
PLA/AT30	70	-	30	0.5	0.5
PLA/AT40	60	-	40	0.5	0.5

3. Results and Discussion

3.1 Mechanical properties

Tensile properties: Tensile strength, tensile modulus, and elongation at break of PLA, untreated and alkali treated sawdust/PLA composites with

different filler contents are shown in Figure 1 (a)-(c). It can be seen that modulus gradually increased with increasing sawdust content due to the reinforcement of sawdust in PLA matrix. However, with increasing sawdust content from 20 to 40 wt%, tensile strength of the composites slightly decreased due to a poor interfacial adhesion between sawdust and PLA matrix. Moreover, at high sawdust content, dispersion of sawdust was poor and sawdust was easy to agglomeration which resulted in a decrease in tensile strength of the composites [15]. Elongation at break of the composites decreased when the sawdust was added into the PLA matrix and decreased continuously with increasing sawdust content. This may be due to decreased deformability of a rigid interphase between the sawdust and the PLA matrix [15].

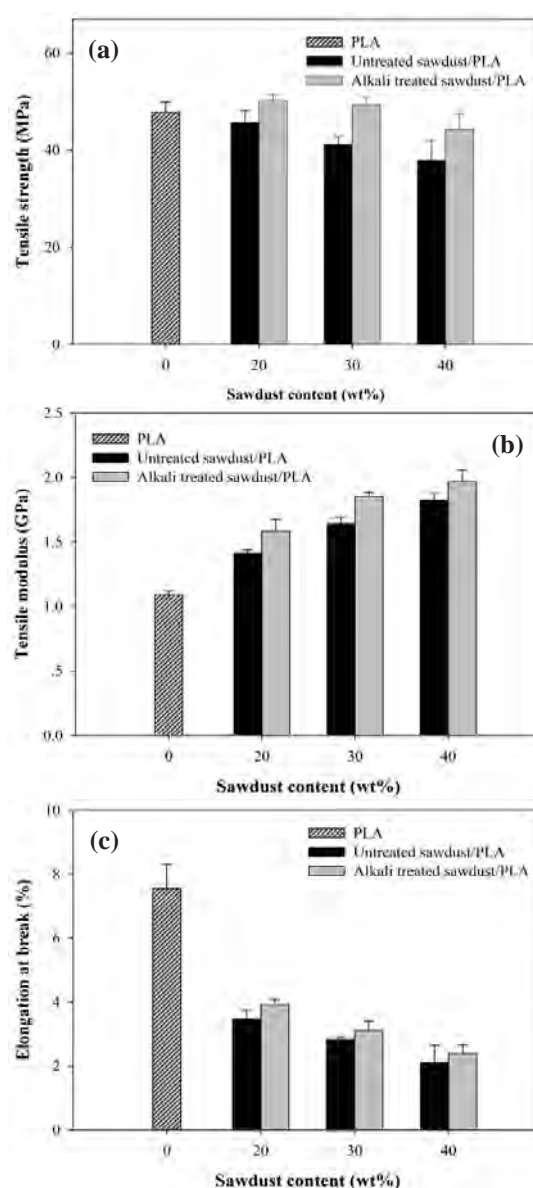


Figure 1. Tensile properties of PLA, untreated and alkali treated sawdust/PLA composites with different filler contents: (a) tensile strength, (b) tensile modulus, and (c) elongation at break

Tensile strength, tensile modulus, and elongation at break of alkali treated sawdust/PLA composites also showed the same trend as untreated sawdust/PLA composites. However, all of the composites filled with alkali treated sawdust exhibited higher tensile properties than the composites filled with untreated sawdust. This was because alkali treatment increased the filler surface roughness resulted in better mechanical interlocking with PLA matrix [16]. When compared with untreated sawdust/PLA composites, alkali treated sawdust/PLA composites at 20, 30, and 40 wt% sawdust content exhibited 10.08%, 19.96%, and 16.64% enhancement in tensile strength, 12.02%, 12.91%, and 7.90% enhancement in tensile modulus, and 12.90%, 9.63%, and 13.18% enhancement in elongation at break, respectively.

Flexural properties: Flexural strength and flexural modulus of PLA, untreated and alkali treated sawdust/PLA composites with different filler contents are shown in Figure 2 (a)-(b). Flexural properties also showed the same trend as tensile properties of sawdust/PLA composites. Flexural modulus increased with increasing sawdust content from 20 to 40 wt%. This was attributed to the addition of the rigid filler into the matrix. However, flexural strength of the composites decreased with increasing sawdust content. This was because a poor filler-matrix interfacial adhesion and filler agglomeration at high sawdust content resulted in difficult stress transfer from matrix to filler [15].

However, flexural strength and flexural modulus of alkali treated sawdust/PLA composites were significantly greater than those of untreated composites. This was due to the enhancement in the interfacial adhesion between sawdust and PLA matrix through mechanical interlocking. When compared with untreated sawdust/PLA composites, alkali treated sawdust/PLA composites at 20, 30, and 40 wt% sawdust content exhibited 27.02%, 29.69%, and 28.95% improvement in flexural strength and 15.38, 17.87%, and 16.59% improvement in flexural modulus, respectively.

Impact properties: Impact strength of PLA, untreated and alkali treated sawdust/PLA composites with different filler contents are shown in Figure 3. It was seen that as sawdust content was increased from 20 to 40 wt%, impact strength of the composites was reduced because the filler agglomeration increased, creating regions of stress concentration [15]. However, the improvement in impact strength was observed in the composites prepared from alkali treated sawdust. This was due to strong interfacial adhesion between the sawdust and the PLA matrix which allowed better matrix to fillers stress transfer during testing. The composites prepared from 20, 30, and 40 wt% alkali treated sawdust showed an improvement of impact strength by 20.02%, 31.02%, and 24.19% compared to those of untreated sawdust/PLA composites.

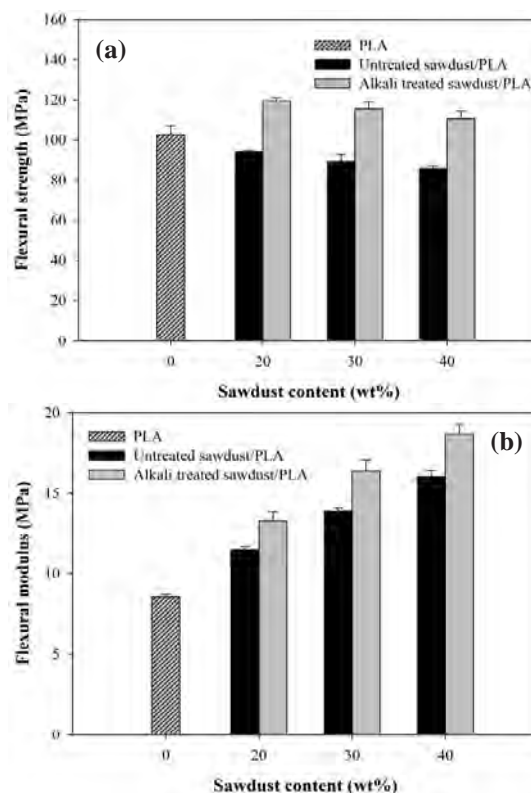


Figure 2. Flexural properties of PLA, untreated and alkali treated sawdust/PLA composites with different filler contents: (a) flexural strength and (b) flexural modulus

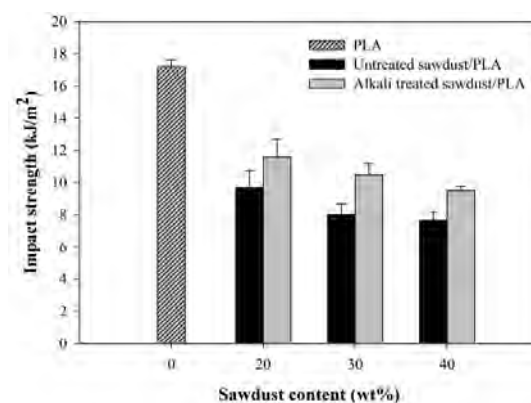


Figure 3. Impact strength of PLA, untreated and alkali treated sawdust/PLA composites with different filler contents

3.2 Morphological properties

Tensile fractured surface morphologies of untreated and alkali treated sawdust/PLA composites are shown in Figure 4 (a)-(f). Figure 4 (a)-(c) showed holes that left after untreated sawdust was pullout from PLA matrix. Gaps between untreated sawdust and PLA matrix were observed. These characteristics indicated poor interfacial adhesion between the filler and the PLA matrix.

However, for all composites filled with alkali treated sawdust, sawdust was embedded in PLA matrix

without gap in the interfacial area indicating good interface adhesion between the filler and the matrix as shown in Figure 4 (d)-(f). These results suggested that alkali treatment provided good compatibility between sawdust and PLA matrix, resulting in significant improvement of mechanical properties of the composites.

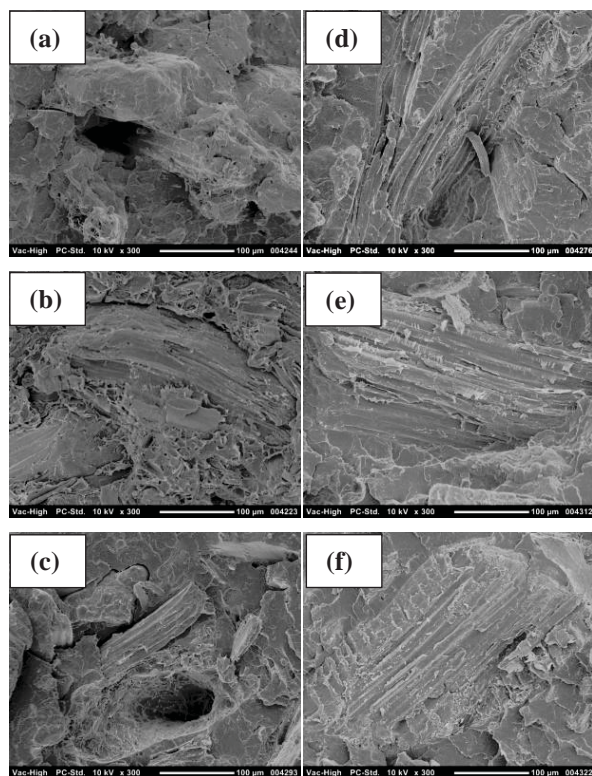


Figure 4. SEM micrographs at 300x magnification of (a) PLA/UT20, (b) PLA/UT30, (c) PLA/UT40, (d) PLA/AT20, (e) PLA/AT30, and (f) PLA/AT40 composites.

4. Conclusions

Tensile modulus and flexural modulus of PLA composites increased with increasing sawdust content whereas tensile strength, flexural strength, impact strength, and elongation at break decreased. Alkali treatment improved the interfacial adhesion between sawdust and PLA matrix leading to the enhancement in the mechanical properties of sawdust/PLA composites. SEM micrographs confirmed that alkali treatment enhanced the interfacial adhesion between sawdust and PLA matrix.

Acknowledgements

The authors would like to thank Suranaree University of Technology and Center of Excellence on Petrochemical and Material Technology for financial support, Piyarat sawmill for supplying iron wood sawdust.

References

- [1] H. Lui and J. Zhang, *J. Polym. Sci. Part B*, **49** (2011) 1051-1083.
- [2] T. Qiang, D. Yu and H. Gao, *J. Appl. Polym. Sci.* **124** (2012) 1831-1839.
- [3] M. Dimonie and M. Rapa, *U.P.B. Sci. Bull.* **72** (2010) 3-10.
- [4] S. H. P. Bettini, B. C. Bonse, E. A. Melo and P. A. R. Muñoz, *Polym. Eng. Sci.* **50** (2010) 978-985.
- [5] C. S. Wu, *Polym. Degrad. Stabil.* **97** (2012) 64-71.
- [6] A. Arbelaiz, B. Fernández, A. Valea and I. Mondragon, *Carbohydr. Polym.* **64** (2006) 224-232.
- [7] E. Petinakis, L. Yu, G. Edward, K. Dean, H. Liu and A. Scully, *J. Polym. Environ.* **17** (2009) 83-94.
- [8] F. Chen, L. Liu, P. H. Cooke, K. B. Hicks and J. Zhang, *Ind. Eng. Chem. Res.* **47** (2008) 8667-8675.
- [9] C. Nyambo, A. K. Mohanty and M. Misra, *Macromol. Mater. Eng.* **296** (2001) 710-718.
- [10] M. Aydin, H. Tozlu, S. Kemaloglu, A. Aytac and G. Ozkoc, *J. Polym. Environ.* **19** (2011) 11-17.
- [11] A. N. Frone, S. Berlioz, J. F. Chailan, D. M. Panaitescu and D. Donescu, *Polym. Compos.* **32** (2011) 976-985.
- [12] N. P. G. Suardana, I. P. Lokantara and J. K. Lim, *Mater. Phys. Mech.* **12** (2011) 113-125.
- [13] L. Liu, J. Yu, L. Cheng and X. Yang, *Polym. Degrad. Stab.* **94** (2009) 90-94.
- [14] A. S. Moyeenuddin, L. P. Kim and F. Alan, *Composites Part A*, **42** (2011) 310-319.
- [15] P. Ming-Zhu, M. Chang-Tong, Z. Xu-Bing and P. Yun-Lei, *J. Appl. Polym. Sci.* **121** (2011) 2900-2907.
- [16] H. N. Tran, S. Ogihara, H. T. Nguyen and S. Kobayashi, *Composites Part B*, **42** (2011) 1648-1656.

MELT SPINNING OF 4-LOBED POLYPROPYLENE FIBERS

Nanjanporn Roungpaisan*, Chureerat Prahsarn, Wattana Klinsukhon,
Natthaphop Suwannamek

National Metal and Materials Technology Center, Pathumthani, 12120 Thailand

**E-mail: nanjaprs@mtc.or.th*

ABSTRACT

Complexity in nozzle hole profile has caused melt spinning of shaped fibers to be complicated and always coped with many problems such as die swell, high pressure and high stress at die exit. In this study, polypropylene of two melt flow indexes (MFI 25 and 12) were melt spun into 4-Lobed fibers under different spinning conditions (temperatures, throughput rates, winding speeds) to investigate influences of polymer melt flow as well as spinning parameters on spinnability and profile of the obtained 4-Lobed fibers. Results showed that polypropylene fiber of lower melt flow (MFI 12) tended to maintain shape profile similar to that of its original nozzle hole, compared to that of higher melt flow (MFI 25), especially at lower spinning temperature (220°C), throughput rate 0.52g/hole/min and winding speed at 300 m/min. At higher spinning temperature, the fiber lobes tended to adhere to one another at the lobe ends. Results suggested that polymer melt flow and spinning temperature were major factors in determining shape profile of the obtained fibers.

Keywords: Die swell; Fiber melt spinning; Cross-sectional fibers; Shaped fibers

1. Introduction

Polypropylene is one of the most widely used polyolefin raw material for fibers processing due to its low cost as well as excellent mechanical and chemical properties. It provides variety in application including ropes and cords, upholstery fabric, carpet, filtration materials, horticulture or agriculture components, and medical care supplies. Shaped fibers have been recently produced commercially, in addition to typical fibers, to obtain special properties such as triangular fiber for luster and silky feel, hollow fiber for bulk and insulation and lobed fiber for greater density in fabric and moisture transport [1]. These varied cross-sectional shaped fibers can be achieved by design configuration of spinneret orifice.

Among many studies on melt spinning of shaped fibers, some had been conducted by numerical simulation to investigate dimensional change during various melt spinning parameter. The results showed that die swell and surface tension were important factors causing deformation of shaped fiber [2-4].

Jung et al. [5] reported deformation of polypropylene and polyester trilobal shaped fibers in terms of shape factor, which was calculated from the radius of circumscribed and inscribed circles in the trilobal shaped fibers.

In this study, polypropylene of two different melt flow rates were melt spun through 4-Lobed spinneret orifice under varied spinning conditions (spinning temperatures, throughput rates, and winding speeds) in order to investigate influence of these parameters on the obtained shaped fibers.

2. Procedure

Materials. Polypropylenes of two melt flow indexes (MFI = 12 and 25 g/10 min, density 0.9 g/cm³) obtained from HMC Polymers were used as received.

Methods. Melt viscosities of the two polypropylene resins were characterized at temperatures studied (220, 240, and 260°C), using rotational rheometer (ARE, Rheometric). Polypropylene fibers were spun through 4-Lobed orifice configuration of 10-hole spinneret, using laboratory fiber spinning machine (Fig. 1). The spinneret orifice has hole pitch of 0.06 mm. The parameters affecting formation of 4-Lobed fibers including spinning temperatures (220, 240, 260 °C), throughput rates 0.34, 0.52 (g/min/hole), and take up velocities 300, 500 (m/min), were studied (Table 1). Cross-sectional features, perimeters and area of the obtained 4-Lobed fibers were characterized, using optical microscope and ImageJ software. The shape factor was calculated (equation 1).

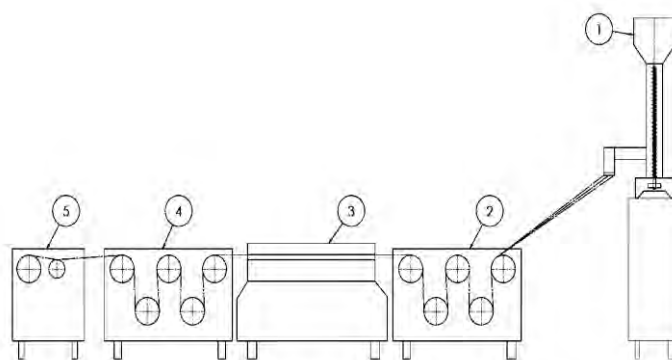


Figure 1. Fiber melt spinning system: Extruder (1), 1st roller unit (2), heated bar (3), 2nd roller unit (4) and winding unit (5).

Table 1. Polypropylene fiber spinning conditions

Parameter	Condition
Polymer	PP
	(MFI: 12, 25)
Nozzle hole shape	4-Lobed
Spinning Temperature (°C)	220, 240, 260 °C
Throughput rate (g/hole/min): TP	0.34, 0.52
(** at screw speed 3,5 rpm)	
Winding (m/min): S	300, 500

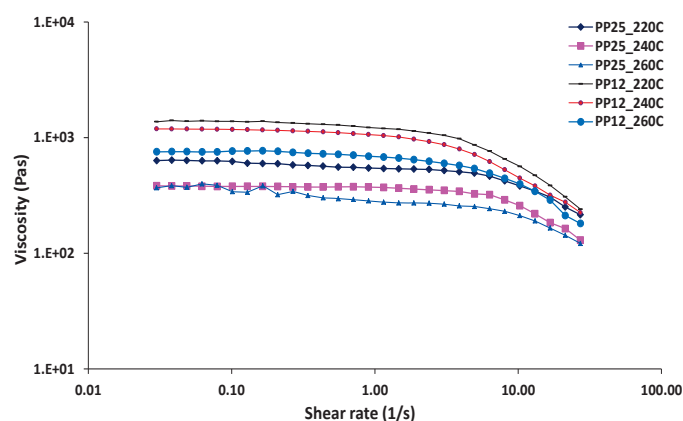


Figure 2. Change of viscosities with shear rate (1/s) of PP12 and PP25 at different temperatures (220, 240 and 260°C).

3. Results and Discussions

3.1 Effect of polymer viscosities

In this study, two polypropylenes of MFI 12 and 25 (referred to as PP12 and PP25, respectively) were employed to study effect of polymer viscosity on fiber spinnability and cross-sectional features observed in extruded 4-Lobed fibers. Polymer melt viscosities measured at temperature 220, 240, and 260°C were shown in Figure 2. PP12 showed higher viscosity than PP25 for all tested temperatures. The viscosities of PP12 and PP25 tended to decrease with increasing temperature. In fiber spinning, polypropylene of lower viscosity (PP25) showed better spinnability than that of higher viscosity (PP12) especially at 220°C. It was noted that pressure of PP12 melt was high, which could lead to high stress acting on the extruded polymer melt. This might cause its spinnability to be more sensitive to polymer viscosity, compared to that of PP25. At 220°C, fiber spinning of 4-Lobed fibers of PP12 showed breakage from time to time such that fibers could be obtained only from one condition (throughput rate 0.52 and take up velocity 300 m/min) as shown in Fig. 4. However, when increasing temperature to 240 and 260°C, good fiber spinnability was obtained. For PP25, fibers could be spun at all conditions (Fig. 5). However, PP12 with higher viscosity tended to maintain shape profile similar to its original 4-Lobed spinneret orifice.

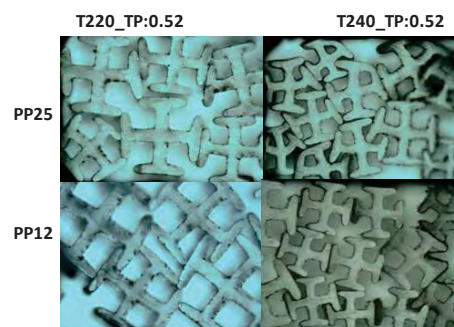


Figure 3. Cross-sectional features of as-spun 4-lobed PP fibers obtained at 220°C (left) and 240°C (right), MFI 25 and 12, throughput rate 0.52g/hole/min (Tp:0.52) (OM, Mag. = 10x)

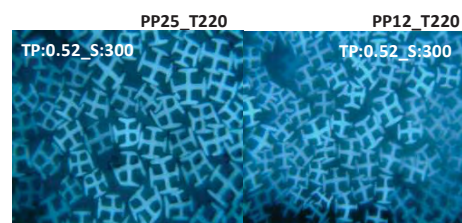


Figure 4. Cross-sectional features of 4-lobed PP25 and PP12 fibers obtained at 220°C, TP:0.52 and winding speed 300 m/min (S:300) (OM, Mag. = 40x).

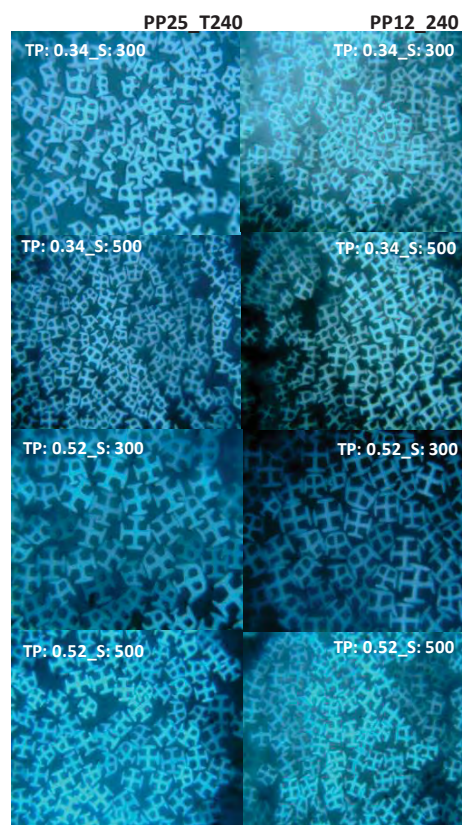


Figure 5. Cross-sectional features of 4-lobed PP25 and PP12 fibers obtained at 240°C, throughput rates 0.34 and 0.52 g/hole/min (TP0.34, TP0.52) and winding speeds; S:300, S500 m/min (OM, Mag = 40x).

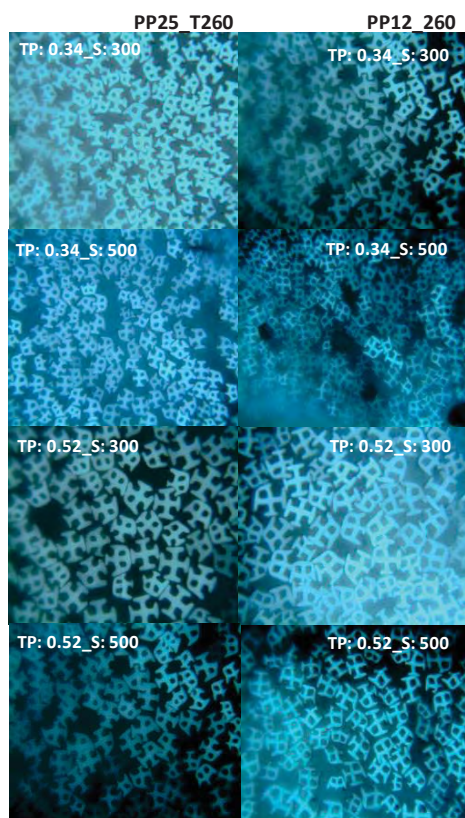


Figure 6. Cross-sectional features of 4-Lobed PP25 and PP12 fibers obtained at 260°C, throughput rates 0.34 and 0.52 g/hole/min (TP0.34, TP0.52) and winding speeds; S:300, S500 m/min (OM, Mag = 40x).

3.2 Effect of spinning conditions on cross sectional feature.

Figure 4-6 shows cross sectional features of 4-Lobed PP25 and PP12 fibers obtained at different spinning conditions. At higher spinning temperature, lobe ends of PP12 and PP25 fibers tended to adhere to one another. This was suspected to be due to higher heat residual in fibers spun at higher temperature.. Teke et al [6] employed numerical model to study effects of processing parameters on fiber melt spinning and reported that solidification point of extruded fiber occurred at different position in spin line when throughput rate and temperature were increased. According to Jung's work [5], higher spinning temperature caused lower solidification point as well as longer deformation zone. This resulted in different trilobal shapes observed in as-spun polypropylene fibers.

Figures 7 and 8 compared cross-sectional areas and perimeters of the obtained 4-Lobed PP25 and PP12 fibers. From results, both area and perimeter tended to decrease with low throughput rate and high winding speed. PP12 fibers showed larger perimeter than PP25 fibers for all spinning conditions. However, the perimeter tended to decrease with increasing spinning temperature (220°C-260°C). As shown in Figure 3, more adhesion of lobe ends was observed in as-spun PP25 fibers. At winding speeds of 300 and 500 m/min, varied shape deformation was observed. This was

suspected to be related to tension on fiber spin line, which could lead to asymmetric force in 4-Lobed shape, thus imbalance shape deformation. At lower spinning temperature (220°C), 4-Lobe PP12 fibers could maintain shape profile similar to its original spinneret orifice.

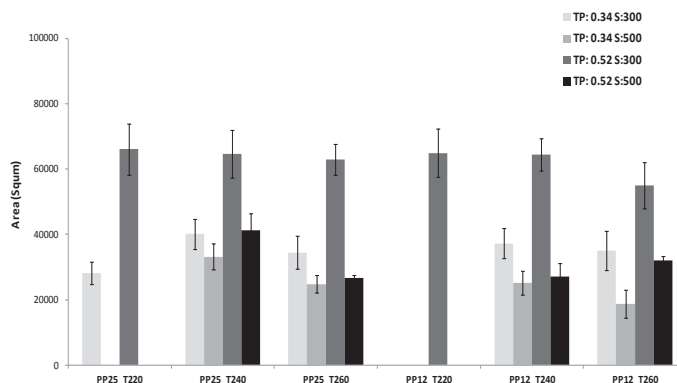


Figure 7. Cross sectional area of 4-Lobed PP25 and PP12 fibers obtained from different spinning conditions (Temperature 220, 240, 260 °C, Throughput rates, TP:0.34, 0.52 g/hole/min and winding speeds; S:300, S500 m/min).

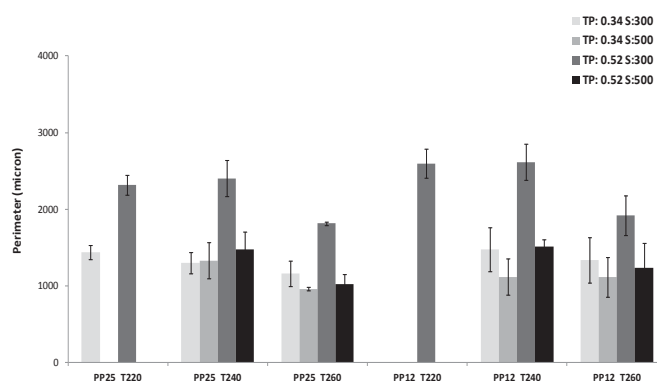


Figure 8. Cross sectional perimeter of 4-Lobed PP25 and PP12 fibers obtained from different spinning conditions (Temperature 220, 240, 260 °C, Throughput rates, TP: 0.34, 0.52 g/hole/min and winding speeds; S:300, S500 m/min.)

3.3 Shape factor of 4-Lobed fibers

Shape factor was calculated from cross-sectional perimeter and area of fibers as shown in Equation (1). It represents similarity of the fiber cross-sectional shape profile with regards to its original orifice shape. [7-8].


$$\text{Shape factor} = \frac{P}{4 \pi a^{1/2}} \quad (1)$$

Where:

P = cross-sectional perimeter of the fiber (μm^2)

A = fiber cross-sectional area (μm^2)

Table 2. Area and perimeter of 4-Lobed spinneret orifice shape.

Orifice profile	Profile Pic.	Area (Squm)	Perimeter (μm)	Shape factor
4-Lobed		331286	8389	4.11

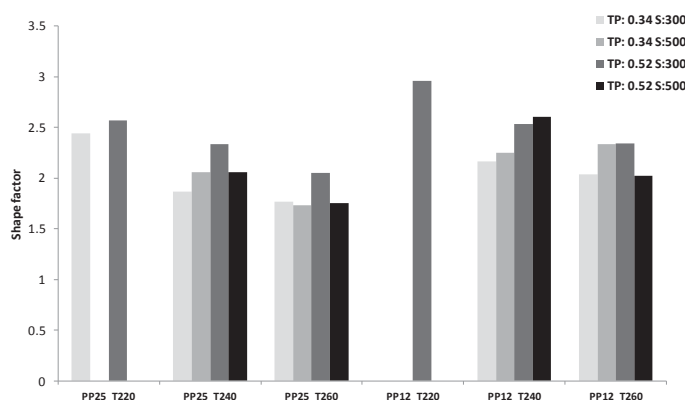


Figure 9. Calculated shape factor of 4-Lobed PP25 and PP12 fibers obtained from different spinning conditions (Temperatures 220, 240, 260 °C, Throughput rates; TP: 0.34, 0.52 g/hole/min and winding speeds; S:300, S500 m/min.)

Calculated shape factor of the 4-Lobed PP25 and PP12 fibers obtained from different spinning conditions were shown in Figure 9. Shape factor of PP12 fibers tended to be higher than that of PP25 for all spinning condition. From results, the highest shape factor value for fibers was 2.96 (PP 12 fibers spun at 220°C) whereas that of spinneret orifice was 4.11 (Table 2.) This implied that the obtained shaped fibers possessed open lobe ends and larger perimeter, compared to those obtained at other conditions. In addition, PP12 fibers tended to maintain open lobe profile during spinning at winding speeds 300 and 500 m/min. whereas PP 25 fibers tended to deform more at the same spinning conditions. However, at low spinning temperature 220°C, spinning of PP12 fibers was very sensitive that breakage occurred frequently. Variation in profile of shaped fibers might affect fiber's properties. Therefore shape factor could be used to help determine appropriate parameter for spinning fibers with desired profile and properties.

4. Conclusions

The study showed that fiber spinning conditions could affect change in cross-sectional profiles of 4-Lobed polypropylene fibers. Results suggested that polymer spinning temperature and polymer melt flow were major factors affecting shape profile of the obtained fibers. Spinning temperature was found to be a significant factor that caused variation in shape profiles. Low spinning temperature was preferable to maintain lobe profile similar to original orifice. Results showed that polypropylene fibers of lower melt flow (MFI 12) tended to maintain shape profile

similar to that of its original nozzle hole, compared to that of higher melt flow PP (MFI 25).

Acknowledgements

This work was financially supported by National Metal and Materials Technology Center, National Science and Technology Development Agency.

References

- [1] Fibrous Materials By Krishan Kumar Chawla University of Alabama Cambridge Solid State Science Series Fibers and fiber product, (1998), pp.8-36.
- [2] H. Kim, K. Chung, and J. R.Youn, *Fibers and Polym.* **1** (2000) 37-44.
- [3] H. Chi, Tsai, C.A. Lin and C.C. Tung, The Elasticity of special-shaped Fiber Simulation by Hydromechanical Simulation Software, *Institute of Textile Engineering Feng chia University*, (2008).
- [4] D.Yao, *Fiber Soc.* (2005) 56-56.
- [5] Il Jung, S.Y. Kim and T.H. Oh, *Text. Res. J.* **80** (2010) 12-18.
- [6] S. Teke and S.Altun, *Acad. J.* **7** (2011) 372-386.
- [7] L.G. Fuller, Production and Characterization of Novel Shaped Fibersfor Fluid Sorption and Transport, *Clemson University*, (2009).
- [8] M. A. Bueno, A.P. Aneja, and M. Renner, *J. Mater. Sci.* **39** (2004) 557-564

MECHANICAL, THERMAL, AND MORPHOLOGICAL PROPERTIES OF THERMOPLASTIC STARCH/POLY(LACTIC ACID) BLENDS

Sujaree Tachaphiboonsap^{1,2}, Kasama Jarukumjorn^{1,2*}

¹ School of Polymer Engineering, Institute of Engineering, Suranaree University of Technology, Nakhon Ratchasima, 30000 Thailand

² Center of Excellence on Petrochemical and Materials Technology, Bangkok, 10330 Thailand

*Author for correspondence; E-mail: kasama@sut.ac.th, Tel. +66 44 224437, Fax. +66 44 224605

Abstract: Thermoplastic starch (TPS)/poly (lactic acid) (PLA) blends were prepared and their mechanical, thermal, and morphological properties were investigated. TPS was obtained from cassava starch and glycerol at ratio of 70:30 w/w. TPS contents were varied from 10 to 40 wt%. Poly(lactic acid) grafted maleic anhydride (PLA-g-MA) was used as a compatibilizer. Tensile and impact properties of the blends were decreased when the amount of TPS was increased. With increasing TPS content, the decomposition temperature of PLA was decreased while the decomposition temperature of TPS was increased. Incorporating PLA-g-MA resulted in an improvement of the mechanical properties of the blends. The compatibilized blends exhibited much finer dispersed phase size.

1. Introduction

Poly (lactic acid) (PLA), derived from renewable resources, is the most widely used biodegradable polymers. PLA possesses high strength and high modulus. However, its high cost and brittleness limit its applications.

Starch has been used as filler for polymers due to its low cost, biodegradable, and availability as a renewable resource. However, melting temperature of starch is close to degradation temperature [1, 2]. Therefore, starch has been modified to obtain thermoplastic starch (TPS). Glycerol is often used as a plasticizer due to its high boiling point and low cost [3]. TPS/PLA blends exhibit low mechanical properties due to poor compatibility between TPS and PLA [4, 5].

The compatibility of TPS/PLA blend can be achieved by adding compatibilizer [6, 7] or modified matrix [8, 9, 10, 11]. Schwach et al. [6] used PLA grafted with amylose (PLA-g-A) to enhance compatibility of TPS/PLA blends. With the addition of PLA-g-A, tensile modulus of the blend did not change but tensile strength and elongation at break increased. Wootthikanokkhan et al. [7] reported that mechanical properties of TPS/PLA blends were increased when poly(lactic acid) grafted with maleated thermoplastic starch (PLA-g-MTPS) was used as a compatibilizer.

In this study, the effects of TPS content and adding compatibilizer on mechanical, thermal, and morphological properties of TPS/PLA blends were investigated.

2. Materials and Methods

2.1 Materials

Poly(lactic acid) (PLA, 4042D) was supplied from Natural Works LLC. Cassava starch was obtained from Bangkok Interfood Co., Ltd. Glycerol was supplied from Carlo Erba Reagenti Co., Ltd. 2, 5-bis (tert-butylperoxy)-2, 5 dimethylhexane (L101) and maleic anhydride (MA) were purchased from Sigma-Aldrich. Poly(lactic acid) grafted with maleic anhydride (PLA-g-MA) prepared in-house was used as a compatibilizer [12].

2.2 Preparation

TPS was obtained from cassava starch and glycerol at ratio of 70:30 w/w. Cassava starch was dried at 70°C for 4 h before mixing. Sample was prepared using an internal mixer (Hakke Rheomix, 3000P). The mixing temperature was kept at 120°C and the rotor speed of 60 rpm. The mixing time was 10 min.

TPS/PLA blends were prepared using an internal mixer (Hakke Rheomix, 3000P). TPS and PLA were dried at 70°C for 4 h before mixing. The mixing temperature was kept at 170°C and the rotor speed of 60 rpm. The specimens were processed by a compression molding machine (Labtech, LP20-B) at the temperature of 170°C and pressure of 100 MPa for 10 min. Designation and composition of TPS/PLA blends are shown in Table 1.

2.3 Characterization

Tensile properties of PLA and TPS/PLA blends were tested according to ASTM D638 using an universal testing machine (Instron, 5565) with a load cell 5 kN and crosshead speed of 1 mm/min.

Izod impact test was performed according to ASTM D256 using an impact testing machine (Atlas, BPI).

Thermal properties of PLA and TPS/PLA blends were analyzed using a thermogravimetric analyzer (Perkin Elmer, SDT 2960). The specimens were heat from room temperature to 600°C with heating rate of 10°C/ min. under nitrogen atmosphere.

Morphological properties of PLA and TPS/PLA blends were performed by a scanning electron microscope (JEOL, JSM-6400). Acceleration voltage of 10 kV was used. The specimens were freeze-fractured in liquid nitrogen and treated with hydrochloric acid (HCl, 6N) for 3 h. After that the specimens were coated with gold before analysis.

Table 1: Designation and composition of TPS/PLA blends

Sample	TPS wt%	PLA wt%	PLA-g-MA phr
PLA	-	100	-
10TPS	10	90	-
20TPS	20	80	-
30TPS	30	70	-
40TPS	40	60	-
10TPS/PLA-g-MA	10	90	5
20TPS/PLA-g-MA	20	80	5
30TPS/PLA-g-MA	30	70	5
40TPS/PLA-g-MA	40	60	5

3. Results and Discussion

3.1 Mechanical Properties

Tensile properties of PLA and TPS/PLA blends are shown in Figure 1. Tensile strength and tensile modulus of PLA decreased with adding TPS but elongation at break increased. This suggested that the presence of TPS led to ductile behavior [8]. With increasing TPS content, tensile strength, tensile modulus, and elongation at break of the blends decreased due to poor interfacial adhesion between TPS and PLA [6]. Similar results were also found by Huneault and Li [11] and Wootthikanokkhan et al. [7]. Tensile strength, tensile modulus, and elongation at break of the blends tended to increase with adding PLA-g-MA due to improved interfacial adhesion between TPS and PLA. Schwach et al. [6] and Wootthikanokkhan et al [7] reported that tensile properties of TPS/PLA blends improved with the presence of compatibilizers.

Impact strength of PLA and TPS/PLA blends is shown in Figure 2. Impact strength of TPS/PLA blends reduced with adding TPS. When PLA-g-MA was incorporated into the blends impact strength increased due to enhanced interfacial adhesion between TPS and PLA. Huneault and Li [11] reported that the improvement of interfacial adhesion between TPS and PLA may enhance ductility of the materials.

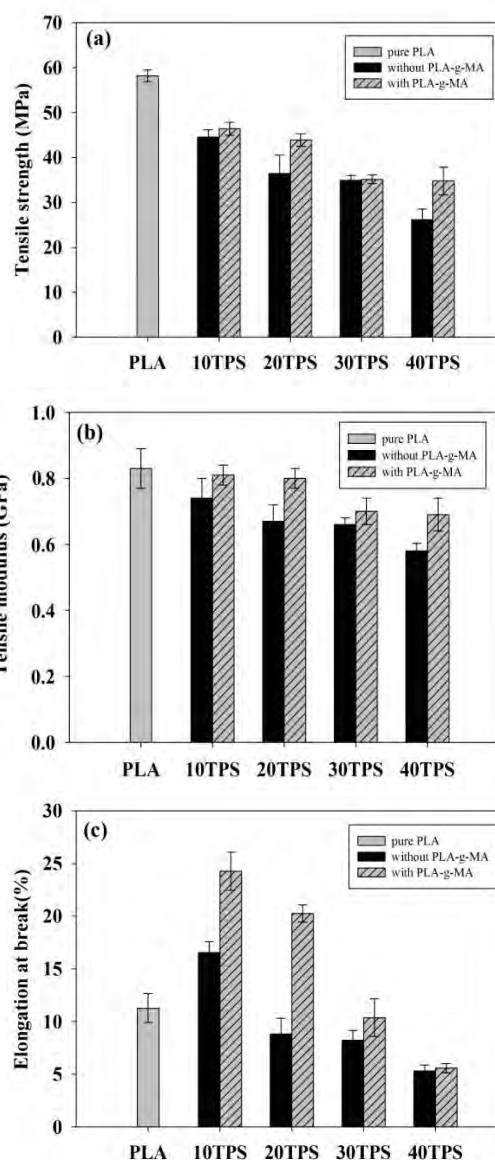


Figure 1. Tensile properties of PLA and TPS/PLA blends: (a) tensile strength, (b) tensile modulus, (c) elongation at break

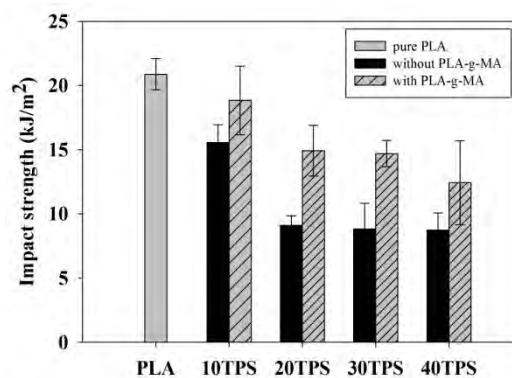


Figure 2. Impact strength of PLA and TPS/PLA blends

3.2 Thermal Properties

TGA curves of TPS, PLA, and TPS/PLA blends are shown in Figure 3. It can be seen that there were two steps in TGA curve of TPS. First step was obtained below 250°C which related to the volatilization of moisture and glycerol. The second step was observed from 280 to 350°C due to the decomposition of TPS [13]. While TGA curve of PLA showed one step relating to thermal decomposition of PLA polymer chain. DTG curves of TPS, PLA, and TPS/PLA blends are displayed in Figure 4. Thermal decomposition temperatures (T_d) of TPS and PLA in the TPS/PLA blends are listed in Table 2. T_d of PLA and TPS were observed at 349.46 and 317.79°C, respectively. It can be seen that PLA had better thermal stability than TPS. T_d of TPS and PLA in the blends decreased when compared with PLA and TPS. Similar results were also found by Wang et al. [4]. The reduction of T_d of PLA was probably because the degradation products of TPS involved thermal degradation of PLA [14]. Petinakis et al. [15] found that small polar molecules such as CO, CO₂, H₂O, CH₄, C₂H₄, and CH₂O were produced when starch decomposed. These molecules could break down PLA chain giving rise to a decrease in T_d of PLA. Shi et al. [16] reported that incorporating TPS into PLA resulted in reduced T_d of PLA. With increasing TPS content, T_d of TPS increased while T_d of PLA decreased. T_d of TPS increased with the addition of PLA-g-MA due to enhanced compatibility between TPS and PLA in the blends [4]. T_d of PLA in the blends did not change significantly when PLA-g-MA was added. Victor et al. [17] also reported that PLA-g-MA showed little effect on thermal stability of starch/PLA blends.

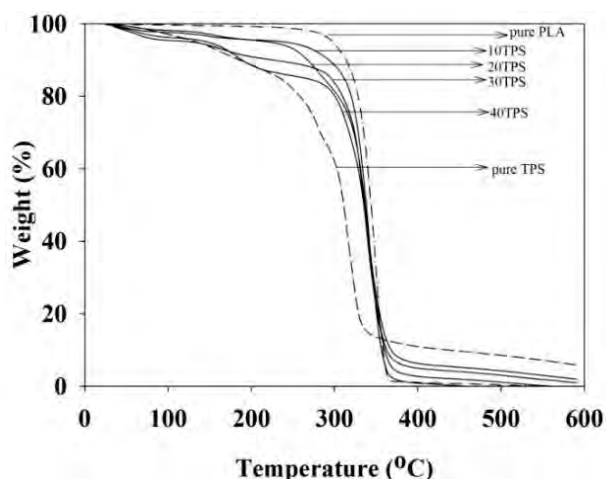


Figure 3. TGA curves of PLA, TPS, and TPS/PLA blends

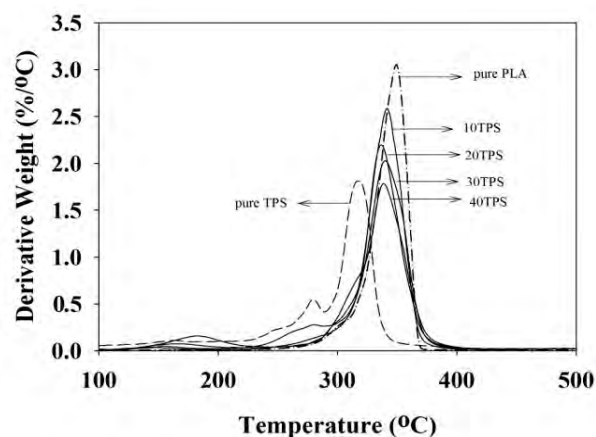


Figure 4. DTG curves of PLA, TPS, and TPS/PLA blends

Table 2: The decomposition temperature (T_d) of PLA, TPS, and TPS/PLA blends

Sample	T_d of TPS °C	T_d of PLA °C
PLA	-	349.46
TPS	317.79	-
10TPS	290.53	341.46
20TPS	301.49	340.19
30TPS	309.02	337.71
40TPS	310.52	337.08
10TPS/PLA-g-MA	309.27	339.30
20TPS/PLA-g-MA	312.78	341.74
30TPS/PLA-g-MA	313.80	337.12
40TPS/PLA-g-MA	314.92	337.77

3.3 Morphological Properties

SEM micrographs of the fracture surface of PLA and TPS/PLA blends are shown in Figure 5. From Figure 5(b) – (e), TPS droplets were observed in PLA matrix. This suggested that TPS/PLA blend was an immiscible blend. The number of the smaller TPS phase domains was observed when TPS content was increased. Similar result was observed by Wootthikanokkhan et al. [7]. With the addition of PLA-g-MA, the droplet size of TPS in the blends was finer than the blends without PLA-g-MA. Huneault and Li [11] found that the phase size of TPS in PLA was reduced with using PLA-g-MA. Wootthikanokkhan et al. [7] also reported that adding PLA-g-MTPS as a compatibilizer resulted in a decrease in particle size of TPS.

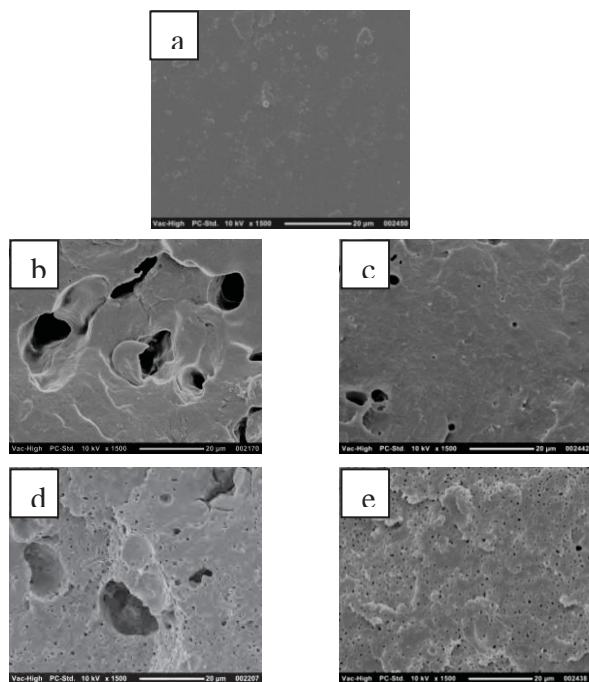


Figure 5. SEM micrographs at 1500x of (a) PLA, (b) 10TPS, (c) 10TPS/PLA-g-MA, (d) 30TPS, and (e) 30TPS/PLA-g-MA

4. Conclusions

Mechanical properties of TPS/PLA blends decreased with increasing TPS content. PLA-g-MA enhanced the compatibility of TPS/PLA blends. The compatibilized blends showed better mechanical properties than the uncompatibilized blends. The decomposition temperature of PLA in the blends was decreased with adding TPS. However, the decomposition temperature of PLA did not change significantly with the presence of PLA-g-MA. SEM micrographs of the compatibilized blends exhibited finer dispersed size.

Acknowledgements

The authors wish to acknowledge Suranaree University of Technology and Center of Excellence on Petrochemical and Materials Technology for financial supports.

References

- [1] G. Nashed, R. P. G. Rutgers and P. A. Sopade, *Starch/Stärke* **55** (2003) 131-137.
- [2] G. H. Yew, A. M. Mohd Yusof, Z. A. Mohd Ishak and U. S. Ishiaku, *Polym. Degrad. Stab.* **90** (2005) 488-500.
- [3] M. Kaseem, K. Haman and F. Deri, *Polym. Sci.* **54** (2012) 165-176.
- [4] N. Wang, J. Yu and X. Ma, *Polym. Compos.* **29** (2008) 551-559.
- [5] N. Wang, J. Yu, P. R. Chang and X. Ma, *Carbohydr. Polym.* **71** (2008) 109-118.
- [6] E. Schwach, J. Six and L. Averous, *J. Polym. Environ.* **16** (2008) 286-297.

- [7] J. Wootthikanokkhan, P. Kasemwananimit, N. Sombatsampop, A. Kositchaiyong, S. Isarankura na Ayuthaya and N. Kaabbuathong, *J. Appl. Polym. Sci.* **126** (2012) 388-395.
- [8] J. Leadprathom, S. Suttiruengwong, P. Threepopnatkul and M. Seadan, *J. Met. Mater. Miner.* **20** (2012) 87-90.
- [9] G. Huliang, H. Shan, S. Fuhui, Z. Jun and T. Guanana, *Polym. Compos.* **8** (2011) 2093-2100.
- [10] J. Wootthikanokkhan, N. Wongta, N. Sombatsampop, A. Kositchaiyong, J. Wong-On, S. Isarankura an Ayuthaya and N. Kaabbuathong, *J. Appl. Polym. Sci.* **124** (2012) 1012-1219.
- [11] M. A. Huneault and H. Li, *Polymer* **48** (2007) 270-280.
- [12] A. Teamsinsungvon, *Physical properties of poly(lactic acid)/poly(butylene adipate-co-terephthalate) blends and their composites*, Master's Thesis, Suranaree University of Technology (2011).
- [13] K. Zhang, X. Ran, Y. Zhuang, B. Yao and L. Doung, *Chem. Res. Chin. Univ.* **25** (2009) 748-753.
- [14] C. T. Vasques, S. C. Domenech, V. L. S. Severgnini, L. A. O. Belmonte, M. S. Soldi, P. L. M. Barreto, and V. Soldi, *Starch/Stärke* **59** (2007) 161-170.
- [15] E. Petinakis, X. Liu, L. Yu, C. Way, P. Sangwan, K. Dean, S. Bateman and G. Edward, *Polym. Degrad. Stab.* **95** (2010) 1704-1707.
- [16] Q. Shi, C. Chen, L. Gao, L. Jiao, H. Xu and W. Guo, *Polym. Degrad. Stab.* **96** (2011) 175-182.
- [17] O. H. Victor, B. Witold, C. Wunpen and L. L. Betty, *Macromol. Symp.* **277** (2009) 69-80.

EFFECT OF ORGANIC ACID DOPANTS ON THE PREPARATION OF POLYANILINE NANOTUBES VIA A SELF-ASSEMBLY METHOD

Sirinan Khunrit¹, Puttaruksa Varanusupakul^{2*}

¹Program of Petrochemical and Polymer Science, Faculty of Science, Chulalongkorn University, Bangkok, 10330, Thailand

²Department of Chemistry, Faculty of Science, Chulalongkorn University, Bangkok, 10330, Thailand

* Author for correspondence; E-Mail:puttaruksa.w@chula.ac.th, Tel. +66 22 187612, Fax. +66 22 541309

Abstract: Polyaniline (PANI) nanotubes were prepared by the self-assembly method in the presence of various organic acid dopants. The organic acids with different functional groups including carboxylic and sulfonic acids containing various alkyl and benzyl moieties were investigated. The scanning electron microscopy (SEM) images and infrared (IR) spectra showed that the morphology and the formation mechanism of PANI nanotubes were influenced by the dopants. It was proposed that the small organic acid dopants were leading to phenazine templating of PANI nanotubes self-assembly while the long hydrophobic hydrocarbon side chains of organic acid dopants were leading to micelle as soft template. Moreover, the formation yield, size, and uniformity of nanotubes were affected by the molar ratio of dopant to aniline as well as the reaction media.

1. Introduction

Polyaniline (PANI) is one of the most useful conducting polymers due to its controllable chemical and physical properties by oxidation and protonation states, easy synthesis, excellent environmental stability, high electronic conductivity, low cost and a large variety of applications such as rechargeable batteries, gas sensor, optical devices and removal of heavy metals. PANI nanostructures have received much attention because of their highly surface area [1-3].

A variety of chemical methods have been developed to synthesize one-dimensional PANI nanostructures, such as wires, tubes, rods, and fibers [4]. The chemical approaches adopted for production of one-dimensional PANI nanostructures are basically divided into hard and soft template (or self-template or template-free) synthesis and other methods such as interfacial polymerization, electrochemical polymerization and self-assembly. Among these methods, self-assembly has been considered as one of the most promising routes in terms of template-free because of its simplicity, low cost and large-scale production. However, there still exists a problem that the product is usually non-uniform. The different morphologies such as nanotubes, nanorods, nanoparticles and nanoflakes coexisted in the products [5]. It is also noted that different dopants including organic acids and inorganic acids as well as chemical nature of the oxidants, concentration of the reactants (especially of aniline and oxidant) and their molar proportions, presence of additives (e.g. surfactants), etc [6] affect morphology, formation mechanism and physical properties of PANI

and have been investigated widely. Low concentrations of acids with respect to aniline and the use of organic acids have usually been needed to obtain PANI nanotubes [7].

Here, we report the synthesis of self-assembled PANI nanotubes doped with different functional groups of organic acids including carboxylic acids (i.e. acetic acid and benzoic acid) and sulfonic acids (i.e. *para*-toluene sulfonic acid; *p*-TSA and dodecylbenzene sulfonic acid; DBSA). Moreover, we synthesized PANI nanotubes in the presence of methanol or HCl aqueous solution. The formation mechanism of one-dimensional PANI nanostructures was discussed based on the relationship between the initial states of soft template and morphologies of the resulting PANI.

2. Materials and Methods

2.1 Chemicals

Aniline monomer (purity≥99.5%) and dodecylbenzene sulfonic acid (DBSA, purity≥98%) were purchased from Sigma-Aldrich. Acetic acid, benzoic acid, *para*-toluene sulfonic acid (*p*-TSA), hydrochloric acid, and methanol were obtained from Merck. Ammonium peroxydisulfate (APS) was purchased from Riedel-deHaen. Aniline was distilled under reduced pressure before use.

2.2 Preparation of PANI nanotubes

The first self-assembled PANI nanotubes doped with the acetic acid, benzoic acid, and *p*-TSA were prepared by dissolving 0.91 mL of aniline monomer in 50 mL reaction solution and 2.86 g of APS was similarly dissolved to provide 50 mL solution at room temperature. The reaction solution contained different molar ratios of dopant to aniline (0.01-1) or mixed solution of dopant and methanol (1 M). The solutions of aniline and oxidant were cooled at 0-5 °C for 30 min and then poured rapidly into a beaker and stirred vigorously for 30 s. The mixture was left still to react for 10 h at 0-5 °C. The product was filtered and washed with deionized water and finally dried in air for 24 h to obtain the PANI.

The second self-assembled PANI nanotubes doped with DBSA were prepared by dispersing 0.46 g of aniline monomer and 0.326 g of DBSA in 80 mL of deionized water to form slightly opaque solution. Then 10 mL of 0.5 M HCl solution was added to this

solution and it turned to a milky mixture gradually. After 30 min, 10 mL (0.5 M) of APS aqueous solution was added to the above mixture and stirred vigorously for 30 s to initiate the polymerization. Then the reaction was allowed to proceed without agitation at 0-5 °C for 24 h. Finally, the precipitates were washed with deionized water and acetone respectively until the filtrate became colorless, and dried in air for 48 h.

2.3 Materials characterization

The morphologies of the PANI were examined by scanning electron microscope (SEM, JSM-5410 LV). The molecular structures of the PANI were identified by Fourier transform infrared spectroscopy (FTIR, Nicolet 6700).

3. Results and Discussion

3.1 Formation mechanism

The self-assembled PANI nanotubes are still not clearly understood although a number of models were proposed [8]. The models of a formation mechanism that have been proposed include phenazine templating theory, micelles as soft template theory and more recent discoveries such as nanosheet curling [9] and nanoparticle agglomeration [10]. Two models, the phenazine templating theory and the micelles as soft template theory were the most described.

When preparing PANI with small organic acid dopants (acetic acid, benzoic acid and *p*-TSA), the self-assembled PANI nanotubes were developed via a phenazine templating mechanism. The aniline oligomers were proposed to form both *ortho*-coupling and *para*-coupling. The phenazine units formed through the oxidation of *ortho*-coupling acted as the initiator for the growth of PANI chains. Then, π - π stacking between phenazine units led to formation of nanotubular structure [8]. The oxidation of some oligomers to form phenazine units is observed and confirms by the FTIR peak at 1414 cm^{-1} (Fig. 1). The intensity of phenazine-like unit peak decreased relative to other structural units after 1-2 h of reaction time [7]. On the other hand, the micelles as soft templates mechanism were adopted when a long hydrophobic hydrocarbon side chain of organic acid (DBSA) was used as the dopant in PANI preparation. The milky solution was observed when mixing the synthesis reagents. The aniline monomer micelles were formed in which hydrophobic long alkyl tails of DBSA were the inner cores of micelles, and anilinium ions were countered with the aqueous ends of DBSA. When adding HCl, the neighboring micelles connected together through chloric ion bridges [11]. The micelles acted as "template-like" to form a nanotubular structure since the micelle size would become bigger by elongation. Consequently, the propagation of the polymerization remained in the outer part of micelles.

Fig. 2 shows FTIR spectra for the PANI nanotubes doped with the various organic acids. The characteristic peaks of PANI nanotubes in FTIR spectra of all

organic acid doped PANI were in agreement with previously reported spectra [5,7] confirming the formation of PANI nanotubes. The band at 1625 cm^{-1} corresponds to the absorption of the C=C ring stretching vibration in newly-formed substituted phenazine-like segments. The bands at 1567 and 1488 cm^{-1} correspond to C-H in-plane of quinonoid and benzenoid, respectively. The band at 1414 cm^{-1} is attributed to totally symmetric stretching of the phenazine heterocyclic ring. The band at 1282 cm^{-1} is ascribed to C-N stretching of the secondary aromatic amine. Phenazine-like units can also be recognized through the bands at 1208 cm^{-1} and by their contribution to the bands at 1144 and 1108 cm^{-1} . The presence of significant amount of 1,2,4-trisubstituted rings indicating the formation of branched and/or substituted phenazine-like segments is revealed by the bands at 864 and 858 cm^{-1} .

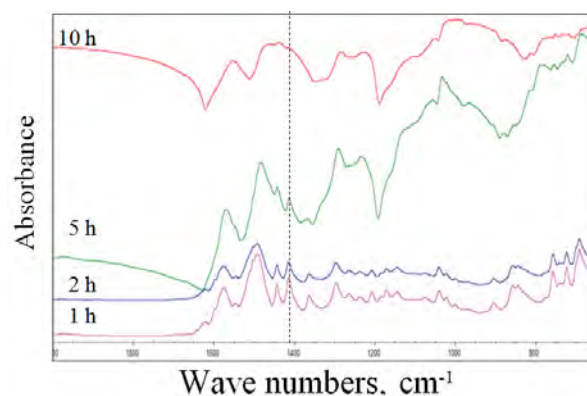


Figure 1. FTIR spectra of PANI intermediates obtained at different reaction stages in the optimum molar ratio. Synthetic conditions : [acetic acid]/[An]= 0.2

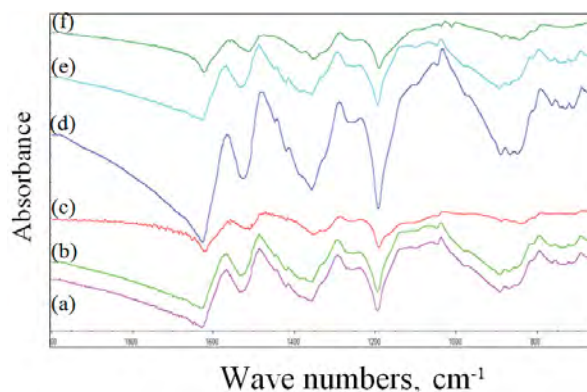


Figure 2. FTIR spectra of PANI nanostructures doped with different organic acids : (a) acetic acid, (b) benzoic acid, (c) benzoic acid+methanol, (d) *p*-TSA, (e) *p*-TSA+methanol and (f) DBSA+HCl

3.2 Morphology

The nanostructures formed by doping PANI with the different organic acids are both tubes and rods as shown in Fig. 3. The coexisting of nanoparticles are observed because abundant presence of anilinium

cations goes against the formation of phenazine which is the prerequisite of nanotubes [5]. However, the large quantity of granules was observed in self-assembled PANI nanotubes doped with DBSA. Since DBSA doped PANI nanotubes were produced through micelles as soft templates mechanism, the cylindrical micelles might be too crowded or the ratio of DBSA to aniline was too high in the micelles. The guide effect of aniline/DBSA cylindrical micelles as soft templates would be destroyed [12].

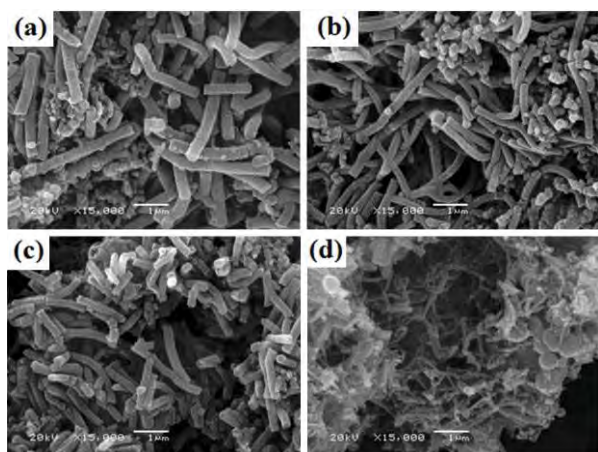


Figure 3. SEM images of PANI nanostructures doped with different organic acids: (a) acetic acid, (b) benzoic acid, (c) *p*-TSA. Synthetic conditions : [dopant]/[An]=0.2; 0-5 °C; 10 h and (d) DBSA+ HCl. Synthetic conditions : [dopant]/[An]=0.2; [HCl]/[An] =1; 0-5 °C; 24 h

Table 1: Effect of the dopants on the outer diameters of PANI nanotubes.

Dopant	Outer diameter [nm], (n=30)	Molecular formula
acetic acid	300±30	CH ₃ COOH
benzoic acid	330±30	C ₆ H ₅ COOH
<i>p</i> -TSA	260±30	CH ₃ C ₆ H ₄ SO ₃ H
DBSA+HCl	110±10	C ₁₂ H ₂₅ C ₆ H ₄ SO ₃ H

From Table 1, the average outer diameters of the nanotubes doped with small organic acids (acetic acid, benzoic acid and *p*-TSA) were in the range of 260-330 nm while those doped with long hydrophobic hydrocarbon side chain of organic acid (DBSA) were smaller (110 nm). Since PANI doped with DBSA was produced through micelles as soft templates mechanism, the complexation of aniline and DBSA had a small averaged micelle size around 91.7 nm [8]. That was different from PANI doped with small organic acids produced through phenazine templating. When oligomeric products were precipitated into “needle-like crystallite offsprings” that serve as template, averaged size of the crystalline was around 250 nm [7]. Moreover, the higher number of -CH₂-

moieties of the same functional group of organic acid dopant (acetic acid vs benzoic acid) resulted in an increase of the average outer diameter of PANI nanotubes.

3.3 Effect of methanol

Fig. 4 shows PANI nanostructures synthesized in the presence of methanol, the nanotubes and nanorods became irregular and lost their uniform morphology. This might be due to the H-bonding between N of amine group of the PANI chain and the OH group of the methanol, which might act as a driving force for the formation of aggregated granules [13]. The H-bonding would prohibit the self-ordering of PANI chain to form nanotube structures because the intermolecular H-bonding interaction was interception of PANI chain stacking and PANI chains extend from them.

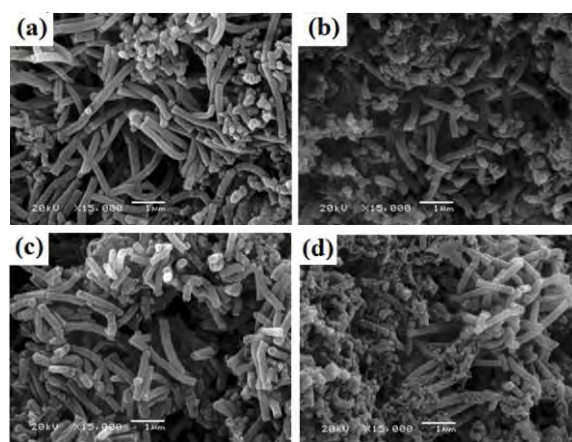


Figure 4. SEM images of PANI nanostructures doped with different organic acids in the presence methanol: (a) benzoic acid, (b) benzoic acid+methanol, (c) *p*-TSA and (d) *p*-TSA+methanol. Synthetic conditions : [dopant]/[An]=0.2; [methanol]=1 M; 0-5 °C; 10 h

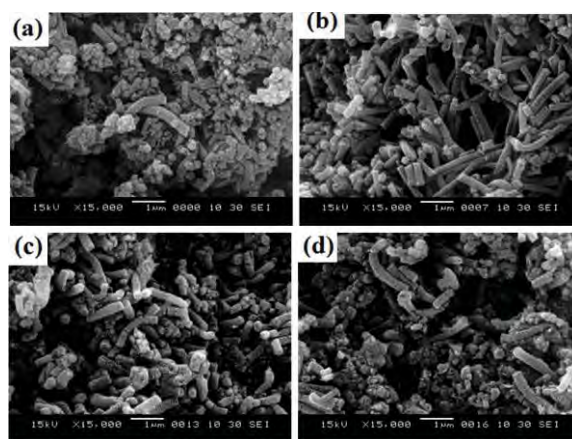


Figure 5. SEM images of PANI-acetic acid synthesized using different molar ratios of dopant to aniline, [acetic acid]/[An] : (a) 0.01, (b) 0.2, (c) 0.6, and (d) 1.0. Reaction conditions: [An]/[APS]=1, reaction time =10 h.

3.4 Effect of molar ratio

PANI nanostructures prepared through phenazine templating were studied. The SEM images of the acetic acid doped PANI prepared at different [acetic acid]/[An] (An = aniline) molar ratios are shown in Fig.5. The uniformity of nanotubes was excellent as the [acetic acid]/[An]=0.2 (yield about 80%) since this molar ratio produced the optimum starting pH of solution (pH=2.5-4) for oxidation of neutral aniline molecules to oligomers having mixed *ortho*- and *para*-coupled aniline constitutional units. *Ortho*-coupled units might undergo intramolecular cyclization to produce phenazine structures that the phenazine units acted as the initiator for the growth of PANI nanotubes. When the oxidation occurred in low molar ratio, the solutions had a pH>4. Under low acidity conditions, the reaction of aniline addition (i.e. oligomer growth) was faster than the subsequent cyclization reactions. The monomer molecules were converted to oligomers having a mixed coupling structure. On the other hand, when the oxidation occurred in high molar ratio, the solutions had a pH<2.5. Under conditions of high acidity, the concentration of the easily oxidizable non-protonated aniline molecules was very low, and consequently the reaction rate was considerably reduced, so that only short oligomers were produced [6].

4. Conclusions

PANI nanotubes doped with various organic acids were prepared through a self-assembly method. The small organic acid dopants were leading to phenazine templating of PANI nanotubes while the long hydrophobic were leading to micelle as soft template. The formation yield, size and uniformity of PANI nanotubes were affected by variety of dopants, formation mechanism, reaction media and [dopant]/[An] molar ratio.

Acknowledgements

This work was supported by Thesis Scholarships of Program of Petrochemical and Polymer Science, Faculty of Science, Chulalongkorn University and Chromatography and Separation Research Unit.

References

- [1] Y. F. Huang and C.W. Lin. *Synthetic Metals*. **159** (2009) 1824-1830.
- [2] Z. Zhang, Z. Wei, L. Zhang and M. Wan. *Acta Materialia*. **53** (2005) 1373-1379.
- [3] L. Zhang, H. Peng, J. Sui, P.A. Kilmartin and J. Travas-Sejdic. *Current Applied Physics*. **8** (2008) 312-315.
- [4] L. Ren and X. F. Zhang. *Synthetic Metals*. **160** (2010) 783-787.
- [5] Z. Huang, E. Liu, H. Shen, X. Xiang, Y. Tian, C. Xiao and Z. Mao. *Materials Letters*. **65** (2011) 2015-2018.
- [6] I. Sapurina and J. Stejskal. *Polymer International*. **57** (2008) 1295-1325.
- [7] J. Stejskal, I. Sapurina, M. Trchova, E. N. Konyushenko and P. Holler. *Polymer*. **47** (2006) 8253-8262.
- [8] C. Laslau, Z. Zujovic and J. Travas-Sejdic. *Progress in Polymer Science*. **35** (2010) 1403-1419.
- [9] Y. F. Huang and C. W. Lin. *Polymer*. **50** (2009) 775-782.
- [10] C. Laslau, Z. D. Zujovic and J. Travas-Sejdic. *Macromolecular Rapid Communications*. **30** (2009) 1663-1668.
- [11] B. Z. Hsieh, H. Y. Chuang, L. Chao, Y. J. Li, Y. J. Huang, P. H. Tseng, T. H. Hsieh and K. S. Ho. *Polymer*. **49** (2008) 4218-4225.
- [12] H. Yin and J. Yang. *Materials Letters*. **65** (2011) 850-853.
- [13] L. Zhang, Y. Long, Z. Chen and M. Wan. *Advanced Functional Materials*. **14** (2004) 693-698.

UREA ABSORPTION BEHAVIOURS OF CASSAVA STARCH BLEND WITH GLUTINOUS RICE STARCH AFTER GAMMA IRRADIATION

Sawittree Rujitanapanich^{1*}, Prartana Kewsuwan² and Siriluk Sangngan³

^{1,3}Department of Chemistry, Faculty of Science and Technology,
Phranakhon Rajabhat University, Bang Khen, Bangkok, Thailand 10220

²Thailand Institute of Nuclear Technology (Public Organization).
Ongkharak, Nakhon Nayok, Thailand 26120

*Corresponding author: sawittree_rj@yahoo.com, Tel. +66 02 5448198, Fax. +66 02 5226609

Abstract: This study aims to investigate urea absorption behaviours at 25%W CS+GS (1:1) at 15 kGy. The preliminary study was to investigate the swelling behaviours of cassava starch (CS) and glutinous rice starch (GS) after being irradiated with gamma rays at different doses, 5, 10, 15, 20, 25 and 30 kGy, with different concentrations of starch weights (20, 25 and 30%). The results revealed that at a dose of 15 kGy, both starches were soft and could maintain their textures. At the concentration of 25% starch weights the result showed that CS could maintain its texture better than GS. However, after increasing the dose of gamma rays, the swelling is more likely decreasing in every concentration. In addition, mixture of CS+GS at 1:1 was studied with 20-30%W. At 25%W with 15 kGy gamma irradiation, the CS+GS texture could maintain its shape. Otherwise, when the dose was increasing more than 15 kGy, the texture is likely to become harder (correlation coefficient, r between dose and swelling = -0.79). Therefore, the urea absorption of CS+GS at a 25%W and 15 kGy gamma irradiation was chose for next study. The urea concentration in the filtrate was determined from the complex compound of urea and p-dimethylaminobenzaldehyde (DMAB) by using a spectrophotometer at the wavelength of 440 nm. The optimum concentration of urea is 10% and the maximum absorption value of urea is 33.52%W. In conclusion the highest release of urea at 8 hour is 2.12 mg/g of CS+GS, and the linear equation focused on release urea was $y = 0.1023x + 1.2329$ with $R^2 = 0.8414$.

Keywords Cassava starch; Glutinous rice starch; Irradiation; Urea absorption

1. Introduction

Starch derived naturally from photosynthesis of plant. It is a polymer of glucose, which composed of amylose and amylopectin molecule. It is usually stored in grain, root as well as other parts in plants. Different types of starch originated from different types of plants. Various attributes of different starch granule are the indicators to types of starch. Amylose comprised of glucose connected by glucosidic linkage type α 1,4. The structure of starch is a long stripe with no extended branch, not easily dissolved in water. On the other hand, amylopectin also has extended branch connected by glucosidic linkage type α 1,6 of which also resulted in better dissolution. Cassava starch (CS) contains 17% of amylose [1]. It is hardly dissolved in

water as when being heated and cool down, it gelatinizes. Glutinous rice starch (GS) comprises of 99.7% amylopectin [2] and shows a better rate of dissolution, compare with amylose. GS will not turn gelatinized when being heated. Starch without amylose will hardly retrogradation, rapidly remoisten [3].

As a result to the characteristic of absorption and swelling behaviours of starch solution is heated. Many researchers have been conducted on topics regarding water absorption as well as the development based on characteristics of starch. To illustrate, the characteristics are based for the release of medicine from tablet, improvement of water absorption in soil, and the use of polymer in diaper Zheng Tong et al. (2009) [4]. The study was conducted for hydrogel absorbent using Sodium hydroxide, interacts with Acrylic acid. The result Polysodiumacrylate was connected with N, N'-methylene-bis-acrylamide in order to control release of urea, found that the rate of urea release was depend on the size of gel bead and cross-link. Gel beads of 3-6 mm. reveal a higher release rate than 20 mm. However, release rate is lower when the crosslink rises. Peerapattana et al. (2010) [5] studied the use of glutinous rice starch (GS) as a sustained release agent for tablet preparations. The GS slurry was physically modified by heat and then dried by spray drying. The tablet containing pregelatinized GS (PGS) and propranolol HCl were prepared by wet granulation method. Less than 80% of propranolol HCl was released in period of 10 h at the drug to PGS ratio of 1:2 and longer than 14 h at the ratios of 1:3 and 1:4.

In this study aims to investigate urea absorption behaviours at 25%W CS+GS (1:1) at 15 kGy. The preliminary study to investigate the swelling behaviours of 20, 25 and 30%W of CS and GS at 5, 10, 15, 20, 25 and 30 kGy.

2. Materials and Methods

2.1 Materials and Instruments

CS was manufactured by Bangkok Starch Industrial Co.Inc (Thailand), GS was produced by Tonjun Co.Inc (Thailand). Urea was purchased from Aja Finechem, p-dimethylaminobenzaldehyde (DMAB) was supplied by Asia Pacific Chemicals Limited.

The Starch were irradiated with Gamma chamber 5000 from TINT. The complex compound of urea and DMAB was detected using a Spectrophotometer of CECIL CE4002 400 SERIES at the wavelength of 440 nm.

2.2 Methods

The swelling of CS and GS.

The study of swelling behaviour of CS and GS can be conducted by separately preparing the solution of CS and GS at concentrations of 20, 25 and 30%W. Then, the mixture was heated until turning clear and sticky and replaced into zip lock bag. The samples were spread out and irradiated by Co-60 at the doses of 0, 5, 10, 12, 15, 20, 25 and 30 kGy. After that, the gel samples were dried at temperature of 70°C in vacuum oven. The obtain dried gel was weighed and soaked in 60 ml of distilled water for 24 hours, then measured the weight of the wet gel and calculated the percentage swelling using formula:

$$\% \text{ swelling} = (W_w - W_d) * 100 / W_d$$

(When 'W_w' is the gel weight after being soaked in distilled water, while 'W_d' is the gel weight before being soaked in distilled water.)

The swelling of mixture of CS+GS

The mixture of CS and GS was prepared in the ratio of 1:1. The concentrations of the CS+GS mixture were 20, 25 and 30%W and the irradiation doses were at 5-30 kGy. Percentage swelling of the CS+GS gels were also calculated.

The study of absorption and release of urea in mixed gels (CS+GS)

For urea absorption and releasing studies, CS and GS were mixed by the ratio of 1:1; applying the intensity level and amount of ray which starch mixture has a high swelling level but the gel texture is still stable soft after being soaked in water. Then, oven dried the starch mixture and study urea absorption by preparing concentrated urea solution of 2, 4, 6, 8, 10 and 12% (W/V). 1 gram starch mixture was placed in 25 ml of various concentration of urea for 24 hours. The remaining urea concentration were determined by combining with DMAB solution and its absorption was measured at the wavelength of 440 nm. In the study of urea release, 1 gram of vacuum oven dried CS+GS were added in 25 ml urea, using the highest level of urea which mixed starch can be absorbed the most for 24 hours. After that, dried the mixture in oven and soaked in 25 ml of distilled water for 0.25, 0.5, 1, 2, 3, 4, 5, 6, 8, 24 and 30 hours. The intensity of emitted urea in the solution was examined. The reaction of DMAB and urea was detected using UV-Spectrophotometer at wavelength of 440 nm according to Figure 1.

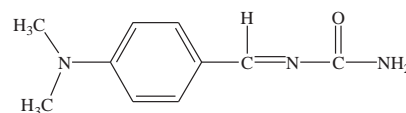
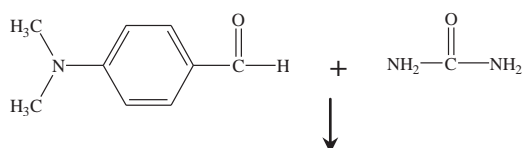
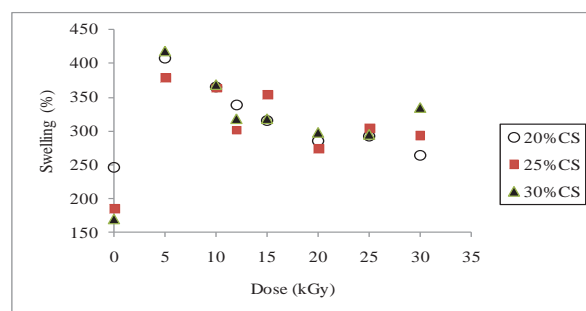


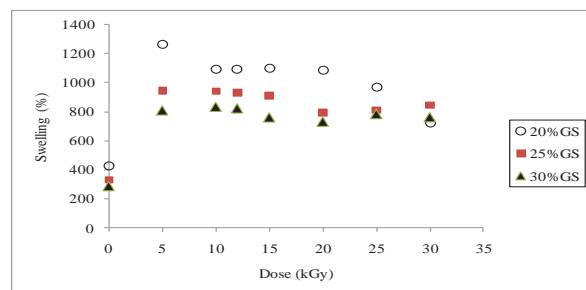
Figure 1 The reaction of DMAB and urea

3. Results and Discussion

The swelling percent of CS and GS as a function of irradiation doses of 0 – 30 kGy at 20, 25 and 30% of CS and GS is shown in figure 2.



(a) at the concentrate 20, 25 and 30% of CS



(b) at the concentrate 20, 25 and 30% of GS

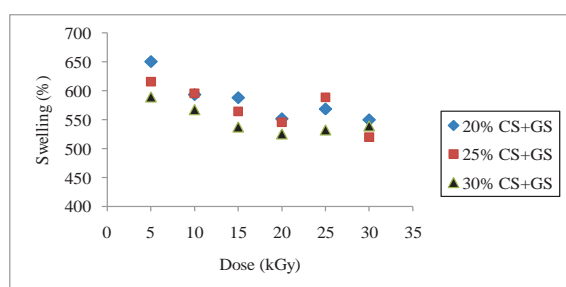
Figure 2. Swelling percent as a function of irradiation doses of 0 – 30 kGy at 20, 25 and 30% of CS and GS

As GS contains as much as 99.7% of amylopectin [2], it is usually very sticky when transformed to liquid. It cannot dissolve and swell in water at room temperature, therefore, GS needs to be modified by heating. The results show that unirradiated CS and GS starch have less swelling than irradiated ones. Thus, radiation effects the change in starch structure. At 5 kGy, CS and GS gels at concentrations of 20, 25 and 30%W showed high swelling of 407.29 ± 14.11 , 378.54 ± 21.33 , 418.63 ± 34.25 and 1262.05 ± 47.89 , 945.28 ± 24.59 , 808.83 ± 66.26 respectively. GS has the higher swelling than CS; however, both gels appear quite soft after soaked in water. For the doses of 10 and 12 kGy, the swelling of CS and GS is diminished. At 15 kGy, GS gel is soft but still in shape. At over 15 kGy, the GS gels turn quite hard at all concentrations and their swellings are also reduced. Therefore, when radiation dose is increased, gel property of CS and GS is worse. N. Nagasawa, T. Yagi et.al (2004) [6] had synthesized

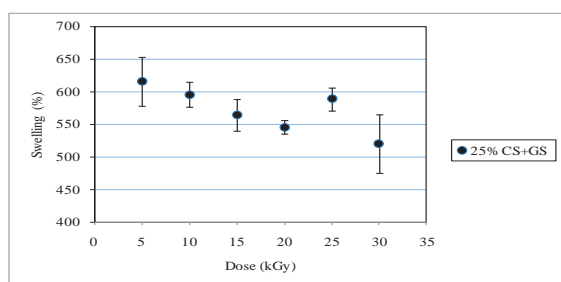
carboxymethyl starch (CMS) hydrogel at different radiation doses and CMS concentrations among 20-50%. The study revealed that 1 gram of dried gel at the concentration of 40% at dose of 2 kGy, was able to absorb 500 grams of distilled water and 29 grams of 0.9% saline water.

When comparing percent swelling among 20, 25 and 30% of CS and GS starch at 15 kGy at 95% confidence level; the highest swelling level of CS is 353.56 ± 31.03 at 25%W and GS is 1099.92 ± 99.58 at 20%W. This replies that starch concentration of 25% has relatively good swelling; CS starch gel stays in shape better than GS while swelling is less. However, swelling tends to reduce when the concentration of starch is increased, as the increased concentration strengthens gel structure and the restoration of amylose is quicker than amylopectin. It is according to the structure of amylopectin which contains branches and being as obstacles for hydrogen bonding between molecules, causing loose connection and fragile gel [3]. The texture of GS gel is softer than CS, as it contains high amylopectin but has higher swelling. Starch with no amylose hardly revert and quickly drenched.

The relationship of swelling percentage and amount of radiation at 20, 25 and 30% of CS+ GS (1:1) is illustrated as figure 3.



(a) at 20, 25 and 30% concentrations of CS+GS mixture



(b) The swelling at 95% confidence level at the 25% concentration of CS+GS mixture

Figure 3. Swelling of CS+GS of dose 5-30 kGy

According to figure 3a), the swelling of CS+GS at 5-10 kGy is quite high for all concentrations; however, gel after soaked in water is soft. At 15 kGy, the appearance of gel is still constant, at 95% confidence level the swelling of 25%W is 564.19 ± 23.78 ($r = -0.79$) (figure 3b). Starting from 20 kGy, the gel has become hard, which replies that mixed starches of

25% at 15 kGy, the gel would still be unchanged after soaked in water. The swelling is rather high when comparing to other doses and concentrations.

The concentration of 25% CS+GS gel at 15 kGy shows a relatively high swelling, while gel appearance after soaked. Urea absorption is studied under concentration of 2-12%W/V. One gram of dried mixed CS+GS gel was soaked in 25 ml. of urea solution for 24 hours. After the swelling gel removed, the concentration of the rest of urea solution was determined by combining with DMAB solution. Then absorbance value was determined at the wavelength of 440 nm. While urea concentration increases, urea absorption percentage is slightly increased up to 10%. When the concentration of urea increase to 12%, absorption percentage started to declined possibly caused by urea emission. The optimum concentration of urea is 10% and the maximum absorption value of urea equals 33.52 ± 3.30 at 95%, confidence level as shown in figure 4.

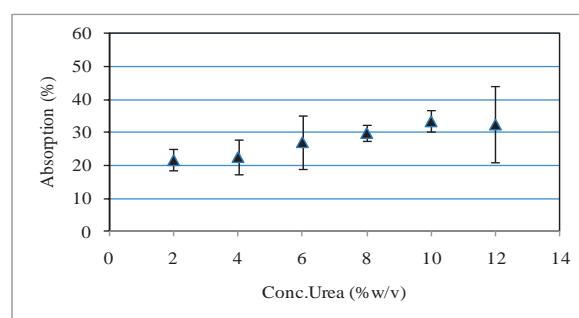


Figure 4. Effect of absorption percentage on urea concentration of 2-12%W/V

For 10% of urea, mixed starch of 25% CS+GS at 15 kGy can absorb the most. Therefore, the study of urea release in CS+GS is investigated in 10% of urea concentration. Dried mixed CS+GS was soaked in 25 ml of 10% urea solution. At 0.25-8.0 hour of soaking time, the concentration of urea was determined.

Figure 5 shows urea release rate for 0.25-8.0 hours.

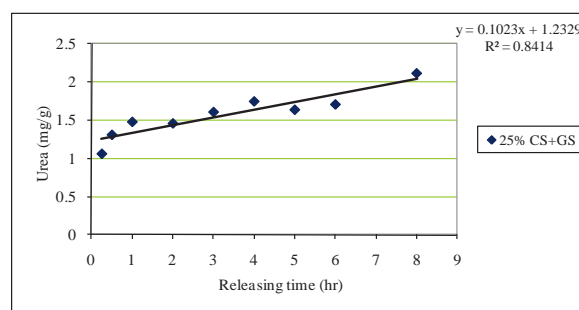


Figure 5. Urea release of 25% CS+GS at different time Periods

At 0.25 and 0.5 hour, urea is released rapidly from dried gel. Urea release rate becomes stable at 1-6 hour. Nevertheless, urea release rate rises highest at 8 hour. When time passes to 24-30 hour, release rate has been

declined less than at 8 hour (not show in the Figure 5) The reduction of release rate is possibly caused by reabsorption of released urea and linear equation of urea release as follow: $y = 0.1023x + 1.2329$ with $R^2 = 0.8414$.

The 25% CS+GS at the dose of 15 kGy is soaked in 10% urea solution for 8 hour. It was found that the urea release rate is 0.21. It is according that GS composes of 99.7% amylopectin, of which cannot dissolved and swell in water at room temperature. Therefore, GS needs to be modified in order to gain preferred characteristics. For example, modification of GS pregel by using heat to reduce releasing rate. However, using heat for modification will negatively resulted in flowing characteristic of GS. However, CS+GS starch is biodegradable, urea release will increase when time passes. Padungkwan Chitropas Nuwat Visavarungroj (2008) [7] has studied on properties of modified glutinous rice starch prepared by alkali treated method used as hydrophilic matrix, by applying sodium hydroxide and hydrochloric acid. The result shows that modified glutinous rice starch has pH of 8-12. The modified starch in sodium hydroxide 1.6 molar, swells less than the one in sodium hydroxide 2.6 molar. The structure of starch will be destroyed, yet the stickiness and swelling are increased for 2.6 molar sodium hydroxide. Therefore, the study of urea release of CS+GS gel by using sodium hydroxide and hydrochloric in different concentration is another alternative to modify the starch.

3. Conclusions

This research provided the basic knowledge of correlated between urea absorption and swelling behaviours of CS and GS with gamma rays in different doses. The resulted showed that at the low irradiation dose of gamma rays around 5 kGy the swelling was higher, but the gel was soft and unstable texture. At 15 kGy, the gel was more stable with soft texture. With gamma rays higher than 15 kGy the gel was stronger texture, but the swelling was decreased. Therefore, the property of gel-like starch will decrease because of increasing of starch concentration and radiation dose. For urea absorption, the resulted found that at 25%W CS+GS of starch, gel stays in shape more than 20 and 30%. With 15 kGy, the optimum concentration of urea is 10% and the maximum absorption value of urea equals 33.52 ± 3.30 . Therefore when urea concentration increases, swelling decreases possibly caused by urea emission. The highest release of urea occurs when 8 hour passes is 2.12 mg/g of CS+GS.

Acknowledgements

This research is financially supported by Phranakhoon Rajabhat University. The authors thank Thailand Institute of Nuclear Technology (Public Organization) for helping the sample irradiation.

References

- [1] A. B. Christine. *Understanding Food: Principles and Preperation*, 3rd. Thomson. Learning, Inc. California (2008), p. 362.
- [2] RS. Kadan, ET. Champagne, GM. Ziegler and AO. Richard. *J Food Science*. **62** (1997) 701-703.
- [3] K. Sriroth and K. Piyachomkwan. *Technology of starch*. Kasetsart University Press, Bangkok, (2007).
- [4] Z. Tong, L.Yuhai, Y. Shihuo and H. Zhonggyi. *J. Biosystems Engineering*. **102** (2009) 44-50.
- [5] J. Peerapattana, P. Phuvarit, V. Srijesdaruk, D. Preechagoon and A. Tattawasart. *J. Carbohydrate Polymers*. **80** (2010) 453-459.
- [6] N. Nagasawa, T. Yagi, T. Kume and F. Yoshii, *Carbohydrate Polymer* **58** (2004) 109-113.
- [7] P. Chitropas and N. Visavarungroj, *J of Agricultural Sci*. **39:3** (Suppl.) (2008) 507-510.

SYNTHESIS OF LACTIC ACID-BASED BLOCK COPOLYMER VIA ATOM TRANSFER RADICAL POLYMERIZATION (ATRP)

Siriporn Pranee¹, Atitsa Petchsuk², Pakorn Opaprakasit³, Mantana Opaprakasit^{1*}

¹ Department of Materials Science, Faculty of Science, Chulalongkorn University, Pathumwan, Bangkok, 10330 Thailand

² National Metal and Materials Technology Center (MTEC), Klong Luang, Pathumthani, 12120 Thailand

³ School of Bio-Chemical Engineering and Technology, Sirindhorn International Institute of Technology (SIIT), Thammasat University, Pathum Thani, 12121 Thailand

* Author for correspondence; E-Mail: mantana.o@chula.ac.th, Tel. +66 218559, Fax. +66 22 185561

Abstract: Biodegradable poly(lactic acid) (PLA) is of interest in commercial use and the research community. In this study, block copolymers of PLA and poly(methyl acrylate) (PMA), which is commonly synthesized from step-growth and chain-growth mechanisms, respectively, are developed. Atom Transfer Radical Polymerization (ATRP) of methyl acrylate is employed using macro-initiators (GPLA-MI), prepared from chemically recycling products of PLA. PLA glycolysate (GPLA) with number average molecular weight (M_n) of ~1,270 g/mol is obtained from glycolysis of commercial PLA using ethylene glycol (EG) at 175 °C for 25 min, and a PLA:EG weight ratio of 1: 0.5. The synthesis of GPLA-MI is carried out by esterification of GPLA and 2-bromoisobutryl bromide (BiB). ¹H-NMR results indicate that a GPLA: BiB molar ratio of 1: 2.5 effectively yields GPLA-MI initiator consisting of BiB terminals. Feasibility of using the obtained GPLA-MI in the preparation of PLA-b-PMA copolymers *via* ATRP is proven by using an MA:GPLA-MI:CuBr:PMDETA molar ratio of 100:1:2:4.

1. Introduction

Poly(lactic acid) (PLA) is biodegradable and can be derived from renewable sources. [1] Many attempts have been pursued in using this environmental-friendly material to replace conventional commodity plastics, *i.e.*, petroleum based polymers. In this regard, many studies have been carried out to enhance properties of PLA by means of blending or copolymerization. Atom Transfer Radical Polymerization (ATRP) technique is a proven synthesis approach for copolymerization of functional monomers with vinyl monomers. [2] Matyjaszewski et al. [3-6] and Goodwin et al. [7] reported a polymerization of vinyl monomers *via* alkyl free radical ATRP by using alkyl halide as initiator and transition metal complex, such as copper, as a catalyze. Recently, ATRP polymerizations of polystyrene, polyacrylate, poly(methyl methacrylate) were reported. [3, 5] Block copolymers can also be synthesized *via* ATRP by utilizing alkyl halide-capped polymer chain as a macro-initiator and vinyl comonomers, to achieve polymers with narrow molecular weight distribution. [2]

This work is aimed to develop block copolymer based on PLA and methyl acrylate (MA). Feasibility of using PLA glycolysate (GPLA), a product from chemically recycling of PLA resin, as a starting material for preparing macro-initiator (GPLA-MI) is

investigated. GPLA-MI is prepared *via* esterification of GPLA with 2-bromoisobutryl bromide (BiB). The block copolymer is then synthesized from GPLA-MI and methyl acrylate (MA) *via* ATRP using CuBr/PMDETA catalyst system in a bulk polymerization process.

2. Materials and Methods

2.1 Materials

Poly(lactic acid) (PLA, NatureWork 4042D) and ethylene glycol (EG, Carlo Erba) were used in the glycolysis reaction. Tetrahydrofuran (THF, Lab scan) was freshly distilled prior to use. Methyl acrylate (MA, 99%) and triethylamine (TEA, 99%) supplied by Aldrich were vacuum distilled over calcium hydride (CaH₂) and stored under N₂ atmosphere. 2-bromoisobutryl bromide (BiB, 98%), copper (I) bromide (CuBr, 98%) and ligands *N, N, N', N'*-pentamethyldiethylenetriamine (PMDETA, 99%) were used as received.

2.2 Characterization

¹H-NMR spectra were recorded on a Bruker Biospin AV-5 at 400 MHz, using CDCl₃ as a solvent and tetramethylsilane (TMS) as an internal chemical shift standard. The number and weight average molecular weights (M_n and M_w) of GPLA, GPLA-MI and copolymers were measured by gel permeation chromatography (GPC) on a Waters 600 controller, using THF solvent with a flow rate of 1 ml/min.

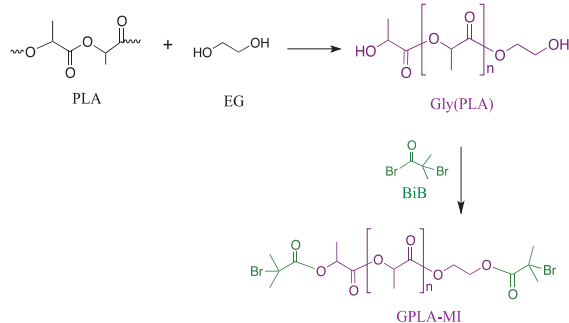
2.3 Glycolysis of PLA resin

Commercial PLA resin and EG (1: 0.5 by weight) were mixed in a four-neck reaction kettle, and refluxed under N₂ atmosphere at 175 °C for 25 min. After the reaction completion, GPLA was recovered by dissolving in CHCl₃ and precipitating in excess ethanol. The GPLA products were dried under vacuum at 50 °C overnight and kept in desiccator.

2.4 Esterification of GPLA

GPLA-MI was synthesized by esterification of hydroxyl-capped GPLA with BiB, as summarized in Scheme 1. The reactions were conducted at GPLA:BiB molar ratios of 1:2 and 1:2.5 by varying GPLA/THF contents (Table 1). For example, GPLA-MI2 was

prepared using a molar ratio of 1:2.5. Essentially, GPLA (5g, 4.0 mmol) was dissolved in 10 ml of freshly distilled THF in a 2-neck round bottom flask at 50 °C for 15 min. Subsequently, TEA (1.4 ml, 10.1 mmol) was added and the solution was stirred under N₂ atmosphere for 15 min. The solution was cooled to room temperature, and BiB (1.24 ml, 10.1 mmol) was added dropwise for over a 15 min period. The reaction mixture was further stirred at 50 °C for 90 min. A yellowish viscous product was obtained after THF solvent removal. The product was then undergone solvent extractions using CHCl₃ and water. The organic phase was washed with 15 ml 1N HCl, saturated Na₂CO₃ solution and brine. After drying over anhydrous MgSO₄, CHCl₃ was removed under reduced pressure. Finally, the product was purified by dissolving in CH₃Cl and precipitating in excess ethanol. The received GPLA-MI was dried overnight at 50 °C under vacuum.



Scheme 1. Preparation of GPLA-MI by capping of GPLA with alkyl bromide

2.5 Synthesis of PLA-*b*-PMA via ATRP

PLA-*b*-PMA copolymer was prepared via ATRP using a CuBr/PMDETA catalyst and a GPLA-MI: CuBr: PMDETA: MA molar ratio of 1: 2: 4: 100. A mixture of GPLA-MI 0.5 g (16.73 mmol), PMDETA 0.139 ml (66.94 mmol) and methyl acrylate 2.44 ml (MA, 1.7 mol) was placed in a 2-neck round bottom flask, which was freeze-pump-thaw degassed for three times and heated to 90 °C. The polymerization was initiated by adding of CuBr 0.048g (33.46 mmol) and continued for 18 hr. The mixture was then diluted with THF, at room temperature, and filtered over a short silica gel column to remove the residue (green color) copper catalyst.

Table 1: Effects of GPLA/BiB molar ratio on esterification of macro-initiator at 50 °C.

Entry	Polymer	GPLA/BiB (by mole)	GPLA/THF (g/ml)	Yield (%)	M _n (GPC)	M _w (GPC)	M _n (NMR)
1	GPLA-MI1	1/2	5/10	NA	NA	NA	NA
2	GPLA-MI2	1/2.5	5/10	21	5000	5900	3050
3	GPLA-MI3	1/2.5	5/25	38	4500	5800	1980
4	GPLA-MI4	1/2.5	5/30	56	5000	5900	2980

3. Results and Discussion

It is observed that GPLA obtained from the glycolysis reaction has low molecular weight value, *M_n* ~ 1,270 g/mol, calculated from ¹H-NMR spectra using equation 1.

$$DP = H^b \left[\frac{H^c + H^d}{4} \right]$$

$$M_n = (DP \times 72) + 62 \quad \text{equation 1.}$$

where DP: degree of polymerization

H^b: methine proton of lactate repeating unit

H^c, H^d: methylene proton of terminal EG groups capped on GPLA's chain ends

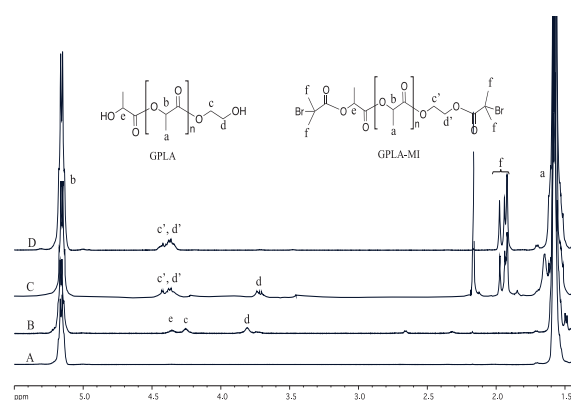


Figure 1. ¹H NMR spectra of PLA (A), GPLA (B), GPLA-MI1 (C) and GPLA-MI4 (D) in CDCl₃

Figure 1. shows ¹H NMR spectra of the commercial PLA (A), in comparison with GPLA (B) and GPLA-MI (C, D). The proton resonance of methyl proton in lactate repeating unit at 1.51 ppm (H^a) shifts to 1.54 ppm, where that of methine proton in lactate repeating unit at 5.09 ppm (H^b) also shifts to 5.15 ppm, after the glycolysis reaction. The CH₂-CH₂-OH terminal group shows proton resonances of methylene at 4.18 ppm (H^c) and 3.74 ppm (H^d). A methine proton (H^e) signal at ~ 4.33-4.36 ppm is associated with the hydroxyl of lactate at the other end of GPLA chains. The presence of these hydroxyl end groups enables the use of GPLA as starting materials for synthesizing of GPLA-MI by reacting with BiB.

H^c and H^d signals are not observed in GPLA-MI4, as shown in Figure 1D. This reflects esterification reaction of CH₂-CH₂-OH by BiB, leading to an appearance of the methylene signals (H^{c'} and H^{d'}) in GPLA-MI at 4.37-4.43 ppm. Since H^{c'} and H^{d'} are located close to H^e, it is challenging to determine whether the lactate OH groups at the other end of GPLA is completely reacted with BiB. The proton resonance at ~1.86-1.91 ppm (H^f) observed in GPLA-MI4 is corresponding to methyl of the bromoesters. The presence of remaining H^c and H^d signals in the spectra of GPLA-MI1 (Figure. 1C), compared to that

of GPLA-MI4, implies that the GPLA:BiB molar ratio of 1:2.5 is more effective than 1:2, in esterification GPLA end groups. Table 1 summarizes effect of the molar ratios on yield and structure of the products, where % yield of GPLA-MIs increases with the GPLA concentration in feed.

Chemical structures of PLA-*b*-MA received from ATRP of MA with GPLA-MI4 in bulk reaction using a CuBr/PMDETA catalyst system are examined by ¹H-NMR and GPC. ¹H NMR spectrum (Figure 2) ensures a success in preparing this block copolymer. The signals at 2.2-2.3 and 3.59 ppm are assigned to methine proton (H^l) and methoxy group (H^s) of methyl acrylate repeating units, respectively. The methine proton (H^h) and methoxy group (Hⁱ) of MA consisting of bromide atom located at the copolymer chain end show signals at 4.94 and 3.67 ppm, respectively. Methylene protons of PMA blocks appear at 1.61-1.87 ppm (H^k). The signal of methyl protons (H^l) at 1.17 ppm is a result from the modification of the methyl groups in bromoester of GPLA-MI (H^f ~ 1.86 – 1.91 ppm) by ATRP.

GPC results indicate that M_n and M_w of the resulting copolymer are 13,400 and 19,100 g/mol. Given that M_n (GPC) of GPLA-MIs is ranging from 4,500 – 5,000 g/mol (Table 1), the calculated M_n of the PLA-*b*-MA product implies that the number of MA repeat units in the copolymer chain is close to the MA content in feed. M_w/M_n obtained in this study is approximately 1.42 which is slightly broader than that of poly(lactide)-*b*-poly(HEMA) (1.2-1.32) prepared by one-pot synthesis of a two-step ROP/ATRP strategy with 2-hydroxyethyl 2-bromo-2-methylpropanoate (HBMP) as a double-headed initiator. [2] This indicates the controlled molecular weight mechanism of the ATRP. It is noted that the slightly high M_w/M_n values of the resulting copolymers are likely due to the incompleteness of the reaction, i.e., the remaining of GPLA-MI, as reflected from the low percentage yield of the reactions. Further study on a preparation of PLA-*b*-MA with GPLA-MI and ATRP in solution systems is undergoing. Effect of GPLA-MI: CuBr: PMDETA: MA molar ratios on molecular weight distribution of PLA-*b*-MA block copolymers will be investigate

4. Conclusions

PLA glycolysates, obtained from glycolysis of PLA resin, possess hydroxyl end groups which is feasible for esterification with BiB, especially with the use of a GPLA:BiB molar ratio of 1:2.5. The GPLA-MI product is successfully used as a macro-initiator in the polymerization of methyl acrylate monomer (MA) via ATRP using a CuBr/PMDETA catalyst system. PLA-*b*-MA block copolymer is produced by a bulk process, where bromide group on GPLA-MI's chain ends act as a free radical generator in the polymerization MA monomers to form PMA blocks.

Acknowledgements

Financial support of this work is partly provided from the 90th Anniversary of Chulalongkorn University Fund (Ratchadaphiseksomphot Endowment Fund). S. Pranee thanks Department of Materials Science, Faculty of Science, Chulalongkorn University for a partial support on academic tuition and expense for attending PACCON 2013.

References

- [1] J. Ren, *Biodegradable Poly(Lactic Acid): Synthesis, Modification, Processing and Applications*, Springer (2010), pp. 1-3.
- [2] F. F. Wolf, N. Friedemann and H. Frey, *Macromolecules*. **42**, (2009) 5622-5628.
- [3] J. Xia and K. Matyjaszewski. *Macromolecules*. **30**, (1997) 7697-7700.
- [4] K. Matyjaszewski and J. Spanswick In: H. R. Kricheldorf, O. Nuyken, G. Swift, (Eds.), *Handbook of polymer synthesis*, Marcel dekker, (2005), pp. 901-905.
- [5] K. Matyjaszewski and J. Xia, *Chem. Rev.* **201**, 2921-2990 (2001).
- [6] K. A. Nanda and K. Matyjaszewski, *Macromolecules*. **36**, (2003) 1487-1493.
- [7] J. M. Goodwin, M. M. Olmstead and T. E. Patten, *J. Am. Chem. Soc.* **126**, (2004) 14352-14353.

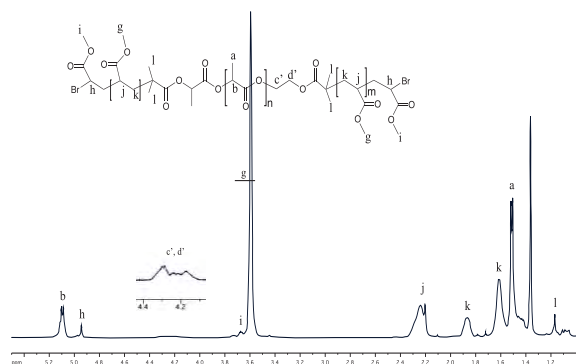


Figure 2. ¹H NMR spectrum of PLA-*b*-PMA in CDCl₃

EFFECT OF CELL STRUCTURE AND POROSITY ON VISCOUS LOSS AND INERTIAL LOSS COEFFICIENT IN CFD SIMULATION

Wuttichai Prukwarun^{1,2}, Sarawut Phupaichitkun^{1,2,*}

¹Department of Materials Science and Engineering, Faculty of Engineering and Industrial Technology, Silpakorn University, NakornPathom 73000, Thailand

²National Center of Excellence for Petroleum, Petrochemicals, and Advanced Materials, Chulalongkorn University, Bangkok 10330, Thailand

* Author for correspondence; E-Mail: psarawut@su.ac.th, Tel. +66 34219663, Fax. +66 34219363

Abstract: Computational fluid dynamic (CFD) simulation of biological structure required nanoscale meshing and consuming very long time for calculation. Simplified this geometry to a single porous layer is necessary. The viscous resistance ($1/\alpha$) and inertial resistance (C_2) coefficients can be investigated by measuring the pressure drop per length ($\Delta P/L$) at different fluid velocity which is difficult for experimental setup. In this work, these coefficients were estimated by using Ergun's equation involving the effect of cell shapes (the square shape for plant cell and hexagonal shape for animal cell), the effect of cell size from 10 to 85 μm and the effect of porosity value of cell membrane from 0.1 to 0.9. The simulation results present the possibility to apply single layer using two flow resistances calculated from CFD simulation in microscale and total porosity of multiple biological cell layer, giving the error less than 5% for all convergence simulation.

1. Introduction

The cell is a principle unit of life. Some cell is large enough to be seen by the human eye. But most cells are far smaller than 1mm; some are even as small as 1 μm . Cell inclusions and macromolecules are smaller than a micrometer and are measured in terms of nanometers. The size of plant cell and animal cell are in range 10 to 100 μm [1]. Cell wall and plasma membrane are around the cell in plant cell but there is only plasma membrane in animal cell. There are many pore inner the cell wall and plasma cell such as, Berestovsky et al. have been reported the pore diameter in cell wall of Characorallina and Bacillus megaterium are not exceed 2.1 and 2.2 nm, respectively[2]. This stated the difficulty to measure the membrane properties for microscopic simulation.

Computational Fluid Dynamics or CFD is the analysis of systems involving fluid flow, heat transfer and associated phenomena such as chemical reactions by means of computer-based simulation. Widely application was found in drying agricultural industry [3-4]. Simulation transport phenomena inner the agricultural products might need powerful computer and long time to simulate especially an irregular undefined size and shape such as the fruit which consisting of many part with different type cell, cell structure and physical properties.

CFD software is used to study the pattern of fluid flow through porous by applying the porous media model. By assuming the stacked foods have porous, Alvarez and Flick use commercial CFD software

(FLUENT) to predict velocity profile of air during cooling[5]. Williams also use FLUENT software to investigate the flow behavior throughout the pulse tube cryocoolers[6]. For porous media model on ANSYS (FLUENT) is using the diffusion of momentum due to the viscous effect term, and the source term that contains the airflow resistance parameter described by Ergun as [4]

$$\frac{\Delta P}{L} = \frac{150\mu(1-\varepsilon)^2}{d_p^2\varepsilon^3}u + \frac{1.75\rho_a(1-\varepsilon)}{d_p\varepsilon^3}u^2 \quad (1)$$

Where L is a grain depth (m), ΔP is static pressure drop (Pa), μ is the dynamic viscosity of air (Pa.s), ρ_a is the density of air (kg m^{-3}), u is velocity (m/s), d_p is average particle diameter (m) and ε is porosity (decimal). In Eq. (1), the first term on the right side represents viscous energy loss and the second term represents kinetic energy loss. The left side term represents the pressure loss per unit depth.

Comparing the momentum equation in ANSYS user guide [7], the viscous and kinetic energy terms of Ergun's equation are expressed as a viscous loss coefficient ($1/\alpha$) and the inertial loss coefficient (C_2):

(2)

$$C_2 = \frac{3.5(1-\varepsilon)}{d_p\varepsilon^3} \quad (3)$$

Porous media in natural resource consisting with multilayer of biological cell therefore the porosity in previous section should be define as the total porosity of cell (ε_t) which are average by area of porosity of cell wall (ε_{cm}) and empty space inner the cell (ε_{ic}), described as:

$$\varepsilon_t = \frac{[(\varepsilon)_{cm}A_{cm}] + [(\varepsilon)_{ic}A_{ic}]}{A_t} \quad (4)$$

Where A_{cm} , A_{ic} and A_t are cell membrane, inner cell and total area respectively (note: these area parameters will replace by volume in 3-dimension case.).

In this work, the effect of cell shapes, cell size and the porosity of cell wall were using for estimated inertial and viscous flow resistances (C_2 and $1/\alpha$). Three interesting for using a simplified geometry which was investigated the optimal base on $\Delta P/L$ in real structure simulation. First scenario, using the flow resistance coefficient which was estimate from $\Delta P/L$ in real structure simulation case and porosity of cell membrane or cell wall (ϵ_{cm}). Second scenario, using the same flow resistance coefficient in first scenario and total porosity (ϵ_t). The last scenario, using the flow resistance coefficient which was directly calculates form Ergun equation and total porosity (ϵ_t). However, the limitation in this work, for using pore size (which was represent in the first paragraph) in realistic to calculate the flow resistance coefficient from Eq.(2) and (3) by varying porosity, you can vary porosity in range over 0.5 because limit value of flow resistance coefficient setting (which are in range -1×10^{20} to 1×10^{20}) on this software. In fact, porosity may be less than 0.5, so the range of porosity is expansion into range 0.1 – 0.9 by using pore size is 50 nm.

2. Materials and Methods

2.1 Geometry

Three types of geometry in simulation were showed in Figure 1. Square shape (1a) and hexagonal shape (1b) were assumed as plant cell and animal cell respectively. The animal cell was assumed as hexagon for ignorance the effect of cell membrane thickness. The length sides were varied as 10, 20, 40 and 80 μm for plant cell and 6.20, 12.40, 24.81 and 49.63 μm for animal cell. The thickness of membrane was fixed at 0.5 μm . The simplified geometry of multiple cell layers into a single layer was showed in Figure 1c. This layer area was fixed at $100 \times 100 \mu\text{m}^2$. Varying the length of plant cell layer from 106 μm to 64 μm and 211 μm , then named the case with L64 and L211, respectively.



Figure 1. Three types of geometry; (a) Square shape (plant cells), (b) Hexagonal shape (animal cells) and (c) Single layer.

2.2 Boundary condition

The CFD simulation was performed in 2-dimension due to the structure inside the layer along the z-direction are the same. The air flow was as velocity inlet with temperature at 353 K. The outlet type was pressure outlet. The cell wall was setting as wood material with pore, inner cell was space area. Reynolds number was calculated for confirm than Laminar and energy model is valid.

2.3 Simulation procedure

2.3.1 Comparing $\Delta P/L$ from the CFD simulation with Ergun equation

Pressure drop per length ($\Delta P/L$) was determined by simulating air flow through the porous layer with mesopore (d_p is 50 nm) [8]. Air velocity (u) was varied as 0.01, 0.05, 0.1, 0.5, 1, 2, 4, 6, 8 and 10 m/s. Fitting curve of $\Delta P/L$ and u as a second order polynomial without intercept value then the viscous and inertial resistance ($1/\alpha$ and C_2) were determined by using Eq.(2) and (3), respectively [7] for each cell wall porosity (ϵ_{cm}). Theoretical $\Delta P/L$ was calculated by using of Ergun equation when μ is 1.7894×10^{-5} , ρ_a is 1.225 kg/m^3 and d_p is 50 nm.

2.3.2 Determination C_2 and $1/\alpha$ of cell structure

Simulation the air flow through biological structure as presented in Figure 1a and 1b with different cell size. The shape sizes were varied; 10, 20, 40 and 80 μm in plant cell and 6.20, 12.40, 24.81 and 49.63 μm in animal cell which have the same area as plant cell. The porosity was varied from 0.1 to 0.9 and using the resistance coefficients ($1/\alpha$ and C_2) determined by previous simulation. The thickness of layer is varied and name as L64, L106 and L211.

From simulation, C_2 and $1/\alpha$ of multilayer biological cell were estimated by plotting correlation curve between $\Delta P/L$ and velocity. These new coefficients were called $1/\alpha_{sim}$ and $C_{2,sim}$, respectively.

2.3.3 Study the possibility of simulation by using simplified single layer geometry

Three scenarios for CFD simulation were using for testing the possibility of simulation by using simplified single layer geometry:

(1) Simulation by using the coefficient of multilayer cell ($1/\alpha_{sim}$, $C_{2,sim}$) and cell wall porosity (ϵ_{cm}) represent the most resistance of flow

(2) Simulation by using the coefficient of multilayer cell ($1/\alpha_{sim}$, $C_{2,sim}$) and total porosity (ϵ_t) represent the real porosity in cell

(3) Simulation by using the theoretical coefficient ($1/\alpha_{cal}$, $C_{2,cal}$) calculated from Ergun equation and total porosity (ϵ_t)

The $\Delta P/L$ results will compare with results simulation from multilayer biological cell in 2.3.2 for validation and conclude the possibility of using single layer model

3. Results and Discussion

3.1 Flow resistances (C_2 and $1/\alpha$) of cell wall

Inertial and viscous flow resistances (C_2 and $1/\alpha$) of biological cell membrane are necessary parameters for momentum transfer simulation by assuming this layer is a single thin layer with low porosity. Although these two parameters can be estimated from the porosity and spherical diameter of particle, the porosity of the membrane is difficult to measure. According to Ergun equation, developed for fluid flowing through the packed bed, assumes the membrane consisting meso-porous

with 50 nm diameters with various porous present in Table 1. The percentage error of pressure drop per unit length ($\Delta P/L$) value calculating from Ergun equation compared with them from CFD simulation using the inertial and viscous flow resistances also presented in Table 1. The errors are in range 0.0299-0.0320 %, this indicates that the results from CFD software and Ergun equation are in the same range due to ANSYS(Fluent) software using simply Ergun with C_2 and $1/\alpha$ for calculation the pressure drop in fluid flow. This also supports the simulation fluid dynamic in biological microstructure for estimate the flow resistances instead of measuring in the next section.

Table 1: Flow resistance coefficient for cell membrane.

Porosity ϵ_{cm}	$1/\alpha$	C_2	Average error %
0.1	4.8600×10^{19}	6.3000×10^{10}	0.0313 ± 0.0064
0.2	4.8000×10^{18}	7.0000×10^9	0.0320 ± 0.0047
0.4	3.3750×10^{17}	6.5625×10^8	0.0319 ± 0.0048
0.6	4.4444×10^{16}	1.2963×10^8	0.0317 ± 0.0044
0.8	4.6875×10^{15}	2.7344×10^7	0.0312 ± 0.0049
0.9	8.2305×10^{14}	9.6022×10^6	0.0299 ± 0.0047

3.2 Effect of biological cell structure

Inertial and viscous flow resistances (C_2 and $1/\alpha$) is determined from previous section (Table 1) are using for simulation the effect of two biological cell structures on momentum transfer in this section. Square and hexagonal structure represented the plant and animal cell respectively. From CFD simulation results,

these two flow resistance values are the coefficients of no intercept second order polynomial function of $\Delta P/L$ in term of superficial velocity. The C_2 and $1/\alpha$ (subscript with 'sim') of square and hexagonal cell structure with different cell wall porosity presents in Table 2 and 3. The viscous resistance value increases when decreasing the cell size due to increasing of the number of cell or the membrane volume for the same equal volume. This effect was also found by Williem [6] and Leong [9]. The resident time of airflow inside the cell is increasing when the size of cell is smaller. In CFD simulation on ANSYS all pore volume is open as stated by user guide [7], increasing the porosity in membrane (ϵ_{cm}) assist the flow and shown in decreasing of viscous resistance coefficients. Simulation fluid flowing through the porous media in laminar region, the pressure drop is less depending on the inertial term (with C_2) in Eq.(1) which might be set as zero following Tang et al work [10], therefore uncertain of C_2 value was found which presented in Table 2 and 3. and the $1/\alpha$ is much higher than C_2 . Considering in animal cells case (hexagonal), the C_2 and $1/\alpha$ is similar tenor with plant cell. The velocity magnitude contour of plant cell and animal cell presents in Figure 2a and 2c, air velocity value is high at core of cell and it is zero nearby wall area which effected by the viscous flow [11]. After the air flowed through the multilayer of cell, they homogenized quickly and the mixing distance is smaller than cell diameter.

Table 2: Inertial and viscous flow resistances of different structure and thickness by varying the porosity of the cell membrane from 0.1 to 0.4

Case	$\epsilon_{cm} = 0.1$			$\epsilon_{cm} = 0.2$			$\epsilon_{cm} = 0.4$		
	ϵ_t	$C_{2,sim}$	$1/\alpha_{sim}$	ϵ_t	$C_{2,sim}$	$1/\alpha_{sim}$	ϵ_t	$C_{2,sim}$	$1/\alpha_{sim}$
Plant 10	0.83	4.04×10^{10}	4.17×10^{18}	0.85	4.72×10^8	4.96×10^{17}	0.89	1.95×10^7	3.48×10^{16}
Plant 20	0.91	6.02×10^{10}	1.91×10^{18}	0.92	3.03×10^{10}	2.64×10^{17}	0.94	1.56×10^8	1.93×10^{16}
Plant 40	0.95	5.48×10^{11}	1.05×10^{18}	0.95	2.27×10^{10}	1.46×10^{17}	0.97	4.41×10^7	1.02×10^{16}
Plant 80	0.97	3.13×10^{11}	7.58×10^{17}	0.97	8.61×10^8	8.83×10^{16}	0.98	3.29×10^7	6.23×10^{15}
Animal 6	0.85	1.70×10^{12}	3.36×10^{18}	0.87	2.66×10^9	4.46×10^{17}	0.90	1.87×10^8	3.13×10^{16}
Animal 12	0.92	1.31×10^{12}	1.71×10^{18}	0.93	1.26×10^{10}	2.38×10^{17}	0.95	-5.57×10^7	1.70×10^{16}
Animal 25	0.96	-7.21×10^{11}	7.36×10^{17}	0.96	1.30×10^9	1.20×10^{17}	0.97	1.05×10^8	9.19×10^{15}
Animal 50	0.97	3.35×10^9	8.30×10^{17}	0.97	2.64×10^8	8.20×10^{16}	0.98	1.76×10^7	5.77×10^{15}
L64	0.90	3.11×10^{11}	2.49×10^{18}	0.92	1.44×10^9	3.03×10^{17}	0.94	-3.07×10^7	2.13×10^{16}
L106	0.92	6.02×10^{10}	1.91×10^{18}	0.93	3.03×10^{10}	2.64×10^{17}	0.94	1.56×10^8	1.93×10^{16}
L211	0.91	1.54×10^{11}	1.49×10^{18}	0.92	7.52×10^{10}	2.08×10^{17}	0.94	1.27×10^8	1.78×10^{16}

Table 3: Inertial and viscous flow resistances of different structure and thickness by varying the porosity of the cell membrane from 0.6 to 0.9

Case	$\epsilon_{cm} = 0.6$			$\epsilon_{cm} = 0.8$			$\epsilon_{cm} = 0.9$		
	ϵ_t	$C_{2,sim}$	$1/\alpha_{sim}$	ϵ_t	$C_{2,sim}$	$1/\alpha_{sim}$	ϵ_t	$C_{2,sim}$	$1/\alpha_{sim}$
Plant 10	0.93	1.26×10^7	4.59×10^{15}	0.96	2.98×10^6	4.85×10^{14}	0.98	1.09×10^6	8.55×10^{13}
Plant 20	0.96	1.89×10^7	2.55×10^{15}	0.98	1.75×10^6	2.69×10^{14}	0.99	5.76×10^5	4.74×10^{13}
Plant 40	0.98	-2.54×10^6	1.44×10^{15}	0.99	8.54×10^5	1.52×10^{14}	0.99	3.26×10^5	2.68×10^{13}
Plant 80	0.98	2.62×10^6	8.21×10^{14}	0.99	5.61×10^5	8.67×10^{13}	1.00	1.81×10^5	1.53×10^{13}
Animal 6	0.93	1.47×10^7	4.13×10^{15}	0.97	2.74×10^6	4.36×10^{14}	0.98	8.92×10^5	7.69×10^{13}
Animal 12	0.96	4.45×10^6	2.24×10^{15}	0.98	1.47×10^6	2.36×10^{14}	0.99	4.50×10^5	4.16×10^{13}
Animal 25	0.98	9.20×10^6	1.21×10^{15}	0.99	8.12×10^5	1.28×10^{14}	1.00	2.53×10^5	2.26×10^{13}
Animal 50	0.99	2.26×10^6	7.60×10^{14}	0.99	5.08×10^5	8.02×10^{13}	1.00	1.53×10^5	1.41×10^{13}
L64	0.96	-1.08×10^7	2.81×10^{15}	0.98	2.24×10^6	2.97×10^{14}	0.99	6.48×10^5	5.22×10^{13}
L106	0.96	1.89×10^7	2.55×10^{15}	0.98	1.75×10^6	2.69×10^{14}	0.99	5.76×10^5	4.74×10^{13}
L211	0.96	-1.92×10^7	2.35×10^{15}	0.98	1.72×10^6	2.48×10^{14}	0.99	5.51×10^5	4.37×10^{13}

3.3 Single layer simulation (3 scenarios)

In this section, simplified geometry as a single layer of porous media was using for investigating the possibility to replace the complicated of biological

structure. The simulation was done in three scenarios and validation with the $\Delta P/L$ which simulated from the real structure in previous section. The percentage of error values were showed in Table 4.

Error of $\Delta P/L$ value using $C_{2, \text{sim}}$ and $1/\alpha_{\text{sim}}$ of $\epsilon_{\text{cm}} = 0.40$, from previous section, give small error than the value using $C_{2, \text{cal}}$ and $1/\alpha_{\text{cal}}$ which calculated from Ergun equation (Eq.4). This caused by the calculating C_2 and $1/\alpha$ value from total porosity ignored the viscous and inertial resistance of cell membrane. Either simulation with ϵ_{cm} or ϵ_t , the error is the same which is necessary to remind for user to beware in using ANSYS (Fluent) for simulation. This because of momentum transfer calculation in this program, the porosity effect was included in C_2 and $1/\alpha$. Although momentum transfer ignore the porosity, this value is important for other part of simulation which using this for estimate the thermal conductivity and reaction surface in heat and mass transfer[7].

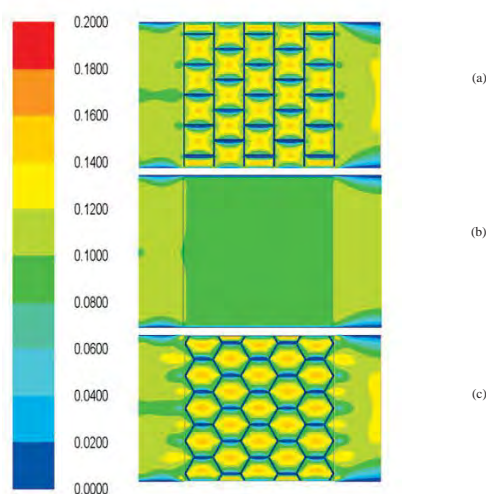


Figure 2. Air velocity (m/s) contour by using 0.1 m/s inlet velocity; (a) Plant 20, (b) single layer and (c) Animal 12

Table 4: Simulation results for 3 scenarios of $\epsilon_{\text{cm}} = 0.40$

Case	Porosity	C_2	$1/\alpha$	% Error
Plant 20	$\epsilon_{\text{cm}} = 0.40$	1.56×10^8	1.93×10^{16}	0.1670
	$\epsilon_t = 0.94$	1.56×10^8	1.93×10^{16}	0.1670
	$\epsilon_t = 0.94$	$1.26 \times 10^{4*}$	$1.63 \times 10^9*$	99.99
Plant 80	$\epsilon_{\text{cm}} = 0.40$	3.29×10^7	6.23×10^{15}	0.0626
	$\epsilon_t = 0.98$	3.29×10^7	6.23×10^{15}	0.0626
	$\epsilon_t = 0.98$	$1.07 \times 10^{3*}$	$1.31 \times 10^7*$	99.99
Animal 12	$\epsilon_{\text{cm}} = 0.40$	-5.57×10^7	1.70×10^{16}	0.0636
	$\epsilon_t = 0.95$	-5.57×10^7	1.70×10^{16}	0.0636
	$\epsilon_t = 0.95$	$2.65 \times 10^{3*}$	$7.25 \times 10^7*$	99.99
Animal 50	$\epsilon_{\text{cm}} = 0.40$	1.76×10^7	5.77×10^{15}	0.1071
	$\epsilon_t = 0.98$	1.76×10^7	5.77×10^{15}	0.1071
	$\epsilon_t = 0.98$	$8.39 \times 10^{2*}$	$8.13 \times 10^6*$	99.99

* calculate from Ergun equation

Table 5: Single layer simulation with different ϵ_{cm}

Case	Average Error (%)					
	$\epsilon_{\text{cm}} = 0.1$	0.2	0.4	0.6	0.8	0.9
Plant 10	2.64 ^a	0.02	0.02	0.02	0.03	0.01
Plant 20	27.16 ^a	3.63 ^a	0.17	0.05	0.03	0.01
Plant 40	14.47 ^a	3.45 ^a	0.10	0.09	0.01	0.03
Plant 80	2.64 ^a	0.16	0.06	0.03	0.01	0.09
Animal 6	12.07 ^a	0.08	0.07	0.03	0.03	0.01
Animal 12	23.33 ^a	0.95	0.06	0.02	0.03	0.02
Animal 25	33.09 ^a	2.59 ^a	0.28	0.08	0.01	0.05
Animal 50	17.13 ^b	0.49 ^b	0.11	0.05	0.01	0.10
L64	8.53 ^a	0.15	0.09	0.10	0.06	0.01
L106	27.16 ^a	3.63 ^a	0.17	0.05	0.03	0.01
L211	56.25 ^a	8.77 ^a	0.02	0.08	0.05	0.02

(a) not convergence for all velocity (b) not convergence (some velocity)

Applying total porosity, $C_{2, \text{sim}}$ and $1/\alpha_{\text{sim}}$ for all ϵ_{cm} , the average error for all velocity presents in Table 5. The error is still high for low ϵ_{cm} (a) even increasing the iteration step up to 5000. Moreover, non-convergence results also found at higher thickness when using membrane porosity lower than 0.2. This might need 30000-40000 iteration which consuming 6-8 times of calculating time. The results of the error and velocity contour indicate that the simplified geometry idea can be used on ANSYS (Fluent) software.

4. Conclusions

CFD simulation of air flow through the multilayer biological cell can replace by using a single layer geometry with total porosity of cell. Inertial and viscous flow resistances (C_2 and $1/\alpha$) of biological cell membrane are necessary parameters for momentum transfer simulation. These coefficients determining from fitting curve of the pressure drop per length ($\Delta P/L$) and fluid velocity by using second order polynomial without intercept value which data results from CFD simulation of microstructure. The error for this algorithm is less than 5 % if the simulation residue is converted. Simulations at very low cell wall porosity need more iteration to get convergent results. For ANSYS user, the porosity is not using for momentum transfer calculation in this case. Integrating the effect of porosity, user has to recalculate the flow resistances coefficient from Ergun equation.

Acknowledgements

This work was done in the laboratory cooperation of National Center of Excellence for Petroleum, Petrochemicals, and Advanced Materials, Chulalongkorn University, Thailand and software funding by department of material science and engineering, Silpakorn University, Thailand.

References

- [1] S.S. Mader, *Biology* 8th ed., McGraw Hill Higher Education, (2003).
- [2] G.N. Berestovsky, V.I. Ternovsky, A.A. Kataev, *Journal of Experimental Botany* **52** (2001) 1173-1177.
- [3] F. Roman, V. Strahl-Schafer, O. Hensel, *Biosystems engineering* **112** (2012) 359-369.
- [4] J. Lawrence, D.E. Maier, *Biosystems Engineering* **110** (2011) 321-329.
- [5] W.M. Clearman, *Measurement and Correlation of Directional Permeability and Forchheimer's Inertial Coefficient of Micro Porous Structures Used in Pulse-Tube Cryocoolers (Thesis)*, Mechanical Engineering, Georgia Institute of Technology (2007).
- [6] G. Alvarez, D. Flick, *Journal of Food Engineering* **80** (2007) 391-401.
- [7] ANSYS, *ANSYS FLUNT 14.0 user's guide*, ANSYS Inc., Canonsburg, PA, (2011).
- [8] K.S.W. Sing, D.H. Everett, R.A.W. Haul, L. Moscou, R.A. Pierotti, J. Rouqurol, T. Siemienieska, *Pure and Applied Chemistry* **57** (1985) 603-619.
- [9] K.C. Leong, L.W. Jin, *International Journal of Heat and Mass Transfer* **49** (2006) 671-681.

- [10] N. Tang, H. Zhang, W. Wang, *Desalination***274** (2011) 120-129.
- [11] W.L. McCabe, J.C. Smith, P. Harriott, *Unit Operations of Chemical Engineering*, **6 ed.**, McGraw-Hill Higher Education, New York, (2001).

PREPARATION OF ZINC OXIDE IMMOBILIZED ON DIATOMITE DERIVED FROM INDUSTRIAL WASTE

Pimtip Tanniratt^{1,2}, Thanakorn Wasanapiarnpong^{1, 2}, Charusporn Mongkolkachit³,
Pornapa Sujaridworakun^{1,2*}

¹Research Unit of Advanced Ceramics, Department of Materials Science, Faculty of Science, Chulalongkorn University, Bangkok, 10330, Thailand

²Center of Excellence on Petrochemical and Materials Technology, Chulalongkorn University, Bangkok, 10330, Thailand

³National Metal and Materials Technology Center, Klong luang, Pathumthani, 12120 Thailand

* Author for correspondence; E-Mail: Pornapa.s@chula.ac.th, Tel. +66 22185541

Abstract: Zinc oxide is an efficient semiconductor which is suitable as an alternative photocatalyst for degradation of several harmful organic pollutants. To enhance the photodegradation performance of pure ZnO, diatomite was used as a porous substrate to immobilize ZnO powder by impregnation and calcination method. In this work, zinc dust waste derived from hot-dip galvanizing process was used as starting materials for synthesis of ZnO and diatomite waste from brewery industries was used as a porous support. The acid treated diatomite was impregnated into zinc nitrate solution, precipitated with NaOH and then calcined at 500°C for 2h. The resultant products were characterized for phase, morphology and surface area by X-ray powder diffraction (XRD), scanning electron microscopy (SEM), and Brunauer Emmett Teller (BET) techniques, respectively. The photocatalytic activity was evaluated by photo degradation of methylene blue solution under UV light. It was obtained that the sample prepared by loading with 20wt% of ZnO on diatomite exhibited the highest photocatalytic performance.

1. Introduction

Recently, advanced oxidation processes (AOPs) of semiconductor photocatalysts have been attracted much attention because their applications can degrade organic pollutions by using only light, catalyst and air [1-3]. Due to its powerful oxidative function, the organic compounds can be degraded into non toxic products. Up to date, it is well known that TiO₂ semiconductor photocatalyst is the most common used photocatalyst for removing the pollutant organic molecules. However, ZnO is also reported as an alternative photocatalyst for degradation of organic molecule in which its activity is comparable to that of TiO₂ [4-5]. On the other hand, the drawbacks of using zinc oxide nano particles in powder form are their agglomeration and difficulty of powder separation after reaction. Several reports have been attempted to solve these problems by immobilizing ZnO particles on porous supports such as activated carbon, zeolite and silica with various preparation processes [6-8]. This was resulted in the enhancement of photocatalytic activity of the composites due to the synergistic functions of absorption and photocatalytic decomposition. Among various supports used, diatomite is one of the excellent absorbing materials

since it has high permeability, high porosity, high absorbability and chemical inertness. Moreover, it is a cheap absorbent [9]. Thus, the aim of this work is to prepare ZnO immobilize on diatomite by simple impregnation method. But, the starting materials used in this work were industrial wastes with has not been reported before. The zinc dust waste derived from hot-dip galvanizing process was used as starting materials for synthesis of ZnO and diatomite waste from brewery industries was used as a porous support. In order to achieve the highest photocatalytic activity for degradation of methylene blue solution, the optimal preparation conditions and loading amount of ZnO on diatomite were investigated.

2. Materials and Methods

At first, diatomite waste derived from brewery industries (Boon Rawd Brewery Co., Ltd) was dried at 105 °C for 24 h. Dried powders were passed through 230-mesh sieve and they were chemically treated with sulfuric acid (H₂SO₄, 98.08% RCI Labscan Limited) [10]. After that it was washed with distilled water and dried. To prepared the zinc salt precursor solution, zinc-dust waste derived from hot dip galvanizing plant (Pacific Pipe Public Co., Ltd) was dissolved in concentrated nitric acid (HNO₃, 95 % AR grade, Merck) until clear solution was obtained. The solution was filtered to remove the impurity [11]. The amount of zinc oxide to be immobilized on diatomite was varied (10%, 20%, 30% 40% and 50% by weight) in solution precursors. Then 3 g of treated diatomite powders were mixed in zinc salt precursor solution which was adjusted to pH value of 10 by adding sodium hydroxide (NaOH, AR grade, Ajax Finechem). The mixture was stirred for 1 h, washed, filtered, dried and calcined at 500 °C for 2 h. The obtained product was characterized for phase, morphology and surface area by XRD (D8-Advance, Bruker AXS Model D8 Discover), SEM (JSM-6400 80 LV, JEOL), BET (Coulter SA 3100), respectively.

The photocatalytic activity of the synthesized powder was evaluated through the degradation of a methylene blue solution under UV- light irradiation (NEC, FL10BLB, intensity of 2 mW/cm²). 0.02 g of sample was suspended in 40 ml of 0.02 mM methylene

blue solution. The suspension was first stirred in the dark for 1.5 h to ensure adsorption/desorption equilibrium prior to irradiation. The irradiated suspensions were then centrifuged to separate the powder from the solution, and the clear solution was analyzed by measuring the absorbance at a wavelength of 664 nm using a UV–VIS spectrophotometer (Perkin Elmer instrument, Lambda 35) to evaluate the photocatalytic degradation of methylene .

Table 1. Properties of ZnO, diatomite and ZnO-diatomite powders.

Samples	S_{BET}^a (m^2/g)	k^b ($\times 10^{-3} \text{min}^{-1}$)	D^c (%)
ZnO	7.64	4.16	56.66
Diatomite	42.49	0.035	6.17
10wt% ZnO-diatomite	37.22	8.8	80.76
20wt% ZnO-diatomite	32.76	10.85	86.12
30wt% ZnO-diatomite	26.02	7.1	74.57
40wt% ZnO-diatomite	25.95	5.81	69.57

^a BET surface area.

^b Reaction rate constant.

^c Photodegradation efficiency at 210 min

3. Results and Discussion

Fig.1 shows XRD patterns of ZnO-diatomite powders prepared from various loading amount of ZnO, diatomite and pure ZnO synthesized from zinc - dust waste. It was shown that treated diatomite waste consisted of cristobalite phase and alpha quartz (JCPDS No.21-1272). The synthesized ZnO shows high crystallinity of ZnO with zincite structure (JCPDS No.36-1451). All of ZnO loaded diatomite samples composed of cristobalite and alpha quartz from diatomite and ZnO zincite. The increase loading amount of ZnO immobilized on diatomite led to relatively increasing in intensity of ZnO peaks in the samples.

Surface morphology of diatomite and ZnO-diatomite were shown in Fig. 2a and 2b. The image of diatomite in Fig. 2a presents clean pore and smooth surface. ZnO-diatomite in Fig. 2b shows rougher surface with deposition of ZnO particles and dissolved silica at high pH [12]

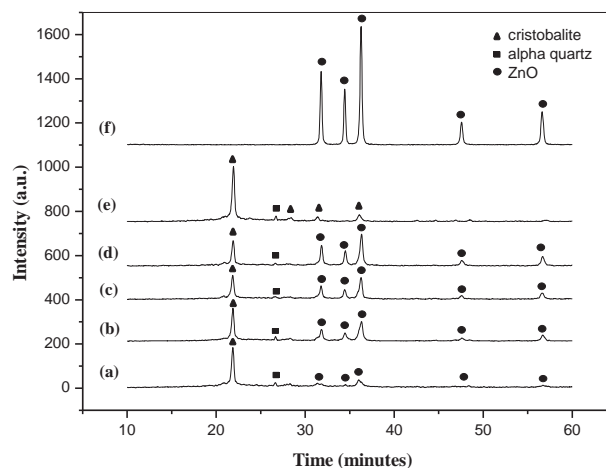


Figure 1. XRD patterns of (a) 10 wt% ZnO-diatomite, (b) 20 wt% ZnO -diatomite, (c) 30 wt% ZnO-diatomite, (d) 40 wt% ZnO -diatomite, (e) diatomite and (f) ZnO

Moreover, the energy dispersive X-ray analysis shown in Fig. 2c confirmed that the ZnO was immobilized on diatomite. EDX Spectra of Zn, O and Si were qualitatively indicated. It was found that amount of ZnO detected from EDX is correlate to that of the initial ZnO loading.

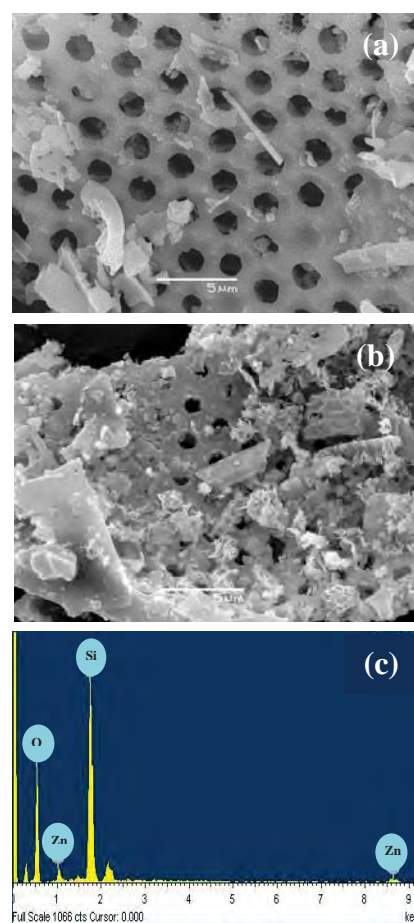


Figure 2. SEM images of (a) diatomite, (b) 10 wt% ZnO-diatomite and (c) EDX of 10 wt% ZnO-diatomite.

Fig.3 shows the photocatalytic activity of samples with various loading amount of ZnO. The photocatalytic efficiency is generally expressed by a rate constant value (k). The k values of ZnO and diatomite were 4.16×10^{-3} and $0.035 \times 10^{-3} \text{ min}^{-1}$. It indicates that diatomite almost has no photocatalytic activity. While, all ZnO-diatomite samples performed higher photocatalytic efficiency than that of pure ZnO as shown in Table 1. The results demonstrate that the highest photocatalytic activity was obtained from sample loaded with 20 wt% of ZnO. However, the increasing amount of ZnO has resulted in the decreasing of the activity. The relative photodegradation efficiencies in the photocatalysts show the following sequences: 20wt% ZnO-diatomite, 10wt% ZnO-diatomite, 30wt% ZnO-diatomite and 40wt% ZnO-diatomite. The enhancement in photocatalytic activity of ZnO-diatomite could be attributed to the more adsorption of methylene blue molecules onto surface of ZnO which probably increases reaction rate on its surface. But increasing amount of ZnO causes aggregation of ZnO particles deposited on diatomite surface. Therefore, surface area of diatomite powder was decreased from 42.43 to 25.95 m^2/g with 40 wt% loading of ZnO as listed in Table 1. It can be suggested that loading amount of ZnO and surface area were important factors affecting on photocatalytic activity of the ZnO-diatomite composite.

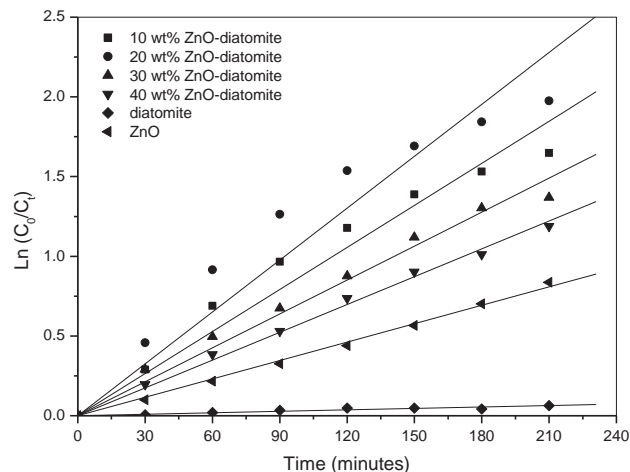


Figure 3. Kinetic of photocatalytic activity of diatomite, ZnO and ZnO-diatomite with various amount of ZnO.

4. Conclusions

ZnO photocatalyst immobilized on diatomite was successfully prepared using industrial wastes by simple impregnation process. It was demonstrated that the ZnO-diatomite showed higher photocatalytic activity for degradation of methylene blue solution than that of pure ZnO and diatomite. The sample loaded with 20wt% of ZnO on diatomite exhibited the highest photodegradation efficiency. The surface area of ZnO-diatomite affected by loading amount and

dispersion of ZnO on diatomite played an important role on its photocatalytic performance.

Acknowledgements

The author would like to acknowledge Center of Excellence on Petrochemical and Materials Technology, Chulalongkorn University, National Metal and Materials Technology Center (MT-B-55-CER-07-289-I), Integrated Innovation Academic Center: IIAC Chulalongkorn University Centenary Academic Development Project (Project Code: CU56-AM04), and the Higher Education Research Promotion and National Research University Project of Thailand, Office of the Higher Education Commission (Project Code: CU56-AM04) for financial support.

References

- [1] R.M. Mohaned, E.S Baeissa, I.A. Mkhallid and M.A. Al-Rayyani, *Appl. Nanosci.* (2012) 1-7.
- [2] M. Claudio, L. Mirco, V.Davide and M.Valter, *Environ. Sci. Technol.* **39** (2005) 8936-8942.
- [3] Z. Meng, and Z. Juan, *Glob. Environ. Pol. Jpn.* **12** 1-9.
- [4] N.Daneshvar, D. Salari and A.R. Khataee, *J. Photochem. Photobiol. A.* **162** (2004) 317-322.
- [5] C. Lizama, J. Freer, J. Baeza and H. Mansilla, *Catal. Today.* **76** (2002) 235-246.
- [6] K. Byrappa, A.K. Subramani, S. Ananda, K.M. Rai, M.H. Sunitha, B.Basavalingu and K. Soga, *J. Mater. Sci.* **41** (2006) 1355-1362.
- [7] G.D. Mihai, V. Meynen, M. Mertens, N.Bilba, P. Cool and E.F.Vansant, *J. Mater. Sci.* **45(21)** (2010) 5786-5794.
- [8] J. Zhai, X. Tao, Y. Pu, X. Fei Zeng and J.E. Chen, *Appl. Surf. Sci.* **257** (2010) 393-397.
- [9] J.X. Lin, S.L. Zhan, M.H. Fang and X.Q. Qian, *J. Porous Mater.* **14** (2007) 449-455.
- [10] Q. Zhu, Y. Zhang, F. Zhou, F. Lv, Z. Ye, F. Fan and P.K. Chu, *Chem. Eng. J.* **171** (2011) 61-68.
- [11] K. Natrchalayuth, *synthesis of zinc oxide photocatalyst nanoparticles from Zn-dust waste by hydrothermal method*, Master's Thesis, Chulalongkorn University (2011).
- [12] K.-J.Hsien, W.-T.Tsai and T.-Y.Su, *J. Sol-Gel Sci. Technol.* **51** (2009) 63-69.

STUDY OF ELECTROSPUN NYLON-6/CHITOSAN COMPOSITE NANOFIBERS

Worakan Sukwanichwichai, Mayuree Hansupanusorn*

Department of Physics, Faculty of Science, King Mongkut's University of Technology Thonburi, Bangkok 10140, Thailand

* Author for correspondence; E-Mail: mayuree.kit@kmutt.ac.th, Tel. +66 24708876, Fax. +66 4278785

Abstract: Nanofibers of nylon-6/chitosan composite with weight ratio of chitosan to nylon-6 between 5 – 25 % were fabricated using electrospinning process. Nylon-6/chitosan solutions were prepared by dissolving chitosan powder (5 – 25 % weight ratio compared to nylon-6) into nylon-6 solution (20 % wt.) in formic acid. Nanofibers were electrospun at a potential of 20 kV and a distance of 20 cm from the target. Morphologies of the obtained nanofibers were investigated by scanning electron microscope. Pure nanofibers were obtained at low chitosan content (5 – 15 % weight ratio) while bead formation was found at higher chitosan content (20 - 25 % weight ratio). It was found that size of nanofibers was decreased at higher chitosan content. Water dynamic contact angle measurements revealed that increased chitosan ratio enhanced the surface hydrophilicity of the composite nanofibers.

1. Introduction

Electrospinning technique has attracted increasing attention because it is a simple and low-cost method for producing continuous ultrafine polymer fibers with diameters ranging from tens of nanometers to a few micrometers. Fiber formation by electrospinning of polymer solutions has been extensively studied in terms of applied voltage, tip to collector distance, feeding rate of polymer solutions and polymer solution properties [1-2]. These fibers with high specific surface areas and porous structure lead themselves to a wide range of applications including filtration [3-4], biological substrate [5-6], optical [7-8] and chemical sensors [9] as well as electrical conductors [10-11].

Chitosan, a (1-4)-linked 2-amino-2-deoxy-D-glucopyranose (in figure 1), is derived from chitin, one was found in sea shell such as shrimp, crab and cuttlebone. Chitosan is biopolymer, has amino and hydroxyl functional groups along the polymer chains. It is well known for its nontoxic, biocompatible and biodegradable properties. In addition, it has several unique properties: it is antimicrobial and inhibits the growth of a wide variety of fungi, yeasts and bacteria, which can be beneficial for use the field of biomedicine [12-14]. It can also adsorb toxic metal ions, which can be beneficial for use in air cleaning and water purification applications [15-16]. These properties arise as a result of protonation of amino groups on the chitosan backbone. So far, preparations of chitosan based nanofibers fabricated by electrospinning have been reported. However, pure chitosan nanofibers were produced very difficult because the high viscosity of chitosan, which limits its spin ability and bead [17]. Recent research has focused

on electrospinning blends of chitosan and other compatible polymers such as poly(vinyl alcohol) (PVA), poly(ethylene oxide) (PEO), poly(ethylene terephthalate (PET), polycaprolactone (PCL), poly(lactic acid) (PLA), nylon-6 and others. These composite nanofibers are more advantageous over the electrospun nanofibers of pure chitosan, because the mechanical, biocompatible, antibacterial and other properties of the nanofibers were enhanced by the addition of these polymers [17].

Although the fabrication of composite nanofibrous membranes based on a series of nylon-6/chitosan complex with different weight ratio of nylon-6 to chitosan using a mixed solvent system have been studied previously [18]. The morphology and diameter of nanofibers were affected by the combination of the polymer blending, ranging from 0.1 to 0.9 μm and non-uniform. In this present work we studied of electrospun nanofiber with nylon-6/chitosan solutions were prepared by dissolving chitosan powder (5 – 25 % weight ratio compared to nylon-6) into nylon-6 solution (20 % wt) in formic acid solvent. The purpose of this investigation was to prepare nylon-6/chitosan blend solution that contained maximum levels of chitosan content in the blend and expect to obtain the electrospun nylon-6/chitosan composite nanofibers having more uniform structure and decreasing diameter.

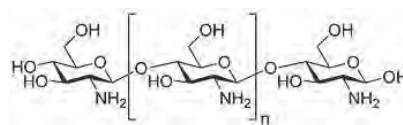


Figure 1. The molecular structure of chitosan [17]

2. Materials and Methods

2.1 Materials

Nylon-6 (AR grade) was obtained from Asia Fiber Public Co. Ltd. Chitosan (medium molecular weight with over 90 - 98 % deacetylation) was purchased from Aldrich Chemistry. Formic acid (analytical reagent grade 98 %) from Fisher Scientific was used to dissolve the blends of nylon-6 and chitosan.

2.2 Solution preparation

Nylon-6 powder was dissolved in formic acid at concentration of 20 wt % (g/ml) and stirred for 3 h at room temperature. Chitosan powder amount of 1 g to 5 g was gradually added into previously nylon-6

solution and stirring until the blend polymer solution to get homogenous. This preparation obtained the blend solutions in weight ratio of chitosan to nylon-6 between 5 – 25 wt% for electrospinning process.

2.3 Electrospinning procedure

Electrospinning procedure was performed at room temperature. The polymer mixed solution was placed in a 3 ml syringe with a metal needle of 0.9 mm in diameter which was connected to the positive electrode. A power supply was used to provide a high voltage, 20 kV to the syringe needle tip (positive electrode) and metal collector (negative electrode). The electrospun fibers were collected on an aluminium foil. The distance between metal needle and collector was 20 cm with solution flow rate of 0.15 ml/min. The collection time was about 2 h per each sample.

2.4 Characterization

The morphology and diameter of the electrospun nanofibers were observed by field emission scanning electron microscope (FE-SEM; Hitachi, S-4700). The diameters of fibers were analyzed using image pro plus visualization software. The surface hydrophilicity of composite nanofibers mats was studied by measuring the water contact angle.

3. Results and Discussion

3.1 Characterization of nylon-6 nanofibers

Initially an attempt was made to blend chitosan onto pure nylon-6 solution in formic acid to forming a blend polymer for electrospinning process. The nylon-6 electrospun nanofibers at various concentrations were initially investigated. Figure 2 shows SEM micrographs of pure nylon-6 electrospun nanofiber using the applied voltage of 20 kV at the syringe to collector distance of 20 cm. All of the obtained nylon-6 nanofiber at 15 – 25 wt% concentrations showed cylindrical shape, with the size of 88 ± 13 nm, 86 ± 11 nm and 33 ± 14 nm, respectively. The average fiber size and size distributions of the nanofiber are shown in figure 3. It can be seen that the 15 – 20 wt% concentrations, very large amount of nanofibers web were obtained while the 25 wt% concentration, electrospun nanofibers were rather not came out due to too-low applied voltage and very more concentration also gives rise to higher solution viscosity. Therefore, the higher nylon-6 solution viscosity is a problem of solubility while adding a various chitosan fractions. In addition, the 15 - 20 wt% concentrations of nylon-6 solution were used to generating of the nylon and chitosan blended electrospun nanofibers in this work.

3.2 Characterization of complex nanofibers

SEM micrographs of the electrospun nanofibers mat that was formed using nylon-6/chitosan blend with varying weight ratios of chitosan to nylon-6 between 5 – 25 wt% (ratio of nylon-6:chitosan was 20:1 – 20:5 wt%) are shown in figure 4. Results showed that the morphology and average diameter of the nanofibers change significantly with respect to the various weight

ratios between nylon-6 and chitosan. The fiber diameter decreased with increasing chitosan content. Therefore, it is shown that the morphology of the composite fibers also changed gradually from the uniform cylindrical shape (5 - 15 wt% chitosan content) onto the ribbon/bead mixed cylindrical shapes with increasing concentration (20 wt% chitosan content). At 25 wt% chitosan content, the fibers formation was nonuniform and became to branch shape. When the chitosan content above 25 wt% nanofibers spinning became impossible under the spinning condition was fixed at 20 kV applied voltage and 20 cm distance.

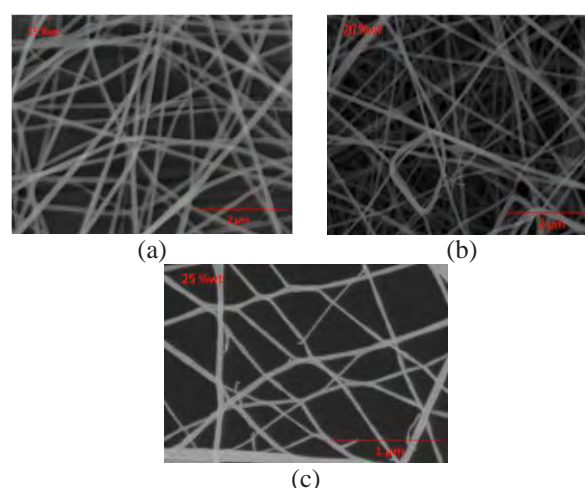


Figure 2. SEM micrographs shown size and morphology of nylon-6 nanofibers with various concentration (a) 15 wt. %, (b) 20 wt%, (c) 25 wt%.

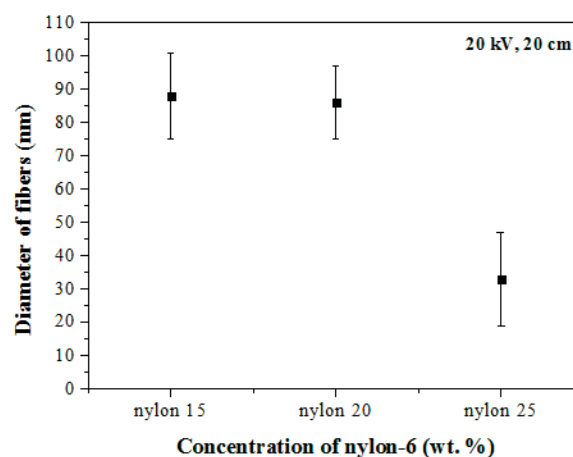


Figure 3. Average diameter and diameter distribution of nylon-6 nanofibers with difference concentration.

The average diameter and diameter distribution of composite nanofibers showed in figure 5. The smaller composite fiber diameter was obtained ranging from 30 to 50 nm. It was reported that the addition of cationic and anionic polyelectrolytes could increase the conductivity of polymer and consequently lead to thinner fibers [19]. Chitosan is a cationic polysaccharide with amino groups which had a higher charge density on the surface of ejected jet formed during electrospinning. As the charges carried by the

jet increases, higher elongation forces are imposed to the jet under the electrical field. It has been known that the overall tension in the fibers depend on the self-repulsion of the excess charges on the jet. Thus, as the charge density increases the diameter of the final fibers becomes smaller [20].

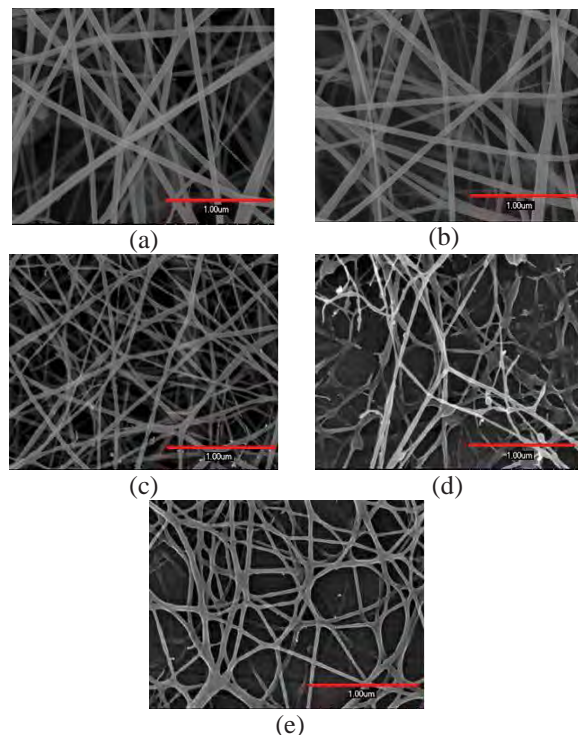


Figure 4. SEM micrographs shown size and morphology of composite nanofibers with various ratio between nylon-6 and chitosan (a) 20:1 wt%, (b) 20:2 wt%, (c) 20:3 wt%, (d) 20:4 wt%, and (e) 20:5 wt%.

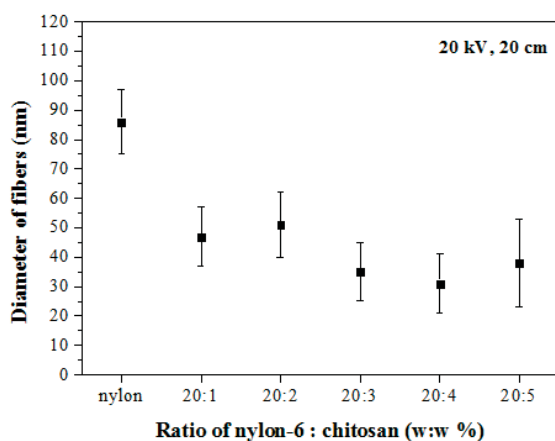


Figure 5. Average diameter and diameter distribution of composite nanofibers with different weight ratio of nylon-6 to chitosan.

The surface hydrophilicity of electrospun nanofibers was studied by the water contact angle measurement. The dynamic water contact angle values at 0th to 350th second after the droplet contacted with

nanofibers was shown in figure 4. It was found that the contact angle decreases gradually from 40° to 30° and this occurs as the content of chitosan in the copolymer increased from 5 to 15 wt% after the 60th second the droplet had contact with the electrospun mats. After about 150 - 350 s, the water droplets were placed on the nanofiber mats, the water contact angle of the pure nylon-6 nanofiber mats was about 70°, while those of the nanofiber mats mixed 5 - 15 wt% chitosan content were closed to 0°. The results also showed that the pure nylon-6 nanofibers had the lowest hydrophilicity (highest water contact angle), while the mat with 15wt% weight ratio of chitosan showed the highest hydrophilicity (smallest water contact angle). This results were confirmed previous speculations that chitosan, has several functional groups that are able to interact with other functionalized polymer. Due to chitosan has four hydroxyl groups, an amine group, and a minor proportion of amide group, which are in general, partially hydrolyzed. All these functional groups enhance the hydrophilic properties of chitosan and so enhance hydrophilicity when complexes with hydrophobic material such as nylon-6. Blend that includes varying amounts of chitosan will affect the degree of hydrophobicity compared to pure nylon-6 system.

Note that the nanofibers mats mixed 5 - 15 wt% chitosan content showed hydrophilicity while those with the nanofibers mats mixed 20 - 25 wt% gave a hydrophilic property. The inset in figure 6 illustrated contact angle with 20 - 25 weight ratio of chitosan to nylon-6 which contact angle were closed to 0° after the 3000th second. Due to the preparation procedure obtained the blend solution in weight ratio of chitosan to nylon-6 between 20 - 25 wt% for electrospinning process, the blend solutions get a more viscous and not completely dissolved. The concentration of blend solution was diluted by adding more amount of formic solvent into the previous blend solution until get homogeneous solution and could be electrospun condition. It is believed that at 20 cm distance between the end tip of the needle and grounded plate, the solvent was completely evaporated when fibers were collected on the ground plate. For this method remained the weight ratio of chitosan to nylon-6 at the same concentration and increasing solubility but higher solution viscosity was obtained. It was found that a little bit of fibers was collected onto the ground plate because of the viscous solvent was clogged at the end of needle tip. The surface properties by the water contact angle measurement of 20 - 25 wt% chitosan content electrospun nanofibers cannot mention. It is believed that most of the fibers were rather not come out during electrospun. The obtained water contact angle values after the droplet contacted showed the surface properties of aluminium foil substrate and did not exhibit nanofibers mats themselves.

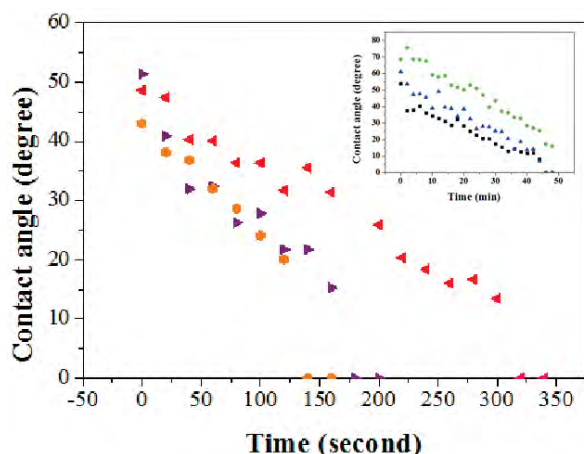


Figure 6. Water contact angle variations of electrospun nylon-6/chitosan blend nanofibers with difference weight ratio of nylon-6 to chitosan: (◄) 20:1 wt%, (◄) 20:2 wt%, (◄) 20:3 wt%, (◄) 20:4 wt%, (◄) 20:5 wt%, (◄) pure nylon-6.

4. Conclusions

The nylon-6/chitosan composite nanofibers with varying weight ratio of nylon-6 to chitosan were successfully by electrospinning process. It was found that increasing chitosan content (5 – 15 wt %), fiber diameter was decreased (50 nm diameter size). The water contact angle was confirmed that increasing chitosan content enhanced the hydrophilic properties of nylon-6/chitosan nanofibers.

Acknowledgements

This work was partially supported by the Graduate Financial Support from the faculty of Science, KMUTT.

References

- [1] A. Formhals, *Process and apparatus for preparing artificial thread*. U.S. Patent 1975504, USA (1934).
- [2] J. Doshi and D.H. Reneker, *Journal of Electrostatics* **35** (1995) 151–160.
- [3] Y. Kyunghwan, K. Kwangsok, W. Xuefen, D. Fang, S.H. Benjamin and C. Benjamin, *Polymer* **47** (2006) 2434–2441.
- [4] Z. Shu, S.S. Woo and K. Jooyoun, *Materials and Design* **30** (2009) 2659–3666.
- [5] D.S. Katti, K.W. Robinson, F.K. Ko and C.T. Laurencin, *J. Biomed Mater Res Part B: Appl Biomater* **70**(2) (2004) 286–296.
- [6] X.H. Zong, S. Li, E. Chen, B Garlick, K.S Kim, D. Fang, et al. *Ann Surg.* **240**(5) (2004) 910–915.
- [7] X. Wang, C. Drew, S.H. Lee, K.J Senecal, J. Kumar, L.A. Samuelson, *Nano Lett.* **2**(11) (2002) 1273–1275.
- [8] J.W. Yoon, S.K. Chae and J.M. Kim, *J.AM.CHEM.SOC.* **129** (2007) 3038–3039.
- [9] H. Liu, J. Kameoka, D.A. Czaplewski and H.G. Craighead, *Nano Lett.* **4**(4) (2004) 671–675.
- [10] H. Dong, V. Nyame, A.G. MacDiarmid and W.E. Jones Jr., *Journal of Polymer Science Part B: Polymer Physics* **42**(21) (2004) 3934–3942.
- [11] M. J. Diaz-de Leon, *Proc. of The National Conference on Undergraduate Research: Kentucky University* (2001).
- [12] N. Angelova, N. Manolova, I. Rashkov, V. Maximova, S. Bogdanava and A. Domard, *Journal of Bioactive and Compatible Polymer* **10** (1995) 285–298.
- [13] R. Jaykumar, M. Prabakaran, S.V. Nair and H. Tamura, *Biotechnology Advances* **28** (2010) 142–150.
- [14] Y. Ma, T. Zhou and C. Zhao, *Carbohydrate research.* **343** (2008) 230–237.
- [15] S. Haider and S.Y. Park, *Membrane Science* **328** (2009) 90–96.
- [16] S. Peng, et al., *Carbohydrate Polymer* **84** (2011) 239–246.
- [17] K. Sun and Z.H. Li, *eXPRESS Polymer Letters* **5**(4) (2011) 342–361.
- [18] Z. Haito, L. Shubai, J.B.W. Christopher, N. Xin, N. Huali and Z. Limin, *Electrochimica Acta* **54** (2009) 5739–5745.
- [19] W.K. Son, J.H. Youk, T.S. Lee, W.H. Park, *Polymer* **45** (2004) 2959.
- [20] X.H. Zong, K.S Kim, D.F. Fang, S.F. Ran, B.S. Hsiao, B. Chu., *Polymer* **43** (2002) 4403.

GUAVA LEAF ESSENTIAL OIL/POLYURETHANE-UREA MICROCAPSULES AND THEIR ANTIMICROBIAL PROPERTY ONTO COTTON FABRICS

Lipda Angkitanont¹ Sireerat Charuchinda^{1,2*}

¹ Center of Excellence in Textiles, Department of Materials Science, Faculty of Science, Chulalongkorn University, 254 Phayathai Road, Wangmai, Patumwan, Bangkok 10330, Thailand

² Center of Excellence on Petrochemical and Materials Technology, Chulalongkorn University, Bangkok 10330, Thailand

* Author for correspondence; E-Mail: sireerat.c@chula.ac.th, Tel. +66 2218 5062, Fax. +66 2218 5561

Abstract: Polyurethane-urea (PUU) microcapsules containing guava leaf essential oil (EO) were prepared by an interfacial polymerization. The effects of various parameters such as stirring rate and amounts of guava leaf EO added on the particle size, morphology, EO loading capacity and oil release of their microcapsules were investigated. It was found that the microcapsules with particle size less than 10 μm and highest EO loading capacity could be prepared by using stirring rate at 14000 rpm and 20 ml of guava leaf EO. The selected microcapsules were then treated onto cotton fabrics by using pad-dry technique. The treated cotton fabrics were further conducted antibacterial test according to the AATCC test method 100 and durability of antibacterial activity on washing, light, perspiration and light with perspiration. Most of treated cotton fabrics with guava leaf EO/PUU microcapsules exhibited antibacterial activity against *Staphylococcus aureus* except the one which exposed to perspiration.

1. Introduction

Currently, functional textiles are the new dimension of “textiles” which are not only for the aesthetic apparels but also for the protective textiles especially in terms of health and hygiene. Many researches onto antimicrobial agent based on natural resources are in increasing demand. Herbs are naturally prosperous and abundant in Thailand. Guava leaves which their essential oil (EO) enriched in cineol, tannins, triterpenes and flavanoids are acclaimed to exhibit antimicrobial activity. Furthermore, its EO is much cheaper than any other EO. Therefore, guava leaves are viewed as one of the new potential alternative natural, non-toxic sources as a potential replacement for chemical antimicrobial agents. Encapsulation of guava leaf EO in polyurethane-urea (PUU) microcapsule was adopted to reduce irritation, and control its release [1-4].

In this study, PUU microcapsules containing guava leaf EO were prepared by an interfacial polymerization. The effects of various parameters including stirring rate and amount of guava leaf EO on morphology, particle size distribution, loading capacity and thermal stability of the microcapsules were investigated. Thereafter, guava leaf EO and its microcapsules were finished onto cotton fabric by padding technique to evaluate the antimicrobial

activity against *Staphylococcus aureus* (*S. aureus*). In addition, durability of antimicrobial performance of the treated cotton fabric to washing, light, light with perspiration and perspiration were also studied.

2. Materials and Methods

2.1 Materials

Guava leaf essential oil (Guava leaf EO) was purchased from Thai-China Flavours & Fragrances Industry Co.,Ltd. Hexamethylene diisocyanate (HMDI) (Fluka), dibutyltin dilaurate (DBTDL) (Sigma-Aldrich), and polyvinyl alcohol (PVA) (Ajex Finechem) were used as the isocyanate, the catalyst, and the protective colloid, respectively. Polyethylene glycol 400 (PEG 400) (Fluka), ethylenediamine (EDA) (Panreac) were also used as the polyol, and the amine, respectively. Ethanol 99.8% (AR grade, Merck) was purchased from T.C. Sathaporn Group Ltd., Part. A bleached plain-woven 100% cotton fabric (183 g/m²) was purchased from Boonchuay Industrial Co., Ltd. Acrylic binder (AC801) (A.C. Burapha Co.,Ltd.) and formaldehyde-free crosslinking component (RUCO coat FX-8011) (V.P.C. Group) were used to fix microcapsules onto cotton fabrics. Polysorbate 80 (TWEEN 80) (Sigma-Aldrich) was also used as a dispersing agent. All reagents were used as received without any further purification.

2.2 Guava leaf EO/PUU microcapsules preparation

Polyurethane-urea (PUU) microcapsules were prepared by interfacial polymerization [4]. The organic phase (OP) was formed by mixing guava leaf EO of 20 mL and 7.5 mL of HMDI. OP was then added into the first aqueous phase (AP1: 125 mL of water and 2.1 g of PVA) to form an emulsion. Emulsification was performed at various stirring rate and time with homogenizer (T18 basic/Ultra Turrax IKA/Malaysia). Subsequently, a second phase (AP2: 25 mL of water, 11.5 mL of PEG 400 and 0.25 mL of DBTDL) was prepared and added to the previous emulsion (OP + AP1) to form the polyurethane wall. Interfacial polymerization was performed at 80 °C with a stirring rate of 150 rpm for 1 h. The third aqueous phase of EDA (AP3: 10 mL of water and 3 mL of EDA) was subsequently added and proceeded for 1 h to form urea.

The obtained microcapsules were firstly washed with an ethanol solution (30% (v/v)) and taken to centrifuge at 5000 rpm for 10 min. Thereafter, the separated microcapsules were then washed two times with distilled water, centrifuged and stored in an aqueous solution of TWEEN 80 to prevent the formation of agglomerates.

2.3 Impregnation of guava leaf EO/PUU microcapsules onto cotton fabric

One hundred millilitre bath of a dispersion of 100 g/L of selected microcapsules, 50 g/L of acrylic binder and 10 mL/L of formaldehyde-free crosslinking agent were applied onto 100% cotton fabric by pad-dry technique at 100% wet pick up. The treated fabric was then dried at room temperature.

2.4 Characterization of guava leaf EO/PUU microcapsules and treated cotton fabric

2.4.1 Morphology of microcapsules and surface characteristic of treated cotton fabrics

2.4.1.1 Optical microscopy (OM)

The morphology and dispersion of microcapsules were recorded with an optical microscope (BH2-UMA) with a magnification of 100.

2.4.1.2 Scanning electron microscopy (SEM)

The morphology of microcapsules and surface characteristic of treated cotton fabrics were investigated by Scanning electron microscope (JEOL-5410LV) under accelerated of 15kV at magnification of 200 and 4000. Samples were sputtered gold surface treatment before testing.

2.4.2 Mean particle size and particle size distribution analysis

The mean particle size (volume mean diameter, $D[4,3]$) and particle size distribution (PSD) of microcapsules were determined by MALVERN Mastersizer Hydro 2000SM. A test using a few drops of microcapsules was performed after a sonification for 30 sec.

2.4.3 Thermal stability of microcapsules

Thermogravimetric analysis (TGA) was performed with the TGA (Mettler Toledo Model TGA/SDTA 851e) under a nitrogen flow from 50 to 500°C at a heating rate of 10°C/min.

2.4.4 Oil loading capacity

Loading capacity of guava leaf EO in PUU microcapsules were investigated by isothermal TGA (Mettler Toledo Model TGA/SDTA 851e) at 120°C for 1 h.

$$\text{Oil loading capacity (\%)} = \left[\frac{W_m - W_0}{W_m} \right] \times 100 \dots (1)$$

where W_m and W_0 denote the weight of microcapsules measured before and after heating guava leaf EO at 120°C for 1 h, respectively.

2.4.5 Oil release content

The release of guava leaf EO from the microcapsules was estimated by measuring the time course of the weight $W_{m(t)}$ of the microcapsules using

isothermal TGA (Mettler Toledo Model TGA/SDTA 851e) at 37°C and 120°C.

$$\text{Oil release content (\%)} = \left[\frac{W_m - W_{t(37^\circ\text{C or } 120^\circ\text{C})}}{W_m - W_{0(37^\circ\text{C or } 120^\circ\text{C})}} \right] \times 100 \dots (2)$$

where W_m , W_0 denote the weight of microcapsules measured before and after exposure at 37°C or heating guava leaf EO at 120°C for 1 h, respectively. W_t denotes the weight of the microcapsules at time t .

2.4.5 Antimicrobial activity determination

The antibacterial activity against *Staphylococcus aureus* (*S. aureus*) (gram-positive bacteria) of treated fabrics was determined quantitatively using agar diffusion method (AATCC 100-1999). The treated and untreated cotton fabrics were UV-sterilized for 20 minutes and incubated for 48 hours. *S. aureus* was chosen for antibacterial test because it is capable of causing various infections of the skin. *S. aureus* infections are common in people with frequent skin injury. Staphylococcal skin infections are seen most commonly in certain occupational groups such as healthcare workers.

2.4.6 Durability of antimicrobial activity

The durability of antimicrobial activity of the cotton fabrics to 10, 15 and 20 washing cycles (ISO105-C10), light exposure (AATCC 16E-2004), perspiration exposure (AATCC 15-2002), and light with perspiration exposure (AATCC 125-2004) were determined.

3. Results and Discussion

3.1 Characterization of microcapsules

3.1.1 Morphology and dispersion of microcapsules

The OM images in Fig.1 (a-d) show that we can prepare the spherical morphology of microcapsules which well-disperse in the medium. In addition, we found that when the stirring rate increases, the particle size of microcapsules decreases.

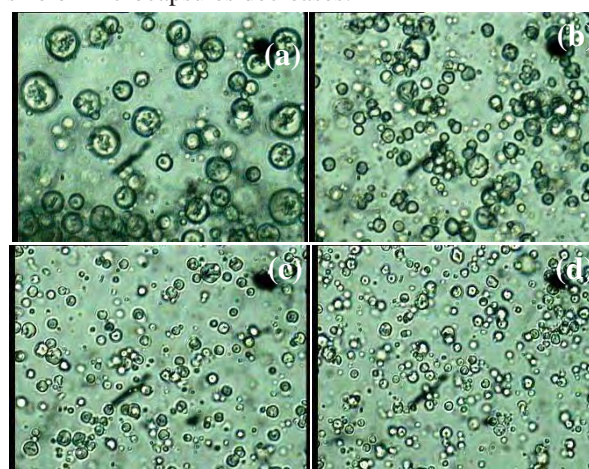


Figure 1. OM images of guava leaf EO/PUU microcapsules prepared with various stirring rate (a) 12000 (b) 14000 (c) 16000 and (d) 18000 rpm.

3.1.2 Mean particle size and particle size distribution

Figure 2 shows the PSD of the microcapsules and the mean particle size ($D[4,3]$) was also presented in

Table 2. The PSD curve of microcapsules shows only one peak with narrow distribution curves evidenced by the span value which were less than 2. This may be

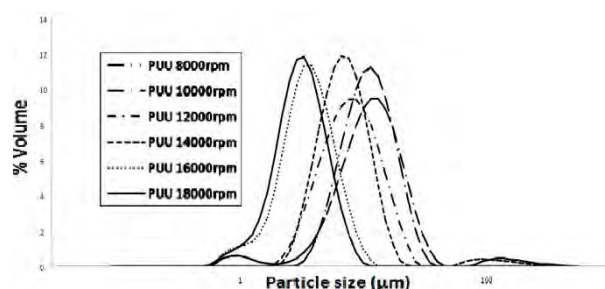


Figure 2. Particle size distribution of guava leaf EO/PUU microcapsules prepared with various stirring rate.

due to the fact that the microcapsules dispersed adequately without any formation of re-agglomeration throughout the entire measurement duration [5]. Furthermore, mean particle size and span of the microcapsules is decreased with the increase of stirring rate as shown in Table 1. It is seen that the mean size of prepared microcapsules with stirring rate from 14000 to 18000 rpm was less than 10 μm and the size distribution was narrow (span value < 1.4).

Table 1 Mean particle size and span of microcapsules prepared with various stirring rate

Stirring rate (rpm)	D[4,3] Mean particle size (μm)	Span
8000	16.3	1.61
10000	11.2	1.26
12000	11.2	1.58
14000	7.0	1.18
16000	3.7	1.33
18000	3.2	1.25

3.1.3 Oil loading capacity

The loading capacity of microcapsules prepared with stirring rate ranging from 12000 to 18000 rpm shown in Table 2 was quite similar approximately 55%.

Table 2 % Loading capacity of microcapsules prepared with various stirring rate.

Stirring rate (rpm)	Loading capacity (%)
12000	55.41
14000	56.06
16000	52.41
18000	56.51

3.1.4 Thermal stability of microcapsules

The dynamic TGA thermogram shown in Fig. 3 indicated that the thermal degradation of the guava leaf EO alone exhibited weight loss due to absolutely evaporation at 200°C. Whereas, the thermal degradation of the PUU microcapsules alone exhibited in two consecutive steps, and the weight loss at the

temperature between 200 and 400°C may be attributed to the decomposition of PUU network [6]. Guava leaf EO/PUU microcapsules exhibited three consecutive

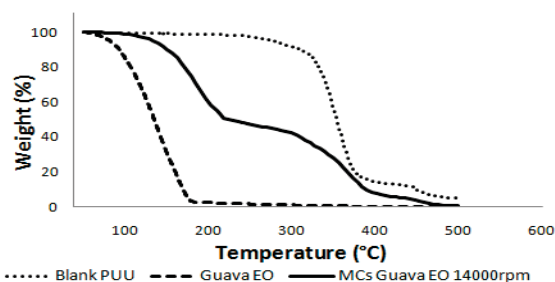


Figure 3. TGA diagram of PUU microcapsules, Guava leaf EO and Guava leaf EO/PUU microcapsules prepared with stirring rate at 14000 rpm.

steps of degradation between 150 and 400°C indicating that guava leaf EO/PUU microcapsules have a better thermal stability than guava leaf EO alone.

Thus, PUU shell could protect guava EO from rapidly releasing under heat exposure.

3.1.5 Oil release rate

The isothermal TGA curves at 37°C and 120°C shown in Fig. 4 indicated that, at first 10 min of 120°C, guava leaf EO extremely released up to 70% when compared to the guava EO/PUU microcapsules which release oil only 30%. Guava EO absolutely evaporated within 30 min, whereas, guava leaf EO/PUU microcapsules absolutely release their oil within 60 min. This revealed that PUU shell could protect guava EO from rapidly releasing under heat exposure.

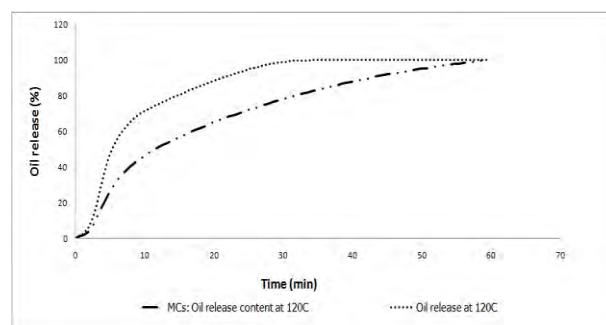


Figure 4. Oil release content of guava leaf EO and guava leaf EO/PUU microcapsules (20 mL of guava leaf EO, 14000 rpm, 5 min)

In this study, the guava leaf EO/PUU microcapsules prepared with 14000 rpm was selected to treat onto cotton fabrics due to their particle size of 7 μm and quite narrow size distribution. Moreover, these microcapsules still contained high loading capacity (56%) when compared to those other microcapsules.

3.2 Characterization of treated cotton fabric

3.2.1 Scanning electron microscopy

SEM images in Fig. 5 (a-b) show that the microcapsules still remain on cotton fabric surface after washing 1 and 10 cycles by impregnation method. However, the amount of microcapsules decreased when the cotton fabrics were conducted to 10 washing cycles.

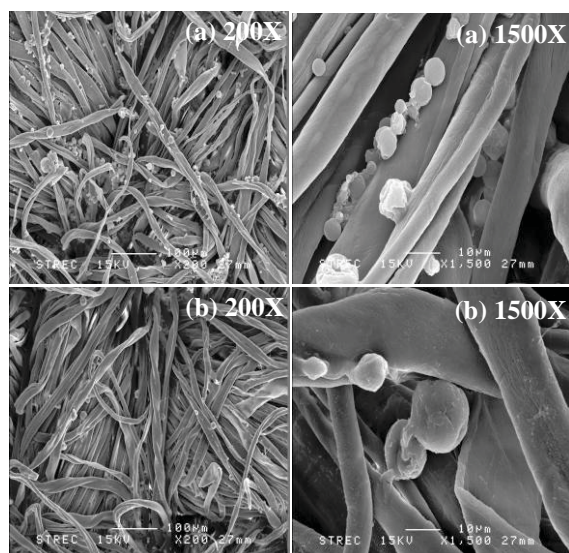


Figure 5. SEM images of cotton fabric treated with guava leaf EO/PUU microcapsules after washing (a) 1 cycle (b) 10 cycles at a magnification of 200x and 1500x

3.2.2 Antibacterial activity and their durability

Table 4 shows the antibacterial activity against *S. aureus* of untreated and treated cotton fabrics with guava leaf EO/PUU microcapsules and their durability to washing, light exposure and perspiration exposure.

Table 4 Antibacterial activity against *S. aureus* of cotton fabrics treated with guava leaf EO/PUU microcapsules and their durability.

Samples	Reduction of bacteria (%)
Untreated	0
0 washing cycle	99.99
10 washing cycles	99.99
15 washing cycles	99.99
20 washing cycles	0
Light exposure	99.80
Light & perspiration exposure	99.90
Perspiration exposure	0

It is seen that the treated cotton fabric with guava leaf EO/PUU microcapsules exhibited excellent antibacterial activity against *S. aureus*. This may be due to the cineol, tannins, triterpenes, and flavonoids composed in guava leaf have the inhibitory effects on the growth of *S. aureus* [1]. Moreover, this antibacterial activity was durable upto 15 washing cycles. Unfortunately, the fabrics exhibited 0%

reduction of bacteria after 20 washing cycles. This is attributed to the fact that the microcapsules was removed from the fabric surface. Thus, the content of guava leaf EO may be not enough to inhibit the growth of *S. aureus*. In addition, the treated fabrics still exhibited excellent antibacterial activity after light exposure and light with perspiration exposure (99.8% reduction of bacteria), whereas, the antibacterial activity was absolutely decreased after perspiration exposure.

4. Conclusions

The PUU microcapsules containing guava leaf EO as a core material were prepared by interfacial polymerization using HMDI, PEG and EDA with various stirring rate (8000-18000 rpm). We can prepare the spherical morphology of microcapsules which well-disperse in the medium. The guava leaf EO/PUU microcapsules prepared with various stirring rate from 14000 to 18000 rpm was less than 10 μm and the size distribution was narrow (span value < 1.4). In addition, the loading capacity of the microcapsules was quite similar approximately 55%. The PUU shell provide a better thermal stability and could protect guava EO from rapidly releasing under heat exposure.

In this study, the guava leaf EO/PUU microcapsules prepared with 14000 rpm was selected to treat onto cotton fabrics by pad-dry technique. It was found that the treated cotton fabric exhibited excellent antibacterial activity against *S. aureus*. Moreover, the treated fabrics show the durability of antibacterial activity to 15 washing cycles, light exposure and light&perspiration exposure. However, the PUU shell could not protect guava leaf EO from perspiration. Thus, the antibacterial activity was absolutely decreased after perspiration exposure.

Acknowledgements

The authors gratefully acknowledge the National Science and Technology Development Agency (NSTDA) for their research grant (Grant No. P-10-10934) and also thank to the 100th Anniversary of Chulalongkorn University Fund for their financial support.

References

- [1] R.M. Pérez, G.S. Mitchell and R.V. Solis, *J. Ethnopharmacol.* **117** (2008) 1-27.
- [2] N. Obinna, C. Nwodo and A. Olayinka, *J. Med. Plant Res.* **2** (2008) 189-192.
- [3] N.R. Sanches, D.A.G. Cortez, M.S. Schiavini, C.V. Nakamura and B.P.D. Filho, *Braz. arch. biol. technol.* **48(3)** (2006) 429-436.
- [4] S.N. Rodrigues, I.M. Martins, I.P. Fernandes, P.B. Gomes, V.G. Mata, M.F. Barreiro and A.E. Rodrigues, *J.Chem. Eng.* **149** (2009) 463-472.
- [5] F.V. Leimann, O.H. Gonçalves, R. A.F. Machado and A. Bolzan, *Mat. Sci. Eng. C.*, **29** (2009) 430-436.
- [6] F. Salaün, G. Bedek, E. Devaux and D. Dupont, *Mater. Lett.* **65** (2011) 381-384.

COMPATIBILITY OF THERMOPLASTIC STARCH/NATURAL RUBBER LATEX BLENDS WITH MALEIC ANHYDRIDE VIA MELTING PROCESS

Nantavat Tangchantra^{1,*}, Jittiporn Kruenate¹, Narachai Chommuang¹
Suchart Supattanapalapol¹, and Kanisorn Jai-eau¹

¹ National Metal and Materials Technology Center, National Science and Technology Development Agency,
114 Thailand Science Park, Phahonyothin Rd. Klong 1, Klong Laung, Pathumthani 12120, Thailand

*E-Mail: Nantavtt@mttc.or.th

Abstract : The compatibility efficiency of thermoplastic starch (TPS)/natural rubber latex (NRL) blends were investigated via mechanical, thermal, and morphological characterization. In order to obtain such effectiveness, the interfacial adhesion between modified NR and TPS and that of the unmodified NR and TPS were compared. The molecular structure of natural rubber latex was modified with maleic anhydride (MA) by using dicumyl peroxide (DCM) as an initiator. The NRL was mixed with DCM and MA via latex solution. After that the mixed latex and cassava starch were gradually kneaded via internal mixer at 120 °C with a rotor speed of 80 rpm. In this work, various of MA contents were employed as a consequence of their compatibility on properties of TPS/NRL blends. Interestingly, scanning electron microscope (SEM) showed that the modified NR phase exhibited good adhesion with TPS matrix. Elastic modulus and tensile strength of TPS /modified-NR blends were profoundly achieved due to the interfacial adhesion. Furthermore, the glass transition temperature of TPS/NR blends increased. Because there was a strong interfacial adhesion between the modified NR and the TPS polymer.

1. Introduction

As a very interesting in bio-degradable polymer from renewable resources, the thermoplastic starch (TPS) has received wide investigation due to its low cost and environmental friendly character. Nonetheless, TPS showed a serious limitation of brittleness and moisture absorption. At present, the main strategies to overcome the brittleness are focused on the use of reinforcement [1] and blend of TPS with other polymers such as PLA [2], polyethylene [3], and poly(butylensuccinate co- adipate) [4]. One of the promising ways to reduce the brittleness of TPS is blending with other softening materials. Cis-1,4-poly isoprene or natural rubber (NR) is an elastic material which can be derived from natural resources. It has optimistic properties such as high elasticity, tensile strength, tear strength, and aging properties. A few studies dealing with the use of rubber in TPS are described as follows: Carvalho [5] reported that TPS/NR blends normally showed less brittle than thermoplastic starch alone and phase separation was also observed in some compositions depended on rubber and plasticizer content. M. Mondragón [6] used natural rubber grafted with the hydrophilic poly dimethylaminoethyl methacrylate to be an efficient compatibilizer to obtain the blends of TPS. This research aimed to study the effect of maleic anhydride as compatibilizer on the properties of TPS/natural

rubber latex (NRL) blends by using dicumyl peroxide as an initiator.

2. Materials and Methods

2.1 Materials

The cassava flour was purchased from Dragon Fish Cassava Flour. The glycerol used as a plasticizer in this study was supplied by Hong Huat Company, Thailand. Natural rubber latex was 60 %DRC with ammonia as a stabilizer. Maleic anhydride (MA) and dicumyl peroxide (DCP) were used as received from sigma-aldrich.

2.2 Thermoplastic starch/Natural rubber blends

Powder of cassava starch was mixed with 1,3 and 5 phr maleic anhydride and 3 phr dicumyl peroxide. Natural rubber latex was stirred for 24 h at room temperature and mixed with plasticizer containing 35 phr glycerol. The dried natural rubber content was kept of 10 phr of starch. These mixtures were directly processed in an internal mixer (Haake Rheomix) equipped with roller rotors and operated at 120 °C 80 rpm. The compounds were fed in a twin screw extruder (LabTech) at temperature of 135 °C and screw speed of 100 rpm and the sample was then prepared for mechanical characterization as sheet-form using compression moulding at 180 °C.

2.3 Morphology Characterization

A field emission scanning electron microscopy (SEM), Hitachi S-3400N, was used to characterize the micro-structure of pure TPS and their blends.

2.4 Thermal Analysis

The glass transition temperature of the samples were measured by differential scanning calorimeter (DSC, Mettler Toledo DSC822e) at a heating rate of 10 °C/min and with a scanning temperature range from 20 °C to 160 °C in N₂ atmosphere.

2.5 Rheological Analysis

Rheological measurements were carried out using a capillary rheometer Rh7 Rosand (Malvern Instruments). After a warm-up period of 4 min at 170 °C, the melt was extruded through a specified capillary at pre-selected speeds of the cross-head. The force corresponding to different plunger speeds was recorded.

2.6 Mechanical Properties

Uniaxial tensile loading tests on the tested samples were performed using an Universal testing machine (Instron 55R450). A constant crosshead speed of 100 mm/min was used. Rectangular samples of 12 mm wide, 0.1 mm thick and a gauge length of 40 mm were employed. Five replicates were used for all blends.

3. Results and Discussion

3.1 Thermal properties

Figure 1 shows DSC thermogram of TPS and their blends indicate that TPS/NR blend without maleic anhydride exhibited glass transition temperature (t_g) of 68.91 °C while addition of maleic anhydride resulted in higher T_g , up to 82.73 °C. The increasing of T_g revealed that the cross-linkage between TPS and NR was occurred by maleic anhydride leading to difficult mobility of amorphous phase.

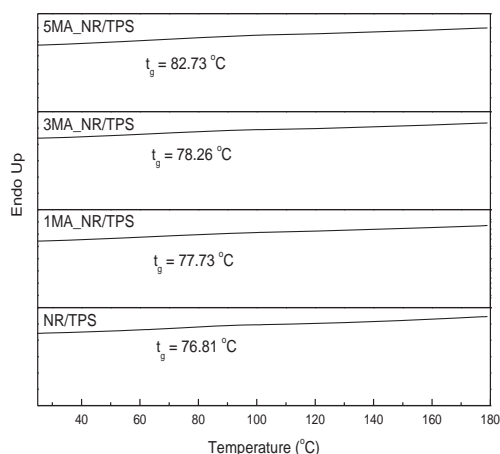


Figure 1. DSC thermogram of TPS blends

3.2 Rheological characterization

Figure 2 shows the relationship between the steady shear viscosity and shear rate for the NR/TPS blends at temperature of 170°C. It could be seen that the viscosity rapidly decreased with increasing shear rate at least during this range of shear rate. All blends exhibited a shear thinning behavior.

The results showed the effect of maleic anhydride (MA) content on the viscosity of the blends at 170°C via capillary rheometer. The steady shear viscosity of the blends increased with increasing the MA content. This behavior could be explained that the molecular chain of TPS become stiffening as the MA molecules strengthen the interfacial interaction between TPS and rubber molecules. In addition, the MA molecules increase in number of cross-linkages between TPS and rubber molecules which could be confirmed via torque characteristic curve (figure 3) and the results could relate to previous study of E. Carone Jr[7].

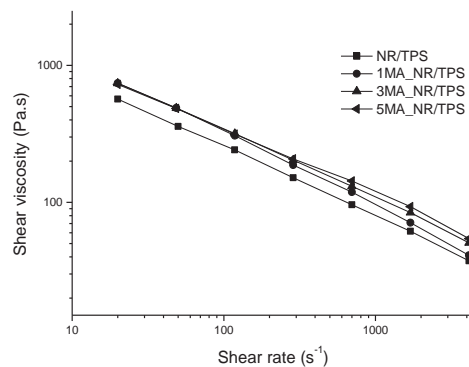


Figure 2. shear viscosity of TPS/NR blends

The torque characteristics of the NR/TPS rubber compounds were determined by using internal mixer. Torque characteristics were plotted for all blends and from the cure characteristics, maximum torque and minimum torque were evaluated. Torque characteristic curves are shown in figure 3. Minimum torque is an indirect measure of the viscosity of the compound. The results revealed that minimum torque of NR/TPS blend without MA content decreased with increasing processing time while NR/TPS blends with MA content had nearly minimum torque of 63-66 Nm at processing time of 3 min. After 3 min processing time, the blends with MA content, maximum torque curve steeply increased because there could be cross-linkage between TPS and rubber molecules by MA and DCP system. Crosslink density easily related to difference between maximum torque and minimum torque. Thus, crosslink density of the blends increased with increasing MA content. Soo-Jin Park, Min-Kang Seo, and Changwoon Nah reported that the minimum and maximum torque, ML and MH, and the difference between them, $\Delta M (=MH-ML)$. The increases in ML and ΔM are related to the increases in viscosity and degree of crosslinking respectively [8].

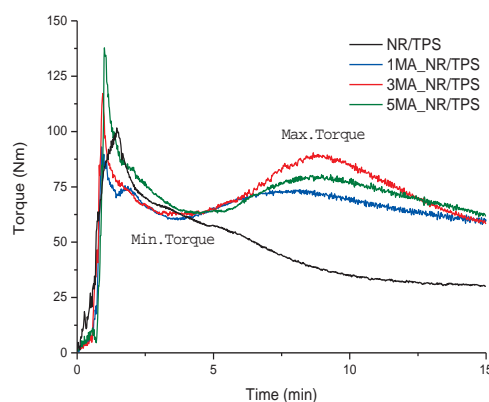


Figure 3. Torque characteristic curve

3.3 Mechanical properties

Tensile strength, Young's modulus and elongation of TPS/NR blends are illustrated in figure 4. The addition of maleic anhydride into the TPS/NR blends

significantly enhanced their mechanical properties. The tensile strength and modulus increased with increasing maleic anhydride contents while elongation decreased. The 1MATPS/NR has tensile strength of 10.27 MPa, modulus of 613.07 MPa, and elongation of 3.53% whereas TPS/NR without MA has only tensile strength and modulus of 8.74 MPa and 588.47 MPa, respectively and elongation of 2.11%. These results indicated that better miscible blends were occurred by using MA as compatibilizer, which in turn unavoidably induced numbers of cross-linkage between NR and TPS.

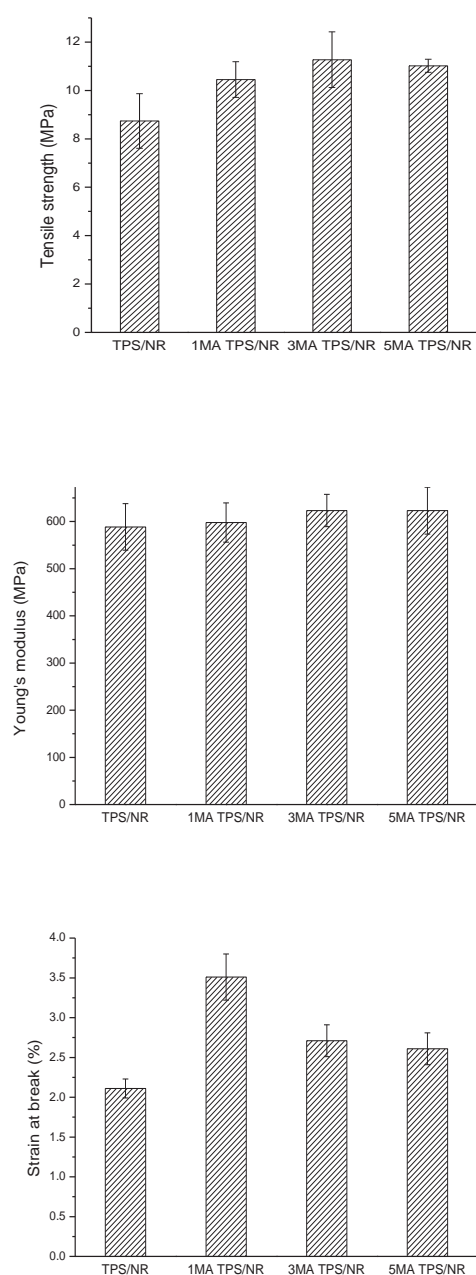


Figure 4. Mechanical properties of TPS/NR blends

3.4 Morphological characterization

Figure 5 shows SEM micrograph of TPS/NR blends, displaying rubber phase in particle form dispersed in TPS matrix. The TPS blend without maleic anhydride as compatibilizer (figure 1a) revealed numbers of rubber clumps and clearly phase separation which indicating lack of interfacial adhesion. This is because NR and TPS are immiscible due to the hydrophobic of NR and hydrophilic of TPS. However, the adhesion between phases for TPS/NR blends containing maleic anhydride resulted in finer dispersion and interfacial adhesion as shown in figure 1 b-d.

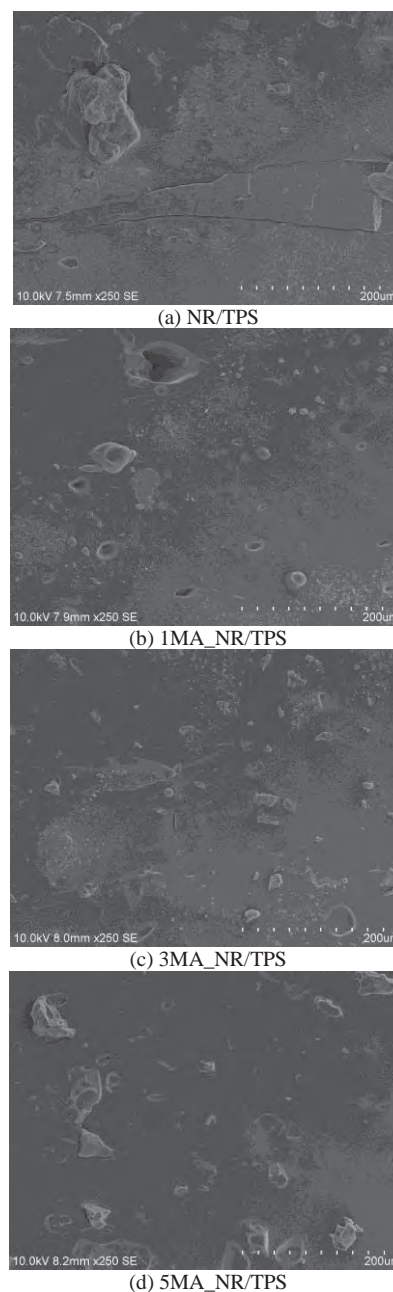


Figure 5. SEM micrograph of TPS/NR blends

4. Conclusion

In this work, the compatibility efficacy of MA contents was studied on physical and mechanical behaviours of NRL/TPS blends which were prepared via internal mixer. The rheological and torque

characteristics revealed that the processability and flowability of the matrix affected both steady shear viscosity and crosslink density. The addition of MA contents in NR/TPS blends with DCP as a radical initiator can induce numbers of cross-linkage and interfacial adhesion between TPS and rubber phases. Accordingly, the results significantly effect on mechanical properties of the NR/TPS composites. It be also found that increasing MA content essentially improved tensile strength, young's moodulus, and strain at break of NR/TPS composites.

Acknowledgment

I would like to thank National Metal and Materials Technology Center and Faculty of science and technology for their financial support and for providing me with an opportunity to carry out this project.

Reference

- [1] A.A.S Curvelo, A.J.F Carvalho, J.A.M Agnelli, *Carbohydrate Polymers* **45** (2002) 183–188.
- [2] E. D. M. Teixeira, A. A.S. Curvelo, A. C. Corrêa, J. M. Marconcinia, G. M. Glenn, and L. H.C. Mattoso, *Industrial Crops and Products* **37** (2012) 61-68.
- [3] W. Shujun, Y. Jiugao, and Y. Jinglin, *Polymer Degradation and Stability* **87** (2005) 395-401
- [4] S. Bocchini, D. Battegazzore, and A. Frache, *Carbohydrate Polymers* **82** (2010) 802-808.
- [5] A.J.F Carvalho, A.E Job, N Alves, A.A.S Curvelo, and A Gandini, *Carbohydrate Polymers* **53** (2003) 95–99.
- [6] M. Mondragón, E.M. Hernández, and J.L. Rivera-Armenta, *Carbohydrate Polymers* **77** (2009) 80–86
- [7] E. C. Jra, U. Kopcaka, and M.C. Gonçalves, *Polymer* **41** (2000) 5929–5935.
- [8] S.P. N. Park, M. Seo, and C. Nah, *Journal of Colloid and Interface Science* **291** (2005) 229–235.

CELL RESPONSE ON ARGON PLASMA TREATED GELATIN FILM

Juthathip Saelee¹, Isarawut Prasertsung², Rattachat Mongkolnavin³,
Chiew San Wong⁴, Siriporn Damrongsakkul^{1*}

¹ Department of Chemical Engineering, Faculty of Engineering, Chulalongkorn University, Bangkok 10330, Thailand

² Department of Industrial Engineering, Faculty of Engineering, Naresuan University, Phitsanulok 65000, Thailand

³ Department of Physics, Faculty of Science, Chulalongkorn University, Bangkok 10330, Thailand

⁴ Plasma Research Laboratory, Department of Physics, Faculty of Science, University of Malaya, Kuala Lumpur 50603, Malaysia

* Author for correspondence ; E-Mail: siriporn.d@chula.ac.th, Tel. +66 22186862

Abstract: Gelatin is derived from collagen by partial hydrolysis under acidic or basic condition. It has been widely used in tissue engineering applications because of the biocompatible and biodegradable properties. Plasma treatment is a technique applied for surface modification without using chemical reagent. In this study, we investigated the effects of argon plasma treatment on the surface properties of gelatin film and the response of L929 mouse fibroblast cells on the treated gelatin film. Argon was chosen as plasma gas because it is an inert gas which has minimal effect on changing surface chemistry. Gelatin film was prepared by solution casting and crosslinked by dehydrothermal (DHT) treatment. The surface of gelatin film was treated by AC 50 Hz plasma. The gas flow rate and treatment time were key parameters to be investigated. The surface topography of crosslinked gelatin film before and after argon plasma treatment was investigated by Atomic force microscope (AFM). The results showed that the surface of untreated gelatin film was fairly smooth and the root mean square (Rms) of surface roughness was around 0.65 ± 0.15 nm. After treated with argon plasma at the flow rate of 1 and 5 sccm for 360 seconds, the surface of gelatin film became rougher and the Rms of surface roughness of the treated film was increased to 24.8 ± 4.23 and 11.5 ± 1.21 nm, respectively. From the results of *in vitro* L929 mouse fibroblast cell culture, argon plasma treatment could not improve cell attachment and proliferation on gelatin films.

1. Introduction

Natural polymer has been studied extensively for medical and tissue engineering applications because of its biodegradability and biocompatibility. Gelatin is a protein obtained by the partial hydrolysis of collagen. Gelatin molecule contains Arg-Gly-Asp (RGD)-like sequence that promotes cell adhesion, migration and proliferation [1]. Gelatin was material for many biomedical applications included wound dressing and drug [1]. To be used in tissue engineering application, surface properties including surface charge, chemical composition, topography and hydrophilicity/hydrophobicity are very important because most biological reactions occur on surfaces or interfaces [2]. Plasma was of interest to be used for modifying gelatin surface because it was free of toxic reagents. From our previous report, Prasertsung, I. *et. al.* [4] modified the surface of DHT-crosslinked gelatin film by using oxygen, nitrogen, and air glow discharge AC 50 Hz plasma systems. They reported that surface topology

of the film was not significantly affected by plasma treatment within the studied plasma condition (oxygen plasma-treated crosslinked gelatin films at 4 watt for 3 to 30 sec). Plasma induced chemical functionalities on gelatin film surface resulting in the enhancement of *in vitro* biocompatibility of the film with bone marrow-derived stem cells. In this work, we focus on the effects of AC 50 Hz plasma system on surface topology of gelatin film. Argon was chosen as plasma gas because it is an inert gas which should have minimal effect on changing surface chemistry.

2. Materials and Methods

2.1 Materials

Type A gelatin was obtained from Nitta Gelatin Inc, Japan. Dulbecco's phosphate buffered saline (PBS), Fetal bovine serum (FBS), penicillin/streptomycin antibiotic, Dulbecco's modified eagle medium (DMEM) were supplied by Hyclone (USA). Trypsin-ethylenediaminetetra acetic acid (EDTA) was obtained from Gibco (Canada).

2.2 Methods

2.2.1 Preparation of crosslinked gelatin films.

Gelatin film was prepared by a solution casting method using 0.05 wt% of type A gelatin solution on glass cover slips (diameter 15 mm). After solvent evaporation in air at room temperature for 24 hr, the film was crosslinked by dehydrothermal process in vacuum oven at 140 °C for 48 hr [3].

2.2.2 Argon plasma treatment

Gelatin film were treated with argon plasma in AC 50 Hz plasma system. The set-up of the plasma apparatus could be found elsewhere [3]. The films were put on electrode in the plasma chamber. The vacuum chamber was pumped down to 0.1 mbar before filled with argon. The argon flow rate was varied 1 and 5 sccm (standard cubic centimeters per minute). The gap between electrodes were varied 2 and 4 cm. The sample were plasma treated for 30 to 360 s.

2.2.3 *In vitro* cell culture

100 μ l L929 mouse fibroblast cell suspension with approximately 2×10^4 cells was seeded on plasma-treated and untreated gelatin films in 24-well tissue culture plates. The cell-grown film samples was kept in DMEM containing 10 vol.% fetal bovine serum and

incubated at 37°C in a 5 vol.% CO₂ incubator for 6, 24 and 48 hr. Cell proliferation was evaluated by DNA assay [5]. The results were reported as the number of cells using a standard curve prepared from L929 mouse fibroblast.

2.3 Characterization of surface property

2.3.1 Surface topography

Surface topography of the plasma-treated and untreated films was examined using atomic force microscopy (AFM, MFP-3D-BIO, Asylum Research, California) in a tapping mode.

2.3.2 Wettability of crosslinked gelatin films

Contact angles of crosslinked gelatin films were measured by sessile drop technique. 20 µl of deionized water was used as a liquid media. After 30 s of dropping, the contact angle of the samples was measured using a contact angle meter (Camplus Micro, Tanteq Inc, USA).

3. Results and Discussion

The surface characteristics of crosslinked gelatin films before and after argon plasma treatment, at the flow rate of 1 and 5 sccm, electrode gap of 2 and 4 cm, as a function of treatment time were observed by AFM. The root mean square (Rms) of gelatin surface before and after argon plasma treatment was shown in Figure 1. The topography of film was shown in Figure 2 (flow rate = 1 sccm, gap = 2 cm). The surface of untreated crosslinked gelatin was relatively smooth (Figure 2(a)) with the root mean square surface roughness (Rms) of 0.65±0.15 nm. After treated with argon, the gelatin surface became obviously rough and irregular (Figure 2(b) – (f)). The Rms was significantly increased with increasing plasma treatment period from 30 to 360 sec. The maximum Rms, obtained from plasma-treated gelatin film at 1 sccm for 360 sec was 24.8±4.23 nm. In general, argon plasma treatment is known to have etching effect on polymer surface and produce nanostructure surface topography [6]. It could be noticed that Rms of plasma-treated crosslinked gelatin films at low argon flow rate and small electrode gap was greatly increased compared to that at high argon flow rate. At low argon flow rate, the number of reactive species in plasma decreases. Consequently, the energy of species increases. Therefore, Rms value of the film was increased.

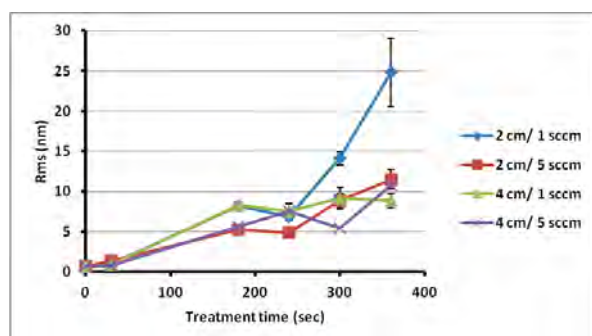


Figure 1. The root mean square (Rms) of surface roughness of argon plasma-treated crosslinked gelatin films as a function of argon flow rate, gap between electrodes and treatment time.

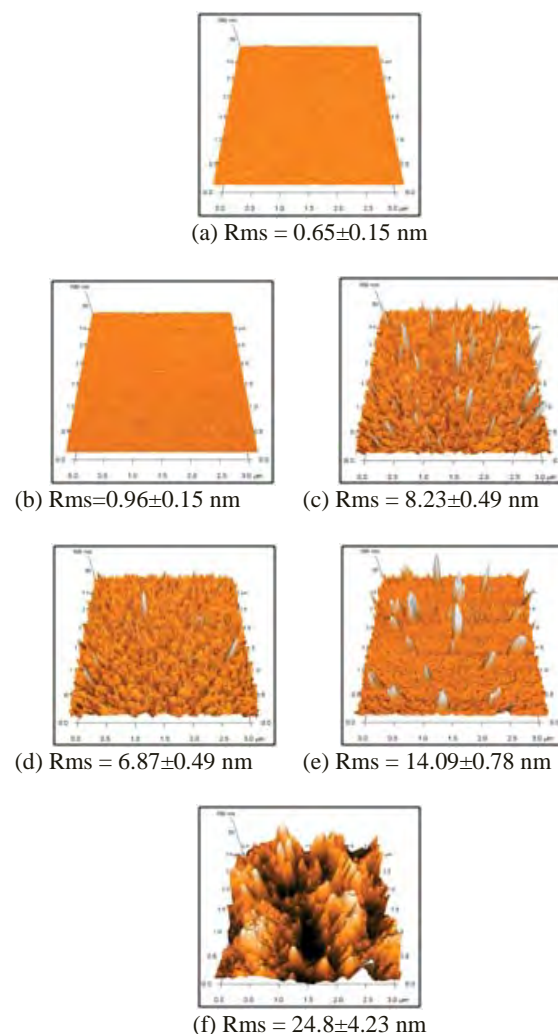


Figure 2. Surface topography of (a) untreated crosslinked gelatin films, and argon plasma-treated crosslinked gelatin films at the flow rate of 1 sccm, 10 watt and 0.15 mbar for the treatment period of (b) 30 sec, (c) 180 sec, (d) 240 sec, (e) 300 sec and (f) 360 sec (data scale 100 nm).

The contact angle values of deionized water on the plasma-treated gelatin films in Figure 3. Untreated crosslinked gelatin film was considered as a hydrophobic surface as noticed from high water contact angle (67°). When treated films with plasma, contact angle was decreased, i.e. the hydrophilicity increased. After argon plasma treatment for 30 sec, the water contact angle of crosslinked gelatin was significantly decreased compared to untreated film. When the crosslinked gelatin films were treated longer than 180 sec at the flow rate of 1, the contact angle was continuous decreasing. The result showed that the water contact angle of plasma-treated crosslinked gelatin films at 5 sccm were the lowest when compared to the ones at 1 sccm. The decreasing of

contact angle of plasma-treated crosslinked gelatin films indicated the improvement of hydrophilicity.

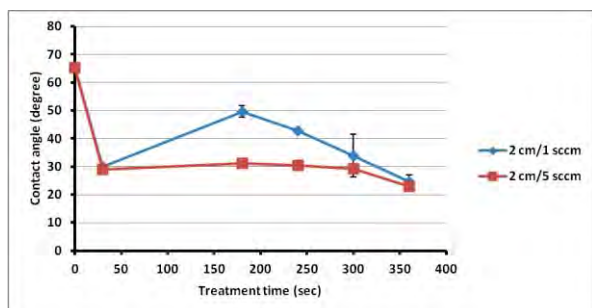


Figure 3. The water contact angle of plasma-treated gelatin films at argon flow rate 1 and 5 sccm, gap between electrodes 2 cm as a function of treatment time.

The results from *in vitro* cell culture on plasma-treated and untreated gelatin films were presented in Figure 4. The attachment and proliferation of L929 mouse fibroblast cultured on the surface of gelatin films and control (tissue culture plate polystyrene, TCPS) for a period of 6h, 24h and 48h showed that argon plasma treatment decreased cell attachment and proliferation on gelatin films.

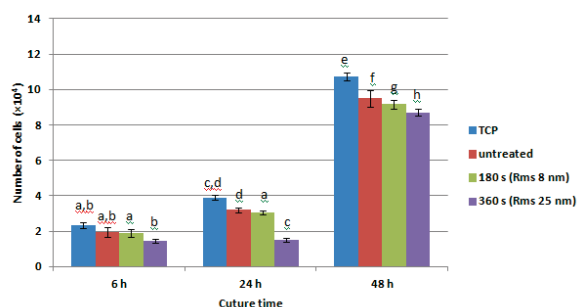


Figure 4. Number of L929 mouse fibroblast attached on tissue culture plate, untreated gelatin film and argon plasma-treated gelatin films at flow rate of 1 sccm, gap of 2 cm, treatment time of 180 and 360 sec. (a, b, c, d, e, f, g and h represented a significant difference at $p < 0.05$)

4. Conclusions

Argon plasma generated from AC 50Hz was used to modify the wettability and surface topology of gelatin film. The plasma could promote hydrophilicity of crosslinked gelatin film. The surface topology of gelatin film was rougher after plasma treatment. The Rms was increased with increasing plasma treatment period to 360 sec and decreasing gas flow rate to 1 sccm. The results from *in vitro* L929 mouse fibroblast cell culture suggested that argon plasma treatment on gelatin films for 180s and 360s at the flow rate 1 sccm lower L929 cell attachment and proliferation on gelatin films.

Acknowledgements

The financial supports from the Research, Development and Engineering (RD&E) fund through The National Nanotechnology Center (NANOTEC), The National Science and Technology Development Agency (NSTDA), Thailand (Project No. P-11-00672) to Chulalongkorn University, Plasma Technology and Nuclear Fusion Research Unit, Chulalongkorn University, and Chulalongkorn University Centenary Academic Development Project are gratefully acknowledged.

References

- [1] B.L. Seal, T.C. Otero, and A. Panitch, *Mater. Sci. Eng., R* **34** (2001) 147-230.
- [2] K. Anselme, *Biomaterials* **21** (2000) 667-681.
- [3] I. Prasertsung, R. Mongkolnavin, S. Damrongsakkul and C.S. Wong, *Surf. Coat. Technol.*, **205** (2010) S133-S138.
- [4] I. Prasertsung, S. Kanokpanont, R. Mongkolnavin, C.S. Wong, J. Panpranot, and S. Damrongsakkul, *J. Biomater. Sci. Polym. Ed.*, **23** (2012) 1485-1504.
- [5] J. Ratanavaraporn, S. Kanokpanont, Y. Tabata and S. Damrongsakkul, *J. Biomater. Sci. Polym. Ed.*, **21** (2010) 979-996.
- [6] Y.C. Wu, T.M. Lee, J.C. Lin, S.Y. Shaw, and C.Y. Yang, *J. Biomater. Sci. Polym. Ed.*, **21** (2011) 563-579.

FABRICATION OF COPPER/SINGLE-WALLED CARBON NANO HORN HYBRID MATERIAL BY MICROWAVE IRRADIATION

Parichat Thipayang¹, Kunio Shinohara², Chantamane Poonjarernsilp³, Tawatchai Charinpanitkul^{1*}

¹Center of Excellence in Particle Technology, Department of Chemical Engineering, Faculty of Engineering, Chulalongkorn University, Bangkok, Thailand

² Division of Materials Science and Engineering, Hokkaido University, Sapporo, Japan

³Department of Chemical Engineering, Faculty of Engineering, Rajamangala University of Technology, Bangkok, Thailand

* Corresponding author's e-mail: ctawat@chula.ac.th Tel/Fax: +66 2 2186480

Abstract: Among various carbonaceous materials, single-walled carbon nanohorns are recognized as a novel material for modern electrodes because of their unique conical structure and high specific surface area. With fast and thorough heating, microwave irradiation could be employed for modifying surface property of SWCNH and hybridizing SWCNHs with metal nanoparticles. In this work SWCNHs with functional groups anchoring on their surface could be experimentally fabricated by microwave irradiation. According to electrostatic attraction of functional groups, the acid treated SWCNHs would be hybridized with copper nanoparticles due to their highly negative charged on their surface as could be confirmed by microscopic analyses using TEM.

1. Introduction

Single-walled carbon nanohorns (SWCNHs), one of the newest carbon nanostructures, were discovered by Iijima in 1999 [1]. An individual CNH is composed of many horn-shaped single-walled tubular graphene with a conical morphology. With their unique characteristics, carbon nanohorns are anticipated to be applicable to some promising applications, such as gas storage media, carrier for drug delivery, catalyst support and electrode material for electrochemical system [2]. Meanwhile, metal-carbon nanohorn hybrid material is an engrossing candidate because of their synergetic characteristics [3, 4]. In order to hybridize metal nanoparticles on carbon nanohorns, it is indispensable to pre-functionalize the surfaces of carbon nanohorns because their surface is strongly hydrophobic [5]. One of simple methods for surface modification is acid treatment. The method creates carboxylic, carbonyl and hydroxyl groups for adsorbing of metal nanoparticles [6]. Usually the method has involved the use of conventional unit operations, such as refluxing and heating. Nevertheless, as a rapid, uniform and more sufficient heating method, microwave irradiation is an attractive alternative [7]. Among various metals, copper has attracted great attention because it has a high thermal and electric conductivity with low-cost and has been widely used in electronic devices. So far, there are only few reports related to preparation of copper/carbon nanohorn hybrid materials. Therefore

as a first step, surface modification of carbon nanohorns using microwave irradiation in prior to preparation of copper/carbon nanohorn hybrid material is worth to investigate systematically.

In this work, acid treated SWCNHs would be experimentally prepared by microwave irradiation with a purpose for fabricating copper/carbon nanohorn hybrid material by an advantage of controllability of their surface modification.

2. Materials and Methods

2.1 Synthesis of single-walled carbon nanohorns (SWCNHs)

Gas-injected arc-in-water (GI-AIW) method was used in this research. Two graphite electrodes were immersed vertically in 2L of de-ionized water. The arc discharge condition was carried out at a constant current 80A and a constant voltage 40V. The anode was a graphite rod (purity 99.9995%) with 3 mm diameter and 100 mm length. The cathode was a graphite rod (purity 99.9995%) with 12 mm diameter and a hole of 8 mm diameter with 25 mm depth on one side, and two channels with 2 mm diameter for injecting gas into the arc zone. The cathode was connected with gas supply tube and settled at top arm (fixed arm). The anode was settled on bottom arm (moving arm) and raised up vertically into cathode hole at a control speed of 1.5mm/s. During the operation, nitrogen gas was supplied through cathode at 5L/min [8]. After the operation finished, sample was collected from the water surface and then dried in oven overnight then characterized.

2.2 Microwave-assisted acid treatment for SWCNH surface modification

100 mg of pristine SWCNHs was ultrasonicated in a mixture of 15ml of 97wt% H₂SO₄ and 5ml of 70wt% HNO₃. The suspension was placed at the middle of a household microwave oven (LG, MS-2127CW, 2450MHz, 800W) and heated with an input power of 360 W for designated irradiation time in a range of 30-180 second. The microwave-treated suspension was filtered, washed with several time of de-ionized water

until neutral and dried in an oven overnight in prior to its characterization.

2.3 Copper/SWCNH hybrid material preparation

A designated amount of $\text{CuSO}_4 \cdot 5\text{H}_2\text{O}$ precursor was added into a mixture of ethylene glycol and NaOH and stirred for 20min. Then 50mg of the acid treated SWCNHs was added into 100 ml of the CuSO_4 solution which was sonicated for 20min. Similar to the acid treatment step, the SWCNH suspension was placed at the middle of a household microwave oven (LG MS-2127CW, 2450MHz, 800W) and heated with a microwave irradiation power of 360W for a designated irradiation time [6]. The suspension was taken from the oven, cooled down to room temperature filtered, washed with several time of de-ionized water and dried in oven overnight in prior to its characterization.

3. Results and Discussion

3.1 Morphology and particle size distribution of synthesized SWCNHs

Figure 1 reveals typical TEM micrographs of the SWCNHs synthesized by GI-AIW method. SWCNH agglomerates exhibit nominal size ranged from 60 to 100 nm. Particle size distribution (PSD) of SWCNH particles determined by dynamic light scattering (DLS) method is. Figure 2 is shown that the particle diameter distribution ranges from 50 nm, with a peak at 142 nm. It should be noted that PSD of the acid treated SWCNHs is only slightly affected by the acid treatment process.

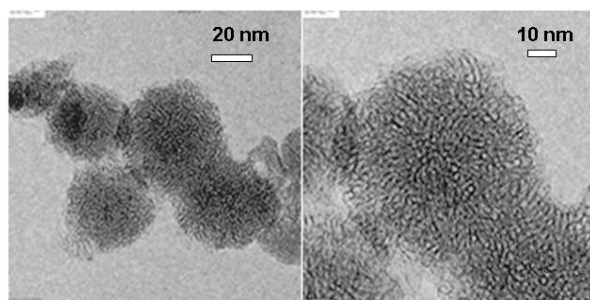


Figure 1 TEM image of agglomerated SWCNHs

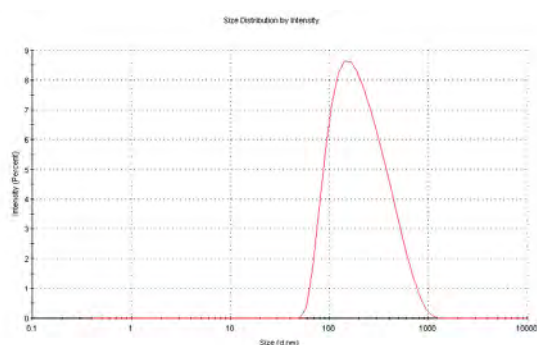


Figure 2 Particle size distribution of typical sample of SWCNHs determined by DLS

3.2 Surface polarity of SWCNHs

Both pristine and acid treated SWCNHs were subject to zeta potential analysis to confirm their surface polarity. As could be observed in Figure 3, the acid treated SWCNHs exhibit higher negative zeta-potential than that of pristine SWCNHs. The zeta-potential of SWCNHs becomes higher negative once they are subject to acid treatment. However, with the irradiation time longer than 45 sec, the polarity of the surface of the acid treated SWCNHs would achieve an equilibrium which results in the saturated zeta potential value. These results would suggest that there is an optimal condition of irradiation time which could provide an equilibrated polarity on the surface of acid treated SWCNHs.

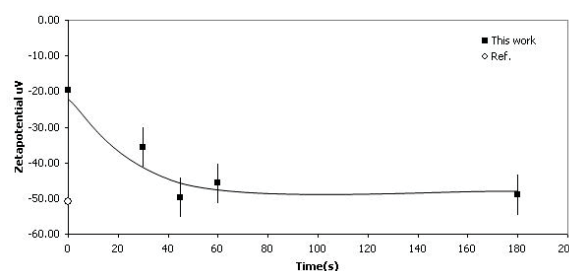


Figure 3 Zeta-potential of SWCNH samples

FT-IR spectroscopy is used for characterizing functional groups which would anchor onto the surface of SWCNHs subject to acid pretreatment. As could be observed in Figure 4, comparison of FT-IR spectra of the pristine and acid treated SWCNHs with difference irradiation time reveal typical valleys at 1194, 1584 and 1735 cm^{-1} . It should be noted that the distinctive valley at 1735 cm^{-1} reveals the existence of C=O stretching bond of carboxylic acid. Meanwhile, the valley at 1584 cm^{-1} could be assigned to C=C stretching bond and another valley at 1194 cm^{-1} is referred to C-O stretching functionality on the surface of the acid treated SWCNHs [6]. The spectral comparison of the pristine SWCNHs and acid treated SWCNHs suggests that there are additional functional groups anchoring onto the surface of the acid treated SWCNHs when compared with the pristine SWCNHs. The deeper valley would suggest the higher content of those functional groups [6]. These results are in good agreement with the higher negativity of SWCNH zeta potentials shown in Figure 3. Both analytical results would suggest that the acid treated SWCNHs would exhibit improved hydrophilicity, which would be beneficial to a process of hybridizing with Cu nanoparticles.

3.3 Morphology of Cu/SWCNH hybrid material and their coating fraction

After the acid treatment, the SWCNHs with modified surface were subject to copper precursor and ethylene glycol with thermal stimulation using microwave irradiation at 360W for 5min. Figure 5(a)-(d) shows TEM micrographs of copper/SWCNH hybrid materials at different microwave irradiation

time. As could be observed in Figure 5(a), some parts of SWCNHs are partially coated with agglomerates of copper clusters. With irradiation time longer than 45 sec, almost of SWCNHs surface are coated with clusters of copper nanoparticles. Functional groups in hybrid material were also analyzed by FT-IR. As depicted in figure 6, FT-IR spectrum of acid treated SWCNHs with irradiation power of 360W for 45sec, exhibit a valley at 1735 cm^{-1} , which is C=O stretching bond of carboxylic acid. However, the valley could not be observed in the sample of Cu/SWCNH hybrid material. Meanwhile, there is a new valley of Cu-O stretching appears at 626 cm^{-1} for the copper/SWCNH hybrid material fabricated under the same microwave irradiating condition[9].

To confirm amount of copper coating on SWCNHs surface, image processing technique is also employed. Volume and area of Cu nanoparticles and SWCNHs are analytically extracted from TEM images using

software of Image J. The coating fraction of Cu nanoparticles on the surface of SWCNHs which are irradiated by microwave for 30, 45 and 60 sec is 19.11%, 19.23%, 21.23% and 28.52%, respectively. These results concurring with zeta-potential results would be attributed to a high contents of negative polarity which would increase possibility of Cu nanoparticle to anchor onto the surface of acid treated SWCNHs[10]. With irradiation time of 60 sec a higher coating fraction could be achieved, suggesting that growth process of Cu nanoparticle clusters on the surface of SWCNHs could be enhanced by a longer stimulating time. Therefore, further investigation of the saturation of coating of Cu nanoparticles on SWCNHs would be our on-going issue.

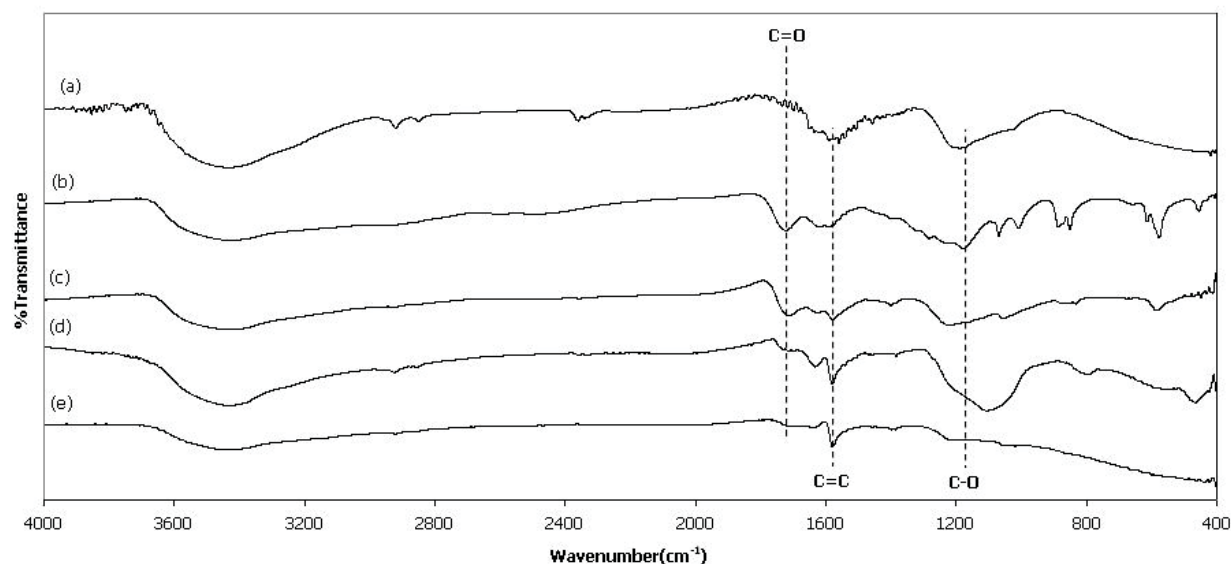


Figure 4 FT-IR spectra of (a) pristine SWCNHs, (b) acid treated SWCNHs at 360 W for 30 sec, (c) acid treated SWCNHs at 360 W for 45 sec, (d) acid treated SWCNHs at 360 W for 60 sec and (e) acid treated SWCNHs at 360 W for 180 sec

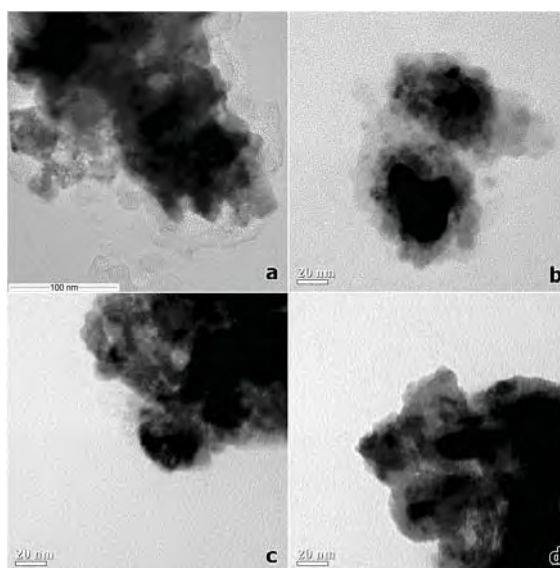


Figure 5 TEM images of hybrid materials of (a) pristine SWCNHs and hybrid materials with different irradiation time of acid treatment process: (b) 30 sec, (c) 45 sec and (d) 60 sec.

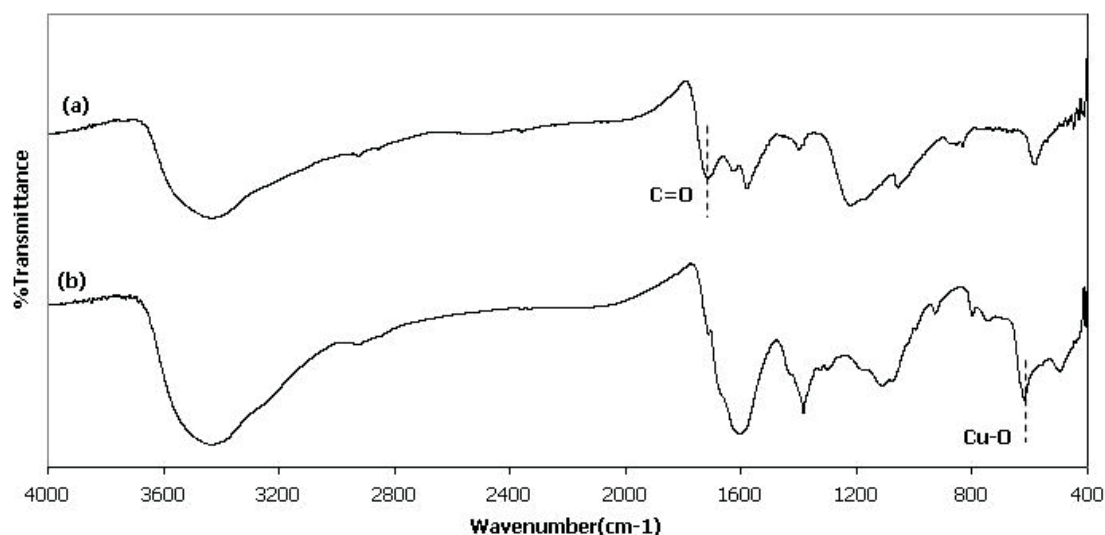


Figure 6 FT-IR spectra of (a) acid treated SWCNHs and (b) Cu/SWCNH hybrid materials fabricated with microwave irradiation at 360W for 45sec.

4. Conclusions

In this investigation, the microwave irradiation has been employed for modifying the surface property of SWCNHs synthesized by GI-AIW method. It should be noted that the processing time of microwave irradiation is in the order of second. The microwave irradiation power of 360 W and the microwave irradiation time of 45 sec could lead to the increased polarity of SWCNH surface. The presence of functional groups on the surface of the acid treated SWCNHs is beneficial to the hybridization of SWCNHs with Cu nanoparticles, resulting in a higher coating fraction of Cu nanoparticles within the Cu/SWCNH hybrid materials.

Acknowledgements

This work is supported by the Centenary Fund of Chulalongkorn University for Center of Excellence in Particle Technology.

References

- [1] S. Iijima, M. Yudasaka, R. Yamada, S. Bandow, K. Suenaga, F. Kokai and K. Takahashi, *Chem. Phys. Lett.* **309** (1999) 165-170
- [2] S. Zhu and G. Xu, *Nanoscale*. **2** (2010) 2538-2549
- [3] H. Lai, J. Li, Z. Chen and Z. Huang, *ACS Appl Mater Interf.* **4** (2012) 2325-2328
- [4] Y. Zhao, J. Li, Y. Ding and L. Guan, *Chemical Commun.* **47** (2011) 7416-7418
- [5] R. Q. Yu, L. W. Chen, Q. P. Liu, J. Y. Lin, K. L. Tan, S. C. Ng, H. S. O. Chan, G. Q. Xu and T. S. A. Hor, *Chem. Mater.* **10** (1998) 718-722
- [6] N. Leelaviwat, S. Monchayapisut, C. Poonjarernsilp, K. Faungnawakij, K.-S. Kim and T. Charinpanitkul, *Curr Appl. Phys.* **12** (2012) 1575-1579
- [7] Y. Yu, L.-L. Ma, W.-Y. Huang, F.-P. Du, J. C. Yu, J.-G. Yu, J.-B. Wang and P.-K. Wong, *Carbon*. **43** (2005) 670-673
- [8] C. Poonjarernsilp, N. Sano, T. Charinpanitkul, H. Mori, T. Kikuchi and H. Tamon, *Carbon*. **49** (2011) 4920-4927
- [9] T. Petrov, I. Markova-Deneva, O. Chauvet, R. Nikolov, I. Denev, J. Univ. Chem. Tech Metal **47** (2012) 197-206
- [10] B. Kim and W. M. Sigmund, *Langmuir*. **20** (2004) 8239-8242

EFFECT OF MODIFIED CARBON NANOTUBE ON PROPERTIES OF THERMOPLASTIC STARCH COMPOSITES

Narachai Chommuang¹, Jittiporn Kruenate¹, Nantavat Tangchantra,^{1,*}
Suchart Supattanapalapol¹, and Thammarak Sooksomsong¹

¹ National Metal and Materials Technology Center, National Science and Technology Development Agency,
114 Thailand Science Park, Phahonyothin Rd. Klong 1, Klong Laung, Pathumthani, 12120, Thailand

* E-Mail: narachac@mtec.or.th

Abstract: Thermoplastic starch (TPS) is an inexpensive material which is biodegradable polymer and can be derived from renewable resources. Unfortunately, TPS exhibited unacceptable disadvantages in terms of mechanical properties, brittle and moisture adsorption. In order to improve the mechanical properties of starch-based materials, the carbon nanotube (CNT) which has been recognised as excellent filler was added into glycerol-plasticized starch by melt mixing process. The morphology of these composites was observed by scanning electronic microscopy (SEM). The rheological behavior was characterized by capillary rheometer. The mechanical properties of TPS/CNT composites were characterized by tensile testing. The results revealed that homogeneous TPS/CNT composite film can be achieved when CNTs content was found to be upto 2 phr. The improvement of CNT content enhanced both the viscosity and mechanical properties of TPS. These materials exhibited highly improved tensile strength and elongation up to 61% and 175 %, respectively with only 2 phr of carbon nanotube content.

1. Introduction

For more than three decades, commercial petroleum-based plastics have been widely used in many applications. After usages, this plastic wastes have caused serious plastic waste problems and landfill depletion since they have high volume to weight ratio and high resistance to degradation. The use of biodegradable plastics obtained from natural resources has become challenging as a strategy to minimize the environmental impact and develop sustainable plastics. There are many biodegradable plastics from natural resources. Starch is one of the most abundant renewable resources and inexpensive materials, which has the potential to replace petroleum-based plastic. Thermoplastic starch (TPS), one of recognizable biodegradable polymers and can be derived from renewable resources, has many advantages over petroleum-based one e.g. non toxic, compostable, and low cost. Unfortunately, TPS exhibited serious drawbacks, limited mechanical properties for some application and moisture sensitivity. To overcome these shortcomings, various efforts have been developed such as chemical modification of starch [1,2], and blending with other polymers [3,4].

Another more promising strategy has been developed based on TPS composites. Carbon nanotubes (CNT) may consist of a one atom thick single-wall nanotube, or a number of concentric tubes

called multi-walled nanotube, having high aspect ratios, elastic modulus and tensile strength up to 1 TPa and 200 GPa respectively [5]. Because of these properties, they seem to be the reinforcement for different types of polymers. Many researchers reported that the addition of carbon nanotubes significantly improved in mechanical and thermal properties of polyethylene [6] and PLA [7]. However, strong Van der Waals interactions among CNT result in their stacking up and aggregation. However, CNT maintains poor solubility and compatibility in aqueous media as well as in organic solvents. To solve this problem, we used modified carbon nanotube (mCNT) by introducing carboxylic acid groups on their surfaces in order to enhance their intermolecular interactions with TPS. The morphology, thermal and mechanical properties were also investigated.

2. Materials and Methods

2.1 Materials

The cassava flour was purchased from Dragon Fish Cassava Flour. The glycerol used as plasticizer in this study was supplied by Hong Huat Company, Thailand. Modified CNT (mCNT) were purchased from Chengdu Organic Chemicals Co. Ltd., China with carboxylic group concentration about 2 wt%.

2.2 Thermoplastic starch/mCNT composites

Powder of cassava starch was mixed with 0.5, 2 and 5 phr mCNT and plasticizer containing 35 phr glycerol. The compounds were then fed into a twin screw extruder (LabTech) at temperature of 135 °C and screw speed of 100 rpm and the sample was then prepared for mechanical characterization as sheet-form using compression moulding at 180 °C.

2.3 Characterization

Transmission electron microscopy (TEM), JEOL JEM-2010, and a field emission scanning electron microscopy (SEM), Hitachi S-3400N, were used to characterize the micro-structure of mCNT and its nanocomposites, respectively. The Raman spectra were recorded on dispersive Raman microscope (Senterra-Bruker Optics).

2.4 Thermal Analysis

The glass transition temperature of the samples were measured by differential scanning calorimeter (DSC, Mettler Toledo DSC822e) at a heating rate of 10 °C/min and with scanning temperature range from 20 °C to 160 °C in N₂ atmosphere.

2.5 Rheological Analysis

Rheological measurements were carried out using a capillary rheometer, Rh7 Rosand (Malvern Instruments). After a warm-up period of 4 min at 170 °C, the melt was extruded through a specified capillary at pre-selected speeds of the cross-head. The force corresponding to different plunger speeds was recorded.

2.6 Mechanical Properties

Uniaxial tensile loading tests on the tested samples were performed using an Universal testing machine (Instron 55R450). A constant crosshead speed of 100 mm/min was used. Rectangular samples of 12 mm wide, 1 mm thick and a gauge length of 40 mm were employed. Five replicates were used for all blends.

2.7 Moisture absorption

TPS sheet was cut into 10mm x 10mm and dried at 90 °C for 12 h. The dried TPS was placed into sealed 75 %RH container at 25±2°C. TPS samples were weighted every 6 h until constant. The moisture content was calculated by eq.1

$$\text{Moisture content} = \frac{\text{Moisture absorbed TPS}}{\text{Dried TPS}} \times 100 \quad (1)$$

3. Results and Discussion

3.1 Characterization

Raman spectrum of mCNT (figure 1) shows that their D band and G band are at 1340 cm⁻¹ and 1577 cm⁻¹, respectively. Therefore, the presence of the G and D bands further indicates that the graphitic structure of carbon nanotubes is preserved. In addition, the I_G/I_D ratio for commercial CNT is 1.39 [8] while the I_G/I_D ratio for mCNT decrease to 0.62 suggesting that some moieties are covalently introduced on the surface of CNT [8,9].

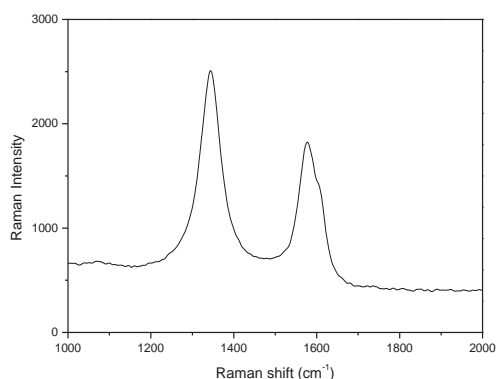


Figure 1. Raman spectrum of mCNT

The morphology of mCNT was observed with TEM, as illustrated in figure 2. The mCNT exhibited multiwall characteristic with central hollow tubes in the center, 10-30 μm in length, 5-10 nm in internal diameter, and 10-20 nm in external diameter. The results found that mCNT are not totally tangled and some well-dispersed individual nanotubes indicating that the modification CNT with carboxylic groups can efficiently prevent CNT from the disruption of their tubular structure and display a considerable debundling effect.

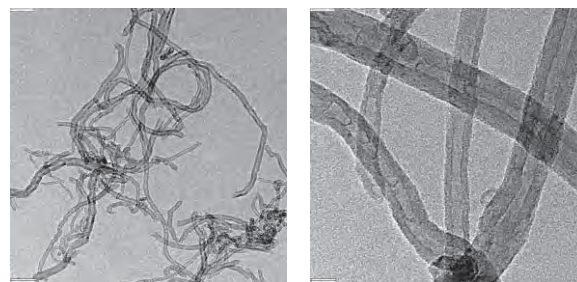


Figure 2. TEM image of mCNT

3.2 Thermal properties

Thermal properties of neat TPS and its composites were investigated by DSC as shown in figure 3, which displays glass transition temperature of plasticized TPS and TPS composites. TPS exhibited glass transition temperature (T_g) at 75.65 °C. The results showed that T_g of plasticized TPS increased with increasing carbon nanotube content. It may be explained that introduction of carbon nanotube could induce strong interphase interaction with the TPS molecule and causing them very difficult to move apart.

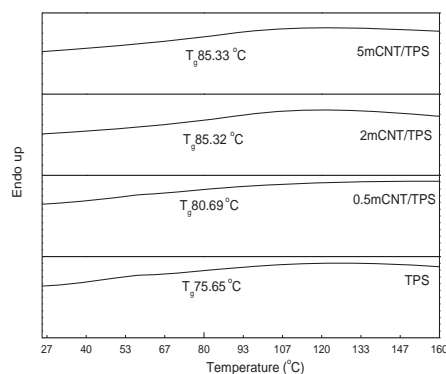


Figure 3. DSC thermogram of neat TPS and TPS composites

3.3 Rheological properties

Figure 4 showed the shear viscosity versus mCNT content at different shear rate. At low shear rate in range of 20 to 300 s⁻¹, the steady shear viscosity of mCNT/TPS composites dramatically increased with the mCNT content. At high shear rate in range of 700 to 2000 s⁻¹, the shear viscosity nearly increased with the mCNT content. Thus, the influence of mCNT

concentrations on viscosity improvement is much higher at low shear rate than at high shear rate. As the nanotube content increases in this composite system, the more chain interaction occur the more shear viscosity increases.

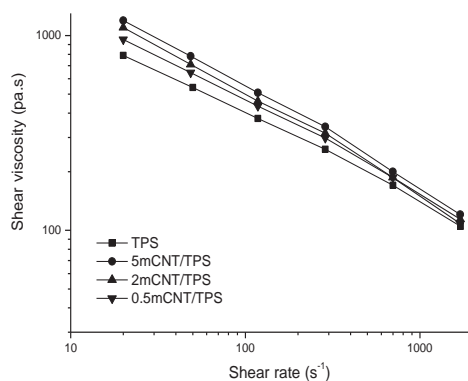


Figure 4. shear viscosity of neat TPS and TPS composites

3.4 Mechanical Properties

The mechanical properties of the TPS/mCNT composites are shown in figure 5. The addition of mCNT significantly improved mechanical properties of TPS composites. The tensile strength and percentage strain at break increased as increasing mCNT content. As the mCNT content increased to 2 phr, the tensile strength of TPS/mCNT nanocomposites could achieve to 16.38 MPa, whereas the tensile strength of the pure TPS was 10.18 MPa. This mechanical improvement was arrived from the surface modification of carbon nanotubes with carboxylic group, the improvement of hydrophilicity of carbon nanotubes and reduce agglomerations was occurred [10]. Therefore, mCNT were greatly benefited to enhance the hydrogen-bonding interactions as well as the dispersion in TPS/mCNT nanocomposites. However, further mCNT content above 2 phr could not significant improve mechanical properties of composites.

In contrast, Young's modulus and elongation at break of mCNT/TPS composites dramatically decreased and increased, respectively. The results could explain that the increase of mCNT leads to increase moisture content, as plasticizer in TPS composites shown in table 1.

Table 1: Moisture content in neat TPS and mCNT/TPS composites

	Moisture content (%)
TPS	4.09
0.5mCNT/TPS	5.86
2mCNT/TPS	6.12
5mCNT/TPS	6.43

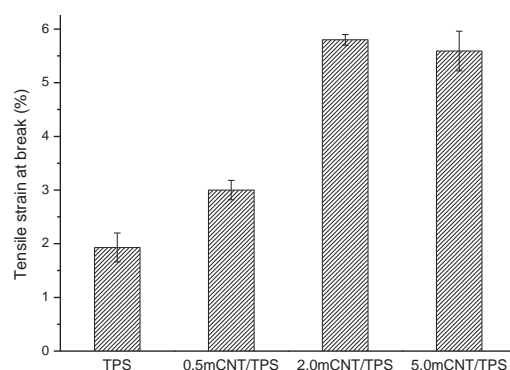
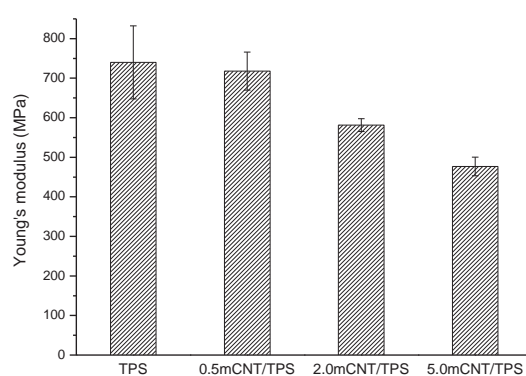
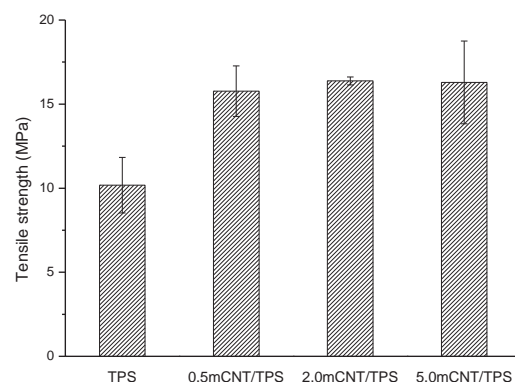


Figure 5. mechanical properties of neat TPS and TPS composites

3.5 Morphological Characterization

Dispersion of mCNT in TPS matrix was one of the key elements to the mechanical properties of the composites. Figure 6 showed SEM images of TPS and TPS composites. SEM images clearly show a homogeneous dispersion of mCNT throughout the TPS matrix at lower mCNT loading below 2 phr. In the composite with 5 phr of mCNT, some carbon nanotubes were found to be agglomerated. They were bundling together in the form of random arrangement.

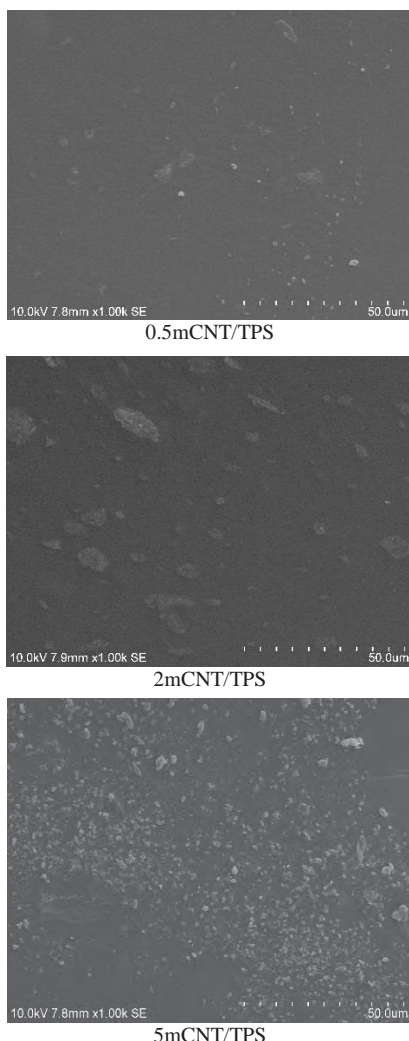


Figure 6. SEM image of neat TPS and TPS composites

4. Conclusions

In this work, the modified carbon nanotube (mCNT) was added into glycerol-plasticized starch by twin-screw extruder. The homogeneous dispersion of mCNT throughout TPS matrix was achieved. The rheological properties of mCNT/TPS composites were found that the shear viscosity of the composites significantly increased as increasing mCNT content. The mechanical properties of mCNT/TPS composites revealed that the tensile strength and elongation of the composites at break considerably increased; whereas, the Young's modulus of the composites meaningfully decreased. This can be explained that the addition of mCNT content can increase in moisture content in the composites matrix.

5. References

- [1] B. Kaur, F. Ariffin and R. Bhat et.al, *Food Hydrocolloids* **26** (2012) 398-404.
- [2] J. Fornal, J. Sadowska, and W. Błaszczak, *Journal of Food Engineering* **108** (2012) 515–522.
- [3] J. Ren, H. Fu, and T. Ren et.al, *Carbohydrate Polymers* **77** (2009) 576–582.
- [4] E. M. Teixeira, A.S. Curvelo, and A. C. Corrêa, *Industrial Crops and Products* **37** (2012) 61–68.
- [5] X. Zhou1, E. Shin, and K.W. Wang et.al, *Composites Science and Technology* **64** (2004) 2425–2437.
- [6] W. Shujun, Y. Jiugao, and Y. Jinglin, *Polymer Degradation and Stability* **87** (2005) 395–401.
- [7] A. L. Brody, *Nano and food packaging technologies converge. Food Technology* **60** (2006) 92–94.
- [8] S.Kanga, D. Yina, and X. Li et.al, *Colloids and Surfaces A: Physicochem. Eng. Aspects* **384** (2011) 363– 367
- [9] E. Titus, N. Ali, and G. Cabral, et.al, *JMEPEG* **15** (2006) 182-186
- [10] G. J. Wang, Z. H. Qu and J. L. Guo et.al, *Acta Chimica Sinica* **64** (2006) 2505–2508

NASAL PACK WITH CONTROLLED RELEASE OF AMOXICILLIN

Pornpan Poonsavaeng^{1*}, Songklot Aeumjaturapat² and Supason Wanichwecharungruang³

¹Program in Petrochemistry and Polymer Science, Faculty of Science, Chulalongkorn University, Bangkok 10330 Thailand

²Department of otolaryngology, Faculty of Medicine, Chulalongkorn University, Bangkok 10330 Thailand

³Department of Chemistry, Faculty of Science, Chulalongkorn University, Bangkok 10330 Thailand

* Author for correspondence; E-Mail: guwai_guwai@hotmail.com, Tel. +66 814105619

Abstract: After sinus surgery, the nasal pack is usually inserted in the nasal cavity to absorb blood and stop bleeding. Bacterial infection may occur since the nasal pack is normally left there for 3 -7 days, therefore, oral antibiotic drugs are prescribed. Hence, the nasal pack material with sustained anti-bacterial property will be useful. Here the poly(vinyl acetal) foam was prepared by crosslinking poly(vinyl alcohol) (0.12 mmol) with formaldehyde (66.53 mmol) and glutaraldehyde (0.42 mmol) under room temperature with 50% sulfuric acid as a catalyst and 20 h of curing time. The obtained foam was open cell structure with approximately 200 μ m diameter. The foam impregnated with amoxicillin-loaded alginate microparticles using poly(vinylalcohol) as binder to adhere the microparticles in foam porous and then release of amoxicillin was investigated.

1. Introduction

Nasal pack is used for absorb blood and stop bleeding in nasal cavity after sinus or removal polyps surgery. Common nasal packing materials are gauze pad and foam. Gauze pad has a low capacity for holding fluid and may harm the soft tissue through its abrasiveness. Abrasiveness of the gauze pad can lead to trauma and inflammation. Foam, however, not only possesses a higher holding fluid property, but also can be formed into a variety of shapes. Polyurethane [1] and poly(vinyl acetal) [2] foams are the two commonly used nasal packing materials.

After insertion of nasal pack for 24-48 hours, infection may occur, which lead to sinusitis, intracranial abscess and toxic shock syndrome (TSS) owing to the growth of *Staphylococcus aureus* [3-5]. Hence the oral antibiotic drugs are necessary. Amoxicillin is a penicillin-like antibiotic. It has broad-spectrum of activity including both gram-positive and gram-negative bacteria, and it is used in a wide range of bacterial infection such as bronchitis, pneumonia, gonorrhea and ears, nose, throat, urinary tract, and skin infections. Amoxicillin works by inhibiting the synthesis of bacteria cell wall. It is commonly used in the form of oral capsules. β -lactam ring of amoxicillin may be degraded by gastric acid, leading to an ineffective drug concentration being delivered to the site of infection after oral administration. Consequently, patient has to take drug at high doses [6].

Sodium alginate is a natural polysaccharide obtained from brown seaweed. It is non-toxic, biocompatible, mucoadhesive, and low cost. The

polymer can undergo mild gelation by addition of divalent cations such as Ca^{2+} [7]. Alginate has been extensively used for biomedical applications such as wound dressing [8], cell culture [9], protein delivery [10] and drug delivery [11].

Here nasal pack material with sustained anti-bacterial property was fabricated based on poly(vinyl acetal) foam and the foam was impregnated with amoxicillin-loaded alginate microparticles. Foam characterization and drug release property were investigated.

2. Materials and Methods

2.1 Materials

Amoxicillin was provided as a gift sample from The Government Pharmaceutical Organization (Bankok, Thailand). Alginic acid sodium salt (viscosity of 2% solution at 25°C 250 cps) and poly(vinyl alcohol) (PVA) (average Mw = 31,000-50,000, 87-89% hydrolyzed) were purchased from Sigma Aldrich (Steinheim, Germany). Formaldehyde and glutaraldehyde were purchased from Merck (Darmstadt, Germany). Calcium chloride was purchased from Carlo Erba (Milano, Italy). TritonX-100 was purchased from Acros Organics (Geel, Belgium).

2.2 Preparation of Poly(vinyl acetal) foam

PVA (4.75 g) was dissolved in distilled water (40.5 ml). Then Triton X-100 (26 μ l) was added into the PVA solution and the mixture was agitated for 10 minutes at room temperature. Sulfuric acid (7 ml of 50% w/w) was added into the mixture and the mixture was agitated for 10 minutes. Formaldehyde (5 ml of 37% w/w in water) was then added to the mixture and agitated for another 10 minutes. After that, glutaraldehyde (0.75 ml of 5% w/w in water) was slowly dropped into the mixture. The agitation (mixing) was stopped when the mixture started to be viscous, then the mixture was poured into the mold for curing (20 h at room temperature). The obtained poly(vinyl acetal) foam was washed with distilled water until pH of the rise water was 5, then it was dried in oven at 60°C for 1 h and kept in dessicator until completely dry. The poly(vinyl acetal) foam was characterized by Scanning Electron Microscopy (SEM).

2.3 Preparation of microparticles

The emulsification gelation method was used to prepare the microparticles [11-12]. Amoxicillin (400 mg) was dispersed in sodium alginate solution (10 ml of 2% w/v in water). The solution was dispersed in vegetable oil containing tween 80 (600 μ l in 60 ml of oil), homogenized at 8000 rpm for 30 minutes. 2M of calcium chloride (25 ml) was added into the solution while homogenizing. The solution was allowed to homogenize for 30 minutes. The solution was centrifuged at 5000 rpm (2687 g) for 20 minutes to separate oil phase. The microparticles in water phase were collected by filtration in vacuum, washed two times with ethanol and one time with distilled water. Then the microparticles were dried by lyophilization. The microparticles were then subjected to Attenuated total reflectance-Fourier Transform Infrared (ATR-FTIR), Scanning Electron Microscopy (SEM) and Transmission Electron Microscope (TEM) analyses. Entrapment efficiency percentage (% EE) of the microparticles were determined from untrapped amoxicillin in filtrate water by UV-visible spectrophotometer.

2.4 Impregnation of microparticles to the foam

The microparticles loaded with amoxicillin (50 mg) were dispersed in PVA solution (5 ml of 1000 ppm PVA solution). Poly(vinyl acetal) foam (4x1x1 cm) was dipped into this solution to absorb the microparticles in porous, dried in vacuum oven at 60°C for 1 h and kept in desiccator. The obtained product was characterized by SEM.

2.5 Control release study of amoxicillin

The impregnated foam was added into simulated nasal fluid pH 6.8 as the release medium. Release study was conducted at 37°C. Aliquots of 5 ml sample was collected at predetermined time points (0, 1, 2, 4, 6, 24, 30 and 48 h), filtered and 5 ml of fresh release medium was replenished to maintain a constant volume. The concentration of amoxicillin in the sample was determined by UV-visible spectrophotometer.

3. Results and Discussion

3.1 Preparation of Poly(vinyl acetal) foam

The poly(vinyl acetal) foam was successfully prepared by crosslinking PVA with formaldehyde and glutaraldehyde. To build up foam, PVA solution was firstly stirred by agitator to create air bubbles. Formaldehyde and glutaraldehyde, were then added to crosslink the polymer chains via acetal bond in order to trap these bubbles. Curing for 20 h was needed to set the foam. After washing, the obtained foam was white with open cell structure with about 200 μ m as observed by SEM (Figure 1).

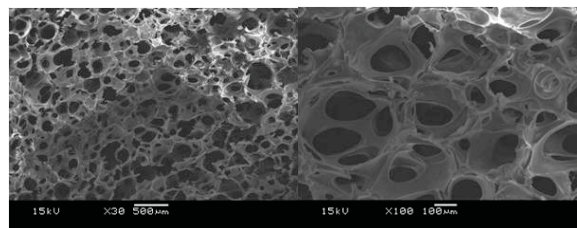


Figure 1. SEM image of the poly(vinyl acetal) foam

3.2 Preparation of microparticles

The ATR-FTIR spectrum of amoxicillin-loaded microparticles (Figure 2c) showed peak at 1583 cm^{-1} (C=O stretching of carboxylate salt of alginate). Amoxicillin peaks were observed at 1772 cm^{-1} (C=O stretching of β -lactam), 1683 cm^{-1} (C=O stretching of amide I) and 1520 cm^{-1} (C=C stretching of benzene ring). The obtained microparticles showed 17% of drug entrapment efficiency. The morphology of microparticles from SEM and TEM images showed a non-spherical morphology and irregular surface, with the size approximately 5-10 μ m (Figure 3).

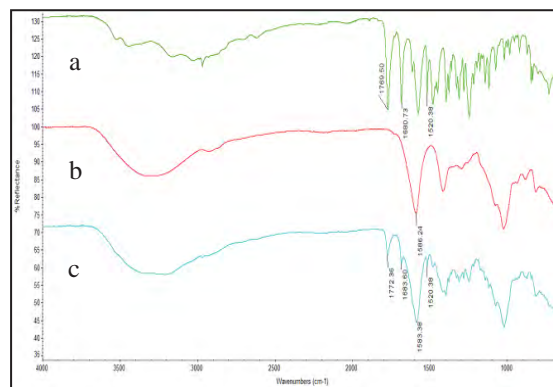


Figure 2. ATR-FTIR spectra of amoxicillin (a), placebo alginate microparticles (b) and amoxicillin-loaded microparticles (c).

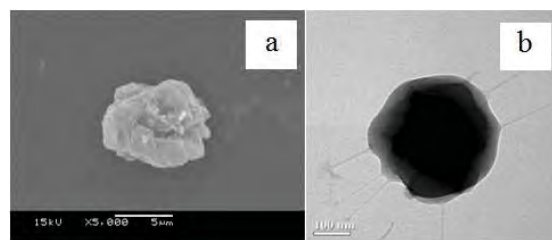


Figure 3. SEM (a) and TEM images (b) of amoxicillin-loaded microparticles.

3.3 Impregnation of microparticles to the foam

The microparticles could penetrate into foam pores due to the smaller size of the microparticles. To adhere these particles in foam porous, PVA solution was used as a binder. SEM images (Figure 4) showed that the microparticles were successfully loaded into foam structure.

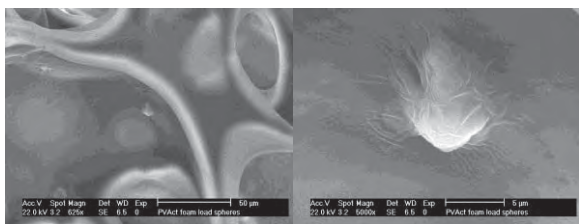


Figure 4. SEM images of amoxicillin-loaded microparticles loaded in foam porous.

3.4 Control release study of amoxicillin

The release profile of amoxicillin from the impregnated foam in simulated nasal fluid pH 6.8 (Figure 5.) showed the constant of releasing rate. Only 15% of amoxicillin was released in 2 days, which indicated the prolong release of the amoxicillin from the foam.

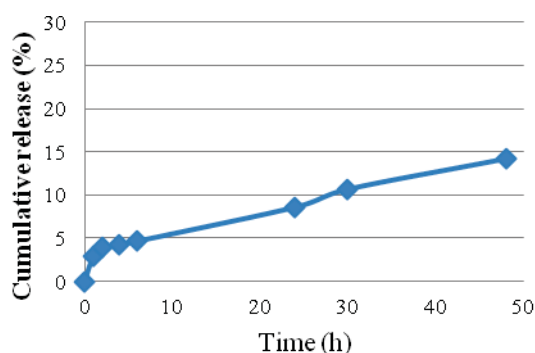


Figure 5. Release profile of amoxicillin from the microparticles.

4. Conclusions

Here we have created a nasal pack material with anti-infection property from poly(vinyl acetal) foam impregnated with amoxicillin-loaded in alginate microparticles. The foam showed controlled release of amoxycillin.

Acknowledgements

We thank the Nanotechnology Center (NANOTEC), NSTDA, Ministry of Science and Technology, Thailand, through its program of Center of Excellence Network and the Centenary Academic Development Project (the Special Task force for Activating Research (STAR) at Chulalongkorn University, for financial provisions.

References

- [1] F. J. Richter. Hydrophylic medical sponge and method of using same, *United States Patent*. 1971, 3566871.
- [2] S. Resnblatt. Medical surgical sponge and method of making same, *United States Patent*. 1978, 4098728.
- [3] A. J. Maniglia, W. J. Goodwin, J. E. Arnold, E. Ganz. Intracranial abscesses secondary to nasal, sinus, and orbital infections in adults and children. *Archives of*

Otolaryngology Head Neck Surgery **115** (1989) 1424-1429.

- [4] H. F. Hull, J. M. Mann, C. J. Sands, S. H. Gregg and P. W. Kaufman, Toxic shock syndrome related to nasal packing. *Archives of Otolaryngology* **109** (1983) 624-626.
- [5] J. A. Jacobson and E. M. Kasworm. Toxic shock syndrome after nasal surgery. Case reports and analysis of risk factors. *Archives of Otolaryngology Head Neck Surgery* **112** (1986) 329-332.
- [6] R. B. Umamaheshwari, S. Ramteke and N. K. Jain. Anti-*Helicobacter Pylori* Effect of Mucoadhesive Nanoparticles Bearing Amoxicillin in Experimental Gerbils Model. *AAPS PharmSciTech* **5** (2004) article 32.
- [7] K. Y. Lee and D. J. Mooney. Alginate: Properties and biomedical applications. *Progress in Polymer Science* **37** (2012) 106–126.
- [8] S. J. Boateng, H. K. Matthews, H. N. E. Stevens and M. G. Eccleston, Wound healing dressings and drug delivery systems: a review. *Journal of Pharmaceutical science* **97** (2008) 2892-2923.
- [9] J. A. Rowley, G. Madlambayan and D. J. Mooney, Alginate hydrogels as synthetic extracellular matrix material. *Biomaterials* **20** (1999) 45–53.
- [10] Y. Zhang, W. Wei, P. Lv, L. Wang and G. Ma. Preparation and evaluation of alginate–chitosan microspheres for oral delivery of insulin. *European Journal of Pharmaceutics and Biopharmaceutics* **77** (2011) 11–19.
- [11] R. Rastogi, Y. Sultana, M. Aqil, A. Alib, S. Kumar, K. Chuttani and A.K. Mishra. Alginate microspheres of isoniazid for oral sustained drug delivery. *International Journal of Pharmaceutics* **334** (2007) 71–77.
- [12] L. S. C. Wan, P. W. S. Heng and L. W. Chan, Drug encapsulation in alginate microspheres by emulsification. *Journal of Microencapsulation* **9** (1992) 309-316.

EFFECTS OF CaCO_3 ON MECHANICAL PROPERTIES AND MORPHOLOGIES OF PP/Co-PP/ CaCO_3 COMPOSITES TRAYS FOR FOOD PACKAGING

Jakkrit Piwsawang¹, Thanyarut Jinkhan^{1,2}, Chiravoot Pechyen^{1,2*}

¹ Department of Packaging and Materials Technology, Faculty of Agro-Industry, Kasetsart University, Chatuchak, Bangkok, 10900 Thailand

² Center for Advanced Studies in Agriculture and Food, KU Institute for Advanced Studies, Kasetsart University, Bangkok 10900, Thailand (CASAF, NUR-KU, Thailand)

* Author for correspondence; E-Mail: chiravoot.p@ku.ac.th, Tel. +66 836166332, Fax. +66 25625045

Abstract: Unmodified calcium carbonate (CaCO_3) fillers were compounded with polypropylene (PP) and copolymer polyethylene (Co-PP) separately in a Brabender plasticorder internal mixer at 180 °C and 50 rpm in order to obtain composites, which contain 0–40 phr (per 100 part of resin) of filler at 40 phr intervals. The morphology development and the mechanical properties of the composites with reference to filler loading were investigated. In terms of mechanical properties, Young's modulus and maximum compression load increased, whereas yield strength and elongation at break decreased with the increase in filler loading of PP/Co-PP/ CaCO_3 composites. Of these the PP/Co-PP exhibited lower yield strength, Young's modulus, and higher elongation at break than CaCO_3 composites (data not show here). Scanning electron microscopy (SEM) was used to examine the structure of the fracture surface and to justify the variation of the measured mechanical properties.

1. Introduction

Polypropylene is a popular plastic that offers a combination of outstanding physical, mechanical, thermal, and electrical properties. Due to excellent chemical resistance in corrosive environments, polypropylene provides excellent resistance to organic solvents and degrades agents attack. It is light in weight, resistant to staining, and has a low moisture absorption rate. Polypropylene is available in two basic types as either homopolymer or copolymer material. Although similar in many respects, each type exhibits distinct differences in both appearance and performance. Homopolymer polypropylene (PP) is the most widely utilized. PP offers a high strength to weight ratio and is stiffer and stronger than copolymer. With good chemical resistance and weldability, PP can be used in many corrosion resistance structures. Copolymer polypropylene (Co-PP) is a bit softer but has better impact strength, is tougher and more durable than PP. Co-PP tends to have better stress crack resistance and lower temperature toughness than homopolymer at the expense of slight reductions in other properties. A large number of end use applications for PP are possible by tailoring grades with specific molecular properties and additives during its manufacture. PP and Co-PP trays are used mainly for ready meals applications or where the food is to be cooked or re-heated in a conventional oven or a microwave while still in the tray, either from a chilled or frozen condition. Isothermal microwave heating at known temperature allows the

separate evaluation of microwave and thermal effects. A microwave assisted extraction device is ideal for this purpose. Studies on the effect of microwaves on inorganic materials into polyethylene have shown that microwaves have little or no effect compared to conventional heating. Calcium carbonate (CaCO_3) is one of the most popular fillers used in the plastic industry. It is widely available around the world, easy to grind or reduce to a specific particle size, compatible with a wide range of polymer resins and economical. It improves mechanical properties (tensile strength and elongation) and electrical properties (volume resistivity). Polypropylene compounds are often filled with calcium carbonate to increase rigidity, a requirement that becomes important at high use temperatures.

In this study, in particular, the effects of CaCO_3 loading on the thermal, physical and mechanical properties of PP/Co-PP and PP/Co-PP/ CaCO_3 composite were studied by differential scanning calorimeter (DSC), fourier transformation infrared (FT-IR), scanning electron microscope (SEM) and instron universal testing machine measurements in detail.

2. Materials and Methods

2.1 Raw material.

PP (polypropylene, HP 6014, homopolymer) was supplied as pellets by HMC Polymers Thailand, Thailand. Co-PP (polypropylene impact copolymer, EP300H) was supplied as pellets by HMC Polymers Thailand. Talc was purchased from Polyline Company, Thailand. Calcium carbonate was purchased from Polyline company, Thailand.

2.2 Preparation of PP/Co-PP/talc Tray.

The PP and Co-PP were mixed in a ratio 50:50 by weight. CaCO_3 was added to the PP/Co-PP of 10, 20, 30 and 40 phr, respectively. The PP/Co-PP / CaCO_3 resin was prepared by a twin screw extruder at 170–220 °C and 30 rpm. The PP/Co-PP / CaCO_3 tray were prepared by injection molding machine at 185–235 °C. Size of rectangular-shaped tray whose height 45 mm,

width at the top 50 mm, width at the bottom 30 mm, thickness 0.67 mm.

2.3 Testing and Characterization of PP/Co-PP/CaCO₃

The compression properties were studied with instron universal testing machine at room temperature. The load cell at 5 kN and crosshead speed 10 mm./min, according to ASTM D695. Reported values were average of three individual measurements. The crystallization behavior, and melting characteristics of the composites were investigated by using a differential scanning calorimetry (DSC 1 star system, Mettler Toledo limited, Thailand) in a nitrogen atmosphere in the heating and cooling rate of 10 °C/min. . In the first heating and cooling scans, the samples were heated from 50 to 230 °C and held at 230°C for 3 minutes to eliminate thermal history, then the non-isothermal crystallization process was recorded from 230 to 50 °C, and a standard status of crystallization was created. Second heating was done at the same scanning rate as the first heating, whereby the melting characteristics of the samples were recorded. FT-IR used Tensor 27, Bruker. The weathered plate was measured by attenuated total reflection (ATR) mode. The surface morphologies of the tray were studied by a scanning electron microscope (Philips XL series scanning electron microscope) with a maximum operating voltage of 10 kV of the apparatus. The sample surface was coated with a thin gold layer by a sputtering machine prior to SEM measurements.

3. Results and Discussion

Chemical changes on PP, Co-PP, CaCO₃ and composites tray were monitored by FTIR. CaCO₃ showed three strong peaks at 1459, 872 and 712 cm⁻¹; these peaks were corresponded to the antisymmetric stretching, in-plane bending, and plane bending vibrations of CO₃²⁻, respectively. (Figure.1) [1-2]. Compositions of CaCO₃ were founded in all of compounded samples.

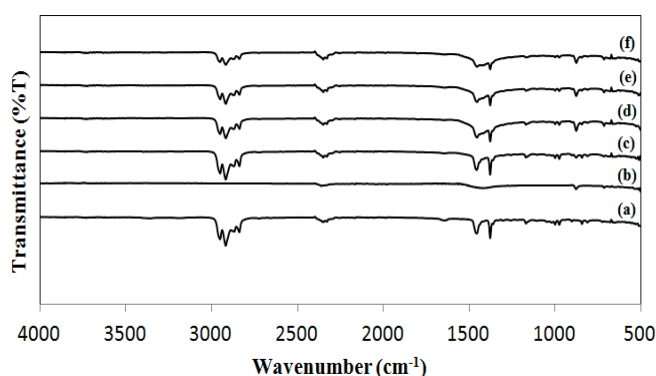


Figure 1. FTIR spectra for (a) control, (b) CaCO₃, (c) PP/Co-PP/CaCO₃ 10 phr, (d) PP/Co-PP/CaCO₃ 20 phr, (e) PP/Co-PP/CaCO₃ 30 phr and (f) PP/Co-PP/CaCO₃ 40 phr

Thermal properties of PP/Co-PP/CaCO₃ compound were analyzed by using DSC technique. Table 1 shows

non-isothermal crystallization and melting temperature of PP/Co-PP and PP/Co-PP filled with CaCO₃ particles (either 10, 20, 30 and 40 wt%). The crystallization temperature (T_c) of PP/Co-PP was observed at about 118.33 °C. Incorporation of CaCO₃ particles of various surface characteristics shifted the T_c value towards a higher temperature while most of the exhibited and crystallization peak, that of PP/Co-PP filled with 30 phr showed one peak. Subsequent melting endotherms of PP/Co-PP and PP/Co-PP filled with CaCO₃ particles (either 10, 20, 30 and 40 wt%) are show in Table 1. Interestingly, all samples showed melting endotherms consistent with that of phase of PP/Co-PP, ie. ~160-162 °C. T_m of PP/Co-PP/CaCO₃ with 40 phr content was lowest at 160.38 °C [3,4].

Table 1: Thermal properties of PP/Co-PP/CaCO₃ tray by DSC

Sample	T_c (°C)	T_m (°C)
Control	125.27	161.84
PP/Co-PP/CaCO ₃ 10 phr	123.13	162.70
PP/Co-PP/CaCO ₃ 20 phr	120.26	161.57
PP/Co-PP/CaCO ₃ 30 phr	122.30	161.41
PP/Co-PP/CaCO ₃ 40 phr	120.55	160.38

Mechanical properties were tested by using compression mode of Instron Universal Testing Machine. Figure 2. shows Young's modulus of PP/Co-PP tray with and without CaCO₃. Young's modulus of PP/Co-PP tray was 231.57 MPa. The highest Young's modulus of polypropylene was 287.10 MPa with CaCO₃ 30 phr. The Young's modulus increased because the incorporation of a second rigid phase into the neat polymeric material significantly enhanced the elastic stiffness. Higher content of the rigid filler subsequently increased the Young's modulus of the composite systems [5]. This was because that, from the young's modulus, the PP/Co-PP composite tray filled with 30 phr of CaCO₃ contents were ductile, and the particle would agglomerates when the content of 40 phr of CaCO₃ was too high, the agglomerates could decrease the young's modulus; while the PP/Co-PP composite filled with high CaCO₃ contents were brittle, the CaCO₃ agglomerates influenced the strength little [6].

Figure 3. shows compressive strength of PP/Co-PP tray with and without CaCO₃. The compressive strength increases with increase in CaCo3 content. Compressive strength of PP/Co-PP tray was 3.22 MPa. The highest compressive strength of PP/Co-PP tray was 4.90 MPa when loading talc was 30 phr. CaCO₃ particles regularly distribute in matrix of PP/Co-PP which shows higher strength. Both of these properties are increased by increase in of filler content for all composites, as expected. It was interesting that, when the CaCO₃ content was low, the compressive

strength of PP/Co-PP composite tray increased, while in the other tree composites, the compressive strength kept almost unchanged or decreased. This was probably that, in the PP/Co-PP composites, the dispersion of CaCO_3 was good, and bonding between CaCO_3 and PP/Co-PP matrix was strong enough, so the microparticles could bear same fraction of the external load, the compressive strength increased; while in the PP/Co-PP composite trays, although the dispersion of CaCO_3 was also good, the interfacial forced between the 30 phr or 40 phr of CaCO_3 particles and matrix PP/Co-PP wasnot strong enough so the compressive strength decreased. It was that, when high content was incorporated, the dispersion of CaCO_3 was very difficult, because microparticles with high surface energy were easy to agglomerate. The agglomerates were easy debond from the matrix.

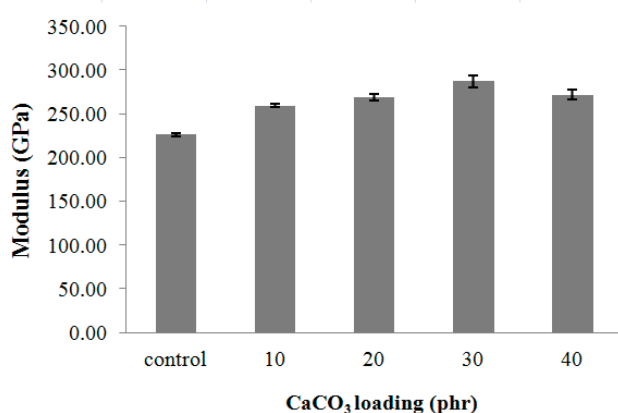


Figure 2. Young's modulus of PP/Co-PP tray with and without CaCO_3

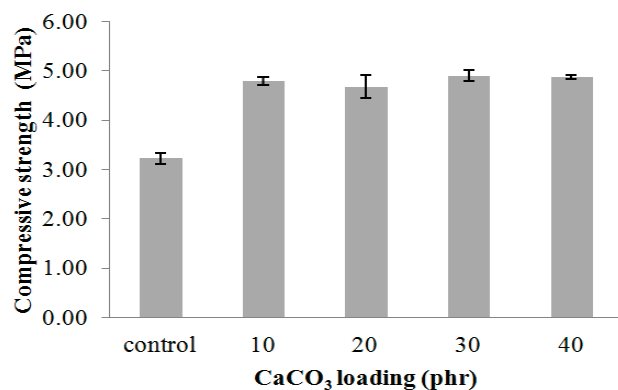


Figure 3. Compressive strength of PP/Co-PP tray with and without CaCO_3

Generally, the crystal structure of a polymer matrix can be significantly affected by the addition of inorganic filler. The alignment of fillers will induce orientation of the polymer crystals during the injection molding process [7]. Surface morphology of PP/Co-PP/ CaCO_3 tray was studied by using scanning electron microscopy (SEM) Fig.4(a) shows smooth surface of PP/Co-PP. The CaCO_3 -filled

composites (Fig.4(b) and (c)) show brittle type failure at all filler loadings. They do not exhibit a tendency towards

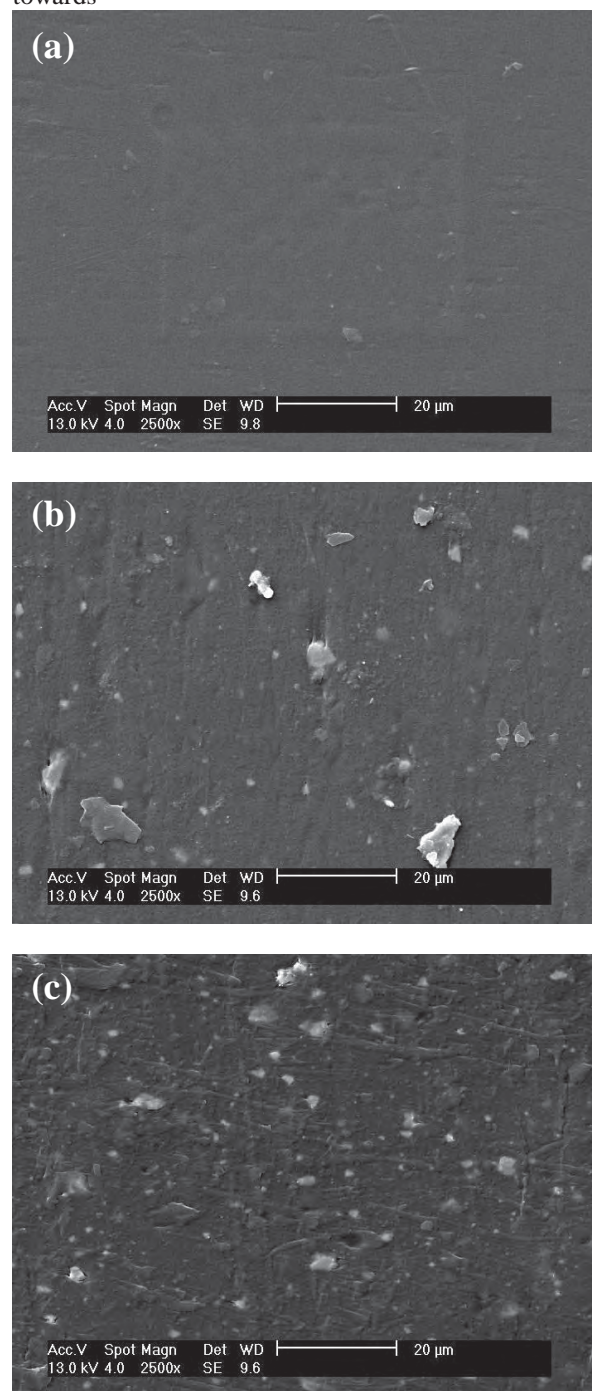


Figure 4. SEM micrographs of PP/Co-PP tray: (a) without CaCO_3 , (b) 20 phr and (c) 40 phr of CaCO_3 loading

the formation of large agglomerates. A significantly stronger CaCO_3 matrix interface is evident from their micrographs. Further, it seems that better filler distribution is achieved in CaCO_3 composites. The differences in fracture morphology correlate with the higher modulus exhibited by CaCO_3 composites. This result confirms that the strength of PP/Co-PP/ CaCO_3 trays could be enhanced by increasing in CaCO_3

content. So, PP/Co-PP/CaCO₃ tray was improved by increase in loading. Hence, the significantly increase in the modulus must be caused by the strong interaction between the polymer and filler, because of the large interfacial between them. We believe that there are two counter balance forces that are affecting the mechanical properties of these composite trays. The reinforcing effect of the CaCO₃ particles. In addition, the strong interaction between the filler and the polymer increased.[8]

4. Conclusions

Production of PP/Co-PP tray, loading CaCO₃ particles improved higher temperature resistance for microwave application. Moreover, strength and compression of PP/Co-OO tray used as matrix could be improved by additional CaCO₃. The results demonstrated that at talc content 30 phr, PP/Co-PP tray was highest temperature resistance and highest strength [9].

Acknowledgements

This study is financially supported by The Graduate School Kasetsart University, Thailand. and Kasetsart University Research and Development Institute (KURDI).

References

- [1] J. Ding, J. Shangguan, W. Ma, Q. Zhong, *Applied Polymer Science*. (2012) 1-13.
- [2] B.A. Bhanvase, D.V. Pinjari, P.R. Gogate, S.H. Sonawane, A.B. Pandit, *Chemical Engineering and Processing*. **50** (2011) 1160–1168.
- [3] S.M. Zebarjad, M. Tahani, S.A. Sajjadi, *Journal of Materials Processing Technology* **155–156** (2004) 1459–1464.
- [4] K. Gorna, M. Hund, M. Vućak, F. Gr'ohn, G. Wegner, *Materials Science and Engineering A* **477** (2008) 217–225.
- [5] A.K. Nurdina, M. Mariatti, P. Samayamutthirian, *Journal of Vinyl & Additive Technology* (2009) 20-28.
- [6] H.G.B. Premalal, H. Ismail, A. Baharin, *Polymer Testing* **21** (2002) 833-839.
- [7] A. Wong, C.B. Park, *Chemical Engineering Science* **75** (2012) 49-62.
- [8] Viera Khunova', Joe Hurst, Ivica Janigova', Vasilij Smatko, *Polymer Testing* **18** (1999) 501–509.
- [9] J. Piwsawang, T. Jinkarn, C. Pechyen, *Advanced Materials Research*. **626** (2013) 711-715.

MICROPARTICLES OF FRAGRANCE: PREPARATION, CHARACTERIZATION AND RELEASE PROPERTY

Ratree Phookchaub^{1*}, Supason Wanichwecharungruang²

¹Program of Biotechnology, Faculty of Science, Chulalongkorn University, Bangkok 10330, Thailand

²Department of Chemistry, Faculty of Science, Chulalongkorn University, Bangkok 10330, Thailand

* Author for correspondence; E-Mail: ratree_phook@hotmail.com, Tel. +66 8 90867135

Abstract: This work focuses on the fabrication of fragrance controlled release system with high fragrance loading. The process involves the fabrication of micron-sized fragrance spheres that combine two release mechanisms, the barrier of Schiff base chemical linkage between fragrant aldehyde or ketone and succinylchitosan and the physical polymer blend barrier. The process requires no preconcentration step to obtain high concentration product. L-carvone was used as a model fragrance. The fabrication involves the synthesis of N-succinylchitosan through the reaction between chitosan and succinic anhydride. Then the obtained product was used in combination with ethyl cellulose and methyl cellulose to encapsulate fragrance by homogenization to obtain L-carvone-loaded microparticles at $72.5 \pm 1.26\%$ loading. The process gave $81.3 \pm 0.97\%$ encapsulation efficiency. The release study under accelerated condition showed that this system could retain the fragranced ketones more effectively than the free ketone.

1. Introduction

Fragrance has been used widely in many fields such as cosmetics, food, textile, detergents, medicine and pharmaceutical industries [1]. However, many of the fragrance molecules are unstable due to their reactive functionalities, such as, alcohols, terpenes, aldehydes and ketones [2], therefore the odor usually fades or changes during storage or use. Therefore, it is of interest to obtain a controlled delivery of the fragrance molecules. Current fragrance delivery technology can be categorized into two groups, those that use physical encapsulation and those that use chemical derivation [3]. The physical encapsulation in which active molecules are surrounded by a layer of material (shell) that prevents their release and the penetration of environmental factors until desired, provides the means to slowly release the active ingredients. Examples of fragrance encapsulation systems include (a) simple coacervation [4] (b) complex coacervation [5] (c) molecular inclusion [6] (d) spray drying [7] (e) spray chilling [8] (f) extrusion [9] (g) freeze drying [10]. Many chemical derivatization have been designed for controlled release such as, Schiff base [11] and acid-labile acetal bonds [12]. The preparations of Schiff base (imine bond) through reaction of aldehydes or ketones with amino groups and of acetal through reaction with

hydroxyl groups in polymeric chains have been demonstrated [13]. Recently, system that combines physical encapsulation and chemical derivatization has also been reported [14]. Nevertheless, process that gives high concentration product without the preconcentration step is very rare. Here we have created a high loading fragrance encapsulation microparticles using imine derivatives of chitosan, ethylcellulose and methylcellulose and demonstrates the controlled release of the system.

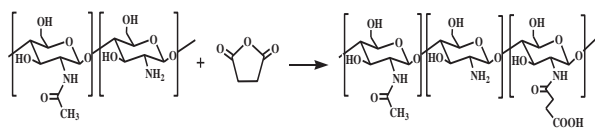
2. Materials and Methods

2.1 Materials

Chitosan ($M_v = 25,000$ Da, 90% deacetylated) was purchased from Taming Enterprises Co., Ltd (Thailand). Succinic anhydride (analytical grade) was purchased from Acros Organics (Geel, Belgium). L-carvone, ethylcellulose (EC) and methylcellulose (MC) were purchased from Sigma Aldrich (Steinheim, Germany). AmberlystTM 15 Wet was purchased from Rohm and Hass Company (Philadelphia, U.S.A.). Ethanol and acetone were purchased from ACI Labscan Limited (Bangkok, Thailand). Acetic acid was purchased from Merck (Darmstadt, Germany). Other reagents were analytical grade and were used without further purification.

2.2 Synthesis of N-succinylchitosan (N-SC)

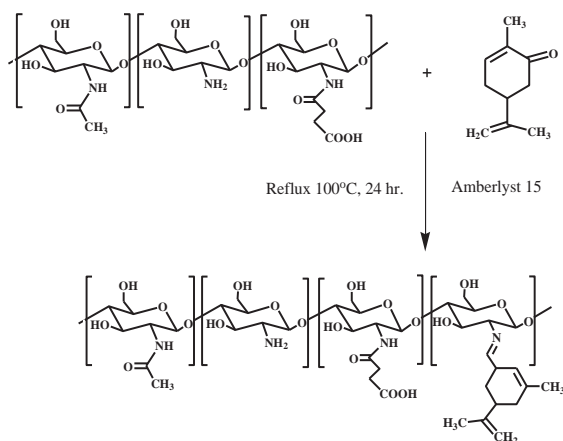
In order to obtain water-soluble property of chitosan polymer, succinyl group, hydrophilic moiety, was firstly grafted on the polymer. N-SC was synthesized according to Scheme 1. Succinic anhydride (0.414 g in 10 mL of acetone) was added drop-wise into acidic chitosan solution (2.01 g in 100 mL of 1% v/v acetic acid) and the mixture was stirred at room temperature overnight. The precipitate was collected by filtration and repeatedly washed with excess acetone, and then dried under vacuum. The product was characterized by Nuclear Magnetic Resonance (NMR; 400 MHz Varian mercury spectrometer, Variance Inc., Palo Alto, USA) and Attenuated total reflectance-Fourier Transform Infrared (ATR-FTIR; Nicolet 6700 FT-IR spectrometer, Thermo Electron Corporation, Madison, WI, USA).



Scheme 1 Synthesis of N succinylchitosan (N-SC)

N-succinylchitosan (N-SC): 88% yields of white powder and 0.19 degree of succinyl grafting. ^1H NMR (D_2O , 400 MHz, δ , ppm): 1.85 (H of acetyl groups), 2.26-2.33 (methylene protons of the succinyl), 2.65 (H2 of glucosamine, GlcN), 3.44-3.73 (H2' of N-acetylglucosamine, GlcNAc, H3, H4, H5 and H6 of GlcNAc and GlcN), 4.38 (H1 of GlcNAc and GlcN). ATR-FTIR (cm^{-1}): 3284 (N-H and O-H stretching), 2874 (C-H stretching), 1639 (C=O stretching of amide I), 1557 (N-H bending of amide II), 1395 (symmetric stretching of COO^- and C-N stretching of amide III), 1319 (C-N stretching of amide III), 1149 (C-O-C stretching) and 1025 (C-O stretching of glucosamine unit).

2.3 Preparation of imine-N-SC



Scheme 2 Preparation of imine-N-SC

Imine-N-SC (Schiff base's derivative) was prepared by heterogeneous phase-grafting reaction [14]. N-SC (100 mg) was dispersed in 20 mL of distilled water. The alcoholic solution (100 mg of L-carvone in 5 mL of ethanol) was dropped into the aqueous phase and the Amberlyst 15 Wet catalyst is added to a reaction system. Then the mixture was refluxed for 24 h at 100°C under nitrogen atmosphere. The amine in N-SC derivatives was allowed to react with ketone (L-carvone) at the weight ratio of N-SC to L-carvone of 1:1, 2:1 and 3:1 (Scheme 2). The imine bond formation was characterized through ATR-FTIR.

2.4 Microparticles formation

L-carvone fragrance was encapsulated into the polymer-blend of EC and MC (EC: MC w/w ratio of 4:1) at L-carvone to polymer weight ratios of 20:1 by microemulsion homogenization. Homogenization of L-carvone in the aqueous solution of imine-N-SC and EC/MC polymers was carried out and the final product was characterized by scanning electron microscopy

(SEM; JSM-6400 scanning electron microscope, JEOL, Tokyo, Japan) and transmission electron microscopy (TEM; JEM-2100, JEOL, Tokyo, Japan). Encapsulation efficiency percentage (%EE), and loading capacity (%loading) of the obtained microparticles were evaluated by performing the hexane extraction on the product and quantifying the L-carvone in the extract by UV-visible spectrophotometer (UV 2500 UV-Vis spectrophotometer, Shimadzu Corporation, Kyoto, Japan) with the aid of a calibration curve.

2.5 Determination of release profiles

Five milliliters of the microparticle aqueous dispersions (pH of 5, prepared from L-carvone to polymer weight ratios of 20:1), were put into a 20 ml flat bottom headspace vial (eight vials for each sample). The vials were left uncovered at 55°C . At the indicated times (0, 1, 2, 3, 5, 8, 11 and 14 days), one of the eight initial vials per sample was pH adjusted to 1.0 with 1 M HCl, filled with 15 ml of hexane and then capped with headspace aluminum crimp caps with PTFE/silicone septa. The hexane layer was then subjected to L-carvone quantification using UV-Vis spectroscopy with the aid of a calibration graph constructed from freshly prepared standard L-carvone solutions.

3. Results and Discussion

3.1 Synthesis and characterizations of N-SC

The successful succinyl moiety grafting was confirmed by NMR and ATR-FTIR. For ^1H NMR spectrum of N-SC in D_2O (Figure 2), signal appearing at 2.26 -2.33 ppm assigned to dimethylene protons of grafted succinyl was observed. Using the integral ratio between 4H from ethyl group of succinyl and 1H from C2 of glucosamine unit (at 2.65 ppm) with 90% deacetylation degree, the degree of grafting could be estimated as 0.19. We found that the obtained chitosan derivative could be apparently soluble in water and also there were amino groups on polymer chain left in order to be coupled with fragrances afterward. ATR-FTIR spectrum (Figure 3) showed new absorption band at 1557 and 1395 cm^{-1} corresponding to N-H bending vibration of amide II and symmetric stretching vibration of COO^- and C-N stretching vibration of amide III, respectively.

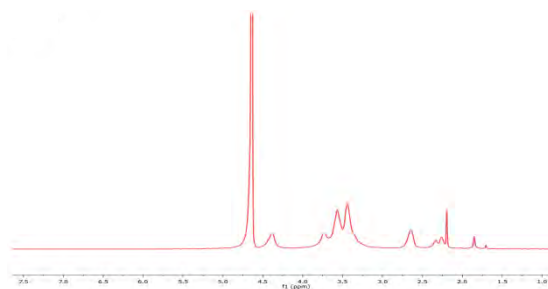


Figure 2 ^1H NMR spectrum of N-SC.

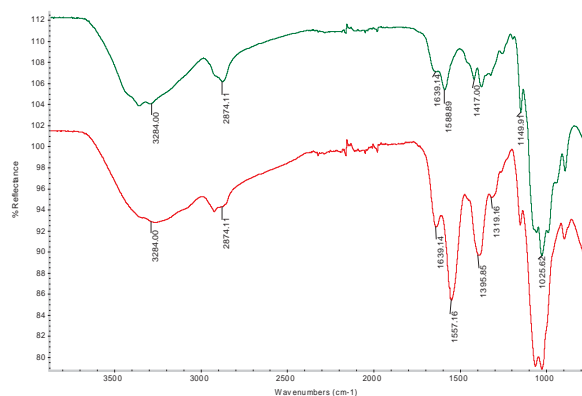


Figure 3 FT-IR spectra of a) chitosan, b) N-SC.

3.2 Preparation of imine-N-SC

In the imine-N-SC was prepared as shown in Scheme 2. Three weight ratios of N-SC to L-carvone (1:1, 2:1 and 3:1) were experimented. IR spectrum of L-carvone-grafted succinylchitosan (Figure 4) showed an absorption peak at 1634 cm^{-1} and 1589 cm^{-1} corresponding to the C=N stretching of imine bond (Schiff base) and the C=C stretching vibration of the aromatic ring, respectively.

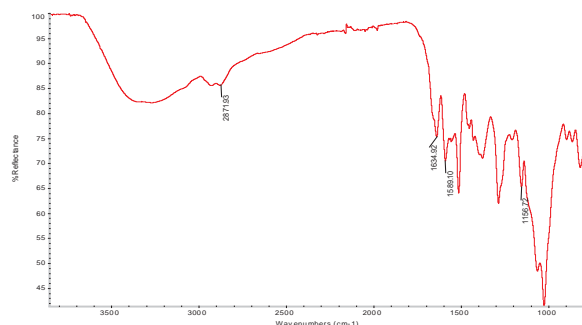


Figure 4 ATR-FTIR spectrum of imine-N-SC.

3.3 Microparticles formation

L-carvone fragrance was encapsulated into the polymer-blend of EC MC and imine derivatives of chitosan by microemulsion homogenization.

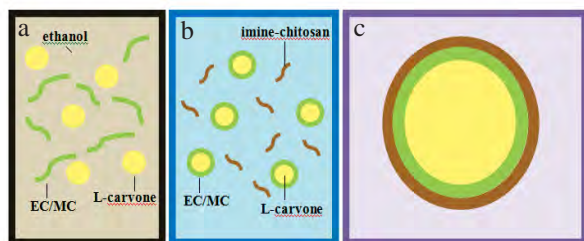


Figure 5 (a) Under homogenization, droplets of L-carvone were suspended in the ethanolic solution of EC and MC. (b) imine derivatives of chitosan was added slowly into polymer-blend solution. (c) microparticles were formed to encapsulate L-carvone.

Encapsulation efficiency and loading capacity were then obtained through analysis of the obtained particle suspensions. Encapsulation efficiency was $81.3 \pm 0.97\%$ and the obtained spheres possessed

fragrance loading of $72.5 \pm 1.26\%$. In order to investigate the morphology of the microparticle, SEM and TEM was acquired, and the SEM and TEM picture indicated microspherical morphology (Figure 6). The Particle sizes of the hydrated (aqueous suspension) L-carvone microparticle were $10 \pm 0.13\text{ }\mu\text{m}$.

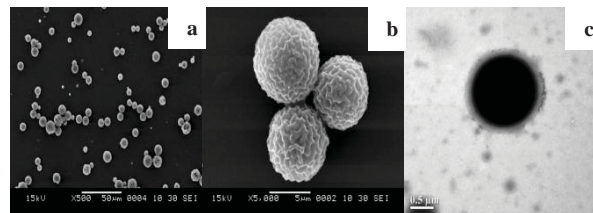


Figure 6 Representative (a, b) SEM and (c) TEM photograph of microparticle.

3.4 Release behavior of L-carvone

An aqueous suspension of the Fragrance encapsulation microparticles was freshly prepared and its L-carvone-release behavior was monitored by UV-Vis spectrophotometer. A controlled release system in this work should be able to protect the L-carvone from the external trigger and should show slow rate of L-carvone release. We examined the release of L-carvone by quantitating the remaining L-carvone molecules. Hexane extraction coupled with acid hydrolysis was used to quantitate the remaining-carvone. As shown in Figures 7, the remaining amount of L-carvone decreased with passing times. All release profiles indicated sustained L-carvone release for the the L-carvone encapsulation microparticles comparing to free L-carvone.

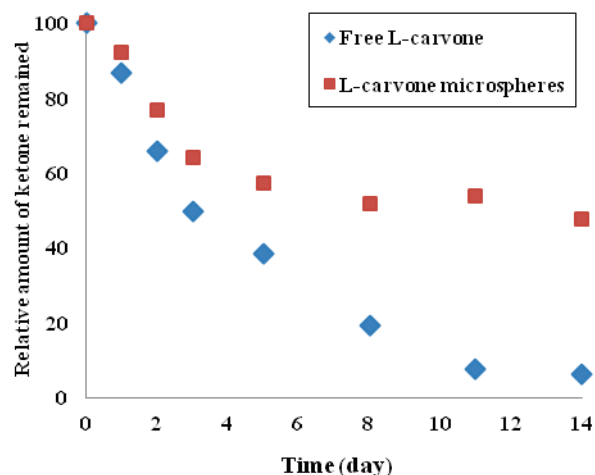


Figure 7 Release profile of L-carvone remained from encapsulation Microspheres compared with free L-carvone.

4. Conclusions

Here a novel loading fragrance encapsulation microparticles using imine derivatives of chitosan, ethylcellulose and methycellulose was successfully created in a form of microparticles. The system contained a chemical derivatization in which the fragrance L-carvone were linked to the NS-chitosan

via imine linkages, and a physical encapsulation in which active molecules are surrounded by a layer of EC/MC polymers. The microparticles showed 14 day slower release of the L-carvone comparing to free L-carvone.

Acknowledgement

We thank the Nanotechnology Center (NANOTEC), NSTDA, Ministry of Science and Technology, Thailand, through its program of Center of Excellence Network and the Centenary Academic Development Project the Special Task force for Activating Research (STAR) at Chulalongkorn University, for financial provisions.

References

- [1] S. Fukumoto, E. Sawasaki, S. Okuyama, Y. Miyake and H. Yokogoshi, Flavor components of monoterpenes in citrus essential oils enhance the release of monoamines from rat brain slices. *Neurosci* **9** (2006) 73–80.
- [2] K.V. Vedantam and T.T. Yong, Fragrance delivery. *Patent Application Publication US A1* (2006) 0172917.
- [3] H. Morinaga, H. Morikawa, Y. Wang, A. Sudo and T. Endo, Amphiphilic copolymer having acid-Labile acetal in the side chain as a hydrophobe: controlled release of aldehyde by thermoresponsive aggregation dissociation of polymer micelles. *Macromolecules* **42** (2009) 2229–2235.
- [4] G. WeiB, A. Knoch, A. Laicher, F. Stanislaus and R. Daniels, Simple coacervation of hydroxypropyl methylcellulose phthalate (HPMCP). *Pharmaceutics* **124** (1995) 87–96.
- [5] J. Xiao, H. Yu and J. Yang J, Microencapsulation of sweet orange oil by complex coacervation with soybean protein isolate/gum Arabic. *Food Chemistry* **125** (2011) 1267–1272.
- [6] S. Branko, Z. Zoran and D. Alfred, Molecular modeling methodology of β -cyclodextrin inclusion complexes. *Molecular Structure* **366** (1996) 113–117.
- [7] S. Apinan T. Kohei, O. Kenji, M. Daisuke, Y. Hidefumi, F. Takeshi, O. Masaaki and L. Pekka, Microencapsulation of lmenthol by spray drying and its release characteristics. *Innovative Food Science and Emerging Technologie* **6** (2005) 163– 170.
- [8] D. G. Oscar, G.G. Lireny and F.G., Microencapsulation of tocopherols in lipid matrix by spray chilling method. *Procedia Food Science* **1** (2011) 1732 – 173.
- [9] J. Uhlemann, B. Schleifenbaum and H. J. Bertram, Flavor encapsulation technologies:an overview including recent developments. *Perfumer and Flavorist* **27** (2002) 52–61.
- [10] A. Wassim, D. Ghania and F. Hatem, Freeze-drying of nanocapsules: Impact of annealing on the drying process. *Pharmaceutics* **324** (2006) 74–82.
- [11] X. Jin, J. Wang, J. Bai, Synthesis and antimicrobial activity of the Schiff base from chitosan and citral. *Carbohydrate Research* **344** (2009) 825–829.
- [12] H. Morinaga, H. Morikawa, Y. Wang, A. Sudo and T. Endo, Amphiliccopolymer having acid-labile acetal in the side chain as a hydrophobe:Controlled release of aldehyde by thermoresponsive aggregation dissociation of polymer micelles. *Macromolecule* **42** (2009) 2229–2235.
- [13] H. Kamogawa, H. Mukai, Y. Nakajima and M. Nanasawa, Chemical Release control-Schiff bases of perfumealdehydes and aminostyrenes. *Polymer Chemistry Edition* **11**(1982) 3121–3129.
- [14] T. Tree-udom, S. P. Wanichwecharungruang, J. Seemork and S. Arayachukeat, Fragrant chitosan nanospheres: Controlled release systems with physical and chemical barriers. *Carbohydrate Polymers* **86** (2011) 1602–1609.

EFFECT OF ELECTRON WITHDRAWING GROUP ON ELECTRICAL CONDUCTIVITY OF POLYTHIOPHENE DERIVATIVE

Songyot Boonkong^{1,2}, Amnard Sittattrakul^{1,2}, Wanchai Lerdwijitjarud^{1,2*}

¹ Department of Materials Science and Engineering, Faculty of Engineering and Industrial Technology, Silpakorn University, Nakhon Pathom 73000, Thailand.

² National Center of Excellence for Petroleum, Petrochemicals and Advanced Materials, Chulalongkorn University, Bangkok 10330, Thailand.

*Corresponding author. E-mail address: wanchai@su.ac.th , Tel. +6634 219663, Fax. +6634 219363

Abstract: In this work, we studied the effect of chemical structure on electrical properties of polythiophene and poly(3-(3-bromopropionyl)-thiophene). Polythiophene and poly(3-(3-bromopropionyl)thiophene) were synthesized by chemical oxidative-coupling of each monomer in dry chloroform using anhydrous ferric chloride as a redox initiator. The 3-(3-bromopropionyl)thiophene monomer was prepared by iodination reaction of thiophene to give 2,3,5-triiodothiophene which was selectively converted to 3-iodothiophene by reaction with zinc and acetic acid. The 3-iodothiophene was then converted to 3-thiophene magnesium iodide by Grignard reaction with magnesium in dry tetrahydrofuran and then transformed to 3-(3-bromopropionyl)thiophene monomer by reaction with 3-bromopropionitrile. The 3-bromopropionitrile derivative of thiophene was converted to 3-(3-bromopropionyl)thiophene by reaction with 20% aqueous hydrochloric acid solution. The chemical structure of the obtained products were characterized by ¹H-NMR and FT-IR techniques. The electrical conductivity under the nitrogen atmosphere of poly(3-(3-bromopropionyl)thiophene) was compared with polythiophene after doping with lithium perchlorate in which the molar ratio of a dopant to each polymer repeating unit was 1:1. The results showed that electrical conductivity of the doped poly(3-(3-bromopropionyl)thiophene and polythiophene were 0.0102 and 0.0183 S.cm⁻¹, respectively. The main reason is that poly(3-(3-bromopropionyl)thiophene) has an electron withdrawing carbonyl group at the 3-position and causes a lowering in electron density in the ring to transport through its main chain.

1. Introduction

Recently, polythiophene has been received an increasing attention for using as gas sensor application. It is also attracted considerable attention due to its easy polymerization, environmental and thermal stability, light weight and high sensitivity to a wide range of volatile organic chemicals (VOCs) [1]. However, it lacks of solubility in solvents and processability which

explains its limited uses. This problem could overcome by the incorporation of substituents to the 3-position of the thiophene ring, which produced not only processable conducting polymers but also allowed the complete chemical and physical characterization of the prepared materials. Specifically, it was found that the introduction of long alkyl side chains increases its solubility in organic solvents, whereas hydrophilic substituents produce polythiophenes that are soluble in water and/or polar solvents [2]. Oscar Bertran et al [3] synthesized poly(3-thiophen-3-yl-acrylic acid methyl ester) by chemical oxidative coupling its monomer in dry chloroform using anhydrous ferric chloride as a redox initiator and found that the obtained polymer could be soluble in a variety of polar organic solvents such as acetone and DMSO.

In this work, we reported the method to synthesize a polythiophene derivatives and also investigated the effect of its structure on electrical properties of polythiophene and their derivative using lithium perchlorate as a dopant.

2. Materials and Methods

2.1 Materials

All materials and solvents were purchased from Fluka, Sigma-Aldrich and Scharlau and were employed without further purification. Molecular sieve was used for drying solvents (chloroform and THF).

2.2 Preparation of 2,3,5-triiodothiophene

A solution of thiophene 10.5 g (0.125 mol), acetic acid (80 ml), water (36.9 ml), dichloromethane (30 ml), sulfuric acid (2.1 ml), iodine (38.1 g), and iodic acid (13.5 g) was refluxed in a three-necked round bottom flask, equipped with a reflux condenser, for 100 h. After that the organic phase was separated and washed with water, 0.1M sodium thiosulfate solution until the solution was clear and followed by washing with water again. The precipitate was filtered off and the remaining solution was evaporated and the residue was recrystallized from ethanol. Finally the obtained 2,3,5-tri-iodothiophene was dried in a vacuum oven

at 60 °C. The yield of the obtained pale yellow product was 50.83 g (88%) [4].

2.3 Preparation of 3-iodothiophene

Water (37 ml), zinc powder (25.45 g) and acetic acid (15 ml) were introduced into a 250 ml three-necked round bottom flask equipped with a reflux condenser and an efficient stirrer. The stirred mixture was heated to boiling for 20 min and 40 g (0.087 mol) of 2,3,5-triiodothiophene was added continuously through the reflux condenser, and the mixture was refluxed for 1 h. The condenser was arranged for downward distillation. Then the mixture was distilled until no more organic substance was distilled off with water. The heavier organic layer was separated, then washed with water and dried over anhydrous magnesium sulfate. The dried organic layer was filtered and fractionated to collect 3-iodothiophene under vacuum at about 100 °C until no more distillate came out. The yield of obtained yellow liquid product was 6.00 g (33.11%) [4], [5].

2.4 Preparation of Highly Reactive Magnesium (Mg*)

Highly reactive magnesium was prepared by the reduction of anhydrous magnesium chloride with sodium using naphthalene as an electron carrier. In a typical preparation, sodium metal 0.223 g (9.68 mmol), naphthalene 0.190 g (1.48 mmol) and anhydrous magnesium chloride 0.448 g (4.71 mmol) were vigorously stirred in 15 ml of freshly distilled THF for 3.5 h at room temperature under nitrogen atmosphere, after that 10 ml of THF was added and finally removed the remaining sodium metal. The newly formed magnesium slurry (black powder) was allowed to settle for 2 h and the supernatant was drawn off via cannula, leaving 4 ml of the solvent to cover the reactive Mg*. Freshly distilled THF was added for 10 ml [6].

2.5 Preparation of 3-(3-bromopropionyl)thiophene

3-Iodothiophene 1.05g (5 mmol) was added to the washed Mg* 7.5 mmol in 15 ml THF. The slurry was stirred at 60 °C under nitrogen atmosphere. After completion of oxidative addition (5-7h), the excess active magnesium (Mg*) was removed out of the organomagnesium solution [6] by a centrifugal apparatus. Then 3-bromopropionitrile 0.670 g (5 mmol) was added to the solution of 3-thiophene magnesium iodide. The solution was stirred at 60 °C for 24 h, after that 20 ml of 20% aqueous HCl solution was added and stirred at 60 °C for 24 h. The organic phase was washed with water for 2×20 ml and the vacuum distillation was performed for removing of THF from the dark-yellow liquid product.

2.6 Polymerization procedure for thiophene and 3-(3-bromopropionyl)thiophene monomer

Chemical polymerization of each monomer was performed by chemical oxidative-coupling in dry chloroform using anhydrous ferric chloride as a redox initiator. This polymerization technique was followed by the method of Elaine Armelin et al [2]. In a 250 ml three-necked flask, 12.98 g (80 mmol) of ferric chloride was dissolved in 60 ml of dry chloroform under nitrogen and stirred for 20 minutes. Then a solution of 20 mmol of monomer in 40 ml of chloroform was added dropwise. The mixture was stirred for 24 h and then stored in the freezer overnight. The reaction mixture was poured into a large excess of methanol (2 L) in order to precipitate the polymer. The precipitated polymer was recovered in chloroform and successively washed with methanol to remove the residual FeCl₃, the residual monomer and small oligomers. Finally, the obtained product was dried under vacuum at 40 °C for 72 h. The yield of dark powder poly(3-(3-bromopropionyl)thiophene) was 41.23 % based on 3-Iodothiophene.

2.7 Characterization

The functional groups of the samples were characterized by using FT-IR (Bruker Optik GmbH: Vertex70, Germany) in the range of 400–4000 cm⁻¹ through pelleting the sample with KBr powder for solid sample and Cell Windows for liquid sample. The chemical structures of the samples were also confirmed by using ¹H-NMR (Bruker: 300 Ultraschield Germany 300 MHz) in CDCl₃.

2.8 Doping polymers with LiClO₄

Polymers 0.03-0.05 g and lithium perchlorate (molar ratio of polymer : dopant is 1:1) were dissolved in 5 ml toluene in vial flask equipped with an efficient stirrer. The solution was stirred for 48 h at room temperature. Then the solution was evaporated in a vacuum oven at 70 °C for 72 h.

2.9 Electrical conductivity measurement

The specific electrical conductivity (σ , S/cm) of each polymer was obtained from measuring the pellet resistance R (Ω) under nitrogen atmosphere at room temperature by using a two-probe electrometer (Keithley 2420) and converted to specific electrical



conductivity by equation $\sigma = \frac{K}{t}$, where t is the pellet thickness and K is the geometric correction factor which is equal to the ratio of w/l , where w and l are the probe width and length respectively. A geometric correction factor was calibrated by using a standard metal sheet with a known specific resistivity. In this study, K is equal to 7.51611×10^{-6} [7], [8].

3. Results and Discussion

The chemical reaction steps for the preparation of 3-(3-bromopropionyl)thiophene which is finally converted to poly(3-(3-bromopropionyl)thiophene) by chemical oxidative coupling are illustrated in Fig 1. The FT-IR spectra in Fig. 2 show the main absorption bands for thiophene, its derivatives and poly(3-(3-bromopropionyl)thiophene). In curve A, the bands at 3108, 3073 1406, 1252, 715 and 833 cm^{-1} correspond to β C–H stretching, α C–H stretching, C=C asymmetric absorption in the thiophene ring, –C–S stretching, α C–H out-of-plane deformation and β C–H out-of-plane deformation, respectively[2],[9]. In curve B, the strong peak of α C–H out-of-plane deformation is not appeared indicating that the α positions (position 2 and 5) of the thiophene ring have been successfully substituted by iodine. In addition, the band at 599 cm^{-1} is related to C–I. Their absorption peaks are confirmed that we have successfully synthesized 2,3,5-triiodothiophene. In curve C, the strong peak at about 763 cm^{-1} confirms that iodine atom at the α -positions of the thiophene ring have been replaced by hydrogen atom which corresponds to 3-iodothiophene. In curve D, the carbonyl group (C=O) appears at 1734 cm^{-1} and the strong peak at 2800-3000 cm^{-1} were due to –CH₂– stretching which confirm that hydrogen at the 3-position of thiophene ring has been replaced by a 3-bromopropionyl group. In curve E, the band at 1724 cm^{-1} corresponding to the carbonyl group and the strong intensity band at the 756 cm^{-1} which is a characteristic of 2,5-disubstituted thiophene rings. Therefore it indicates that the coupling of thiophene ring occurs preferentially at 2 and 5 positions [9]. However, polythiophene shows this characteristic peak at 787 cm^{-1} as indicates in Fig 3A.

The structure of thiophene and their derivatives was confirmed by ¹H-NMR technique and the ¹H-NMR spectra are shown in Fig. 4. The chemical shifts at 7.0-8.0 ppm are assigned to the aromatic protons on thiophene ring. The chemical shift of Fig. 4C and 4D are higher than in Fig. 4A and 4B which are due to the electron withdrawing carbonyl group in the 3-position on thiophene ring which indicates that we have successfully synthesized poly(3-(3-bromopropionyl)-thiophene).

The specific electrical conductivity of polythiophene and its derivative with lithium perchlorate as a dopant was then studied and the results are shown in Table 1. The result shows that the specific electrical conductivity of polythiophene was higher than that of poly(3-(3-bromopropionyl)-thiophene) which is due to poly(3-(3-bromopropionyl)thiophene) has an electron withdrawing carbonyl group at the 3-position and causes a lowering in electron density in the ring to transport through its main chain.

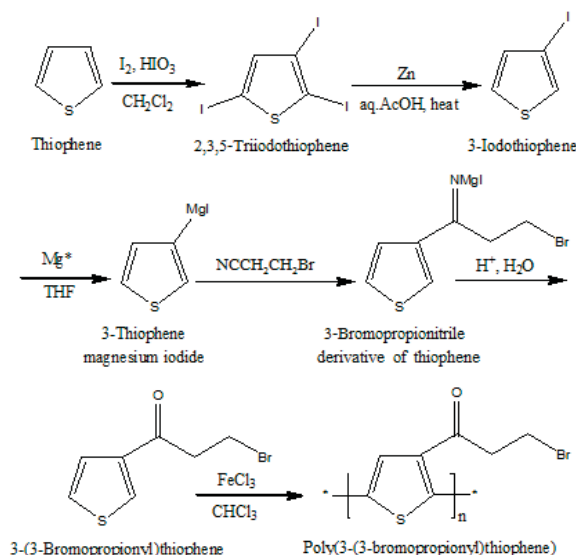


Fig 1. Chemical reactions for the preparation of poly(3-(3-bromopropionyl)thiophene) from thiophene.

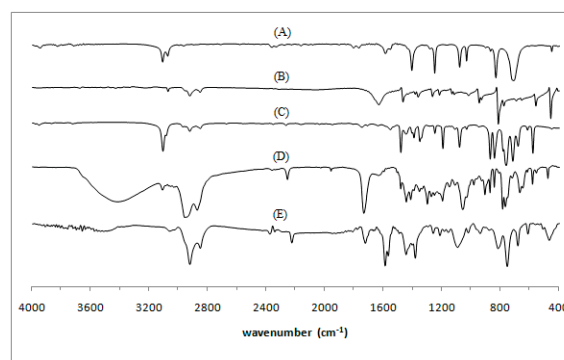


Fig .2 FT-IR spectra of (A) Thiophene, (B) 2,3,5-Triiodothiophene, (C) 3-Iodothiophene, (D) 3-(3-bromopropionyl)thiophene and (E) poly(3-(3-bromopropionyl)thiophene).

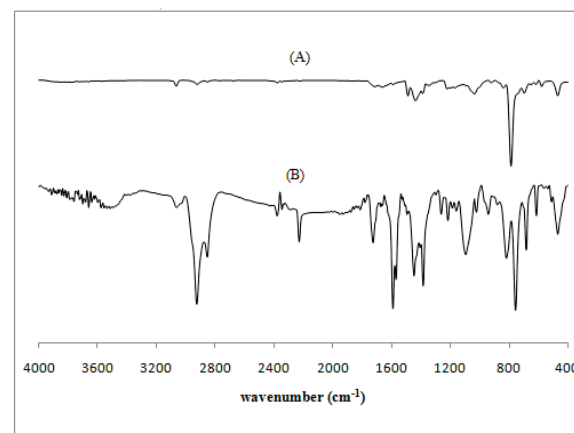


Fig 3. FT-IR spectra of (A) Polythiophene and (B) poly(3-(3-bromopropionyl)thiophene).

Table1: Electrical conductivity of polymers

polymer	t(cm)	R(M Ω)	σ (S/cm)
polythiophene	0.0418	174	0.0183
Poly(3-(3-bromo-propionyl)-thiophene)	0.0101	1300	0.0102

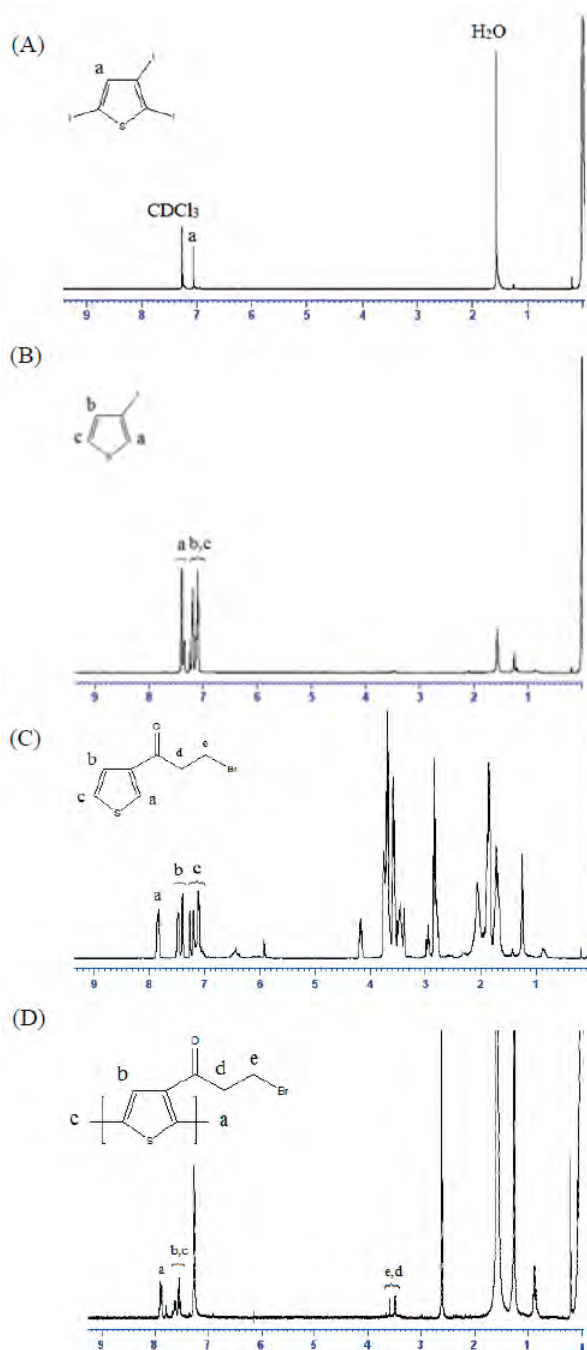


Fig 4. ^1H -NMR spectra of (A) 2,3,5-Triiodothiophene, (B) 3-Iodothiophene, (C) 3-(3-bromopropionylthiophene and (D) poly(3-(3-bromopropionylthiophene).

4. Conclusions

Polythiophene and poly(3-(3-bromopropionyl)-thiophene) could be successfully prepared by chemical oxidative coupling polymerization of each monomer with anhydrous ferric chloride as a redox initiator. The electron withdrawing effect of the carbonyl group on the 3-derivatized polythiophene has influenced the efficiency to transport electrons along the polymer main chain and causes a lowering in electron density in the ring and therefore its electrical conductivity is decreased.

References

- [1] F. Kong, Y. Wang, J. Zhang, H. Xia, B. Zhu, Y. Wang, S. Wang and S. Wu, The preparation and gas sensitivity study of polythiophene/SnO₂ composites, *Materials Science and Engineering B*, 150, (2008), 6–11
- [2] E. Armelin, O. Bertran, F. Estrany, R. Salvatella and C. Aleman, Characterization and properties of a polythiophene with a malonic acid dimethyl ester side group, *European Polymer Journal*, 45, (2009), 2211–2221
- [3] O. Bertran, P. Pfeiffer, J. Torras, E. Armelin, F. Estrany and C.s Aleman, On the structural and electronic properties of poly(3-thiophen-3-yl-acrylic acid methyl ester), *Polymer*, 48, (2007), 6955-6964.
- [4] S. Gronowitz and A. Hornfeldt, Thiophene: Synthesis of Thiophene with Group VII Substituents, (2004), p 720-721, 728
- [5] M. Tishler, A.J. Zambito and R.B. Jobson, *Organic Syntheses*, Coll. Vol. 5, (1973) p.149.
- [6] R.D. Rieke, S. Kim and X. Wu, Direct Preparation of 3-Thienyl Organometallic Reagent: 3-Thienylzinc and 3-Thienylmagnesium iodide and 3-Thienylmanganese Bromide and Their Coupling Reaction, *Org. Chem.*, 62, (1997), 6921-6927.
- [7] N. Puanglek, A. Sittatrakul and W. Lerdwijitjarud, Enhancement of Electrical Conductivity of Polypyrrole and Its Derivative, *Sci. J. UBU*, Vol. 1, No. 1, p 35-42
- [8] W. Prissanaroon, L. Ruangchuay, A. Sirivat and J. Schwank, Electrical conductivity response of dodecylbenzene sulfonic acid-doped polypyrrole films to SO₂–N₂ mixtures, *Synthetic Metals*, 114, (2000), 65-72.
- [9] K. Lakshmi, Development of Thermoplastic Conducting Polymer Composites based on Polyaniline and Polythiophene for Microwave and Electrical Application, Department of Polymer Science and Rubber Technology, Cochin University of Science and Technology, (2007), p116-118

SCREEN PRINTING OF COTTON AND SILK FABRICS WITH A NATURAL DYE FROM LAC

Buppha Somboon¹, Nootsara Narumol¹, Cattaleeya Pattamaprom², Monthon Nakpathom^{1*}

¹ National Science and Technology Development Agency, National Metal and Materials Technology Center, Textile Laboratory, Pathumthani, 12120 Thailand

² Department of Chemical Engineering, Faculty of Engineering, Thammasat University, Pathumthani, 12120 Thailand

* Author for correspondence; E-Mail: monthonn@mtc.or.th, Tel. +66 2 5646500, Fax. +66 2 5646446

Abstract: Due to an increasingly environmental and toxic awareness over the utilization of synthetic dyes in textile industry, a significant attention in natural dyes has been revived. In this research, the possibility of using a natural dye from lac (*Laccifer lacca Kerr.*) as printing colorants on cotton and silk fabrics was investigated. The selected screen printing technique was composed of natural dye extraction by boiling and evaporation, followed by preparation of printing paste, printing on fabrics, drying, color fixation by steaming and soaping. The major goal of this research was to enhance the printing quality of lac dye by pre-mordanting, meta-mordanting and post-mordanting with alum as well as tartaric acid or tannin. The color strength and color fastness to washing and light of the resultant printed fabrics were subsequently evaluated. Based on the experimental results, it was found that the most appropriate improvement of screen printing of lac dye was obtained when pre-mordanting with alum as well as pre-mordanting with tannin were performed on cotton fabrics, whereas pre-mordanting with alum and pre- or meta-mordanting with tartaric acid gave the best results in case of silk fabrics. The color fastness to washing and light of both printed cotton and silk fabrics were at fair to good level.

1. Introduction

As a result of a current demand of eco-friendly and biodegradable products, the interest of natural dye application has been revived [1,2]. Compared to synthetic dyes, natural dyes are believed to be safer alternatives. Despite of their lower toxicity, natural dyes have the following disadvantages; limited availability, low color yield, poor reproducibility, and inferior fastness properties. In order to obtain high color yield, different shades and good fastness properties, metallic salt mordants such as alum, iron sulfate, and copper sulfate are normally employed. Such enhanced characteristics are due to their ability to form coordination complexes with the dye molecules.

Most researches have been focused on the application of natural dyes in dyeing aspects. There is, however, limited works on natural dye printing technology. Agarwal *et al.* studied printing of cotton fabrics with peepal bark dye [3]. Boonroeng *et al.* reported the effect of pre-mordanting and steaming time on printing of cotton fabrics with neem tree bark [4]. Rekaby *et al.* examined

pigment printing of natural dyes from alkanet and rhubarb on wool, silk, cotton and flax fabrics using different metallic mordants [5]. Abou-Okeil and Hakeim used chitosan to improve copper sulfate binding of wool fabrics before printing with a natural lawsone dye [6]. Hakeim *et al.* studied the effect of molecular weight of chitosan on natural color printing of curcumin on cotton [7].

Regarded as one of the most important red natural dyes, lac dye is a resinous protective secretion of the small insect found on the twigs of a number of host trees mainly found in India, China and Southeast Asia [8,9]. This water soluble red dye is composed of a mixture of at least five derivatives of hydroxy anthraquinone carboxylic acids (Figure 1), known as laccaic acids [10]. Stick lac has been used as a raw material to produce seedlac and shellac, which are used in varnishes, paints and printing inks. During the production, the red dye is removed by extraction several times with water and regarded as effluent discharge. It was known that this anionic lac dye has low affinity for cotton and the dyed fabric exhibited poor fastness properties even in the presence of mordants [8,11].

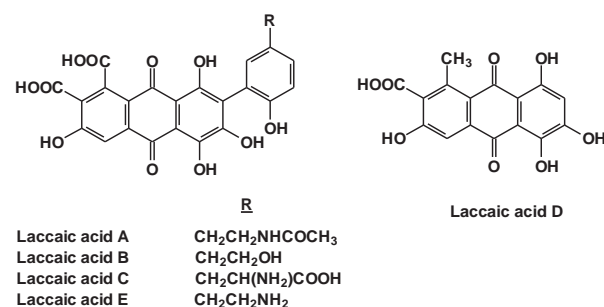


Figure 1. Chemical structures of laccaic acids

In this current work, we explore the screen printing of cotton and silk fabrics with a natural dye from lac (*Laccifer lacca Kerr.*) using three different mordanting methods, i.e., pre-mordanting, meta-mordanting and post-mordanting with alum as well as tartaric acid or tannin. The color strength in terms of *K/S* values and color fastness to washing and light of the printed fabrics were also evaluated.

2. Materials and Methods

2.1 Materials

Commercially scoured and bleached twill woven cotton fabric (208 g/m²) and degummed silk woven fabric (77 g/m²) were used. Natural lac dye was obtained from the northeastern part of Thailand. The following laboratory grade mordants were used, alum (aluminium potassium sulfate, AlK(SO₄)₂·12H₂O, Asia Pacific Specialty Chemicals Ltd., Thailand), tannin and tartaric acid (Merck Ltd.). Guar gum (thickener), Matexil WAKBN (wetting agent) and Marcobac CM (as preservative) were used to prepare printing pastes. Lavenol PA (soaping agent), was supplied by Boonthawee Chemephan Co., Ltd., Thailand.

2.2 Natural dye extraction

The color components of lac dye was extracted by boiling material in water for 1 hour and then filtered. The lac dye solution was later evaporated until 4%Brix concentration was obtained. From visible absorption measurement results, this lac dye solution showed a maximum absorption peak (λ_{max}) at approximately 485-487 nm, which was a characteristic of laccaic acids A and B [10].

2.3 Printing paste preparation

First, the stock thickener paste was prepared as the following recipe: Guar gum thickener 300 g/kg; antifoaming agent 5 g/kg; antibacterial agent (1% w/v) 20 g/kg; urea 200 g/kg and water 475 g/kg. The printing paste was prepared by mixing the lac dye solution and the thickener paste each at 500 g/kg except in the case of meta-mordanting method where a required amount of mordants was added at x g/kg (x = 10, 25 or 50 g/kg) and the thickener paste was reduced to 500-x g/kg. The printing paste mixture was stirred vigorously to produce a homogeneous paste.

2.4 Printing Procedure

The printing paste was applied to the fabrics through the flat screen manually. The printed fabrics were then dried at room temperature and fixed by steaming at 102-105°C for 40 min. Finally, the printed fabrics were successively rinsed with cold water, warm water, soaped with an aqueous solution of 1 g/L LAVENOL PA at 100°C for 5 min, rinsed with cold water and then air dried.

2.5 Mordanting with alum

To investigate the effect of mordanting with alum on *K/S* values of cotton and silk fabrics printed with natural lac dye, these following experiments were conducted. For pre-mordanting method, the fabric was immersed in 10, 25 or 50 g/L of alum solutions and padded on a padding mangle at 80%wpu (wet pick up). After padding, the sample was dried at 100°C for 3 min before

used for printing. In meta-mordanting method, different alum concentrations (10, 25 or 50 g/kg) were added during printing paste preparation. For post-mordanting method, the printed fabric was immersed in 10, 25 or 50 g/L of alum solutions, padded on a padding mangle at 80%wpu, and then dried at 100°C for 3 min.

2.6 Mordanting with alum and tartaric acid or tannin

The fabric was first pre-mordanted with alum at the concentration of 25 g/L as the same procedure as previously described and then used to study the effect of tartaric and tannin mordants. For pre-mordanting method, the alum mordanted fabric was immersed in 10, 25 or 50 g/L of tartaric acid or tannin solutions and padded on a padding mangle at 80%wpu. After padding, the sample was dried at 100°C for 3 min before used for printing. Meanwhile, in meta-mordanting method, different tartaric acid or tannin concentrations (10, 25 or 50 g/kg) were added during printing paste preparation. For post-mordanting method, the printed fabric was immersed in 10, 25 or 50 g/L of tartaric acid or tannin solutions, padded on a padding mangle at 80%wpu, and then dried at 100°C for 3 min.

2.7 Testing and Measurements.

The color strength (*K/S* value) of the printed samples was evaluated using Datacolor 650 spectrophotometer with illuminant D65 at 10 degree observer. The *K/S* value is a function of color depth and is calculated by the Kubelka-Munk equation, $K/S = (1-R)^2/2R$, where *R* is the reflectance of the printed fabrics. The color fastness to washing and light and crocking of the printed samples was determined according to ISO 105-C01:1989 and ISO 105-B02:1994, respectively. The color change of the printed samples was assessed using grey scale ratings, ranging from 1 (very poor), 2 (poor), 3 (fair), 4 (good) to 5 (excellent).

3. Results and Discussion

The *K/S* values of cotton and silk fabrics printed with natural dye from lac with the presence of alum mordant were illustrated in Figure 2. The *K/S* values of printed cotton and silk fabrics were 0.40 and 0.79, respectively. It is clear that mordanting with alum enhanced the color yield of natural lac dye printed on both cotton and silk fabrics, irrespective of mordanting methods and mordant concentrations. This is because this mordant would form an insoluble complex with the dye on the substrate, thus improving the substantivity of the dye to the fiber [1]. Pre-mordanting with alum at the concentration of 25 g/L also yielded maximum *K/S* values of 1.36 for cotton and 2.15 for silk. However, after the printed fabrics was subjected to

color fastness to washing test, only the grey scale ratings of very poor to poor were obtained.

To further increase K/S values and wash fastness property, mordanting with tartaric acid or tannin with different mordanting methods and concentrations in addition to pre-mordanting with alum at 25 g/L was carried out in later experiments. The effect of mordanting with alum and tartaric acid or tannin on K/S values and color fastness to washing and light properties of printed cotton and silk fabrics are listed on Tables 1 and 2. For cotton fabrics, it was found that tannin mostly gave better K/S values than tartaric acid for cotton fabrics. Tannin is known for its ability to bind with cellulosic fibers as a result of the formation of hydrogen bond between phenolic hydroxyl groups of tannin and the hydroxyl groups of cellulose [5]. It also can act as metal chelating agents for metallic salt mordants, including alum [12]. Therefore, this combination of tannin and alum mordants provides much stronger fiber-mordant interactions, resulting in more availability of dye sites. Although pre-mordanting with tannin yielded slightly lower K/S values than meta- and post-mordanting, it provided better wash fastness results, i.e. fair to good ratings (3-4), irrespective of tannin concentration.

On the contrary, higher color yield was apparently obtained with tartaric acid in case of silk fabrics. This was probably due to a synergistic effect of alum and tartaric acid mordants. They are usually used together for mordanting protein fibers during dyeing with natural dyes [13]. Tartaric acid is believed to brightens the color shade as well. Pre- and meta-mordanting with tartaric acid not only gave higher K/S values than post-mordanting, but also showed better wash fastness property, i.e. poor to fair (2-3) compared to very poor to poor (1-2). The light fastness of fabrics printed with natural dye from lac in this study was generally poor to fair (2-3) for cotton and poor to good (2-4) for silk.

4. Conclusions

Red natural dye from lac could be used to print cotton and silk fabrics with screen printing technique with the aid of mordanting with alum, tartaric acid and tannin. The improvement in color yield and color fastness property of the printed fabrics

depended on the methods of mordanting and the types of mordant used. Of the three mordanting methods, pre-mordanting with alum followed by pre-mordanting with tannin gave the best results for cotton. Similar results were obtained for silk when pre-mordanting with alum followed by pre- or meta-mordanting with tartaric acid was performed.

References

- [1] H.T. Deo and B.K. Desai, *J.S.D.C.*, **115** (1999) 224-227.
- [2] H.T. Lokhande and V.A. Dorugade, *Am. Dyestuff Reporter*, **88** (1999) 29-34.
- [3] R. Agarwal, N. Pruthi and J.S.S. Singh, *Man-Made Text. India*, (2007) 367.
- [4] S. Boonroeng, P. Boonkerdrum, M. Chadee and R. Sangkumpra, The qualities improvement of improvement of cotton printed with natural dye from the neem tree bark in the International Conference on the Role of Universities in Hands-On Education Rajamangala University of Technology Lanna, Chiang-Mai, Thailand (2009), pp. 1-7.
- [5] M. Rekaby, A.A. Salem and S.H. Nassar, *The J textile Institute*, **100** (2009) 486-495.
- [6] A. Abou-Okeil and O.A. Hakeim, *Color. Technol.*, **121** (2005) 41-44.
- [7] O.A. Hakeim, A. Abou-Okeil, L.A.W. Abdou and A. Waly, *J. Appl. Polym. Sci.*, **97** (2005) 559-563.
- [8] S. Saxena, V. Iyer, A.I. Shaikh and V.A. Shenai, *Colourage*, **87** (1997) 23-28.
- [9] D. Rastogi, M.L. Gulrajani and P. Gupta, *Colourage*, **47** (2000) 36-40.
- [10] M. Chairat, V. Rattanaphani, J.B. Bremner, S. Rattanaphani and D.F. Perkins, *Dyes Pigm.*, **63** (2004) 141-150.
- [11] M. Suri, B. Sethi, D.K. Bedi and S. Anand, *Colourage*, **47** (2000) 13-18.
- [12] R. Mongkholrattanasit, J. Kryštůfek, J. Wiener, and M. Viková, *J. Text. Inst.*, **102** (2011) 272-279.
- [13] <http://www.spin-knit-dye.com/natural-dyes-mordants.html> (Retrieved February 18, 2013).

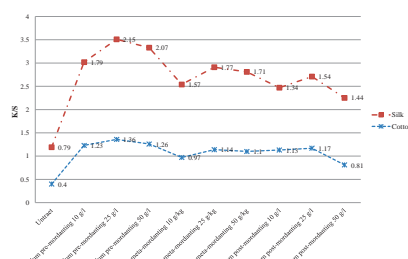



Figure 2. K/S of cotton and silk fabrics printed with natural dye from lac (mordanting with alum)

Table 1: K/S values and fastness properties of cotton fabrics printed with natural dye from lac.

Alum	Mordant		Sample	K/S	Wash fastness			Light fastness		
	Mordanting methods	Conc.			DE*	Color change	Color staining		DE*	Color change
							Cotton	Wool		
Pre-mordanting at 25 g/L	-	-		1.67	28.57	1	4-5	4-5	5.68	2-3
	Tartaric acid pre-mordanting	10 g/l		2.04	25.59	1	4-5	4-5	6.59	2
		25 g/l		2.02	27.70	1	4-5	4-5	3.79	3
		50 g/l		1.26	27.17	1	4-5	4-5	6.78	2
	Tartaric acid meta-mordanting	10 g/kg		1.65	23.19	1	4-5	4-5	6.18	2-3
		25 g/kg		1.62	24.52	1	4-5	4-5	8.72	1-2
		50 g/kg		1.21	38.21	1	4-5	4-5	10.74	1-2
	Tartaric acid post-mordanting	10 g/l		1.93	26.76	1	4-5	4-5	5.34	2-3
		25 g/l		0.81	24.52	1	4-5	4-5	7.39	2
		50 g/l		0.68	28.57	1	4-5	4-5	5.68	2-3
	Tannin pre-mordanting	10 g/l		2.00	2.25	3-4	4-5	4-5	3.90	3
		25 g/l		2.42	2.64	3-4	4-5	4-5	5.26	2-3
		50 g/l		1.76	3.35	3	4-5	4-5	8.35	2
	Tannin meta-mordanting	10 g/kg		2.10	7.41	2	4-5	4-5	3.67	3
		25 g/kg		2.53	4.27	2-3	4-5	4-5	3.31	3
		50 g/kg		1.43	1.67	4	4-5	4-5	8.32	2
	Tannin post-mordanting	10 g/l		3.04	6.48	2	4-5	4-5	5.71	2-3
		25 g/l		2.58	4.68	2-3	4-5	4-5	8.18	2
		50 g/l		2.23	2.01	4	4-5	4-5	8.10	2

Table 2: K/S values and fastness properties of silk fabrics printed with natural dye from lac.

Alum	Mordant		Sample	K/S	Wash fastness			Light fastness		
	Mordanting methods	Conc.			DE*	Color change	Color staining		DE*	Color change
							Cotton	Wool		
Pre-mordanting at 25 g/L	-	-		1.52	9.67	1-2	4-5	4-5	6.05	3
	Tartaric acid pre-mordanting	10 g/l		3.50	4.94	2-3	4-5	4-5	5.44	2-3
		25 g/l		3.40	4.04	3	4-5	4-5	4.21	3
		50 g/l		2.84	3.69	3	4-5	4-5	2.90	3-4
		10 g/kg		2.92	5.29	2-3	4-5	4-5	4.50	2-3
	Tartaric acid meta-mordanting	25 g/kg		2.62	2.58	3-4	4-5	4-5	2.81	3-4
		50 g/kg		2.55	4.49	3	4-5	4-5	3.41	3
		10 g/l		2.05	10.6	1-2	4-5	4-5	3.76	3
	Tartaric acid post-mordanting	25 g/l		1.81	14.42	1	4-5	4-5	6.24	2
		50 g/l		1.52	9.67	1-2	4-5	4-5	4.96	2-3
		Tannin pre-mordanting	10 g/l		1.75	0.71	4-5	4-5	4-5	3.90
	25 g/l			3.40	3.40	3	4-5	4-5	3.40	3
	50 g/l			3.50	1.65	4	4-5	4-5	5.57	2-3
	Tannin meta-mordanting	10 g/kg		2.55	1.79	4	4-5	4-5	8.26	2
		25 g/kg		2.62	2.21	3-4	4-5	4-5	2.89	3-4
		50 g/kg		2.84	1.40	4	4-5	4-5	5.46	2-3
	Tannin post-mordanting	10 g/l		2.92	1.85	4	4-5	4-5	6.77	2
		25 g/l		2.05	1.94	4	4-5	4-5	6.43	2
		50 g/l		1.81	3.94	3-4	4-5	4-5	6.11	2-3

SYNTHESIS OF SINGLE-WALLED CARBON NANOTUBES FROM FERROCENE-ETHANOL MIST USING VERTICAL CVD TECHNIQUE

Kittipong Jantharamatsakarn¹, Sutichai Chaisitsak^{1*}

¹ Department of Electronics Engineering, Faculty of Engineering, King Mongkut's Institute of Technology Ladkrabang, Bangkok, 10520 Thailand

*E-mail: kcsutich@kmitl.ac.th

Abstract: This paper presented the synthesis of single-walled carbon nanotubes (SWCNTs) from ferrocene-ethanol mist using a home-built vertical CVD (chemical vapor deposition) system. The tiny mist was generated using a high-frequency ultrasonic vibration. The effects of the furnace temperature (800-1050 °C) and total flow rate of argon gas (300-2500 sccm) on the formation of SWCNTs were investigated using high-resolution scanning electron microscopy (SEM) and Raman spectroscopy. The furnace temperature and the flow rate of carrier gas were found to determine the diameter and crystallinity (area intensity ratio of G-band to D-band; I_G/I_D) of nanotube. The increasing growth temperatures and the decreasing total flow rate of argon gas resulted in the formation of SWCNTs with larger diameter and high crystallinity. This method does not require vacuum and hazardous gases and is economical and easily scalable for synthesis of SWCNTs.

1.Introduction

Since the discovery of carbon nanotubes (CNTs) by Iijima in 1991[1], have attracted much interest due to their extraordinary mechanical, electrical and optical properties [2-3]. The type of CNT consist of multi-walled carbon nanotube (MWCNT) and single-walled carbon nanotube (SWCNT). The SWCNT has less defect than MWCNT and also can be conducting or semiconducting which depend on structure of SWCNT [4-5]. The synthesis of CNT has several method, such as arc discharge [6], laser vaporization [7] and chemical vapor deposition (CVD) [4-5,8]. The CVD method is the most appropriate for industrial scale production, owing to low cost and low deposition temperature [4-5].

The CVD method has been huge developed, in order to synthesize CNTs continuously and increase the purity of CNTs [9]. Recently, Maruyama et al. has reported the synthesis of SWCNTs from liquid alcohols (methyl, ethyl) and Fe-Co catalysts using a thermal CVD [10-11]. These resulted in a high yield of the SWCNT owing to the role of the decomposed OH radicals. The reaction of OH radical with solid carbon reduces the formation of soot and hence restricts the generation of amorphous carbon in the SWCNT product [10]. Subsequently, Zhu et al.[12], were the first to succeed in the synthesis of long strands of

SWCNTs from n-Hexane with ferrocene and thiophene using floating catalyst method in a vertical furnace. Moreover, Ranadeep et al. [9], reported the synthesis of SWCNTs from alcohol and ferrocene with thiophene catalyst using floating catalyst in a vertical furnace.

In this study, we presented the deposition of thin film SWCNT from ferrocene-ethanol mist using CVD technique under atmospheric pressure. This system was established in vertical direction. In this technique, the mist of ferrocene-ethanol solution was generated by atomizer. Ethanol and ferrocene were used as a carbon source and a catalyst precursor, respectively. The advantage of this synthesis did not need to use vacuum pump and hazardous gas, such as H_2 , CH_4 , CO . In this paper, the effects of furnace temperature and total flow rate of carrier gas on the formation of nanotubes were investigated using field-emission scanning electron microscopy (FE-SEM) and Raman spectroscopy.

2.Experimental

Single-walled carbon nanotubes (SWCNTs) were synthesized by chemical vapor deposition (CVD) method using the tiny mist of liquid hydrocarbon [4]. Here, a home-built vertical CVD system was used (Fig. 1b). Our home-built CVD apparatus consisted of a furnace (500 mm in length), a quartz tube (55mm in outer diameter and 1200 mm in length), a mass flow controllers (MFC), an atomizer (~1.7 MHz, 20-30 W), Ar carrier gas (purity 99.99%) and a precursor solution, as shown in Fig. 1(a). Ethanol (C_2H_5OH ; purity 99.8%) and ferrocene ($Fe(C_5H_5)_2$; purity 98%) were used as a carbon source and a catalytic source, respectively. A precursor was prepared by dissolving ferrocene powder (1 wt.%) in ethanol solution; the solution was ultrasonically stirred for 30 minutes, then transferred into the container attached to the atomizer. After connecting all equipment (Fig. 1(a)), argon was fed into the system to eliminate oxygen from the system. Then, the furnace was heated to the setting temperature in ~30 min. After furnace temperature was stable, the atomizer was turned on, creating a small droplet of ferrocene-ethanol in the reactor. After 30 min of deposition time, the atomizer was turned off

and the reactor cooled down to room temperature under argon atmosphere. A silicon substrate used for collecting the CNTs was set at the outside zone of the furnace [4], about 5 mm away from the end of the furnace. It should be noted that the resulting CNTs grew on the silicon substrates as a black mat-like film that could be easily scraped off.

The characterization of Thin-film CNT was performed by field-emission scanning electron microscopy (FE-SEM). Raman spectroscopic measurements were also carried out at room temperature using Ar laser (514 nm)

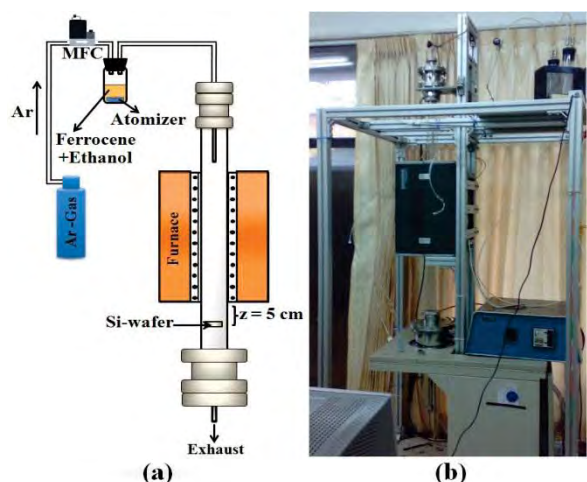


Figure 1. Schematic diagram of the vertical CVD system used for growing SWCNTs

3.result and discussion

3.1 Effect of the furnace temperature

To investigate the effect of temperature on the formation of CNTs, the furnace temperature was varied in the range of 800-1050°C, while the total of argon flow rate and ferrocene/ethanol ratio were kept constant at 2500 sccm and 1 wt.%, respectively.

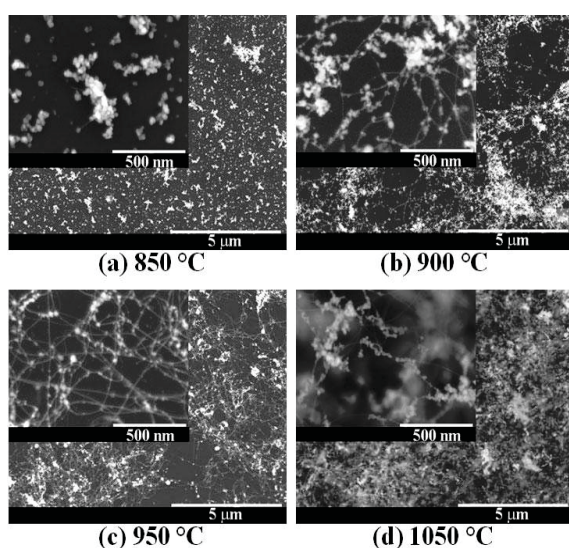


Figure 2. SEM images of CNT films deposited at different temperature: (a) 850°C, (b) 900°C, (c) 950°C and (d) 1050°C. Growth parameters: total flow rate of Ar gas: 2500 sccm, ferrocene/ethanol ratio: 1.0 wt.%.

Figure 2 shows the SEM images of CNTs grown at different temperatures. These SEM images show a significant temperature-dependent morphological change. At the temperature 850°C and below, very short-length and low density CNTs were found. On the other hand, when the temperature was increased to 900°C and above, the long-length and high density CNTs could be obtained, as shown in Fig. 2(b-d). Although further increase in furnace temperature to 1050°C could enhance the amount of long tubes in the films, the amount of large catalyst particles which identified as iron/iron oxide [4] also increased. This could be attributed to the excessively high supply of both carbon and catalysts under a high temperature.

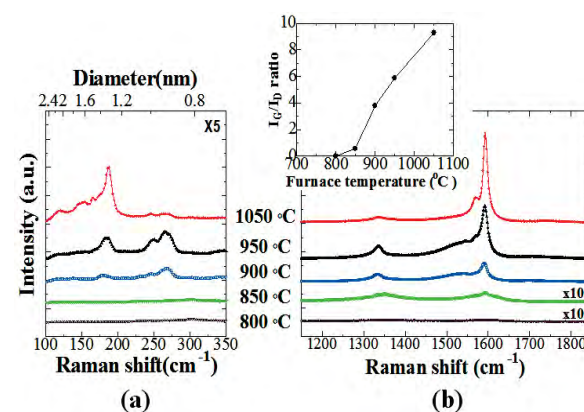


Figure 3. Raman spectra in (a) low-frequency region and (b) high-frequency region of CNT films deposited at different furnace temperature. Inset in (b) shows the corresponding I_G/I_D values. Growth parameters: total flow rate of Ar gas: 2500 sccm, ferrocene/ethanol ratio: 1.0 wt.%.

Figure 3(a) and 3(b) show the corresponding Raman spectra in radial breathing mode (RBM) frequency region and high-frequency region, respectively. The spectra in RBM (100-350 cm^{-1}) are very sensitive to the diameter of SWCNTs [13]. The intense G-band at 1530–1590 cm^{-1} is assigned to the tangential mode of the highly ordered graphite, while the broad D-band at 1330 cm^{-1} is generally associated with disordered or nanocrystalline carbons [13]. As shown in Fig. 3(a), the CNTs synthesized above 850°C showed RBM peaks between 170 cm^{-1} and 270 cm^{-1} . The corresponding diameters of SWCNTs were in the range of 0.9 –1.4 nm, using the empirical relation $d_t = 248/\omega_{\text{RBM}}$, where d_t and ω_{RBM} are the tube diameter (nm) and the Raman shift (cm^{-1}) respectively [13]. A clearly observed multiple-splitting of the G-band in Fig. 3(b) also provides a reliable indication of a presence of SWCNTs within the samples [13]. Moreover, it was found that the RBM peak in low

frequency region shifted toward lower frequencies with increasing the furnace temperature, indicating that the diameter of SWCNTs tended to become larger. It has been previously observed that an increase in temperature results in an increase in catalyst particles size due to the higher agglomeration rate of catalyst particles, thereby forming larger diameter nanotubes [14-15].

Inset in Fig. 3(b) shows the relative area intensities of the G band to D band (i.e. I_G/I_D), which used as an estimate of the quality of the SWCNTs sample. The result shows that the I_G/I_D value increased with increasing the temperature, indicating an increase in crystallinity of the films. This crystallinity enhancement could be possibly due to the etching effect of OH radical decomposed from the ethanol under high temperatures [10, 16]. In this experiment, the CNTs synthesized at 1050°C exhibited the highest I_G/I_D value of about 9.2. However, the optimal temperature for this study was 950°C, since the CNTs synthesized at this temperature showed the lowest amount of impurity particles in the material (Fig. 2)

3.2 Effect of the carrier gas flow rate

In order to investigate the effect of carrier gas flow rate on the formation of CNTs, the total flow rate of Ar was set in the range of 300-2500 sccm, while the furnace temperature and ferrocene/ethanol ratio were kept constant at 950°C and 1 wt.%, respectively

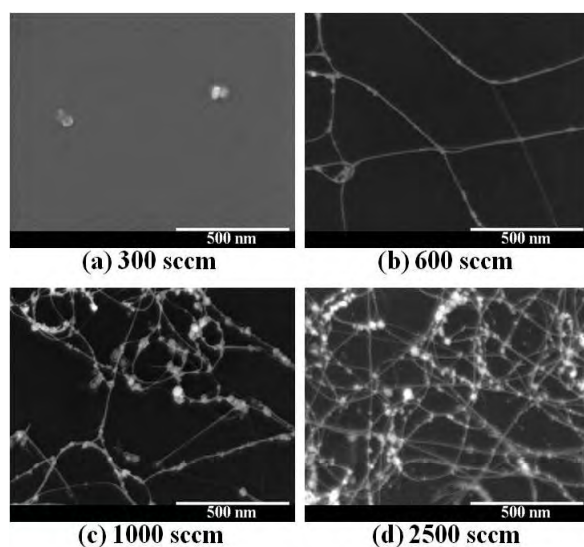


Figure 4. SEM images of CNT films deposited at different total flow rate of Ar: (a) 300 sccm, (b) 600 sccm, (c) 1000 sccm and (d) 2500 sccm. Growth parameters: furnace temperature: 950°C, ferrocene/ethanol ratio: 1.0 wt.%.

Figure 4 shows SEM images of the CNTs synthesized at the different Ar flow rate; (a) 300 sccm, (b) 600 sccm, (c) 1000 sccm and (d) 2500 sccm. As shown in the figure, the flow rate of Ar affected the length of CNTs. For the synthesis under a low flow rate (less than 600 sccm), only large number of particle

impurities was found, as shown in Fig. 4(a). This could be due to the excessively long residence time in the reactor which provides a greater opportunity for catalyst particles to aggregate forming larger particles [17]. For the synthesis under a higher low flow rate, however, the long-length and high density CNTs formed and tended to increase with increasing the flow rate (Fig. 4(b-d)). This could be attributed to the increased feed of carbon to the metal particles, due to the optimum residence time of the catalyst [18].

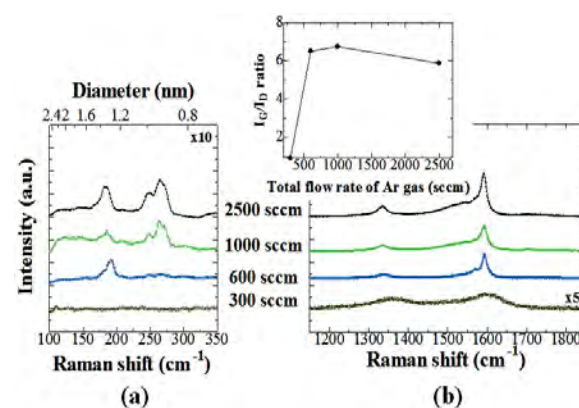


Figure 5. Raman spectra in (a) low-frequency region and (b) high-frequency region of CNT films deposited at different flow rates. Inset in (b) shows the corresponding I_G/I_D values. Growth parameters; furnace temperature: 950°C, ferrocene/ethanol ratio: 1.0 wt.%.

For the synthesis under a medium and high flow rate (600 – 2500 sccm), the I_G/I_D value of films did not change with the flow rate, indicating no significant change in crystallinity (Fig. 5(b)). However, it was found from the RBM peaks in Fig. 5(a) that the RBM peak shifted toward lower frequencies with decreasing the flow rate, indicating that the diameter of SWCNTs tended to become larger. This could be assumed that the lower flow rates lead to the longer residence time which provides a greater opportunity for Fe catalyst particles to collide and to aggregate forming larger particles [17]. As a consequence, the diameter of CNTs becomes larger. On the other hand, the RBM peaks did not appear when grown at a 300 sccm flow rate. This result was consistent with the SEM results described earlier.

4. Conclusions

In this paper, we have presented a simple and low cost method to synthesize SWCNTs by using a vertical CVD apparatus. This method was performed at a normal pressure (1atm) using the mist of ferrocene-ethanol. The effects of the furnace temperature (800-1050°C) and total flow rate of argon gas (300-2500 sccm) on the formation of SWCNTs were investigated using high-resolution scanning electron microscopy (SEM) and Raman spectroscopy.